Mitigation Strategies for Calcium-Magnesium-Aluminosilicate (CMAS) Attack on Environmental Barrier Coatings

---

A Dissertation

Presented to

the faculty of the School of Engineering and Applied Science

University of Virginia

---

in partial fulfillment
of the requirements for the degree

Doctor of Philosophy

by

Rebekah Ireland Webster

May 2019

APPROVAL SHEET

This Dissertation
is submitted in partial fulfillment of the requirements
for the degree of
Doctor of Philosophy

Author Signature: ____________________

This Dissertation has been read and approved by the examining committee:

Advisor: Elizabeth Opila

Committee Member: Jon Ihlefeld

Committee Member: Andres Clarens

Committee Member: Bi-Cheng Zhou

Committee Member: Valerie Wiesner

Committee Member: ____________________

Accepted for the School of Engineering and Applied Science:

Craig H. Benson, School of Engineering and Applied Science

May 2019

Acknowledgements

First, I would like to thank the Office of Naval Research (ONR) and Rolls-Royce (RR) for providing funding for this research. Special thanks go to program managers Dr. David Shifler (ONR) and Dr. Li Li (RR). Thank you to my advisor, Beth, for her guidance and support throughout my Ph.D. Thank you for making me a better scientist and being a role model I will always strive to emulate. Thank you to my committee for their helpful comments. Thank you especially to Dr. Valerie Wiesner for giving me the opportunity to intern with her at NASA Glenn. I am lucky to have had not one, but two amazing women scientists as mentors during my Ph.D. I would like to thank Professor Alexandra Navrotsky, Dr. Sergey Ushakov, and the UC Davis Peter A. Rock Thermochemistry Lab for bringing me with them to the Advanced Photon Source (APS) and introducing me to high temperature synchrotron levitation experiments. I would also like to thank Dr. Chris Benmore and Dr. Rick Weber from Argonne National Laboratory for their assistance at the APS. Thank you to my groupmates, past and present, who have helped me in the lab. Thank you to Joe Hagan for helping me get started, Rob Golden for training and laboratory advice, and Bonnie McFarland and Lucas Herweyer for assistance with ICP. Thank you to Cameron Miller for helping me with sample preparation, testing, and characterization. Thanks also to Jeroen Deijkers for training on SPS. Thank you to the research staff at UVa who have trained me on various characterization equipment: Richard White, Joe Thompson, Michal Sabat, Diane Dickie, and Cathy Dukes. Thank you to the MSE administration team for all of their hard work. Finally, a big thank you to all of my Opila groupmates. I will always cherish our time together and our friendships. Thank you especially to Cory Parker for navigating grad school/life with me. Thank you to my parents and Nathan for being endless supplies of love, inspiration, encouragement, and support. Thank you to all of my family and friends.

Abstract

Calcium magnesium alumino-silicate (CMAS) attack is a pressing issue in the development of environmental barrier coatings (EBCs) for ceramic matrix composites (CMCs). CMAS originates as siliceous debris such as sand or volcanic ash, which can be ingested into aircraft turbine engines during flight. At temperatures greater than ~1200°C, CMAS melts and can penetrate EBC materials, causing premature coating failure.

There is debate in the literature as to whether EBC materials sought for CMAS mitigation should be reactive or nonreactive with molten deposits. Due to the presence of coating defects such as grain boundaries, cracks, and pores, which are susceptible to CMAS penetration, it is hypothesized that an EBC material that reacts rapidly with CMAS to form a protective crystallized layer is better able to resist CMAS infiltration compared to one that is inert. This hypothesis was confirmed in the current work through investigation of the interaction behavior between CMAS and either rare earth (RE) titanates, RE silicates, or standalone apatite ($Ca_2RE_8(SiO_4)_6O_2$; a commonly observed reaction product between RE coatings and CMAS) at 1300°C. The results of this work show that inducing rapid crystallization at the coating/glass interface reduces the ability for CMAS to penetrate defects and leads to slower infiltration. Of the EBC materials studied, Yb_2SiO_5 (YbMS) was best able to resist CMAS infiltration. YbMS reacted quickly with the glass to form either apatite or $Yb_2Si_2O_7$ (YbDS), depending on the initial CMAS composition. Infiltration in YbMS was drastically slower than in the current standard EBC material, YbDS, which did not react with CMAS to form new crystalline phases and was instead penetrated via grain boundaries.

The effect of EBC microstructure on CMAS infiltration behavior was explored in model materials containing controlled amounts of YbMS within a YbDS matrix. YbMS was introduced either as “splats” (to model an air plasma spray (APS)-deposited EBC) or as a “fine dispersion.” The addition of YbMS to YbDS improves overall material resistance to CMAS infiltration. It was determined that including ≥ 20

vol% YbMS was beneficial in reducing glass penetration, as compared to phase pure YbDS. Model APS coatings exhibited a combination of grain boundary attack (of the YbDS matrix) and reactive crystallization of YbMS granules (most notably to form apatite). The formation of apatite slowed the incoming CMAS front. Fine dispersion samples were not penetrated as deeply as model APS materials due to glass spreading on their surfaces.

Experimental viscosity data was obtained for several CMAS-related melts. The effect of Ca/Si ratio and Al_2O_3/MgO content was assessed. Increasing the Ca/Si ratio (from 0.37 to 0.73) and MgO content (to 20 mol%) resulted in decreased viscosity, while increasing the Al_2O_3 content (to 30 mol%) resulted in increased viscosity. Results were compared to three viscosity models commonly cited in the literature (by FactSage, Fluegel, and Giordano et al.). The FactSage model was unequivocally the best at describing experimental viscosity data. CMAS viscosity was related to coating infiltration using melt infiltration models available in the literature. Infiltration cannot be described without considering the formation of crystalline reaction products between coating and glass.

The findings from this work address critical questions related to EBC design for CMAS mitigation. EBCs deposited by APS will contain coating defects such as grain boundaries and pores. Thus, material selection should seek to maximize reactivity between the coating and glass to form favorable phases that can slow incoming CMAS. The addition of YbMS to YbDS drastically improves the ability for model materials to resist infiltration. This is an important insight, as actual APS-deposited YbDS coatings will contain some YbMS. The results of this study show that a critical amount of YbMS is needed to induce improved behavior. This suggests that APS processing techniques can be tailored to optimize CMAS mitigation while maintaining other critical coating requirements. Finally, experimental viscosities for CMAS glasses were obtained and it was found that the FactSage model is best suited for future applications needing to describe glass viscosity. Current coating infiltration models indicate that EBC porosity is the most important coating-related parameter and glass viscosity is the most important

CMAS-related parameter in predicting CMAS infiltration rates. Additionally, EBC phase constitution is critical, as reaction product formation between the coating and CMAS can block pores/penetration pathways. However, none of the available models accurately described experimental coating infiltration results.

Table of Contents

List of Figures

List of Tables

1. Introduction

The growing demand for more efficient gas turbine engines has resulted in significant increases in aircraft turbine operating temperatures (Figure 1.1). Advances in the development of nickel-base superalloys, thermally protective coatings for superalloy components (thermal barrier coatings, TBCs), and cooling technologies have allowed superalloy components to reach nearly their melting temperature during operation [1-6]. With this limitation in mind, new material systems that can withstand higher temperatures are of interest. Silicon carbide (SiC)-based ceramic matrix composites (CMCs) are an attractive alternative to nickel-base superalloys, as they are lighter and can reach higher temperatures with reduced need for cooling air [2, 7-9], as shown in Figure 1.1.

Silicon carbide (SiC) is highly resistant to oxidation in dry air due to the formation of a slow growing, protective silica (SiO_2) scale [10, 11]. However, when exposed to a combustion environment containing water vapor, such as that experienced in turbine engines, SiO_2 will react to form gaseous silicon hydroxide ($Si(OH)_4$) [12]:

$$SiC + \frac{3}{2}O_2(g) \rightarrow SiO_2 + CO(g) \tag{1.1}$$

$$SiO_2 + 2H_2O(g) \rightarrow Si(OH)_4(g) \tag{1.2}$$

To prevent this reaction from taking place, SiC-based CMCs require a non-reactive, protective topcoat, referred to as an environmental barrier coating (EBC) [13].

The protective quality of an EBC is threatened when the coating comes into contact with calcium magnesium alumino-silicates (CMAS) [9, 14, 15]. CMAS originates as sand, ash, and other types of siliceous debris that can be ingested with the intake air of an aircraft engine. CMAS melts ~1200°C and can thus deposit in the molten state on the engine's hot-section components. Failure of the coating occurs via a combination of thermochemical and thermomechanical interactions. EBC constituents can rapidly dissolve in the melt and re-precipitate as new crystalline phases. Coefficient of thermal expansion (CTE) differences between the glass or the reaction layer and the coating/underlying CMC can lead to spallation, which compromises the EBC's hermetic properties. The search for coating materials that are resistant to CMAS attack remains critical.

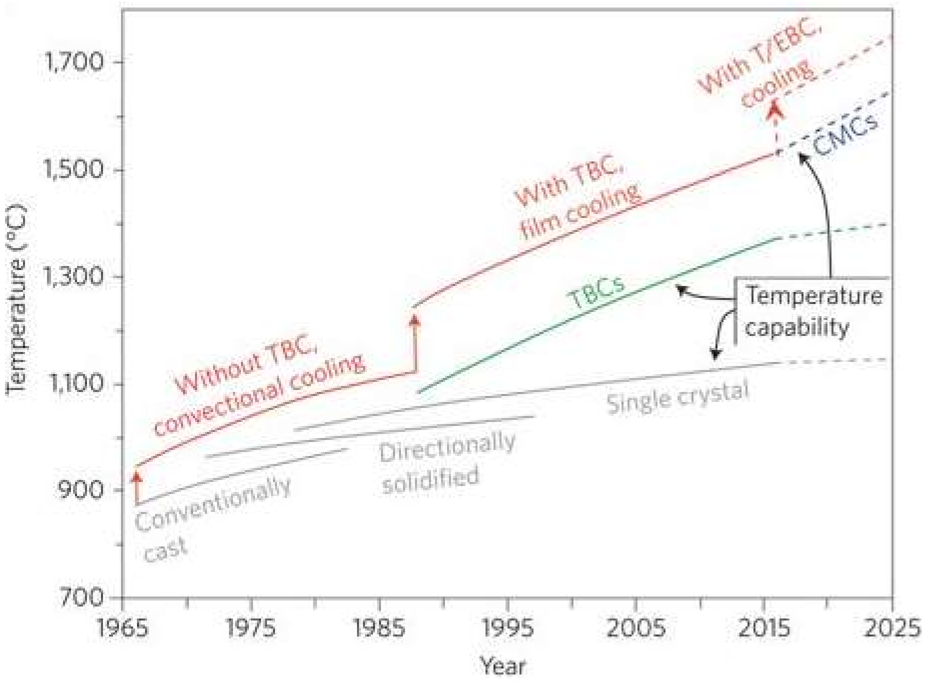

Figure 1.1. *The evolution of gas turbine inlet temperature resulting from advances in nickel-base superalloy design, cooling mechanisms, and ceramic coatings. The implementation of CMCs as a replacement material for nickel-base superalloys will allow continued temperature increases. From [2].*

1.1 Sources and composition/properties of CMAS deposits

The earliest known observations of CMAS deposit-induced corrosion were made around the early 1990s on aircraft engines serviced in desert environments [16-19]. These deposits were sand-type and were mostly composed of SiO_2 and CaO with moderate amounts of MgO, Al_2O_3, and FeO_x, and trace amounts of NiO, TiO_2, Na_2O, and/or K_2O. The presence of NiO and TiO_2 has been attributed to erosion of upstream engine components [20]. The deposit compositions, described by their predominant oxides, can be found in Figure 1.2 and are compared to natural sand sources. Also of interest and plotted in Figure 1.2 are the compositions of some volcanic ash-type deposits. Engine failure in aircraft flying near volcanic eruption plumes had been investigated as early as in the '90s [21], but became a significant problem during the 2010 eruption of Iceland's Eyjafjallajökull volcano, which caused a week-long air traffic shutdown in Europe and nearly two billion dollars in economic loss [22-24]. Volcanic ash glasses are also SiO_2 rich, but typically contain less CaO and more Al_2O_3, FeO_x, Na_2O, and K_2O (Figure 1.3a). In laboratory experiments, synthetic compositions based on the chemistry of sand and ash-type deposits are typically prepared from constituent oxides. Previously studied models can be seen in Figure 1.2; many are simplified to only contain CaO-MgO-Al_2O_3-SiO_2.

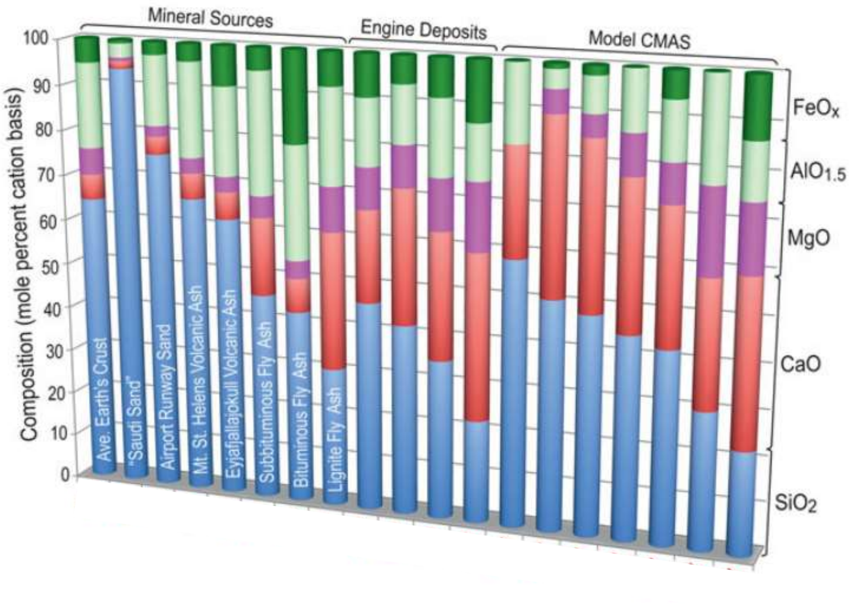

***Figure 1.2**. Composition range of calcium magnesium iron alumino-silicates (CMFAS; mol% cation basis) based on mineral sources, engine deposits, and model preparations from the literature. From [20].*

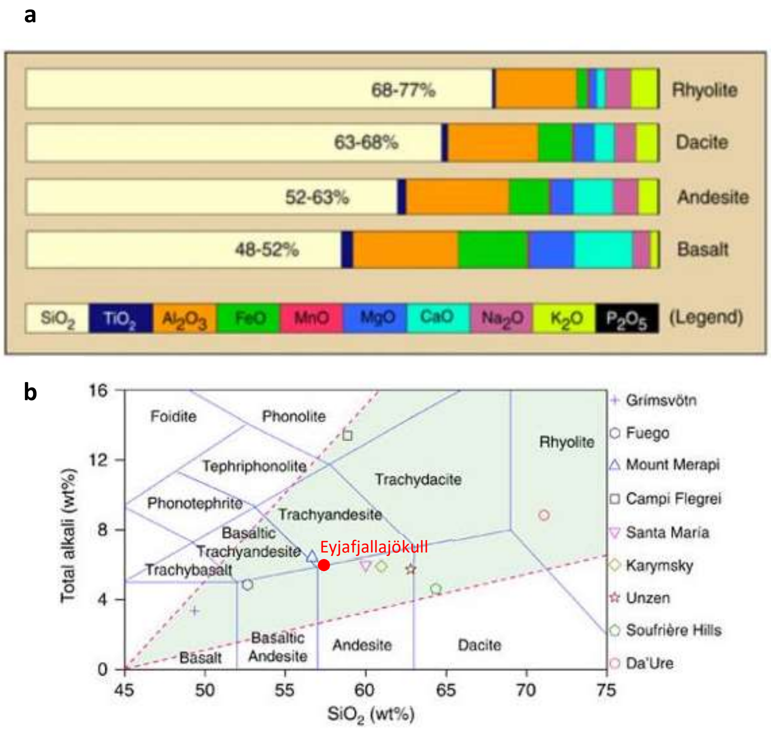

***Figure 1.3**. (a) Typical compositions for relevant volcanic ash geochemistries. (b) Geochemical classifications of ash as a function of SiO_2 and alkali content. The composition space for ash samples from past eruptions is plotted. From [23, 24].*

It is evident that there can be relatively large variations in CMAS composition depending on the source. In considering CMAS interaction with protective barrier coatings (thermal and environmental barrier coatings), researchers are most concerned with CMAS in the molten state; therefore, the properties of CMAS that are of great importance, and that can distinguish variations in glass composition, include melting temperature and viscosity.

The range of possible liquid compositions was probed at 1300 and 1500°C using calculated phase equilibria for the CaO-$AlO_{1.5}$-SiO_2 (CAS) ternary, as well as CAS with constant 10 mol % FeO_x and/or MgO [14, 25]. In looking at the CAS ternary (Figure 1.4a), it can be seen that melting will initialize, depending on composition, at eutectic temperatures of 1185 or 1257°C. At 1300°C (Figure 1.4a), the liquid phase field is narrow with respect to $AlO_{1.5}$ concentration but encompasses a wide CaO/SiO_2

range. As temperature is increased to 1500°C (Figure 1.4b), the melt composition range expands with respect to both $AlO_{1.5}$ and CaO/SiO_2.

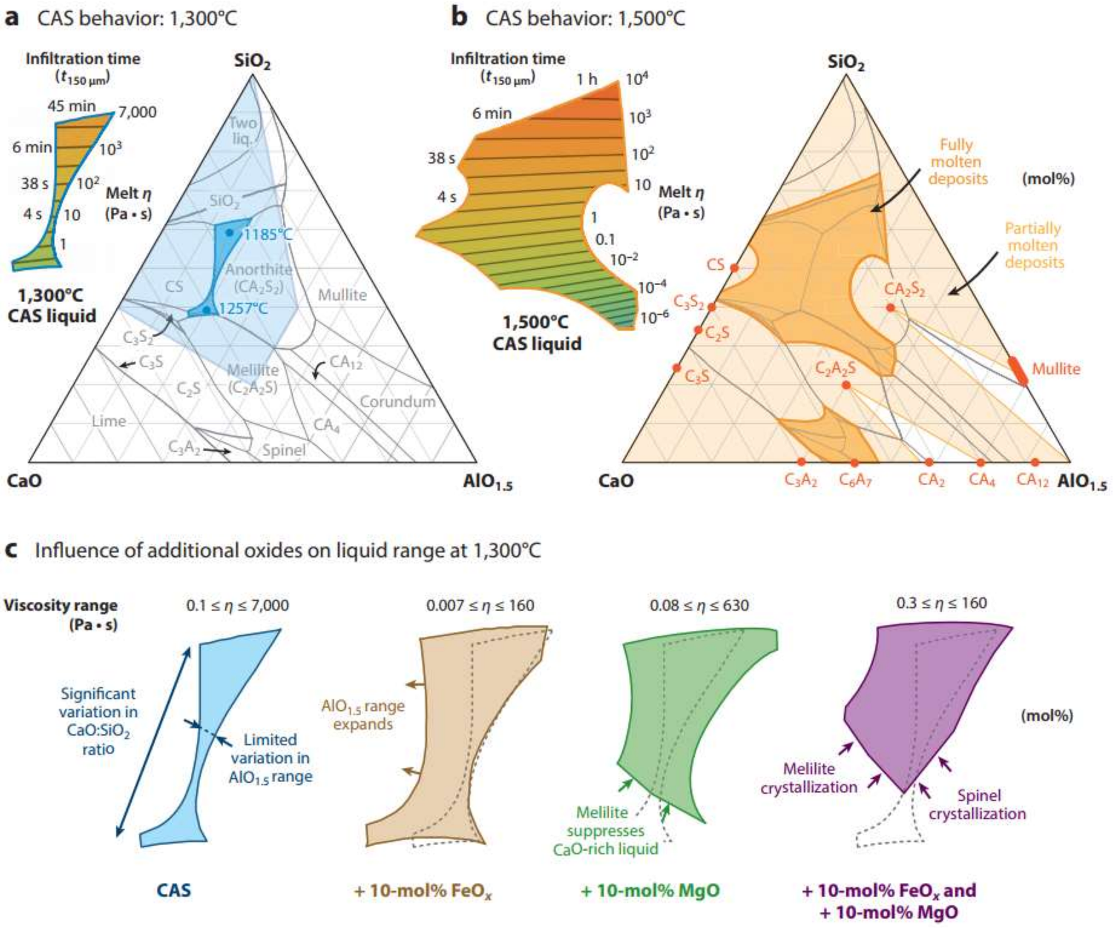

***Figure 1.4**. Ternary $CaO-AlO_{1.5}-SiO_2$ phase diagram at (a) 1300°C and (b) 1500°C. Shaded areas indicate molten and partially molten deposits. The viscosities (η, Pa·s) of the molten deposits at each temperature, according to the Giordano et al. model, are inset in (a) and (b), along with time to complete infiltration of a 150 μm thick 7YSZ TBC. The influence of FeO_x and MgO on the liquid phase field at 1300°C is presented in (c). From [14].*

The addition of 10 mol % FeO_x and/or 10 mol % MgO to CAS increases the range of $AlO_{1.5}$ dissolved in the liquid phase at 1300°C (Figure 1.4c). In looking at the CaO/SiO_2 range, however, 10 mol % MgO and combined 10 mol % MgO with 10 mol % FeO_x suppresses the CaO-rich portion of the liquid field to some degree due to the crystallization of melilite (MgO alone) and spinel (MgO and FeO_x). Despite some restriction to CaO/SiO_2, it can be concluded that at ≥ 1300°C, CMAS and CMFAS compositions with a relatively wide CaO/SiO_2 range and $AlO_{1.5}$ content should be considered in experimental and modelling approaches.

In addition to Al_2O_3, MgO, and FeO_x, Na_2O and K_2O have also been reported as deposit additions, although typically in much smaller quantities (Figure 1.3a). The presence of even a small amount of alkali metal oxide in a CMAS deposit can significantly decrease its solidus temperature. Thermodynamic calculations have been used to predict that the inclusion of Na_2O and K_2O contents in volcanic ash and sand-based compositions cause the start of melting to occur at temperatures up to 325°C lower than when these chemistries are ignored [14]. However, it is likely that these constituents volatilize when exposed in a water vapor-containing engine environment.

The viscosity (in Pa·s) is also labeled alongside the liquid phase fields plotted in Figure 1.4a/b. Viscosity describes the ability of a glass to flow and, ultimately, penetrate open channels or defects in a T/EBC. Viscosities as low as 10^{-6} Pa·s are calculated (for CAS at 1500°C; Figure 1.4b) according to the Giordano-Russell-Dingwell model [26]. According to this model, and considering a 150 µm thick TBC (7 wt% Y_2O_3 stabilized ZrO_2, or 7YSZ), it would take about 6 min for glass with a viscosity of 10^3 Pa·s (9 orders of magnitude higher than the lowest reported viscosity in Figure 1.4b) to reach complete infiltration. Other viscosity models, such as those based on the FactSage Viscosity Module and Melt Database [27] and Fluegel [28], have also been used to describe CMAS melts. Wiesner et al. experimentally measured the viscosity of a synthetic sand glass with the composition 23.3CaO-6.4MgO-3.1Al_2O_3-62.5SiO_2-4.1Na_2O-0.5K_2O-0.04Fe_2O_3 (mol %) for comparison to the Giordano et al., FactSage, and Fluegel models [29]. The log viscosity (η, in Pa·s) experimental and model data for the glass is plotted versus temperature in Figure 1.5. It is shown that the FactSage and Fluegel models more closely match the data obtained experimentally; values from the Giordano et al. model overestimate by at least an order of magnitude. There are a number of other empirical (alongside the Giordano et al. and Fluegel models) and structure-based (such as FactSage) viscosity models that are relevant for describing CMAS melts [30]; these will be discussed in more detail in Chapter 4.

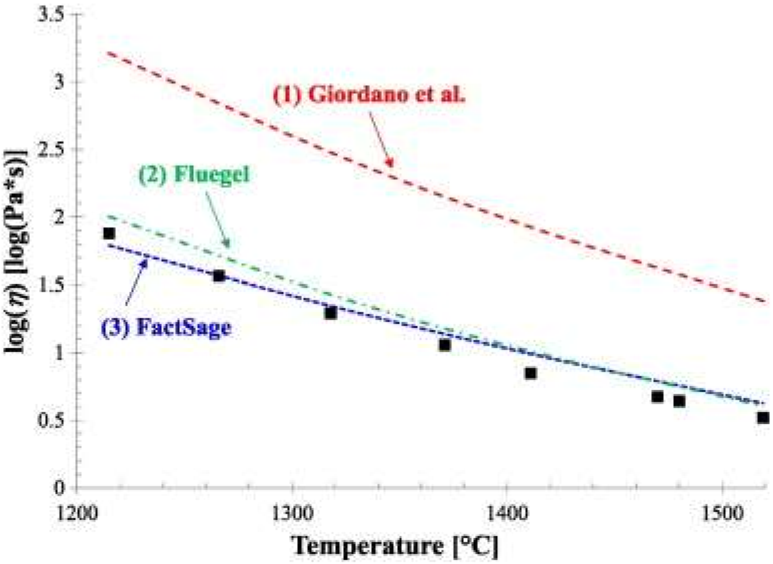

***Figure 1.5**. Log viscosity (Pa·s) plotted vs. temperature (°C). Black squares indicate experimental data for a 23.3CaO-6.4MgO-3.1Al_2O_3-62.5SiO_2-4.1Na_2O-0.5K_2O-0.04Fe_2O_3 (mol%) glass from [28] and are compared to three different models from the literature.*

Some researchers refer to optical basicity (OB, Λ), in addition to melting and viscosity behavior, when describing CMAS deposits [31, 32]. The concept of optical basicity is based on Lewis acid-base theory, which defines acids as electron acceptors and bases as electron donors. The optical basicity of a metal oxide describes the ability of the oxygen anion to donate electrons; cations with high polarizability draw electrons away from oxygen, making such metal oxides weak bases (low OB), whereas cations with low polarizability allow oxygen to donate electrons to available cations, making such metal oxides strong bases (high OB). To put this in perspective, pure SiO_2 (acid) has an OB of 0.74 while pure K_2O (base) has an OB of 1.40. The OBs are calculated for a wide spread of CMAS compositions (similar to those in Figure 1.1) and are presented in Figure 1.6. Interestingly, despite large variations in composition, OBs fall within a rather narrow range of 0.49-0.75, suggesting that deposit reactivity is similar.

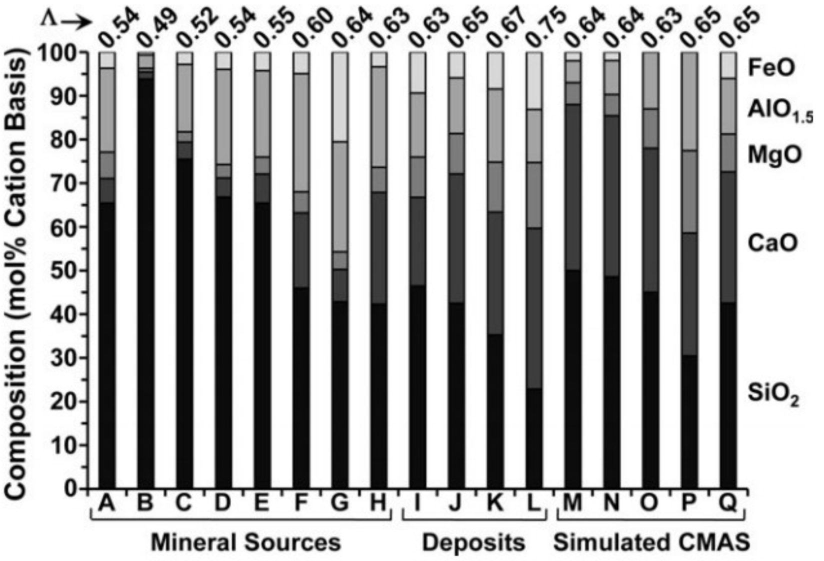

Figure 1.6. *Optical basicity (Λ) given as a function of CMAS composition. From [30].*

1.2 TBC interaction with CMAS: Formation of apatite

Thermal barrier coatings (TBCs) for superalloy components consist of a metallic bond coat, a thermally grown oxide (TGO), and a ceramic top coat—to date, typically 7YSZ [3]. The topcoat architecture is usually processed by electron beam physical vapor deposition (EB-PVD) and is columnar/porous to accommodate coefficient of thermal expansion (CTE) mismatches between the metal substrate and the ceramic coating and to lower the thermal conductivity of the coating. The microstructure of an EB-PVD YSZ TBC is given in cross-section in Figure 1.7. CMAS is able to infiltrate the open channels of an EB-PVD TBC and, upon cooling, cause stiffening of the topcoat which can lead to coating delamination [20]. Mitigation strategies involve limiting the extent of CMAS infiltration in the TBC; the most promising is to promote rapid reaction between the coating and the melt to form stable crystalline phases that seal coating flow channels [20, 33].

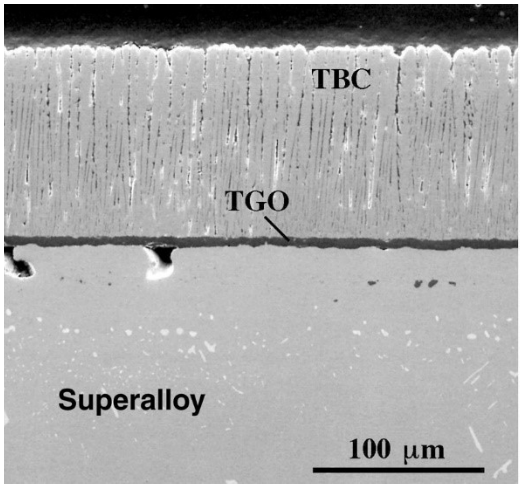

Figure 1.7. *Cross-sectional image of a YSZ thermal barrier coating (TBC) deposited by EB-PVD on a superalloy substrate. At high temperature, a thermally grown oxide (TGO) of Al_2O_3 forms on the metal, below the TBC. From [34].*

7YSZ has shown limited resistance to CMAS attack [35-38]. When exposed to CMAS of composition 33CaO-9MgO-13$AlO_{1.5}$-45SiO_2 (or 33Ca-9Mg-13Al-45Si), the coating dissolves and re-precipitates as Y_2O_3-depleted, tetragonal zirconia (t-ZrO_2) [35]. Without enough Y_2O_3 within the re-precipitated ZrO_2 to maintain the metastable tetragonal phase, it transforms into the monoclinic structure upon cooling, which is accompanied by an unfavorable ~5% volume change [39]. Krämer et al. determined that 7YSZ was fully impregnated after ≤ 4 h at 1240°C [35]. Changes to the melt chemistry revealed similar results. YSZ exposed to a simulated volcanic ash glass was infiltrated at temperatures as low as 1100°C, which caused depletion of Y_2O_3 from the coating [37]. However, complete destabilization of the tetragonal phase was not observed. Zircon ($ZrSiO_4$) crystallites were formed instead, but they were not able to effectively block coating porosity from continued CMAS penetration.

The rare earth (RE) zirconate system, $RE_2Zr_2O_7$/$RE_4Zr_3O_{12}$, was first studied by Krämer et al. [33]. Gadolinium zirconate ($Gd_2Zr_2O_7$, GZO) coatings deposited by EB-PVD were exposed to CMAS (composition 33Ca-9Mg-13Al-45Si) for 4 h at 1300°C. The coating dissolved in the CMAS melt and reprecipitated as a ZrO_2-based cubic fluorite phase and an oxyapatite silicate, nominally $Ca_2RE_8(SiO_4)_6O_2$.

GZO infiltration depth was limited to about 30 µm after 4 h (Figure 1.8). This was attributed to the fast formation (within tens of seconds) of highly stable apatite phase that sealed the TBC surface.

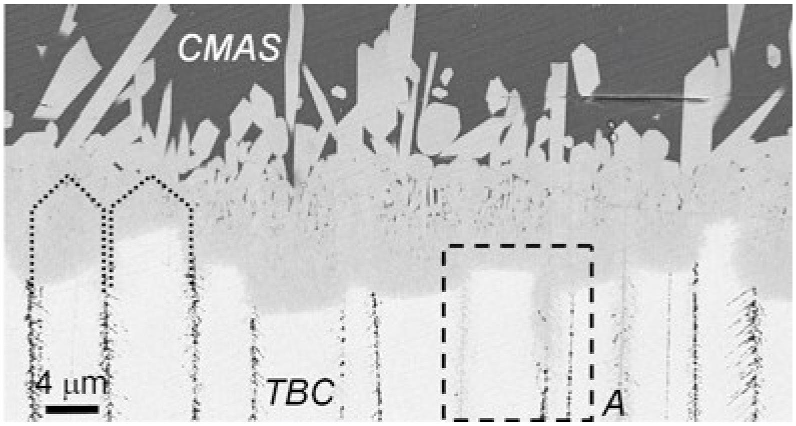

***Figure 1.8**. Back scattered electron (BSE) cross-section image of reaction zone between GZO and CMAS after 4 h at 1300°C. Dotted lines on the left outline the approximate shape and height of the original column structure. From [33].*

Other RE zirconates (RE=Yb, Y, Sm, Nd, Ce, and La) have also been reported to form apatite upon reaction with CMAS [40-44]. Poerschke et al. reported that RE zirconates with a smaller RE^{3+} ion radius (i.e. Y, Yb) were less successful in forming apatite [45]. This was due to diminished availability of RE_2O_3 able to contribute to the apatite phase. Instead, large amounts of RE_2O_3 reprecipitated in ZrO_2 or other RE_2O_3-containing silicate phases, such as garnet, with slower crystallization kinetics than apatite. The initial composition of the infiltrating melt can also favor formation of phases other than apatite. For example, Schulz and Braue saw apatite formation in $La_2Zr_2O_7$ coatings exposed to a model sand-type CMAS but $La_2Si_2O_7$ after exposure to a CaO-lean, SiO_2-rich volcanic ash deposit [44].

The crystal structure of apatite (viewed along its c-axis) is found in Figure 1.9 [46]. Its corresponding chemical formula can be represented by $REE1_4REE2_6(SiO_4)_6O4_2$ (REE=RE element). The SiO_4^{4-} tetrahedra in the structure are arranged in such a way that there exist open channels along the c-axis of the hexagonal unit cell. One channel is occupied by a single column of 9-oxygen-coordinated REE1 sites; the other is made up of a ring of six columns of REE2, with each REE2 being coordinated by 7 oxygen atoms. Oxygen atoms that are not covalently bound in the SiO_4^{4-} tetrahedra occupy O4 anion sites, which sit in the center of REE2 rings. Apatite group minerals are largely accommodating of structural distortions and chemical substitutions. The range of possible apatite stoichiometries in the CaO-SiO_2-$YO_{1.5}$ system is outlined in Figure 1.10 [47]. The "defect free" apatite is given by $Ca_2Y_8(SiO_4)_6O_2$. Calcium ions (Ca^{2+}) can replace Y^{3+} – charge balance is accounted for by the creation of vacancies (□) at the O4 site. The theoretical limit in this direction is $Ca_4Y_6(SiO_4)_6(O\square)$ and is denoted by the number "4" in Figure 1.10. Alternatively, $YO_{1.5}$ can substitute for CaO, which, in the most likely case, is accompanied by cation vacancies. Given in Figure 1.10 by the number "2," CaO-free apatite has the stoichiometry $Y_{9.33}\square_{0.67}(SiO_4)_6O_2$.

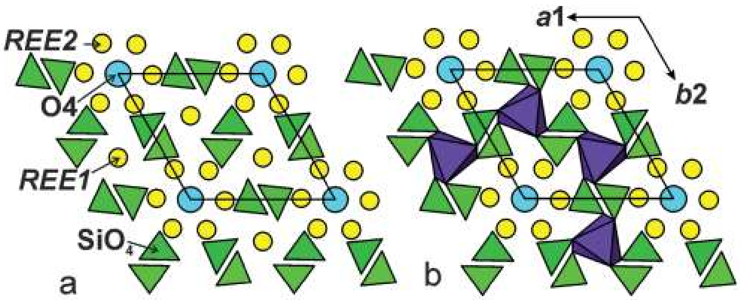

***Figure 1.9**. The crystal structure of rare earth silicate apatite viewed along the c axis: (a) schematic and (b) schematic with REE1–O polyhedral shown as (purple) trigonal prisms. From [46].*

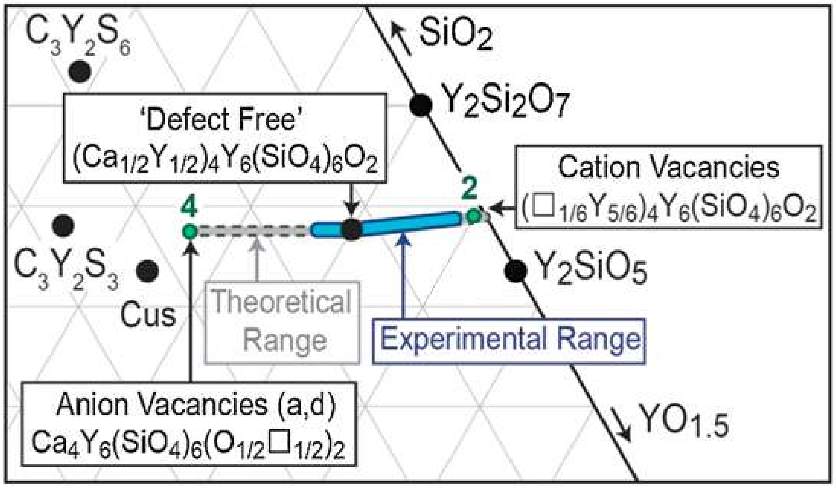

***Figure 1.10**. Portion of the CaO-SiO_2-$YO_{1.5}$ phase diagram outlining the observed/theoretical range for apatite stoichiometry. From [47].*

1.3 EBC interaction with CMAS

The primary purpose of an EBC for ceramic components is to prevent the volatilization of the protective SiO_2 thermally grown oxide in a combustion environment [9, 13]. However, in addition to thermochemical stability in high-temperature, high-velocity steam, EBCs must also [13]: 1) have a CTE that closely matches that of the underlying CMC, to prevent coating cracking and delamination due to thermal expansion mismatch, 2) maintain a stable phase during thermal cycling, to prevent unfavorable volumetric changes in the coating, 3) remain inert in contact with the CMC and/or bondcoat, to prevent deleterious reactions, and 4) have a sufficiently low oxygen diffusivity, to limit oxidation of underlying CMC components. Current state-of-the-art EBCs are the RE silicates (RE_2SiO_5 and $RE_2Si_2O_7$) and are promising due to increased chemical stability at high temperature and reduced volatility in steam environments as compared to the second generation EBC, barium strontium aluminum silicate (BSAS) [48].

On top of the above stated requirements, EBCs must also be CMAS resistant, as the expected coating surface temperature is well above the melting temperature of most CMAS deposits. RE silicate/CMAS interactions have been studied most extensively for RE=Y,Yb. There is some debate in the literature regarding the mitigation mode sought for EBCs exposed to CMAS [14]. Some argue that materials that are unreactive with CMAS are more favorable, as EBCs are nominally dense and do not require rapid sealing of open channels as in TBCs. Theoretically, CMAS could stagnate in equilibrium with the coating material at the EBC surface. EBCs are deposited by air plasma spray (APS), a process that involves ceramic powders being fed through a plasma, which melts the powder, before being rapidly ejected onto a substrate. This results in a fairly dense microstructure composed of layers or "splats." A cross-section image of an APS deposited $Yb_2Si_2O_7$ coating is given in Figure 1.11. Although it provides high density, APS processing leads to a complicated microstructure that can include secondary phases (such as Yb_2SiO_5 in Figure 1.11), splat boundaries, grain boundaries, cracks, and pores [49]. These defects can be pathways for CMAS infiltration; therefore, an alternative mitigation mode in which rapid reaction between the EBC/glass to form a crystalline interfacial layer may reduce the overall consumption of coating material in a mechanism similar to that desired for TBCs.

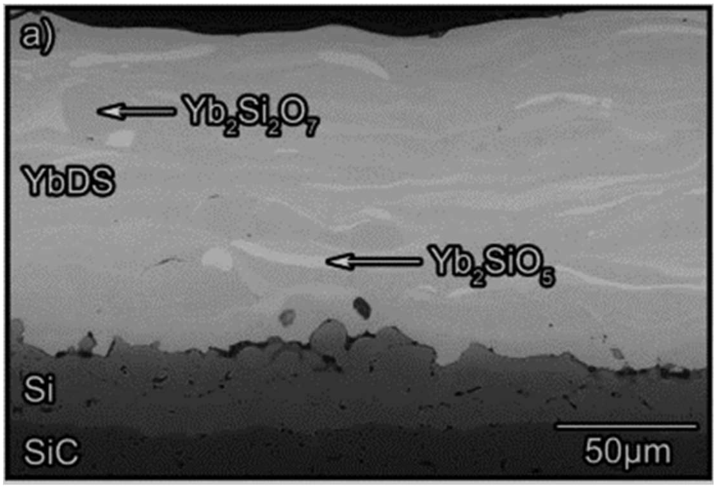

Figure 1.11*. Cross-section BSE image of an APS deposited $Yb_2Si_2O_7$ coating (containing Yb_2SiO_5) atop Si/SiC. From [50].*

Apatite formation has been reported in RE_2SiO_5/CMAS studies. Grant et al. described the formation of a Y:Ca silicate apatite phase at the interface between dense yttrium monosilicate (Y_2SiO_5) and CMAS after heat treatment at 1300°C [15]. The apatite reaction layer's ability as a barrier to attack, however, was compromised by the presence of amorphous intergranular pathways which allowed dissolution of the coating to continue. Ytterbium monosilicate (Yb_2SiO_5) has also been shown to react rapidly with CMAS to form apatite. Stolzenburg et al. probed powder mixtures of coating and glass at 1300°C and saw fast dissolution of Yb_2SiO_5 to form the apatite phase [51]. Ahlborg and Zhu exposed bulk Yb_2SiO_5 to CMAS at 1500°C and observed apatite formation at the sample surface and within grain boundaries [52].

Conflicting results have been reported on the stability of the disilicates, $Y_2Si_2O_7$ and $Yb_2Si_2O_7$, in contact with CMAS. Poerschke et al. exposed both dense, phase pure $Y_2Si_2O_7$ and APS $Y_2Si_2O_7$ (containing some Y_2SiO_5) to CMAS containing 5 mol % Fe (CMFAS) [53]. Both sample types exhibited apatite formation; surface recession of the material was about twice that observed in Y_2SiO_5 [15], with values reaching approximately 200 µm after 24 h at 1300°C. Ahlborg and Zhu reported the presence of the apatite phase in exposed $Y_2Si_2O_7$ at both 1300 and 1500°C [52]; as seen in Y_2SiO_5, amorphous glass was present at the grain boundaries and samples with a bulk thickness of approximately 4 mm were completely infiltrated after 200 h at 1500°C. Turcer et al. also observed fast reaction of $Y_2Si_2O_7$ with CMAS to form apatite at 1500°C, with a reaction layer ~300 µm thick after 24 h [54]. For the case of $Yb_2Si_2O_7$, Stolzenburg et al. saw dissolution in contact with CMAS at 1300°C but no formation of new crystalline phases [51]. Turcer et al. reported grain boundary attack of $Yb_2Si_2O_7$ resulting in “blister” cracking of the sample – only a very small amount of apatite formation was observed [55]. Zhao et al. investigated the interaction between $Yb_2Si_2O_7$ layers deposited by APS and CMAS and reported the formation of apatite, however the reaction occurred preferentially at Yb_2SiO_5 segregates [56]. It appears that the choice of RE cation has an effect on the propensity of the EBC silicate to react with CMAS to form apatite; because the ability to form apatite is greater in $Y_2Si_2O_7$ than $Yb_2Si_2O_7$, it may follow that RE^{3+} with a larger ionic radius (Y^{3+}=0.92 > Yb^{3+}=0.86 Å [57]) are preferred in the production of apatite, as has been suggested for RE zirconates [45].

The effect of the RE cation on RE silicate reaction with CMAS has been investigated. RE mono- and disilicates with RE = Sc^{3+} (ionic radius=0.81 Å), Lu^{3+} (0.85), Yb^{3+}, Y^{3+}, Gd^{3+} (0.97), Eu^{3+} (0.98), and La^{3+} (1.14) [57], were exposed to CMAS at either 1200°C (RE_2SiO_5 [58]) or 1400°C ($RE_2Si_2O_7$ [59]) in a water vapor containing environment. In the disilicate system, $RE_2Si_2O_7$ with RE = Y, Gd, Eu, or La formed apatite in contact with CMAS while $RE_2Si_2O_7$ with RE = Sc, Lu, or Yb did not. In the monosilicate system, RE_2SiO_5 with RE = Gd, Eu, and La formed only apatite and anorthite in contact with CMAS, while RE_2SiO_5 with RE = Lu, Yb, and Y formed phases in addition to apatite, including cyclosilicate, garnet, disilicate, and/or anorthite. These results further suggest that apatite formation is coordinated with RE cation size.

The reaction of the RE silicates with CMAS starts with the dissolution of the coating in the melt. Once a critical concentration of RE_2O_3 in the melt is reached, apatite can begin to precipitate. The ensuing reactions will either form crystallized products that consume the melt or result in an equilibrium state of liquid and remaining, undissolved coating [14].

$$4RE_2Si_2O_7 + 2CaO \rightarrow Ca_2RE_8(SiO_4)_6O_2 + 2SiO_2 \tag{1.3}$$

In the above reaction, $RE_2Si_2O_7$ consumes CaO from the melt while concomitantly rejecting an equivalent amount of SiO_2 in the formation of apatite. The melt is not consumed and so the reaction will continue until the residual melt is depleted in CaO and the driving force for apatite formation is eliminated. RE monosilicates, however, actually consume SiO_2 from the melt, in addition to CaO, in the formation of apatite:

$$4RE_2SiO_5 + 2CaO + 2SiO_2 \rightarrow Ca_2RE_8(SiO_4)_6O_2 \tag{1.4}$$

leading to a reduction in the melt volume and an enrichment in the remaining glass of MgO and Al_2O_3.

The composition of the CMAS deposit, specifically in terms of amount of CaO and SiO_2, can affect the propensity of silicate EBCs to form the apatite phase. The Y/Yb silicate results discussed above were in contact with CMAS melts having a CaO/SiO_2 ratio ≥ 0.72. RE mono- and disilicate materials have also been exposed to CMAS deposits containing less CaO and more SiO_2 (CaO/SiO_2 ratio < 0.72).

Summers et al. varied the CaO/SiO_2 content in deposits applied to $Y_2Si_2O_7$ and determined that below a critical CaO/SiO_2 threshold (about 0.25 at 1300/1400°C), apatite does not form [60]. Recession of the coating is instead governed by the coating's solubility limit in the melt. It was observed that recession of $Y_2Si_2O_7$ decreased with decreasing deposit CaO content (Figure 1.12).

Apatite formation was also halted in Yb_2SiO_5 exposed to a volcanic ash CMAS with a CaO/SiO_2 ratio of 0.09 [61]. Jang et al. instead reported the formation of a thin layer of $Yb_2Si_2O_7$ at the reaction interface. The thickness of the $Yb_2Si_2O_7$ layer was much less than that of apatite formed between Yb_2SiO_5 and CMAS containing higher amounts of CaO [61].

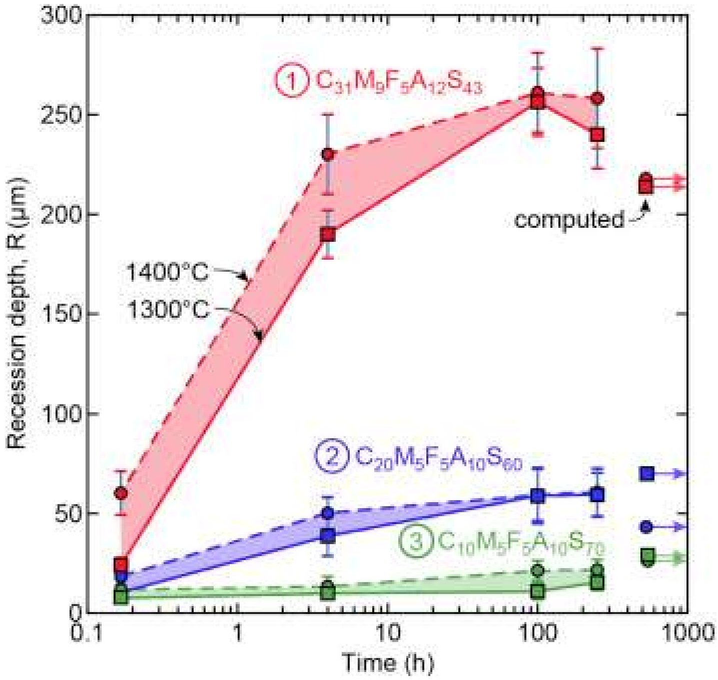

***Figure 1.12**. Recession depth in $Y_2Si_2O_7$ coatings exposed to CMFAS deposits of varying CaO/SiO_2 at 1300/1400°C. With decreasing CaO content, recession depth also decreases. From [60].*

There are limited data on coating recession and/or reaction zone thickness in apatite-forming EBCs exposed to CMAS. Coating recession (which has also been referred to as coating infiltration) is a measurement of how deep into an EBC CMAS is able to reach, and is usually determined with respect to the EBC's original surface (un-recessed material). Reaction zone thickness describes the thickness of the crystallized layer formed between the EBC and CMAS. This layer can extend above the initial coating surface and therefore is not always synonymous with coating recession. Figure 1.13 compiles known data from the literature for Y_2SiO_5 and Yb_2SiO_5 after reaction with CMAS of composition 33Ca-9Mg-13Al-45Si (mol %).

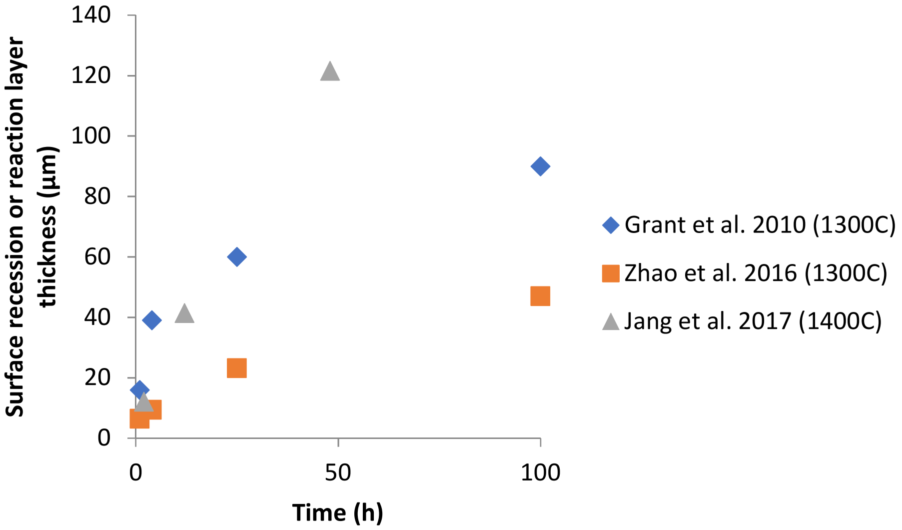

***Figure 1.13**. Surface recession/reaction layer thickness for Y_2SiO_5 and Yb_2SiO_5 exposed to CMAS (33Ca-9Mg-13Al-45Si) at 1300 and 1400°C for times up to 100 h. Data from [15, 56, 61].*

In addition to CMAS composition, there are many factors that must be considered when comparing different studies; these include temperature, CMAS loading, loading type, and EBC microstructure (i.e. dense vs. APS deposited). The Grant et al. study, giving Y_2SiO_5 recession as a function of time, was performed at 1300°C with a CMAS loading of 12-13 mg/cm^2 applied as a pellet on top of a dense sample [15]. The Zhao et al. study plots reaction zone thickness (calculated assuming full density of the apatite layer) after Yb_2SiO_5 exposure at 1300°C to a CMAS pellet with a loading of 7-8 mg/cm^2 [56]. The Yb_2SiO_5 in this study was APS deposited. A nominally dense apatite reaction layer was observed in APS Yb_2SiO_5, however, interestingly, this was not the case for APS $Yb_2Si_2O_7$ from the same study. Preferential reaction of Yb_2SiO_5 secondary phases in the coating with CMAS to form apatite was observed, which resulted in a discontinuous reaction layer. Figure 1.14 shows a schematic of the interaction zone in this material.

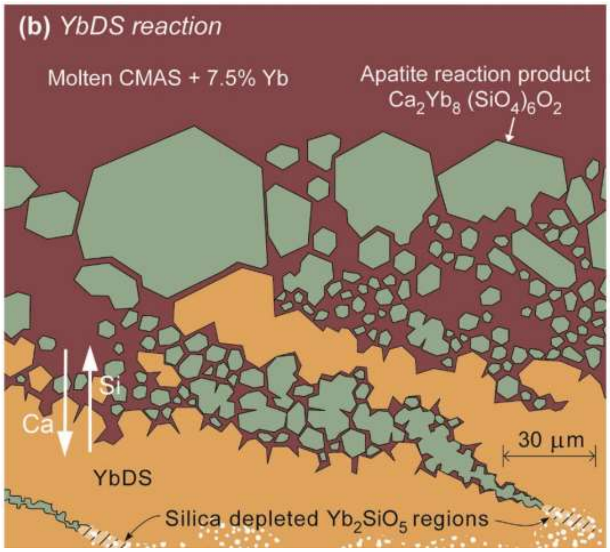

***Figure 1.14**. A schematic of the proposed reaction mechanism between APS-deposited $Yb_2Si_2O_7$ and secondary Yb_2Si_O5 and CMAS. From [56].*

Finally, Jang et al. studied CMAS with a concentration of ~40 mg/cm^2, applied as a paste, to Yb_2SiO_5 at 1400°C and reported reaction zone thickness [61]. Obviously, the variability in testing procedure makes it difficult to compare competing studies; there is a need for a standard test procedure. In looking at Figure 1.13, it can be deduced that the EBC/CMAS measured reaction thickness/recession depth for $(Y/Yb)_2SiO_5$ after exposure for ~100 h is on the order of 100 µm.

1.4 Novel coating materials – RE titanates

It is common practice in the glass-ceramic industry to promote controlled crystallization of a glass through the use of a nucleating agent; typical nucleating agents include TiO_2 and ZrO_2 [62]. Aygun et al. applied this approach in their study on CMAS interactions with 7YSZ [37]. The authors reported increased coating resistance to CMAS (compared to 7YSZ alone) for samples containing 20 mol% Al_2O_3 and 5 mol % TiO_2 as a solid solution. The Al_2O_3 and TiO_2 were incorporated to serve as a reservoir of Al and Ti solutes, promoting crystallization by shifting the glass from the pseudo-wollastonite phase to the more easily crystallized anorthite phase and providing nucleation sites, respectively.

A novel approach for incorporating TiO_2 in the EBC/CMAS system involves the addition of RE mono and RE dititanates (RE_2TiO_5 and $RE_2Ti_2O_7$, respectively) to the coating. The following displacement reactions are proposed [63, 64]:

$$RE_2TiO_5 + SiO_2 \leftrightarrow RE_2SiO_5 + TiO_2 \quad [1.5]$$

$$RE_2Ti_2O_7 + 2SiO_2 \leftrightarrow RE_2Si_2O_7 + 2TiO_2 \quad [1.6]$$

with the idea that the RE titanates will consume SiO_2 from incoming CMAS, forming RE silicates and releasing TiO_2 to promote further crystallization, *in-situ*.

A report on RE titanate resistance to CMAS was recently published on a novel TBC system, $BaRE_2Ti_3O_{10}$ (RE=La, Nd) [65]. Nominally dense pellets of $BaRE_2Ti_3O_{10}$ were exposed to CMAS (22Ca-19Mg-14Al-45Si, mol %) at 1250°C for up to 10 h. In addition to apatite, calcium titanate ($CaTiO_3$) was also formed in the reaction zone. A reaction zone thickness of approx. 30 µm was seen after 10 h at temperature—a value that is comparable to the GZO system and gives promise for a RE-containing titanate ceramic as a CMAS-resistant layer.

1.5 Dissertation Objectives

1.5.1 Chapter 2: CMAS interaction with RE titanates and RE silicates – crystallized reaction layer formation

There has been debate in the literature as to whether EBC materials sought for CMAS mitigation should be reactive or nonreactive. It is hypothesized that choosing an EBC material that reacts rapidly with CMAS to form a crystallized layer is a more viable strategy for CMAS mitigation compared to choosing one that is inert. This hypothesis is evaluated in Chapter 2. The objective of this chapter is to assess the interfacial reaction between RE titanates, RE silicates, and standalone apatite (a common reaction product between RE coating materials and CMAS) and CMAS to determine 1) the ability of coating constituents to react rapidly with molten glass to form a crystallized layer and 2) the effectiveness of the crystallized layer to slow or prevent glass ingress. Surface infiltration and reaction zone thickness measurements were compared, along with phase and microstructural evolution.

1.5.2 Chapter 3: EBC phase constitution and microstructure effects on CMAS infiltration and reaction

EBCs are typically deposited by air plasma spray (APS), which can lead to a complicated microstructure containing multiple phases. The objective of this chapter is to explore the effects of phase constitution and microstructure on CMAS attack in ytterbium silicate materials. Ytterbium disilicate ($Yb_2Si_2O_7$) samples containing controlled amounts of Yb_2SiO_5 (10-30 vol%) were prepared as model materials having either a “splat” or “fine dispersion” microstructure. Model materials were exposed to CMAS having both high and low Ca contents and their behavior was compared to that of the phase pure materials explored in Chapter 2. Results will be used to advise optimal microstructures for APS-deposited EBCs.

1.5.3 Chapter 4: Viscosity of CMAS melts

The objective of Chapter 4 is to obtain experimental viscosity values for CMAS melts and compare to data from viscosity models frequently cited in the literature. The results of this study will inform on which viscosity models best represent deposit compositions. The effect of CaO/SiO_2 ratio, MgO content, and Al_2O_3 content on CMAS viscosity will also be evaluated. Infiltration in RE silicates as a function of CaO/SiO_2 ratio will be related to glass viscosity in an effort to determine viscosity effects on CMAS infiltration in EBCs.

2. Chapter 2: CMAS interaction with RE titanates and RE silicates – crystallized reaction layer formation

2.1 Introduction

There has been debate in the literature as to whether EBC materials sought for CMAS mitigation should be reactive or nonreactive with molten deposits. There are three approaches to mitigating CMAS degradation in EBCs [14]. In the first, coating materials that minimize reactivity with CMAS are sought. This approach assumes a nominally dense coating wherein the primary degradation mode is not melt infiltration – the glass is expected to stagnate at the coating surface. The second approach alternatively seeks to maximize reactivity between the EBC and CMAS so that the depth to which CMAS can reach before being neutralized is reduced (similar to the prevailing mitigation mechanism in TBCs). Finally, the third strategy is to overlay a sacrificial barrier, such as the TBC $Gd_2Zr_2O_7$ (which reacts with CMAS to form new crystallized phases), at the surface of an EBC. This apparent knowledge gap in coating design leads to the following research questions:

- *What is the optimum strategy for mitigating CMAS degradation in EBCs?*
- *Is the rapid reaction of EBCs with CMAS to form a crystallized reaction product layer a viable strategy for CMAS infiltration mitigation?*
- *Do reactive coating materials slow CMAS infiltration compared to non-reactive coating materials?*

It is hypothesized that an EBC material that reacts rapidly with CMAS to form a crystallized layer is better able to resist CMAS infiltration compared to one that is inert. APS coating defects such as grain boundaries, cracks, and pores, are susceptible to CMAS penetration. This hypothesis was tested in the following chapter by comparing interaction behavior between current/potential coating materials, RE titanates and RE silicates, with CMAS. Interaction between apatite (a common reaction product between coating materials and CMAS) and CMAS was also studied. The objective of this chapter was to assess the interfacial reaction between these materials and CMAS to determine 1) the ability of coating constituents to react rapidly with molten glass to form a crystallized layer and 2) the effectiveness of the crystallized layer to slow or prevent glass ingress. Surface infiltration and reaction zone thickness measurements were compared, along with phase and microstructural evolution. It was determined that EBC materials that react rapidly with CMAS to form crystallized phases – most notably apatite – were more slowly infiltrated than materials that did not react to form these phases. This report is the first to: 1) systematically vary EBC composition to probe the two main competing mitigation strategies proposed in the literature, 2) expose standalone apatite to CMAS, and 3) compare the effect of CMAS composition on infiltration behavior in multiple, and similar, material systems.

Chapter 2 is divided into 5 sections, based on material: a) TiO_2, b/c) RE titanates, d) RE silicates, and e) standalone apatite (Table 2.1). Sections a) and b) (i.e. a) CMAS + TiO_2 and b) RE titanates + SiO_2) examine simplified material systems, rather than full EBC + CMAS interactions, to aid in mechanistic understanding. The ability to form a crystallized reaction zone is related to CMAS infiltration in these materials. Material behaviors are compared in the discussion in an effort to validate the proposed EBC mitigation strategy. The most promising EBC material(s) are acknowledged.

***Table 2.1**. Outline for Chapter 2. Research questions proposed for each material/reaction system, along with the experimental techniques utilized to answer them, are given.*

	Research Questions	**Experimental Techniques**
(a) CMAS + TiO_2	Do TiO_2 additions nucleate or enhance CMAS crystallization? How much TiO_2 is needed? What phases form?	Box furnace exposures (powder samples) DSC XRD SEM Light microscopy
(b) RE titanates + SiO_2	Do RE titanates react with SiO_2 to form new crystalline phases? Does TiO_2 form as expected?	Box furnace exposures (powder samples) XRD
(c) RE titanates + CMAS	How do these materials behave in contact with CMAS (react, don't react)? How does that influence coating penetration? What phases form? Does CMAS composition have an effect on behavior? Should this material be considered as an EBC?	Box furnace exposures (powder and bulk samples) Levitation heating/cooling XRD SEM
(d) RE silicates + CMAS		Box furnace exposures (bulk samples) XRD SEM
(e) Apatite + CMAS		Box furnace exposures (bulk samples) XRD SEM Levitation heating (Appendix B) Dilatometry (Appendix B)

2.2 (a) CMAS + TiO_2

I. Experimental

i. Sample preparation

The baseline effect of TiO_2 on CMAS crystallization was explored prior to investigation of RE titanate/CMAS interactions. CMAS glass with a composition of 33CaO-9MgO-13$AlO_{1.5}$-45SiO_2 (mol % of single cation species) was prepared by mixing oxide powders (99.9% purity CaO from Sigma Aldrich, St. Louis, MO, and 99.99% MgO, 99.9% Al_2O_3, and 99.9% SiO_2 from Alfa Aesar, Haverhill, MA) with water to form a paste that was ball-milled with zirconia media (95% purity, Glen Mills, Clifton, NJ) for 4 h. The mixture was next dried and the resulting powder was melted in a Pt-5%Au crucible (Heraeus, Hanau, Germany) in a box furnace (CM Furnaces 1706 FL, Bloomfield, NJ) at 1300°C. The melt was air quenched and the resulting glass ground to a fine powder with mortar and pestle. The composition of the glass powder was confirmed by digesting approximately 50 mg of sample in a 1:1:1:1 (by volume) mixture of concentrated, Trace Metals Grade HCl:HF:HNO_3 with deionized H_2O, diluting the solution, and analyzing it using an inductively coupled plasma optical emission spectrometer (ICP-OES; Thermo Scientific iCap 6000 Series, Waltham, MA). The glass powder's amorphous character was confirmed by x-ray diffraction (XRD; PANalytical X'pert, Westborough, MA). For CMAS + TiO_2 compositions, the respective amount (5-20 wt%) of TiO_2 powder (99.8% rutile, Alfa Aesar) was mixed in with the CMAS glass powder. Nominal compositions for each mixture (0-20 wt% TiO_2) are displayed in mole % in Table 2.2.

Table 2.2. *Weight % TiO_2 additions and corresponding CMAS + TiO_2 compositions in mole %.*

	Mole %				
Weight % TiO_2	**CaO**	**MgO**	**$AlO_{1.5}$**	**SiO_2**	**TiO_2**
0	33	9	13	45	0
5	31.8	8.7	12.5	43.5	3.5
10	30.6	8.4	12.1	41.7	7.2
12.5	30	8.2	11.8	40.9	9.1
15	29.4	8	11.6	40.0	11
20	28.1	7.7	11.1	38.2	14.9

ii. Differential Scanning Calorimetry (DSC)

Differential scanning calorimetry (DSC) was carried out using a Netzsch STA 449 F1 (Burlington, MA) to determine CMAS and CMAS + TiO_2 thermal events associated with heating to and cooling from the melt. Powder samples (approx. 50-150 mg) were cold-pressed to 6.35 mm (1/4") diameter pellets. CMAS DSC pellets, containing no TiO_2, were pre-treated in a box furnace for 4 h at 1200°C to promote intrinsic crystallization. This was done to parallel DSC measurements by Zaleski et al. [66] in the determination of glass melting temperature. DSC pellets were contained in Pt-20%Rh pans for all experiments. DSC scans were performed in flowing (40 mL/min) Ar gas, from room temperature to

1300°C with a ramp rate of 10°C/min. A ramp rate of 10°C/min was chosen as a baseline and to mimic box furnace tests, described in the following sections. Temperature and sensitivity calibrations were performed prior to any sample testing as outlined in the supplied Proteus Analysis software package, using the same sample pans and gas environment. Background scans were also performed prior to each sample run, using the same thermal cycle, sample pan, and gas environment, and were subtracted from the measured sample curve.

iii. Box furnace heat treatments: "Ramped" profile

Box furnace heat treatments were performed in stagnant air wherein samples were heated to and cooled from either 1300°C or 1500°C at a rate of 10°C/min. Samples were held for 10 min at temperature ("ramped" profiles; Figure 2.1a) to parallel DSC measurements. Approximately 200 mg of CMAS or CMAS + TiO_2 powder sample was contained in a Pt-5%Au crucible for testing. The CMAS powder was not sintered prior to experiment as was done for DSC measurements; because crystallization behavior on cooling from the melt was of interest, crystallization of the sample at 1200°C before holding (and melting) at 1300/1500°C was not desired. The larger powder batch size, compared to DSC experiments, was chosen for more extensive characterization. Triplicate samples were run for each experiment. Resulting glass/ceramic products were either crushed to a fine powder for XRD analysis, epoxy-mounted and polished for cross-section imaging by light microscopy (Hirox Digital Microscope KH-7700, Hackensack, NJ) and scanning electron microscopy (SEM; FEI Quanta 650, Hillsboro, Oregon), or mounted on an aluminum stub for SEM plan-view imaging. Semi-quantitative energy dispersive spectroscopy (EDS; Oxford Instruments Aztec X-MaxN 150, Abingdon, Oxfordshire, UK) was also used in conjunction with the SEM. SEM samples were coated (Technics Hummer Sputter Coater, Hayward, CA) with a thin layer of gold/palladium prior to characterization to provide a conductive surface. Images were taken in backscattered electron (BSE) and secondary electron (SE) modes.

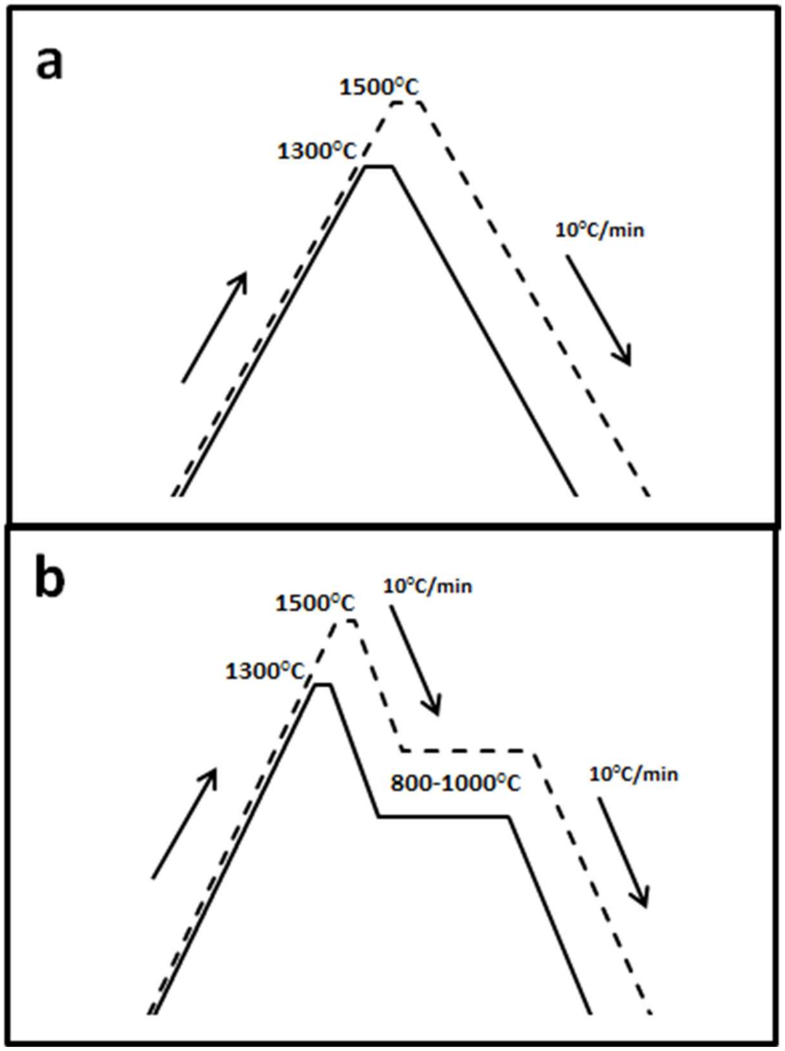

Figure 2.1*. "Ramped" (a) and "flight" (b) heat treatment profiles.*

iv. Box furnace heat treatments: "Flight" profile

"Flight" profiles (Figure 2.1b) were also performed in the box furnace to better simulate engine operation cycles. These involved equilibration above the liquidus followed by holding for various times at temperatures below the solidus to understand how the degree of undercooling affected crystallization of CMAS and CMAS + TiO_2. Specifically, heat treatments involved the following: heating to either 1300/1500°C at a rate of 10°C/min and holding at temperature for 30 min, cooling to a temperature between 800-1000°C at a rate of 10°C/min, holding at the intermediate temperature for either 1 h or 5.5 h, and finally cooling to room temperature at a rate of 10°C/min. Holding at the intermediate temperature for 1 h or 5.5 h was done to simulate a 1.5 h or 6 h flight (not including the time required for heating and cooling at a rate of 10°C/min), respectively, wherein the initial "take-off" temperature (1300/1500°C) comprises a small fraction of the total time in air. The effect of varying the intermediate (or "cruise") temperatures (800-1000°C) was also explored.

II. Results

i. Evaluation of thermal events by DSC

The initial onset temperatures of melting (on heating; T_m) and crystallization (on cooling; T_c) events for CMAS and CMAS + TiO_2 pressed powders are compiled in Table 2.3. The glass transition temperature (T_g; inflection point) is also reported. All values reported are the average of three data points, except for the CMAS T_c and T_g, in which only a single event could be discerned from the three curves used. The DSC curves for CMAS alone and CMAS + 20 wt% TiO_2 are also shown (Figure 2.2).

Table 2.3. *Melting (T_m), crystallization (T_c), and glass transition (T_g) temperatures measured by DSC for CMAS and CMAS + TiO_2 compositions. Consolidated CMAS glass powder (0 wt% TiO_2) was devitrified at 1200°C for 4 h prior to testing. CMAS + TiO_2 (5-20 wt% TiO_2) compositions were introduced into the DSC as CMAS glass powder mixed with rutile TiO_2, consolidated into a green pellet.*

Weight % TiO_2	**T_m (°C)**	**T_c (°C)**	**T_g**
0	1239 ± 4	1148	764
5	1202 ± 8	n/a	775 ± 2
10	1213 ± 1	n/a	771 ± 4
12.5	1213 ± 7	n/a	762 ± 11
15	1219 ± 4	1178 ± 20	769 ± 1
20	1209 ± 6	1155 ± 29	771 ± 4

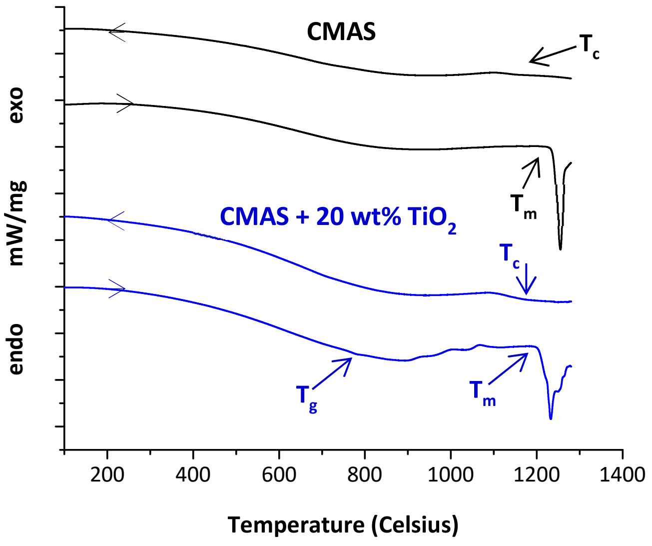

Figure 2.2. *DSC curves for CMAS (black curve) and CMAS + 20 wt%* TiO_2 *(blue curve) heated to and from 1300°C at 10°C/min. Arrows on curves indicate heating and cooling.* T_m *and* T_c *represent melting and crystallization onset temperatures, respectively.* T_g *represents the glass transition temperature. Peaks pointing downward represent endothermic events and peaks pointing upward represent exothermic events. Transformation temperatures are given in Table 2.3.*

For CMAS alone, T_m and T_g agree relatively well with temperatures reported in the literature [66]. The T_g reported in Table 2.3 was unexpected, as the consolidated powders were crystallized at 1200°C prior to DSC measurement. This meant that some glass remained in the sample. Upon cooling, there does not appear to be significant crystallization. For one run, there was a slight exothermic region, indicating crystallization, beginning at approximately 1148°C. With the addition of 5 wt% TiO_2 to CMAS, the onset of melting is decreased to an average temperature of 1202°C and there is no longer evidence of any exothermic region (i.e. crystallization) upon cooling. Titania additions of 10, 12.5, 15, and 20 wt% all resulted in a lower T_m than that measured for CMAS alone. Cooling curves for CMAS + 5, 10, and 12.5 wt% TiO_2 did not show any crystallization upon cooling. For 15 and 20 wt% TiO_2, T_c is increased compared to CMAS alone. There is increased scatter in the T_c data compared to data collected for T_m and T_g; as will be discussed later, this is likely due to heterogeneous nucleation and crystallization on the

DSC pan. As can be seen in Figure 2.2, it appears that the melting endotherm for CMAS + 20 wt% TiO_2 contains more than one event. The three small exothermic peaks that appear prior to melting likely correspond to intrinsic crystallization of the CMAS and were visible in DSC curves for all CMAS + TiO_2 compositions (they are not seen for CMAS alone in Figure 2.2 because it was pre-crystallized).

ii. Ramped heat treatment: Box furnace

The results obtained for samples heat treated in a box furnace agreed well with those seen by DSC. Resulting CMAS, CMAS + 10 wt% TiO_2, and CMAS + 20 wt% TiO_2 samples after holding at 1300°C and cooling at 10°C/min are shown in Figure 2.3.

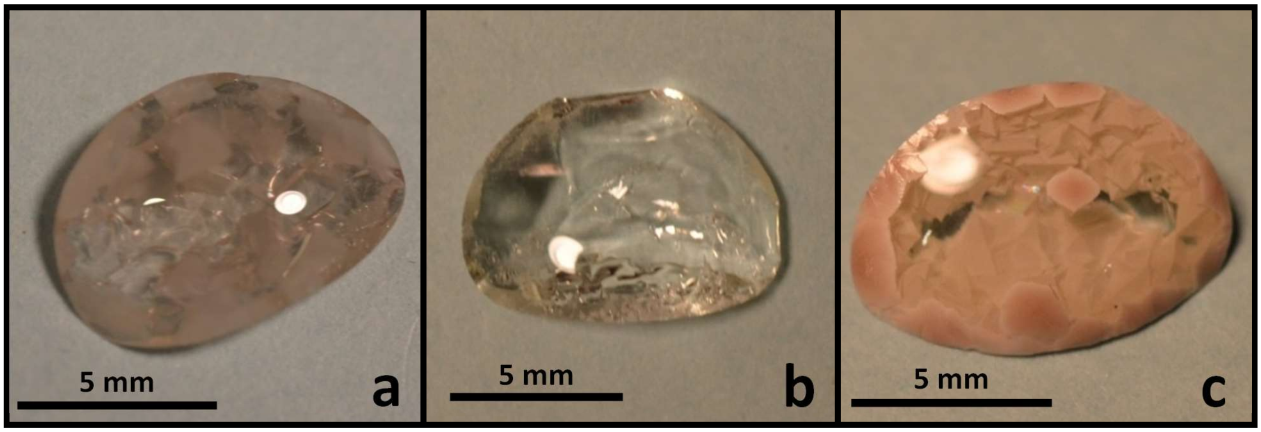

***Figure 2.3**. Resulting samples after box furnace heating to/from 1300°C at 10°C/min (10 min hold time at 1300°C) for (a) CMAS alone, (b) CMAS + 10 wt% TiO_2, and (c) CMAS + 20 wt% TiO_2.*

CMAS alone formed a small amount of crystalline product after cooling at 10°C/min, as demonstrated by the opaque regions of the pellet in Fig. 2.3a. Indeed, qualitative XRD suggested the presence of melilite ($(Ca)_2(Al,Mg)[(Al,Si)SiO_7]$), which is a solid solution with end-members akermanite ($Ca_2MgSi_2O_7$) and gehlenite ($Ca_2Al_2SiO_7$). Figure 2.4 shows XRD spectra for the CMAS sample shown in Figure 2.3a, alongside the CMAS + 10 and 20 wt% TiO_2 samples (Figure 2.3b and c) after heat treatment. EDS mapping indicated that the melilite was Mg-rich and Al-poor, suggesting that it was more akermanitic. With a slower cooling rate of 2.5°C/min, melilite peaks in the XRD spectrum became more prominent and SEM surface and cross-section analysis confirmed that little glass remained in the pellet. XRD suggested the presence of a small amount of additional phase(s) for CMAS cooled at 2.5°C/min as compared to 10°C/min; the peaks for the phase(s) were small and broad, making phase determination difficult, however their position suggests the presence of at least some diopside (Ca(Mg,Al)(Si, Al)$_2$O$_6$). The XRD spectrum for this sample is also plotted in Figure 2.4.

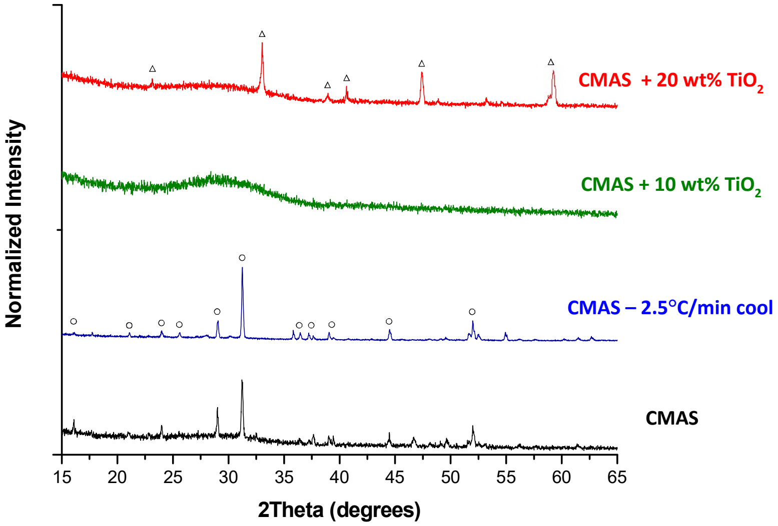

Figure 2.4. *XRD spectra for CMAS, CMAS + 10 wt% TiO$_2$, and CMAS + 20 wt% TiO$_2$ after 10 min at 1300°C followed by cooling at 10°C/min. The XRD spectrum for CMAS cooled at 2.5°C/min is also included. Circles indicate the melilite phase and triangles indicate CaTiO$_3$.*

Titania additions of 5 and 10 wt% decreased the resulting amount of crystalline phase, as was expected from the respective DSC cooling curves. Figure 2.3b shows the clear and colorless glass product obtained from CMAS + 10 wt% TiO$_2$ mixed powder heated in a box furnace at 1300°C with a cooling rate of 10°C/min. XRD spectra confirmed that both 5 and 10 wt% TiO$_2$ products were almost completely amorphous (Figure 2.4). At 12.5 wt% TiO$_2$, the product appeared mostly glassy, similar to CMAS + 10 wt% TiO$_2$, however very small, dendritic crystals were visible in cross section, emanating from contact with the Pt-Au crucible. No phases were identifiable by XRD but increasing TiO$_2$ content to 15 and 20 wt% increased the relative size of the crystals and made it possible to determine that they were calcium titanate (CaTiO$_3$; Figure 2.4). Figure 2.5 shows an SEM cross-section BSE image and the corresponding EDS maps for $CaTiO_3$ formed in CMAS + 20 wt% TiO_2 after heat treatment. $CaTiO_3$ formation was localized, as EDS confirmed that the bulk glass composition was similar to the nominal starting composition.

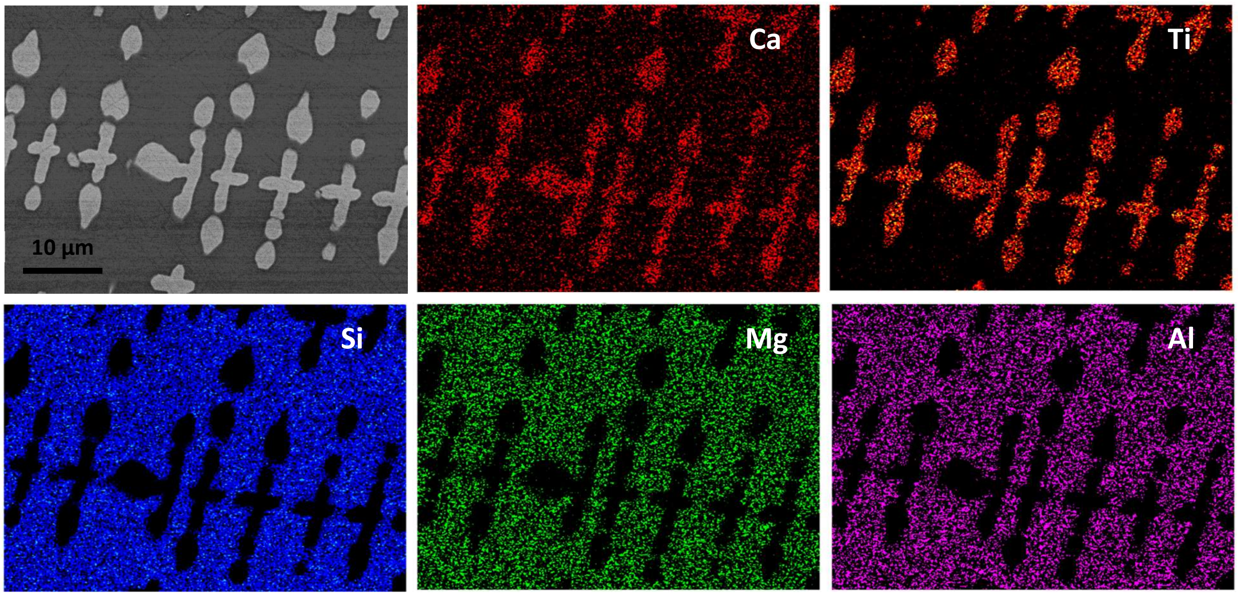

***Figure 2.5**. EDS maps of $CaTiO_3$ crystals formed in CMAS + 20 wt% TiO_2 samples after 10 min at 1300°C in box furnace followed by cooling at 10°C/min.*

Results obtained by DSC suggest that the $CaTiO_3$ dendrites begin to crystallize at temperatures as high as ~1200°C (Table 2.3) after cooling from melts at 1300°C. Equilibration of the melt at 1500°C rather than 1300°C showed little qualitative difference in the $CaTiO_3$ formed. This is potentially significant, as cooling from 1500°C instead of 1300°C for non-$CaTiO_3$-forming mixtures CMAS and CMAS + 5 wt% TiO_2 resulted in more glassy end products. CMAS + 20 wt% TiO_2 was also cooled at rates well above 10°C/min. Samples were heated to 1300°C and held for 10 min in the box furnace prior to turning it off. The rate of cooling was roughly determined from the furnace's digital temperature display and the rate ranged from approximately 249°C/min (1250-1200°C) to 43°C/min (1000-950°C) in the crystallization temperature region of interest. While the size of crystals formed was decreased, $CaTiO_3$ was still detectable even at this higher cooling rate. CMAS alone, subjected to the same furnace conditions, showed no detectable crystallinity. Both CMAS alone and CMAS + 20 wt% TiO_2 were amorphous after quenching from 1300°C in air.

iii. Flight heat treatment (900°C hold): Box furnace

Melilite was formed from CMAS alone after both 1 h and 5.5 h at 900°C following equilibration at 1300°C, as determined by XRD (Figure 2.6). Cross-sectional light microscope imaging showed that there was not much difference between crystals grown at either time and that most crystals seemed to grow from contact with the crucible. Melts equilibrated at 1500°C however, did not show any evidence of crystallization after holding at 900°C. For CMAS + 5 wt% TiO_2, the only temperature/hold profile that showed any sign of crystalline product was for 1300/900°C (5.5 h). XRD for this sample was mostly amorphous with a few peaks likely attributed to melilite (Figure 2.6).

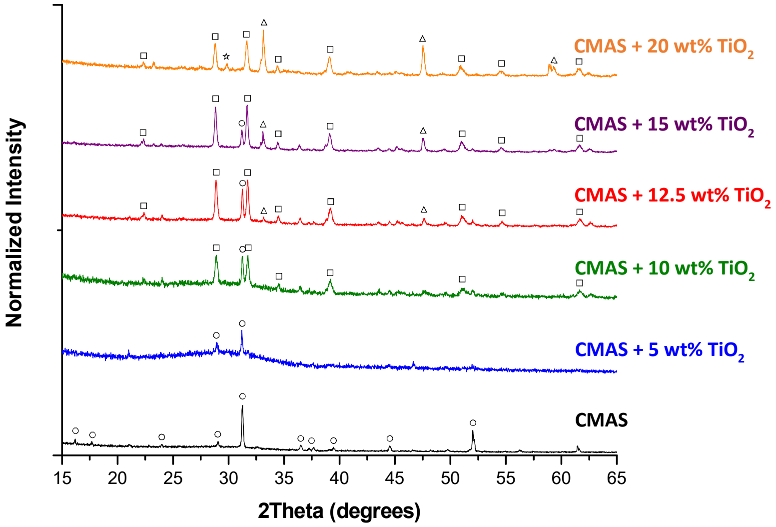

***Figure 2.6**. XRD spectra for CMAS and CMAS + TiO_2 samples after 30 min at 1300°C and 5.5 h at 900°C. Circles indicate melilite, triangles – $CaTiO_3$, squares – paqueite, and stars – diopside.*

Interestingly, with the addition of 10 wt% TiO_2 to CMAS, a new phase appeared after holding at 900°C. XRD confirmed the presence of paqueite ($Ca_3TiSi_2(Al,Ti,Si)_3O_{14}$) along with melilite for the 1300/900°C (5.5 h) profile (Figure 2.6). A cross-section of the product material suggested that the paqueite phase formed as spherulites within the glassy matrix. It was difficult, however, to distinguish how the paqueite formed in relation to melilite; crystal formations such as that observed in cross-section for CMAS alone after 1300/900°C (5.5 h) were not visible. Equilibrating at 1500°C decreased the number of visible crystals formed. Holding at 900°C for 1 h instead of 5.5 h after equilibration at either melt temperature did not produce any evidence of crystallinity.

A TiO_2 content of 12.5 wt% produced small $CaTiO_3$ crystals in contact with the crucible, as seen in the ramped profile experiments, for all temperature/hold profiles. Paqueite and melilite formed within the remaining glass matrix and were detected by XRD (Figure 2.6). Again, small spherulites were seen in cross-section and appeared to grow larger with increased time at 900°C. Holding at 1500°C instead of 1300°C decreased the number of resulting crystallites. Similar results were obtained for CMAS + 15 wt% TiO_2, however $CaTiO_3$ and spherulites were larger than for CMAS + 12.5 wt% TiO_2 after all temperature/hold profiles. XRD indicated a decrease in the amount of melilite present in relation to paqueite as compared to CMAS + 10 or 12.5 wt% TiO_2 (Figure 2.6). Cross-section imaging of the resulting pellet following 1300/900°C (5.5 h) showed little remaining glass content.

For CMAS + 20 wt% TiO_2, melilite peaks were no longer visible via XRD for any temperature/hold profile (Figure 2.6). Calcium titanate and paqueite were the main phases detected by XRD, however a peak, likely attributed to diopside, was also observed. Figure 2.7 shows cross-section light microscope images of CMAS + 20 wt% TiO_2 after all temperature/hold profiles and demonstrates the effect of the melt equilibration temperature on crystallization. Calcium titanate dendrites in contact with the crucible surface were seen as expected, and paqueite spherulites had grown in the remaining glass. A melt equilibration temperature of 1500°C (Figure 2.7c) shows less spherulites after 1 h at 900°C compared to the 1300/900°C sample (Figure 2.7a). After equilibration at 1300/1500°C and 5.5 h at 900°C (Figure 2.7b and 2.7d), there are more paqueite growths, surrounded by secondary phase, than after 1 h. The morphology of paqueite spherulites appeared to remain the same as that seen for 12.5 and 15 wt% TiO_2, however lath-like structures and a new, less prominent phase were seen in between paqueite growths.

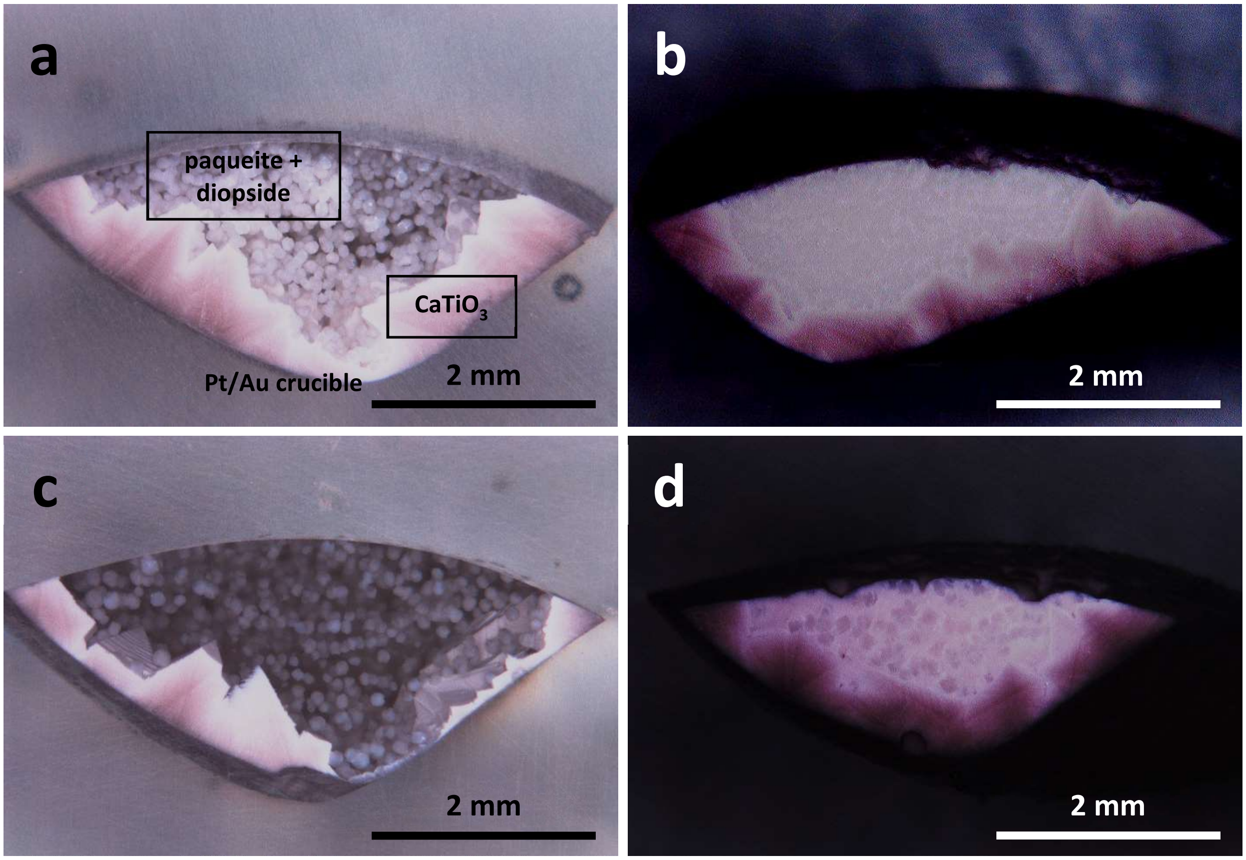

***Figure 2.7**. Cross-section light microscope images of CMAS + 20 wt% TiO_2 after box furnace exposures at (a) 1300/900°C (1 h), (b) 1300/900°C (5.5 h), (c) 1500/900°C (1 h), and (d) 1500/900°C (5.5 h). Images (b) and (d) are heavily contrasted and dark to better show morphology. Image (a) indicates the side of the sample in contact with the Pt/Au crucible and reaction products.*

Figure 2.8 shows cross-section (a,b) and plan-view (c,d) SEM images contrasting the internal structure and surface of 15 and 20 wt% TiO_2 samples after heat treatment at 1300/900°C (5.5 h). Comparing these images, it is evident that some morphological and compositional differences exist between CMAS + 15 and 20 wt% TiO_2 after heat treatment. Unlike for CMAS + 15 wt% TiO_2, CMAS + 20 wt%TiO_2 shows spherulite growths connected by high contrast (by BSE) lath-like structures. These laths and the darker phase present around them are surrounded by an even darker matrix phase (Figure 2.9). These secondary phases are present for all temperature/hold profiles, however it does not appear that they surround all 1 h spherulite growths. Instead, they seem to be around paqueite growths that are near each other or have begun to impinge. This is not the case for CMAS + 15 wt% TiO_2, as depicted in Figure 2.8a and 2.8c wherein growths are seen in contact with one another.

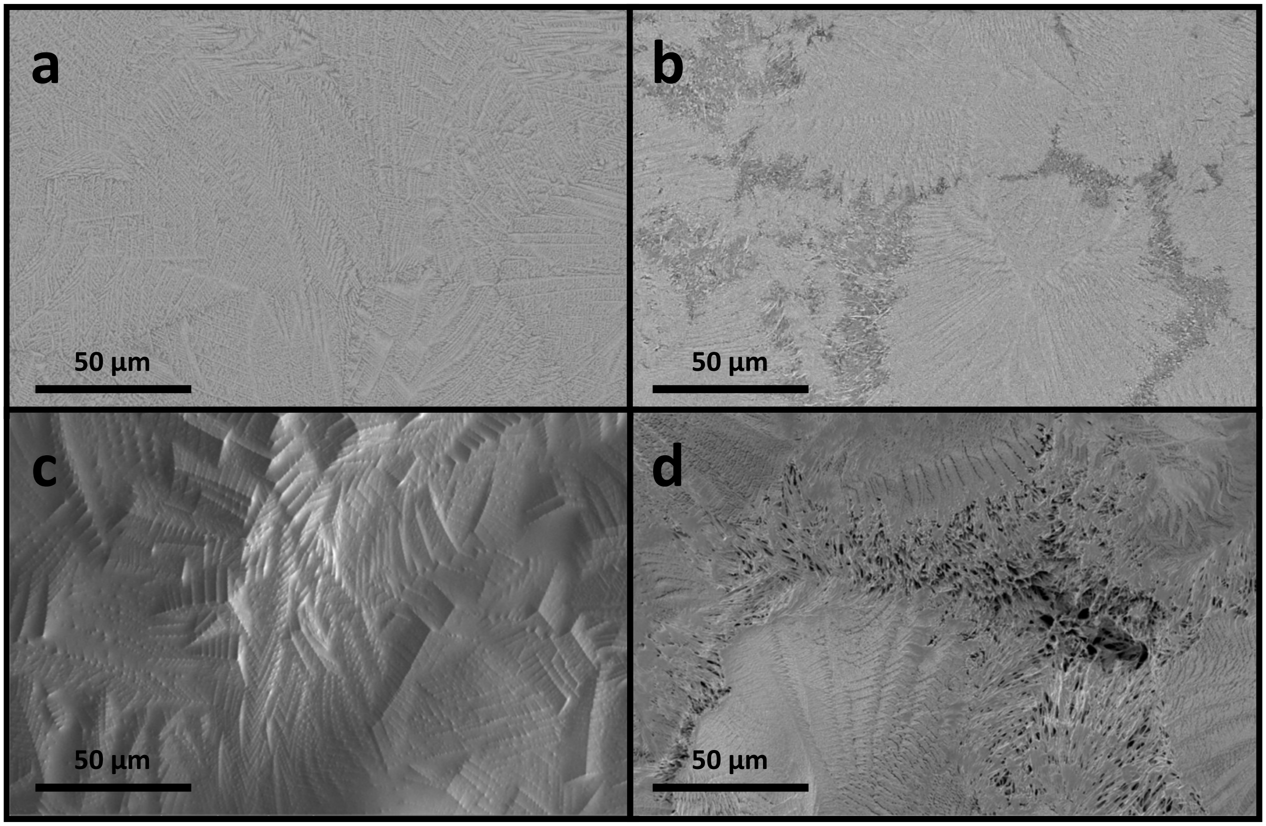

Figure 2.8. *(a,b) Cross-section BSE (c,d) and plan-view SE images for (a,c) CMAS + 15 and (b,d) 20 wt% TiO_2 after 1300/900°C (5.5 h) in box furnace showing differences in crystallization morphology. Calcium titanate not shown.*

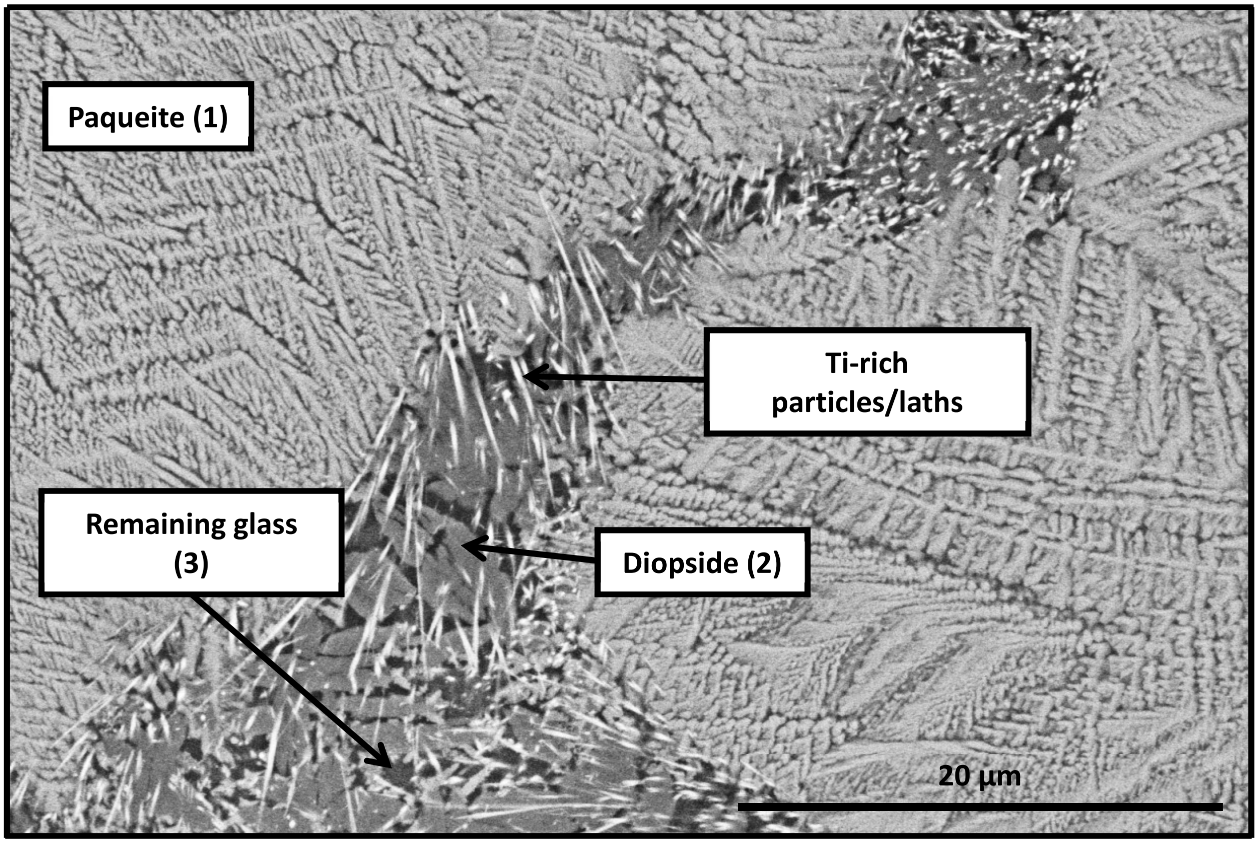

***Figure 2.9**. Higher magnification BSE cross-section image of CMAS + 20 wt% TiO_2 after 1300/900°C (5.5 h) in box furnace. Brightness and contrast of image have been altered to show different phases (paqueite, diopside, remaining glass, and Ti-rich particles/laths).*

Average EDS compositions of the 3 different points (denoted 1-3 in Figure 2.9) can be seen in Table 2.4 for melts equilibrated at 1300°C and 1500°C. The bright particles/laths observed were difficult to perform point EDS on accurately, however it was roughly determined that these structures were Ti-rich. It does not appear that a melt equilibration temperature of 1300°C or 1500°C has a significant effect on the composition of phases formed (differences are within a couple atomic %). The phase denoted by the number 1 in Figure 2.9 appears to roughly fit the paqueite phase composition $Ca_{2.5}Ti_{1.5}AlMg_{0.5}Si_{3.5}O_{14}$, indicating that Mg is soluble in the paqueite structure. Phase 2 most likely corresponds to the diopside phase that was detected by XRD. The remaining glassy matrix (Phase 3) is enriched in Si and Al and depleted in Ca, Mg, and Ti compared to the nominal CMAS + 20 wt% TiO_2 composition.

Table 2.4. *Average EDS compositions for points 1-3 from Figure 2.9 for CMAS + 20 wt% TiO_2 equilibrated at 1300/1500°C followed by 5.5 h at 900°C. The nominal composition of CMAS + 20 wt% TiO_2 is also given.*

	Atomic %				
	Ca	**Mg**	**Al**	**Si**	**Ti**
1 (1300°C)	29.5	6.5	12.0	37.5	14.5
1 (1500°C)	29.0	7.3	11.8	37.1	14.8
2 (1300)	22.8	16.2	11.9	38.8	10.3
2 (1500)	23.2	16.2	11.9	38.4	10.3
3 (1300)	21.5	4.1	16.1	50.4	7.9
3 (1500)	22.2	3.8	15.1	52.2	6.7
Nominal	28.1	7.7	11.1	38.3	14.9

iv. Flight heat treatment (variable "cruise" temperature): Box furnace

Finally, the effect of varying the intermediate or "cruise" temperature was investigated for CMAS and CMAS + 20 wt% TiO_2 melts equilibrated at 1300°C. CMAS samples were held for 5.5 h at 950°C and 1 h and 5.5 h at 1000°C. After 5.5 h at 950°C, CMAS remained mostly glassy. There were some peaks discerned via XRD which were attributed to melilite (Figure 2.10). This was also the case after 1 h at 1000°C. By 5.5 h, the sample had been mostly converted to melilite (Figure 2.10). The presence of a small amount of diopside was also likely based on XRD.

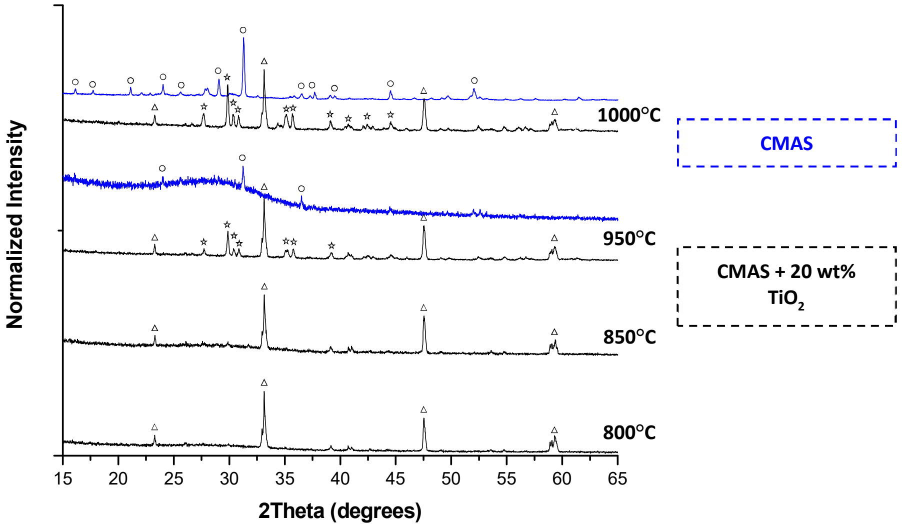

Figure 2.10*. XRD spectra for CMAS (blue) and CMAS + 20 wt% TiO_2 (black) after 30 min at 1300°C and 5.5 h at either 800, 850, 950, or 1000°C. Circles indicate melilite, triangles – $CaTiO_3$, and stars – diopside.*

For CMAS + 20 wt% TiO_2 samples, temperatures of 800, 850, 950, and 1000°C were used with hold times of 1 h and 5.5 h. For all hold temperatures and times, $CaTiO_3$ was detected (Figure 2.10). At 800°C, holding for 1 h did not produce any crystalline material other than $CaTiO_3$. After 5.5 h, in addition to $CaTiO_3$, a small number of ≤10 µm particles could be seen in the remaining glass by cross-section light microscopy. However, other than $CaTiO_3$, no phases were detected by XRD (Figure 2.10). After 1 h at 850°C, a greater number of similar spherical particles no larger than approximately 50 µm were observed. After 5.5 h, the spherulites had grown in size and number within the remaining glass and resembled those seen after holding at 900°C, suggesting that some paqueite and diopside were present. This was difficult to distinguish via XRD (Figure 2.10). Unlike at 850°C, holding at 950°C for 1 h did not produce any phases additional to $CaTiO_3$. After 5.5 h, cross-sectional imaging showed that the resulting sample was apparently completely crystalline. The crystalline phase was confirmed by XRD to be diopside (Figure 2.10). Similarly, at 1000°C, holding for 5.5 h converted remaining glass to diopside (Figure 2.10). After only 1 h at 1000°C, some diopside had formed but glass remained.

III. Discussion

i. Intrinsic CMAS crystallization behavior

It is first necessary to establish a baseline for CMAS crystallization behavior before considering the effect of external oxides/coating constituents. It is apparent that the model CMAS used does not inherently have a propensity for crystallization. Lowering the cooling rate from 10 to 2.5°C/min enhances the crystallization of the melilite phase and allows formation of diopside (Figure 2.4). Such a low cooling rate, however, is not indicative of expected coating conditions. Zaleski et al. calculated that for a TBC having a 0.5°C/μm temperature gradient across the coating, and with a melt penetration rate of 1 μm/s, the cooling rate of glass penetrating a TBC would be ~30°C/min [66]. In an EBC, it may be expected that cooling rate would not even be considered, as these coatings, unlike TBCs, are nominally dense. Theoretically, CMAS should stagnate at the high temperature (nearing 1500°C [48]) surface. However, APS processing of EBCs gives rise to pores and cracks which are susceptible to CMAS infiltration. A thermal gradient would be expected if one assumes that there is some cooling of the underlying CMC. Despite this, and barring any chemical interaction with the coating, penetration of an EBC by the CMAS investigated here would likely not be halted by its intrinsic crystallization.

Holding at 900°C did not have much effect on the amount or type of crystalline product formed. Significant crystallization was not evident until 5.5 h at 1000°C (Figure 2.10). The observed phase was melilite. Wiesner and Bansal probed the crystallization behavior and kinetics of a synthetic sand CMAS glass with a composition of 23.3CaO-6.4MgO-3.1Al_2O_3-62.5SiO_2-4.1Na_2O-0.5K_2O (mol %) [67]. This glass remained amorphous after 10 h at 900°C but appeared fully crystalline by XRD/SEM analysis after 20 h at 925°C or 5 h at 960°C. The phases evolved included $CaSiO_3$ (wollastonite) and an Al-containing diopside. Wollastonite and diopside were also observed at 900°C in similar glass compositions studied by Xiao et al [68].

FactSage free energy minimization calculations were performed for the CMAS composition investigated in this study using the Equilibrium Module and FToxide database, including SLAGA [27], to compare the thermodynamically expected phases at 800-1000°C to those observed experimentally. Akermanite is predicted to form between 850 and 1000°C and diopside is predicted between 800 and 1000°C. Wollastonite and anorthite ($CaAl_2Si_2O_8$) are also expected in this temperature range, although they were not observed. The pseudo-quaternary CaO-MgO-Al_2O_3-SiO_2 (constant 10 wt% MgO) phase diagram [69] indicates that the CMAS composition used in this study falls along the melilite/diopside phase boundary (Figure 2.11). The difference in observed phases between this study and the studies of Wiesner and Bansal and Xiao et al. is likely due to a greater CaO content. The crystallization behavior of CMAS is clearly sensitive to relatively small changes in both composition and undercooling temperature.

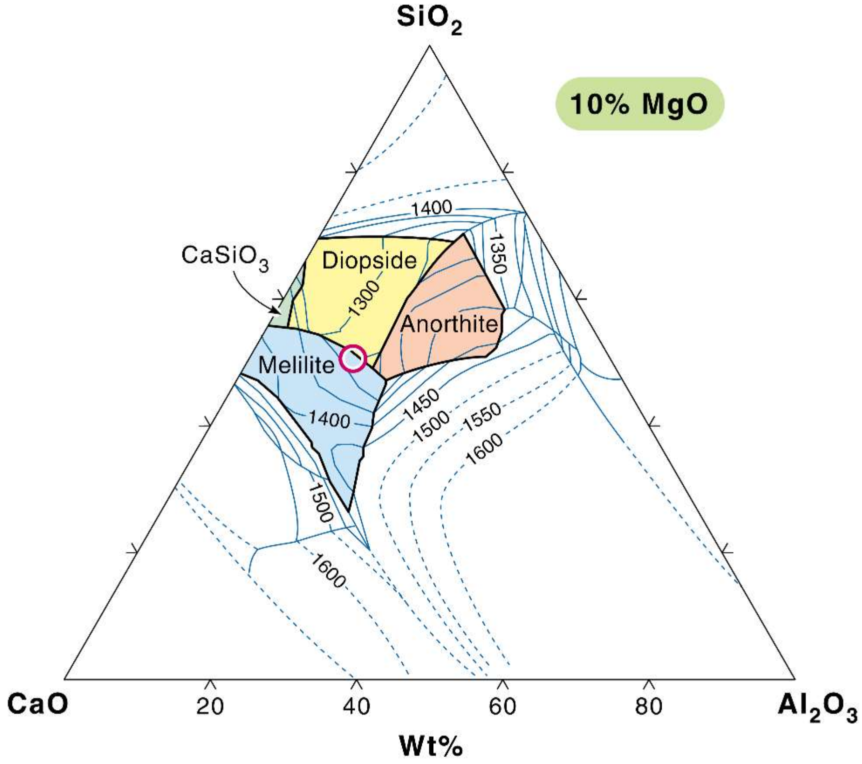

***Figure 2.11**. Pseudo-quaternary CaO-Al_2O_3-SiO_2 with constant 10 wt% MgO phase diagram. The red circle indicates the approximate location of the CMAS composition used in the current study. Phase fields of relevance to this study are labeled. Adapted from [69].*

Because CMAS is difficult to crystallize under engine working conditions, it would be ideal for an EBC (or TBC) under attack to rapidly react with CMAS and contribute chemical constituents that pull CaO and SiO_2 from the melt to form favorable crystalline phases that could potentially block further ingress. Depletion of CaO and SiO_2 from the incoming glass would also increase its melting temperature. It is observed in Figure 2.11 that depletion of CaO or SiO_2 from the composition under study increases its resulting liquidus temperature.

ii. Effect of TiO_2 additions on CMAS crystallization

The addition of TiO_2 to glasses is known to nucleate crystallization under some conditions [62]. Previous studies [37, 70, 71] on the effect of TiO_2 as a nucleating agent in similar glass compositions to that studied here suggest that additions around 5-10 wt% (3.6-7.2 mol%; Table 2.2) will likely not aid crystallization of CMAS. Indeed, in the current study, significant crystallization was not detected until about 12.5-15 wt% TiO_2 was added to the glass. In looking at the SiO_2-TiO_2 and CaO-SiO_2-TiO_2 phase diagrams [72, 73], it is noted that the lowest melting eutectics correspond to a TiO_2 content of ~10 and 17.5 wt%, respectively. Therefore, one may expect that CMAS containing these amounts of TiO_2 would be the better glass formers [74]. In this study, glasses containing 10-12.5 wt% TiO_2 were the least able to crystallize following a “ramped” heat treatment; a result that most closely agrees with the SiO_2-TiO_2 binary phase diagram.

Increasing the TiO_2 content to 15-20 wt% significantly increased the ability of the glass to crystallize. Calcium titanate formed heterogeneously in contact with the crucible surface for both compositions. Results obtained by DSC indicate that $CaTiO_3$ formed at temperatures as high as about 1200°C; however, there was much scatter in the T_c data, likely due to the heterogeneous nature of $CaTiO_3$ crystallization. The difference between the 15 and 20 wt% TiO_2 samples was the absence of melilite and presence of diopside in CMAS + 20 wt% TiO_2 held at 900°C (Figure 2.6).

FactSage was used to determine the expected phases for CMAS + 20 wt% TiO_2 at 800-1000°C, as was done for CMAS alone. At all temperatures, $CaTiO_3$, diopside, anorthite, and sphene ($CaSiTiO_5$) were predicted. Thermodynamics for the paqueite phase were not available, which may explain the discrepancy in calculated versus observed phases. Golovchak et al. presented XRD data on a TiO_2-containing CMAS glass ($19.6CaO$-$12.2MgO$-$7.2Al_2O_3$-$40.8SiO_2$-$20.2TiO_2$; mol%) held at 1200°C [75]. They observed rutile, anorthite, $CaSiTiO_5$, and in some cases, diopside. Confirming the results shown in the current work, the amount of TiO_2 added to CMAS, as well as the undercooling temperature, can result in the crystallization of a variety of phases.

In analyzing the microstructure of the CMAS + 20 wt% TiO_2 glass after heat treatment (Figures 2.8 b,d and 2.9), it can be hypothesized that the spherulitic growths nucleated within the glass matrix, consuming its constituents to form paqueite, as was seen in samples containing 10-15 wt% TiO_2. However, as the growths developed, the remaining glass became saturated in Ti due to its higher initial concentration (Table 2.2). This saturation resulted in the expulsion of TiO_2 laths and particles, which acted as nucleation sites for subsequent diopside growth. At temperatures of 950 and 1000°C, only diopside was observed, suggesting that its solubility tolerance for Ti is greater than in paqueite.

The role of TiO_2 as a “nucleating agent” in the overall crystallization process, however, is unclear. Nucleation and/or crystallization of glasses can be promoted by such agents in the following ways: 1) the nucleating agent, undissolved in the melt, can act as itself a site for further crystalline phases to form [76, 77]; 2) the nucleating agent can promote glass immiscibility or phase separation, leading to crystallization [78]; or 3) the agent added in sufficient quantity can shift the composition to a phase field that is more easily crystallized. Aside from the TiO_2 laths/particles seen for CMAS + 20 wt% TiO_2 held at 900°C, no evidence of TiO_2 crystallites near the centers of the growing paqueite or melilite phases was discerned, as may be expected if TiO_2 was acting as a physical seed. There was also no glass immiscibility observed. Instead, it appears that the addition of sufficient quantities of TiO_2 shifts the composition of the CMAS-TiO_2 system to a phase field that includes paqueite and $CaTiO_3$.

2.2 (b) RE titanates + SiO_2

I. Experimental

i. RE titanate sample preparation

Sample preparation conditions for the RE titanates were guided by the phase diagrams shown in Figure 2.12. Ytterbium and yttrium monotitanates (Yb_2TiO_5 – YbMT, Y_2TiO_5—YMT; collectively, REMT) and dititanates ($Yb_2Ti_2O_7$—YbDT, $Y_2Ti_2O_7$—YDT; collectively, REDT) were prepared by mixing stoichiometric Yb_2O_3/Y_2O_3 (≥99.9% purity, Alfa Aesar, Haverhill, MA) and TiO_2 (99.8% purity, Alfa Aesar) powders. The mixtures were ball milled with zirconia media for ~24 h. After mixing, REMT powders were heat treated in a Pt-5%Au crucible for 6 h at 1500°C in a stagnant air box furnace and REDT powders were treated for 6 h at 1200°C. YbMT, YbDT, and YDT are phase pure between 1200-1500°C (Figure 2.12a and b). YMT was also heat treated at 1300°C to avoid any phase transformations during experimentation at 1300°C; YMT has 3 polymorphs in the temperature region of interest (Figure 2.12b). After ~22 days at 1300°C, YMT was almost phase pure and, surprisingly, took on the hexagonal structure (denoted β in Figure 2.12b). All materials were then ball-milled for an additional 24 h and sieved ≤75 µm (3" diam. sieve set with US standard 200 mesh, MTI Corp., Richmond, CA). Phase composition was confirmed using XRD.

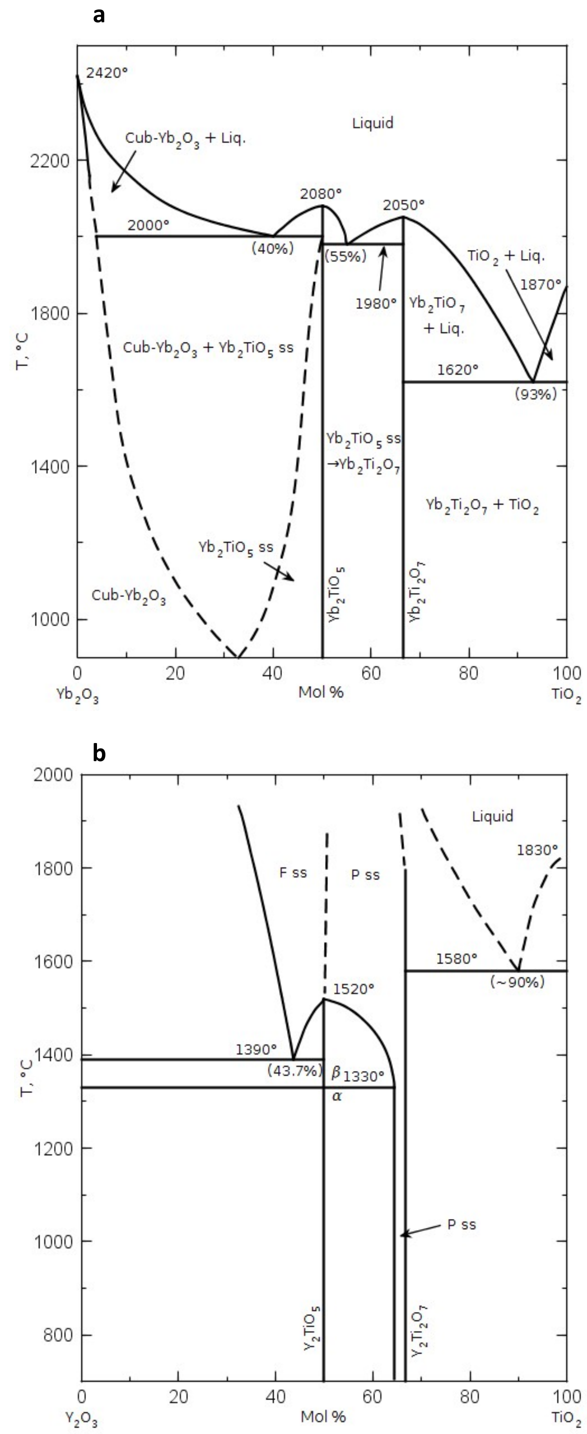

Figure 2.12. *Pseudo-binary phase diagrams for (a) Yb_2O_3-TiO_2 [79] and (b) Y_2O_3-TiO_2 [80].*

ii. RE titanates + SiO_2

REMT and REDT powders, prepared from their constituent oxides, were mixed with amorphous SiO_2 powder (>99% purity, Alfa Aesar) in either a 1:1 or 1:2 mol ratio, respectively, to explore the displacement reactions described by Equations 1.5 and 1.6 (Chapter 1) and repeated below:

$$RE_2TiO_5 + SiO_2 \leftrightarrow RE_2SiO_5 + TiO_2 \tag{2.1}$$

$$RE_2Ti_2O_7 + 2SiO_2 \leftrightarrow RE_2Si_2O_7 + 2TiO_2 \tag{2.2}$$

The YMT used in these experiments was prepared at 1500°C (as described in the previous section). Approximately 150 mg of each mixture was then heat treated in a Pt-5%Au crucible for 100 h at 1300°C in the stagnant air box furnace (with a cooling rate of 40°C/min). Phase identification before and after reaction was performed via XRD.

II. Results

REMT and REDT were determined to be phase pure and their XRD spectra are shown in Figures 2.13 and 2.14 (labeled "baseline") alongside the spectra for Y/Yb titanates + SiO_2 after heat treatment. YMT treated for ~22 days at 1300°C did show a small amount of remaining Y_2O_3.

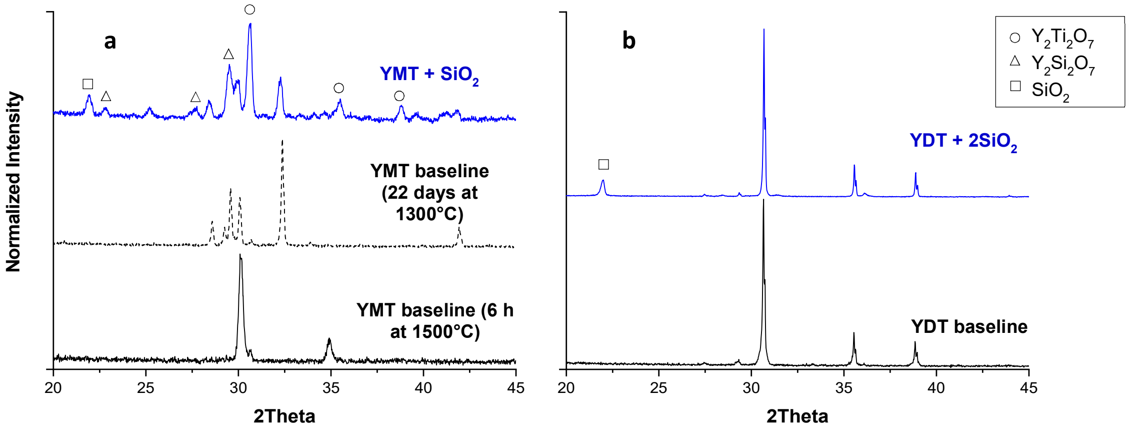

***Figure 2.13**. (a) YMT baseline XRD spectra after heat treatment for 6 h at 1500°C (resulting in the Fss/Pss cubic phase given in Figure 2.12) and ~22 days at 1300°C (the β-phase given in Figure 2.12) compared to YMT + SiO$_2$ after 100 h at 1300°C. (b) YDT baseline XRD spectrum compared to YDT + 2SiO$_2$ after 100 h at 1300°C. Phase identification included Y$_2$Ti$_2$O$_7$ (circles), Y$_2$Si$_2$O$_7$ (triangles), and cristobalite SiO$_2$ (squares).*

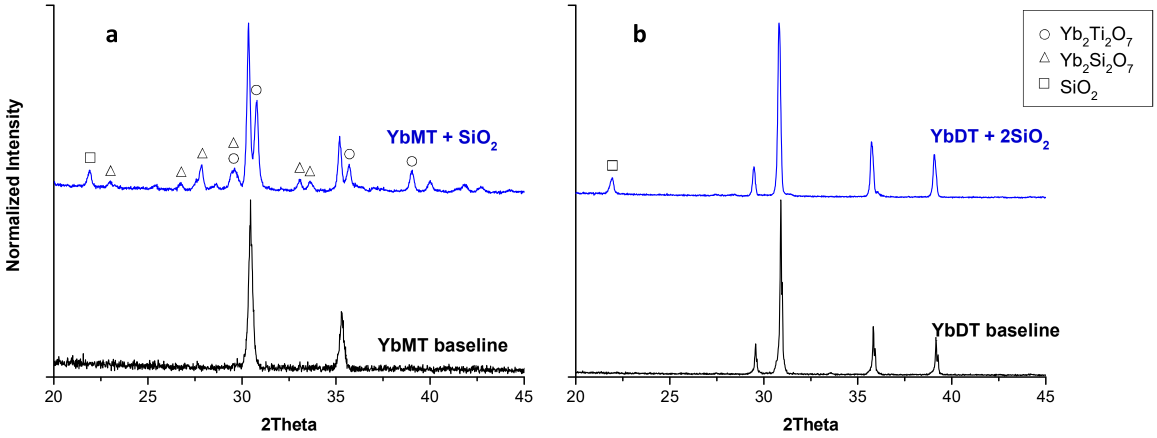

***Figure 2.14**. (a) YbMT baseline XRD spectrum compared to YbMT + SiO$_2$ after 100 h at 1300°C. (b) YbDT baseline XRD spectrum compared to YbDT + 2SiO$_2$ after 100 h at 1300°C. Phase identification included Yb$_2$Ti$_2$O$_7$ (circles), Yb$_2$Si$_2$O$_7$ (triangles), and cristobalite SiO$_2$ (squares).*

New phases, including REDT and RE$_2$Si$_2$O$_7$, were observed in REMT:SiO$_2$ after heat treatment. No peaks for TiO$_2$ were detected. REMT did not completely react, as “baseline” REMT peaks remained in the spectra. A peak at ~22° 2θ indicated the presence of cristobalite, meaning that some of the initially amorphous SiO_2 had crystallized. The YMT material prepared by heat treatment at 1500°C transformed from a cubic fluorite/pyrochlore solid solution to the hexagonal β structure upon exposure at 1300°C. This led to future YMT sample preparation involving long durations (up to about 22 days) at 1300°C to achieve phase purity at this temperature. There were no additional exposures between YMT prepared at 1300°C and SiO_2 but YMT prepared at 1300°C was used in following sections to explore its reaction with CMAS. For REDT:SiO_2, there was no evidence of reaction. The REDT “baseline” peaks were retained and the cristobalite peak was also observed.

III. Discussion

FactSage was utilized to determine the viability of Equations 2.1 and 2.2 for the yttria system [81, 82], for which thermodynamic data are available. Favorable reactions were determined at 1300°C (ΔG = -51 and -24 kJ/mol, respectively), suggesting that both REMT and REDT would react with SiO_2 to form RE silicates and TiO_2. Instead, REMT reacted to form REDT and $RE_2Si_2O_7$ (Equation 2.3) while REDT remained inert (Figures 2.13 and 2.14).

$$RE_2TiO_5 + SiO_2 \leftrightarrow \frac{1}{2}RE_2Ti_2O_7 + \frac{1}{2}RE_2Si_2O_7 \qquad [2.3]$$

Equation 2.3 was also evaluated by FactSage for RE = Y and was determined to be slightly more energetically favorable (ΔG = -70 kJ/mol) than the reaction between YMT + SiO_2 to form TiO_2 (Equation 2.1). RE titanates were shown not to react with SiO_2 to release TiO_2. Thus, the proposed mechanism for TiO_2 to influence CMAS crystallization is unlikely to occur.

2.2 (c) RE titanates + CMAS

I. Experimental

i. Powder interactions

REMT and REDT powders were mixed with CMAS in a 70:30 wt% ratio, respectively, to understand the phase evolution of RE titanates with CMAS. Powder mixtures were exposed at 1300/1500°C for 10 min and 4, 24, and/or 96 h in the stagnant air box furnace. A ramp rate of 10°C/min was used. These tests were modeled after a previous investigation by Stolzenburg et al. on Yb silicates [51]. The CMAS used was of composition 33CaO-9MgO-13$AlO_{1.5}$-45SiO_2 and was prepared as described previously for CMAS + TiO_2 experiments (**2.2 (a)**). After heat treatment, the reacted powders were ground with mortar and pestle and were mixed in a 50:50 wt% ratio with Al_2O_3 (corundum; 99.9% purity, Alfa Aesar) for reference intensity ratio (RIR) quantitative XRD measurements. The RIR method relates the intensity of the crystalline phases of interest (in this case, REMT and REDT) peaks to the intensity of the standard (Al_2O_3) peak in the quantification of crystalline and amorphous weight fractions [83]. The following equation was used:

$$\chi_\alpha = \left(\frac{I_{(hkl)\alpha}}{I_{(hkl)\beta}}\right)\left(\frac{I^{rel}_{(hkl)\beta}}{I^{rel}_{(hkl)\alpha}}\right)\left(\frac{\chi_\beta}{RIR_{\alpha,\beta}}\right) \tag{2.4}$$

where χ_α and χ_β correspond to the weight fraction of REMT/REDT and Al_2O_3, respectively, $I_{(hkl)\alpha}$ and $I_{(hkl)\beta}$ are the intensities of the REMT/REDT and Al_2O_3 peaks for a given hkl, respectively, and $RIR_{\alpha,\beta}$ is the reference intensity ratio that was experimentally determined. RIR values for REMT and REDT were determined by preparing a 50:50 wt% ratio mixture of either REMT or REDT with Al_2O_3 and dividing the 100% intensity peak for REMT/REDT by the 100% intensity peak for Al_2O_3. RIR values for YbMT, YMT, YbDT, and YDT are given in Table 2.5. The Al_2O_3 (113) reflection, located at ~43.3°2θ, was used in all calculations. All samples were run in triplicate and average values are reported. Because the 100% intensity peak for both the RE titanates and Al_2O_3 was used, the ratio $I^{rel}_{(hkl)\beta}/I^{rel}_{(hkl)\alpha}$ was taken as unity in Equation 2.3.

***Table 2.5**. The hkl reflections/peak positions (100% intensity) used to determine RIR values for REMT and REDT.*

Phase	Reflection	Peak Position (°2θ)	RIR
Yb_2TiO_5	(111)	30.3	6.8
Y_2TiO_5	(102)	32.3	3.4
$Yb_2Ti_2O_7$	(222)	30.8	10.2
$Y_2Ti_2O_7$	(222)	30.7	7.9

The validity of the obtained RIRs was evaluated by analyzing a known mixture of either REMT or REDT with amorphous SiO_2. The uncertainty associated with RIR values for YbMT, YMT, YbDT, and YDT was nominally 5-8, 2-3, 1, and <1 wt%, respectively.

ii. Levitation melting and cooling

1. Sample preparation

Samples for melting and cooling experiments on the 6-ID-D beamline levitator at the Advanced Photon Source (APS) at Argonne National Laboratory were prepared at the UC Davis Peter A. Rock Thermochemistry Laboratory. Previously described material, CMAS and CMAS + 20 wt% TiO_2 glass powders, as well as powder mixtures of RE titanate with CMAS in a 70:30 wt% ratio, were melted in a copper hearth in air with a 400 W CO_2 laser (Synrad Firestar i401, Mukilteo, WA). Powders were lased until they formed a spherical “bead.” Once this shape was acquired, the laser was turned off to quench the sample. Samples were then re-melted under air flow in an aerodynamic levitator similar to the one used at APS. Sample beads were ~2-3 mm in diameter. EDS analysis of the beads after melting suggested that there were no significant changes in sample chemistry following laser preparation.

2. Levitation experiments

XRD experiments were performed in the Debye-Scherrer geometry using an aerodynamic levitator on beamline 6-ID-D at APS. The beam wavelength was 0.123573 Å and the sample to detector distance was ~1130 mm. The experimental setup is described in detail by Weber et al. [84, 85]. A simplified schematic of the setup is given in Figure 2.15.

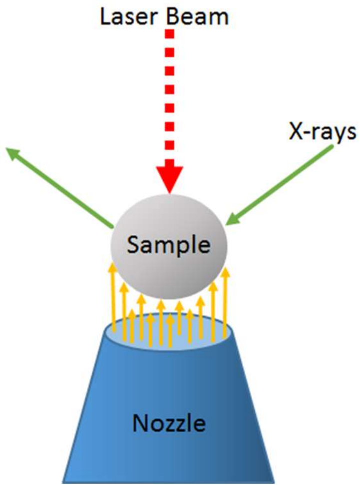

Figure 2.15. *Schematic of the levitation setup at the Advanced Photon Source. Courtesy of Rachel Guarriello, UVa.*

Sample beads were levitated in O_2 gas. Gas flow was adjusted to ensure consistent rotation of the sample. The height of the nozzle was adjusted so that diffraction occurred only at the surface of the bead. Samples were melted and then cooled at ~10, 50, and/or 100°C/s. Note that these cooling rates are in °C/s while previously described box furnace experiments involved cooling rates of °C/min. Temperature was measured by a single band Chino IR-CAS3CS pyrometer (Tokyo, Japan). PID control of the laser power with feedback from the pyrometer was used to control the cooling rate. The exposure time was set to 0.1 s per frame, with either 60, 10, or 5 summed exposures per diffraction image for cooling rates of 10, 50, and 100°C/s, respectively. “Dark” images, wherein the x-ray was turned off, were collected periodically and automatically subtracted from following diffraction images.

3. Data analysis

Integration of the diffraction image files was done using FIT2D software [86]. The x-ray wavelength was set to 0.123573 Å. Input values for sample to detector distance, rotation and tilt angles, and x-ray beam coordinates were calibrated from diffraction images of levitated CeO_2, collected at room temperature.

Refinement of the x-ray data was carried out in GSAS-II [87]. Instrument parameters were defined by the aforementioned CeO_2 calibration. Sample peaks were refined with respect to position, intensity, and Gaussian and Lorentzian widths. GSAS powder diffraction files were then converted into a format that could be read by High Score for phase analysis.

Post-levitation sample beads were also epoxy-mounted and cross-sectioned for imaging and chemical analysis by SEM/EDS. Samples were polished and coated with a thin layer of gold/palladium prior to analysis. Images were taken in the BSE mode.

iii. Pellet interactions

The results of the aforementioned experiments on RE titanates + CMAS powder mixtures (described in Section *i.*) led to interest in further testing of Yb_2TiO_5 in pellet form. YbMT powders were prepared as described in Section **2.2 (b)** I. *i.*, but were sieved to ≤32 µm and ball milled an additional 24 h for a final powder size of ~≤5µm. Approximately 15 g of YbMT powder was then mixed with about 10 drops of a solution of ~2 wt% polyvinyl alcohol (PVA; Sigma Aldrich, St. Louis, MO) in deionized water. The powders were transferred to a 20 mm diam. graphite die (Beaumac Company, Inc., Epsom, NH) coated with a thin layer of boron nitride paint (ZYP Coatings, Inc., Oak Ridge, TN). A load of approximately 5 MPa was applied to the die using a benchtop hydraulic press (MTI Corp. Desk-Top Powder Presser, Richmond, CA). The pressed powders were heat treated for 10 h at 1500°C in a stagnant air box furnace with a ramp up rate of 5°C/min and a ramp down rate of 7.5°C/min. The sintered pellet was sectioned into ~10 x 10 x 1-2 mm thick samples for testing. Sample surfaces were polished to 1200 grit with SiC paper (Buehler, Lake Bluff, IL) and cleaned prior to testing. Density of the samples was measured in deionized water using Archimedes' Method and was ~95% that of the theoretical.

CMAS powders were pressed (using the benchtop hydraulic press) into 6.35 mm (1/4") diameter pellets that were heat treated for 4 h at 1200°C in the box furnace. The size of the pellets was kept between ~35-45 mg for a CMAS loading of ~35-45 mg/cm^2. In some tests, a loading of either 17.5-22.5 mg/cm^2 (low load) or 70-90 mg/cm^2 (high load) was utilized. The CMAS pellets were placed on the surface of the YbMT samples as shown in Figure 2.16. Exposures were performed in the box furnace for 10 min and 4, 24, and 96 h at 1300°C with a heating/cooling rate of 10°C/min. "Double loading" experiments were also performed; after 96 h at 1300°C in contact with a CMAS load of 35-45 mg/cm^2, samples were subjected to a second CMAS load of 35-45 mg/cm^2, and were put back in the box furnace for an additional 4, 24, or 96 h. All samples were epoxy-mounted and cross sectioned after heat treatment. Half of the sample was used for SEM/EDS and half of the sample was removed from the epoxy mount and analyzed by XRD. EDS analysis was semi-quantitative. XRD samples were analyzed as bulk specimens first and then subsequently ground to a fine powder for powder analysis. SEM/EDS samples were coated with a thin layer of gold/palladium prior to characterization. Images were taken in BSE mode. ImageJ [88] was used to stitch SEM images and measure infiltration depth/reaction zone thickness.

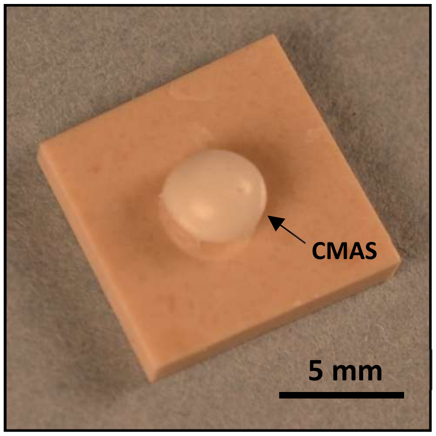

***Figure 2.16**. YbMT coupon with CMAS pellet on surface prior to high temperature exposure.*

II. Results

i. Powder interactions

REMT reacts quickly with CMAS to form new crystalline phases; spectra for YbMT exposed to CMAS for 10 min at 1300/1500°C are shown in Figure 2.17a. After only 10 min at 1500°C, YbMT peaks have completely disappeared and are replaced by those for YbDT, apatite ($Ca_2Yb_8(SiO_4)_6O_2$), and a garnet phase ($Yb_6Mg_5Si_5O_{24}$). At 1300°C, YbMT completely reacts by 24 h (Figure 2.18a). YbDT, apatite, and garnet are present to 24 h at 1300°C; garnet is only evident in the 10 min sample at 1500°C (Figure 2.17a). YMT (β) reacts slower with CMAS than does YbMT (Figure 2.18a). YMT + CMAS reaction products include YDT, Y apatite, and Y garnet.

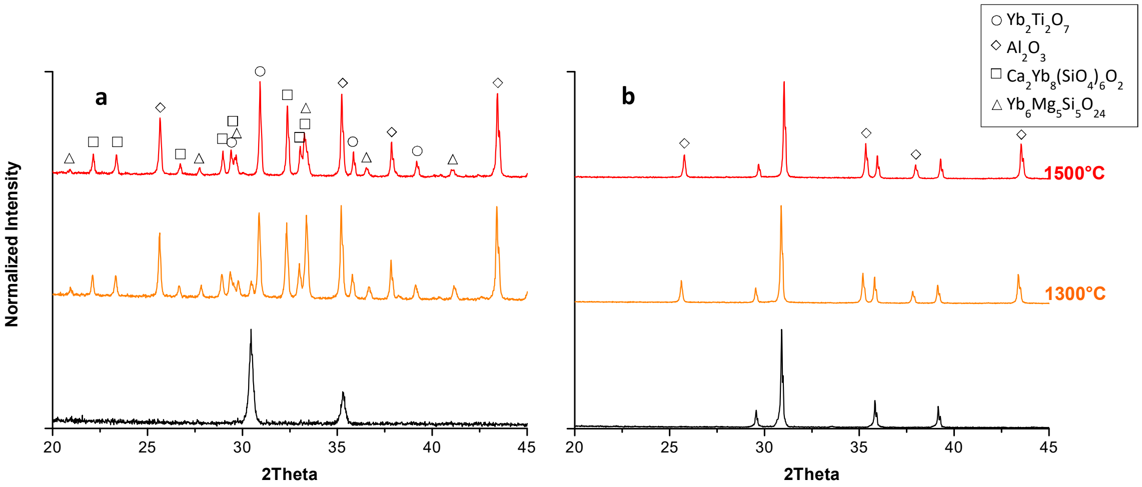

***Figure 2.17**. XRD spectra for (a) YbMT after exposure to CMAS for 10 min at 1300/1500°C and (b) YbDT after exposure to CMAS for 96 h at 1300/1500°C. Phase identification included $Yb_2Ti_2O_7$ (circles), Al_2O_3 (diamonds), $Ca_2Yb_8(SiO_4)_6O_2$ – apatite (squares), and $Yb_6Mg_5Si_5O_{24}$ – garnet (triangles). The presence of Al_2O_3 is from RIR measurements.*

As expected from the REDT + SiO_2 powder mixture results, REDT mixed with 30 wt% CMAS did not react to form any crystalline phases at either 1300 or 1500°C at any time. Figure 2.17b gives the XRD spectra for YbDT + CMAS after 96 h at 1300/1500°C. The spectra for YDT + CMAS are similar. There is no change between baseline YbDT and reacted samples; the peaks that do not correspond to YbDT in the 1300 and 1500°C spectra belong to the reference standard Al_2O_3 used for RIR measurements. Although crystallization between the two reactants does not occur, dissolution of REDT in CMAS is evident. Figure 2.18b plots the remaining REDT content, determined by RIR, versus amount of time at 1300°C. The amount of REDT remaining after exposure stagnates at approximately 40 wt% for all times tested. This was also the case at 1500°C.

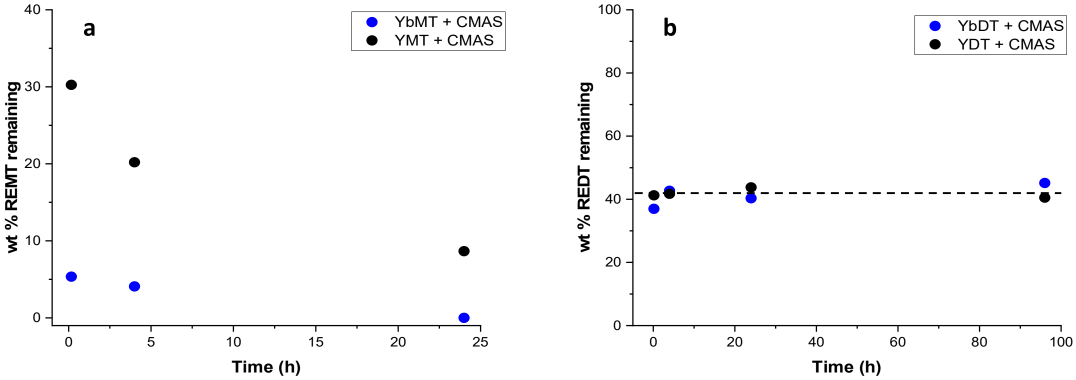

***Figure 2.18**. Amount of (a) REMT and (b) REDT remaining (in wt%) after powder reaction with CMAS at 1300°C.*

The mole percent equivalents for 70:30 wt =% RE titanate + CMAS mixtures are given in Table 2.6 for comparison to RE titanate + SiO_2 mixtures. The amount of CMAS in these experiments is ~8-28 mol% greater than the SiO_2 content in RE titanate + SiO_2 samples, but was used in order to compare to results from the literature. The molar percentages for individual elements in each mixture, based on a CMAS composition of 33CaO-9MgO-13$AlO_{1.5}$-45SiO_2, are given in Table 2.7.

***Table 2.6**. Relative amounts of RE titanate and SiO_2/CMAS in wt% and/or mol%.*

	YbDT	**CMAS**	**YDT**	**CMAS**	**YbMT**	**CMAS**	**YMT**	**CMAS**
wt%	70	30	70	30	70	30	70	30
mol%	19	81	25	75	22	78	30	70
	YbDT	**SiO_2**	**YDT**	**CMAS**	**YbMT**	**SiO_2**	**YMT**	**CMAS**
mol%	33	67	33	67	50	50	50	50

***Table 2.7**. Relative amounts of RE titanate and CMAS constituents in mol%.*

	Yb	Y	Ti	Ca	Mg	Al	Si
YbMT + SiO_2	50		25	-	-	-	25
YMT + SiO_2		50	25				25
YbDT + $2SiO_2$	33.3		33.3	-	-	-	33.3
YDT + SiO_2		33.3	33.3				33.3
YbMT + CMAS	30.5		15.3	17.9	4.9	7.0	24.4
YMT + CMAS		37.3	18.7	14.5	4.0	5.7	19.8
YbDT + CMAS	24.2		24.2	17.0	4.7	6.7	23.2
YDT + CMAS		28.8	28.8	14.0	3.8	5.5	19.1

ii. Levitation melting and cooling

Levitation melting/cooling results for CMAS and CMAS + 20 TiO_2 are provided in this section, rather than Section **2.2 (b)**, for direct comparison to results for RE titanates + CMAS. CMAS and CMAS + 20 wt% TiO_2 beads did not crystallize on cooling from the melt at 10°C/s in the APS levitation setup. Cross-section images of the resulting glassy beads can be found in Figure 2.19. EDS analysis of the beads indicated that there were no significant changes in sample chemistry after levitation melting and cooling.

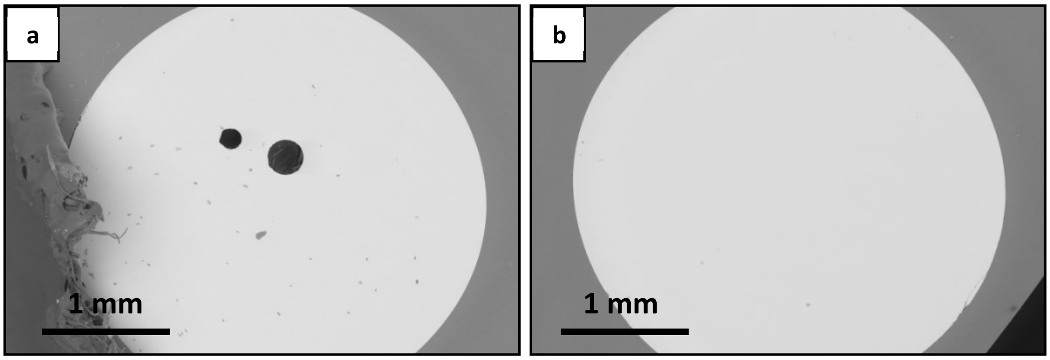

***Figure 2.19**. Cross-section BSE images of (a) CMAS and (b) CMAS + 20 wt% TiO_2 (compositions given in Table 2.2) beads after cooling from the melt at 10°C/s in the APS levitation setup.*

Beads prepared from a mixture of 70 wt% YbMT/30 wt% CMAS melted at ~1650-1700°C. On cooling at 10°C/s, the onset temperature for crystallization was ~1350°C. The observed crystalline phases included YbMT and YbDT (Figure 2.20). There is at least one other phase present, as additional peaks are seen in Figure 2.20, however identification of these peaks was unsuccessful. The microstructure of the cooled bead can be seen in cross-section in Figure 2.21. Higher cooling rates of 50 and 100°C/s resulted in glassy end products. YbDT + CMAS melted at ~1700-1750°C and remained glassy under all cooling conditions.

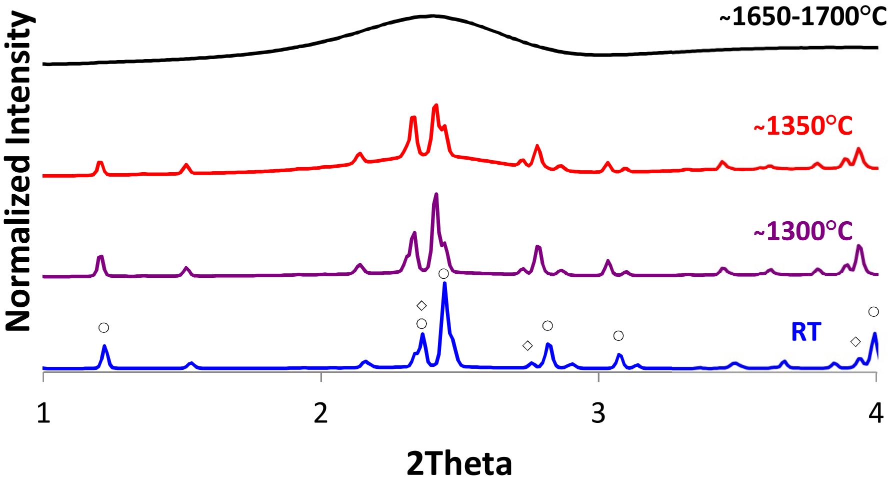

***Figure 2.20**. Spectra for YbMT + CMAS after cooling at 10°C/s in the levitation setup. Circles indicate $Yb_2Ti_2O_7$ and diamonds, Yb_2TiO_5.*

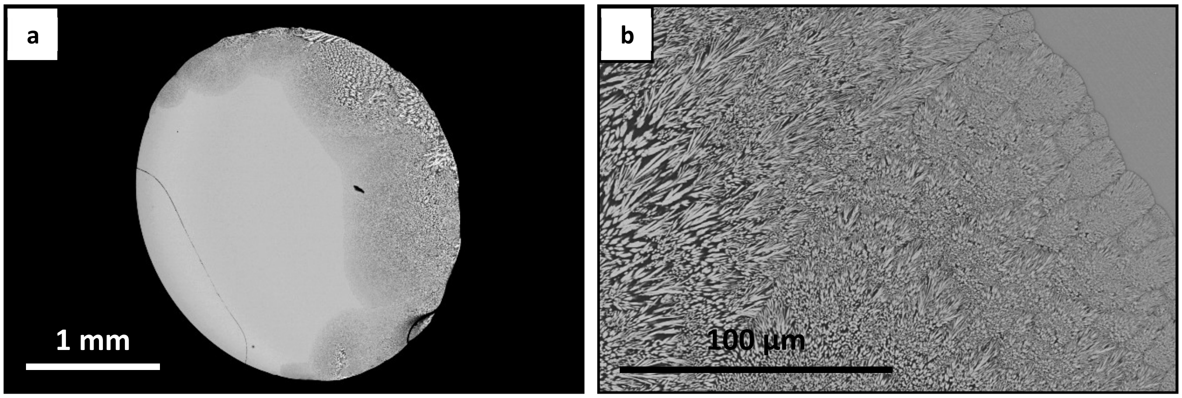

***Figure 2.21**. Cross-section BSE images of a Yb_2TiO_5 + CMAS bead after cooling from the melt at 10°C/s in the APS levitation setup. Image (b) is a higher magnification of the crystallized material/glass interface evident in (a).*

XRD spectra for YMT + CMAS and YDT + CMAS cooled at 10°C/s in the levitation setup are given in Figure 2.22a and b, respectively. Both mixtures melted at ~1700-1750°C. For YMT + CMAS, the onset of crystallization was ~1500°C and reaction products included apatite, YDT, and possibly $YTiO_3$. Crystallization was also evident in samples cooled at 50 and 100°C/s. YDT + CMAS recrystallized YDT after cooling at 10°C/s, but not 50 or 100°C/s. The onset of crystallization was ~1425-1475°C. Cross-section images of YMT + CMAS and YDT + CMAS beads after levitation melting and cooling at 10°C/s are given in Figure 2.23. The crystallization results obtained via levitation melting/cooling are in contrast with box furnace powder interaction studies carried out at 1300°C, wherein YbMT + CMAS showed a greater extent of crystallization than YMT + CMAS (Figure 2.18a).

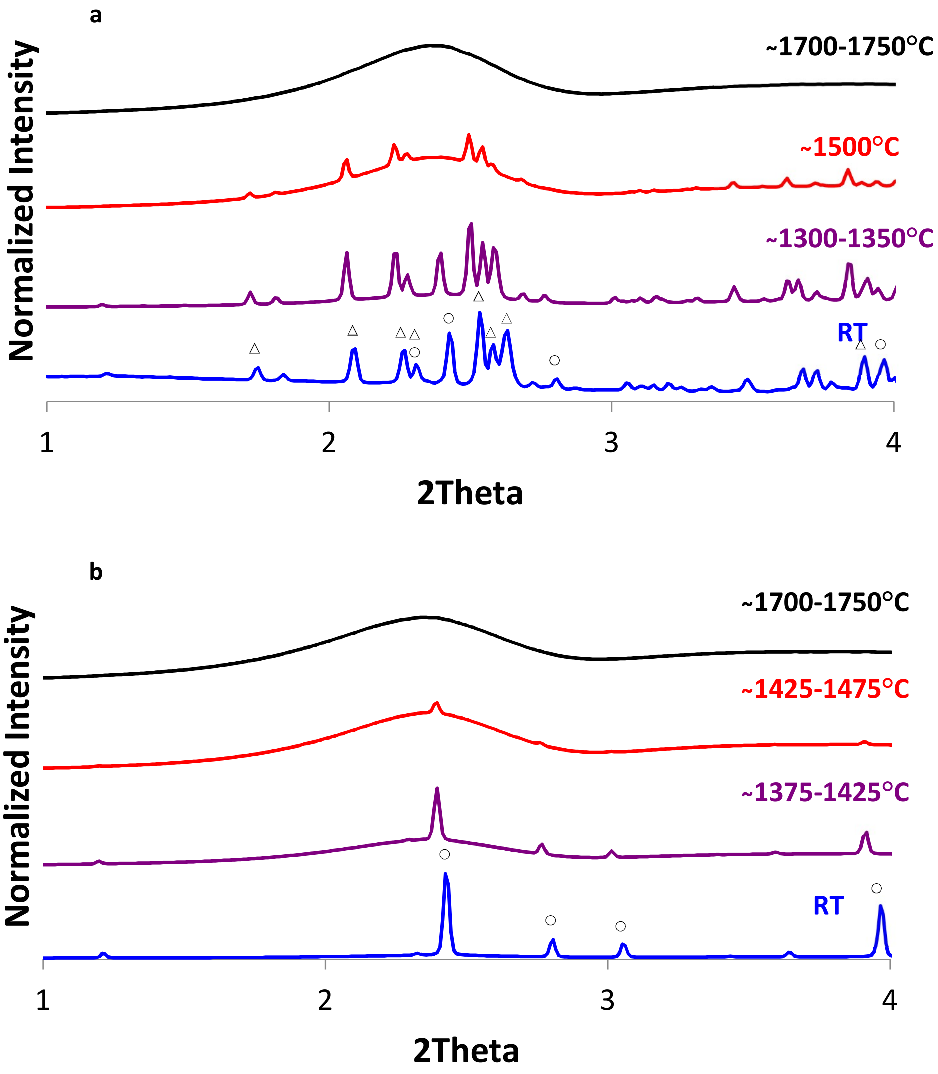

***Figure 2.22**. Spectra for (a) YMT + CMAS and (b) YDT + CMAS after cooling at 10°C/s in the levitation setup. Circles indicate $Y_2Ti_2O_7$ and triangles, Y apatite.*

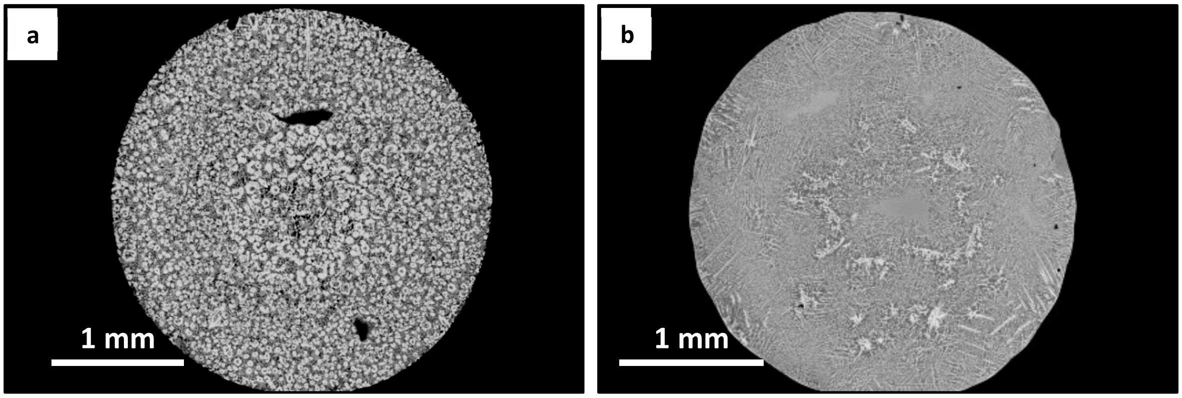

***Figure 2.23**. Cross-section BSE images of (a) YMT + CMAS and (b) YDT + CMAS beads after cooling from the melt at 10°C/s in the APS levitation setup.*

iii. Pellet interactions

YbMT was prepared as a dense sample, due to its ability to react rapidly with CMAS to form new crystallized phases, for testing with CMAS to determine reaction kinetics and phase morphology. Difficulty in preparation of phase pure YMT precluded it from further study. Figure 2.24 shows an example of a YbMT + CMAS pellet after heat treatment.

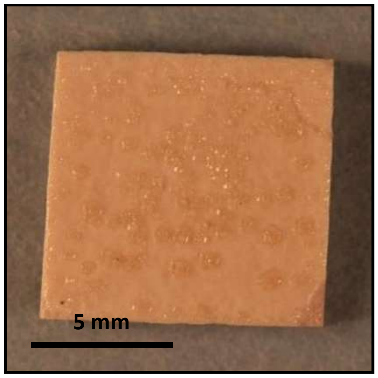

***Figure 2.24**. YbMT coupon after exposure to CMAS at 1300°C for 96 h. Note raised bubbles on the surface of the sample.*

The reaction zone interface for YbMT + CMAS samples as a function of time can be seen in cross-section in Figures 2.25 and 2.26. Figure 2.26 expands the images in Figure 2.25a and 2.25d and gives labeled reaction products. For all test times, the CMAS pellet melted and spread across the entire surface of the YbMT sample. After 10 min (Figure 2.25a, 2.26a) and 4 h (Figure 2.25b) at 1300°C, a relatively thin layer of intermixed apatite and YbDT had formed at the reaction interface. The apatite phase precipitated as “needles” with their elongated direction normal to the sample surface. Glass remained at the surface. Dendritic crystals, most likely garnet, could be found within the remaining glass. After 24 h (Figure 2.25c) and 96 h (Figure 2.25d, Figure 2.26b), there was no longer glass at the surface. The reaction zone layer had thickened considerably and contained, in addition to apatite and YbDT, garnet and a Ca/Ti-rich phase. These phases were large, globular, and interspersed with the apatite and YbDT. XRD analysis of bulk and powdered samples confirmed the presence of apatite and garnet after 10 min at temperature, and apatite, garnet, and YbDT after 4, 24, and 96 h. The crystal structure of the Ca/Ti-rich phase was not confirmed via XRD.

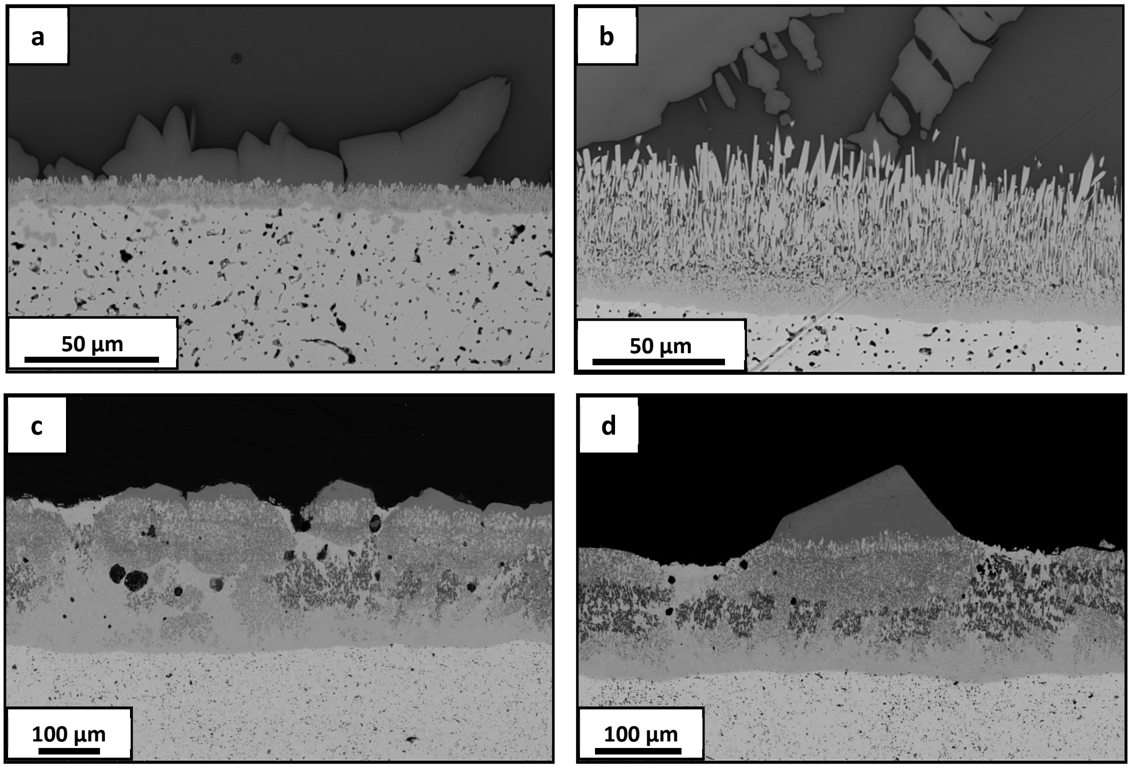

Figure 2.25. *Cross-section BSE images of the YbMT/CMAS interface after (a) 10 min, (b) 4 h, (c), 24 h, and (d) 96 h at 1300°C.*

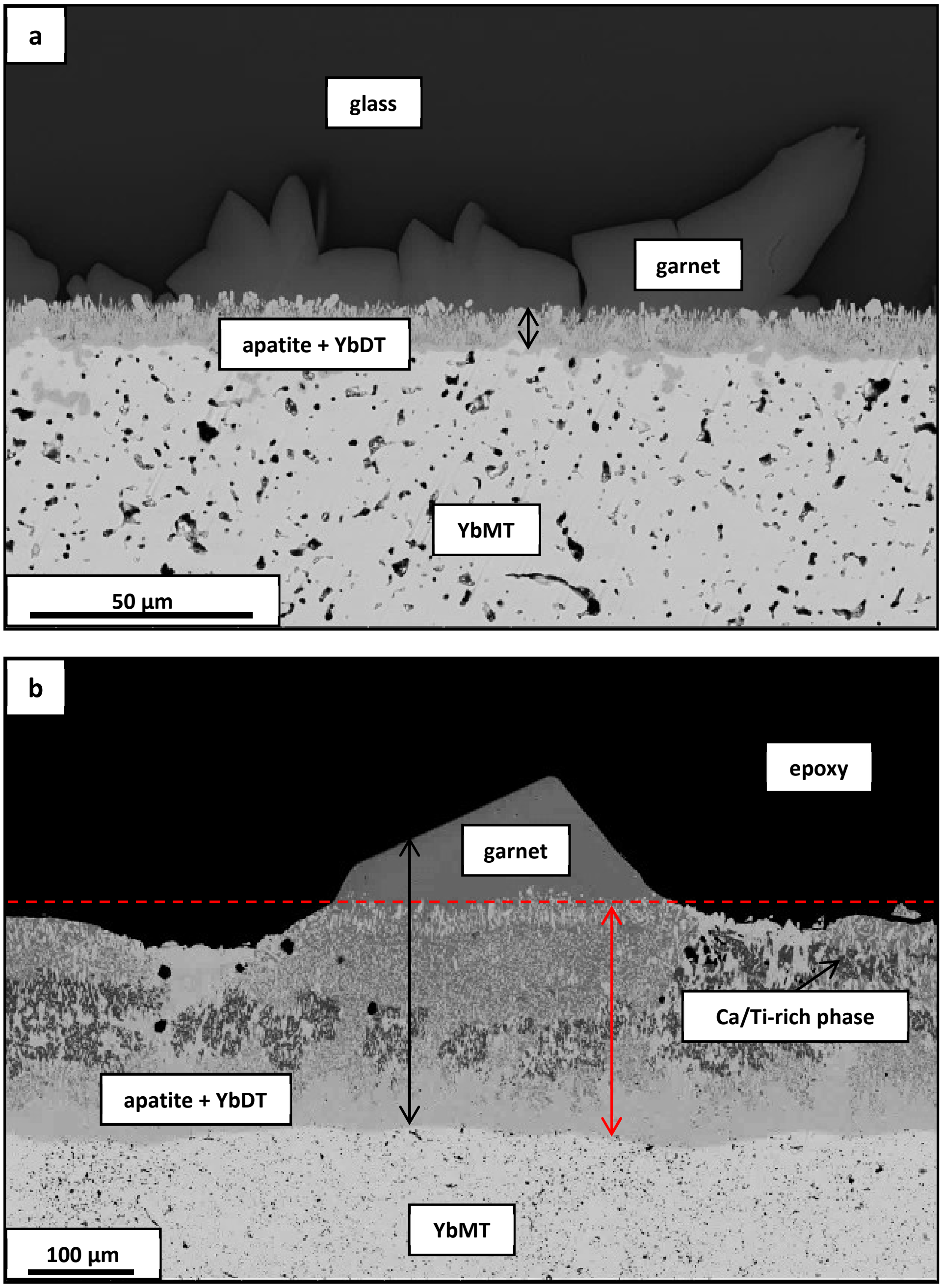

Figure 2.26. *YbMT/CMAS interface after (a) 10 min and (b) 96 h at 1300°C. Reaction products are labeled. Black arrows indicate reaction zone thickness. In (b) the red arrow indicates infiltration.*

Measurements of the reaction zone thickness were taken and are plotted in Figure 2.27. Measurements were performed across the sample surface at ~100 μm increments. Examples of such measurements are given in Figure 2.26 by black arrows. For samples exposed for 24 and 96 h, infiltration depth (red arrow in Figure 2.26b) was also able to be measured. As can be seen in Figure 2.24 for a 96 h sample, the longer duration samples exhibited a surface marked by raised regions or bubbles. The original surface of the sample was assumed from the position of the raised regions. Infiltration depth was considered as the length from the horizontal dashed red line in Figure 2.26b to the YbMT/reaction zone interface. Results are also plotted in Figure 2.27. There was no significant difference between reaction zone thickness and infiltration depth based on this method.

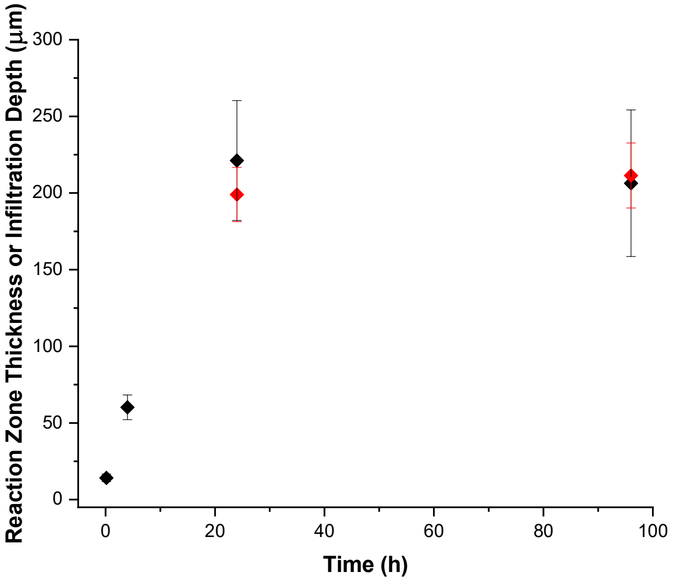

***Figure 2.27**. Reaction zone thickness (black data points) and infiltration depth (red data points) measurements for YbMT exposed to CMAS at 1300°C.*

After 10 min and 4 h, the reaction zone thickness is 14.2 ± 2.5 μm and 60.2 ± 8.1 μm, respectively. At 24 h, the average thickness/infiltration depth increases to ~200-225 μm with more scatter in the data. The reaction zone/infiltration depth does not increase from 24 to 96 h. This suggests that, at 1300°C and with a loading of ~35-45 mg/cm^2, CMAS fully penetrates/reacts with YbMT by 24 h.

CMAS loads between ~17.5-22.5 mg/cm^2 (low load) and ~70-90 mg/cm^2 (high load) were also investigated. Reaction zone thickness was measured after 4, 24, and 96 h at 1300°C. These values are plotted in Figure 2.28, along with those for the 35-45 mg/cm^2 (medium load) YbMT + CMAS samples. All three loads gave similar results at 4 h, when glass was still present at the surface of the samples. For the high load sample, it was apparent that glass had wicked over the edges and pooled between YbMT and the platinum on which it sat. At 24 h, the high load reaction zone thickness is comparable to that of the medium load sample. It is assumed that the high load thickness would be greater, had CMAS not wicked over and reacted with the sides and bottom of the sample, as also seen in the 4 h sample. The low load sample showed decreased zone thickness after 24 h (an average of ~145 µm) compared to the medium and high load samples; within error, however, the reaction zone thicknesses were not different between the three samples. By 96 h, the low and high load average thicknesses had increased to ~240 and 270 µm, respectively. The high load sample had again reacted with CMAS that had gone over its sides. The reaction zone thickness measured at the bottom of the sample was comparable to that at its surface. As at 4 and 24 h, there was no significant difference between sample loads due to large scatter in the data. In all cases, the microstructures of the low and high load samples are nearly identical to that for the 35-45 mg/cm^2 (medium load) samples.

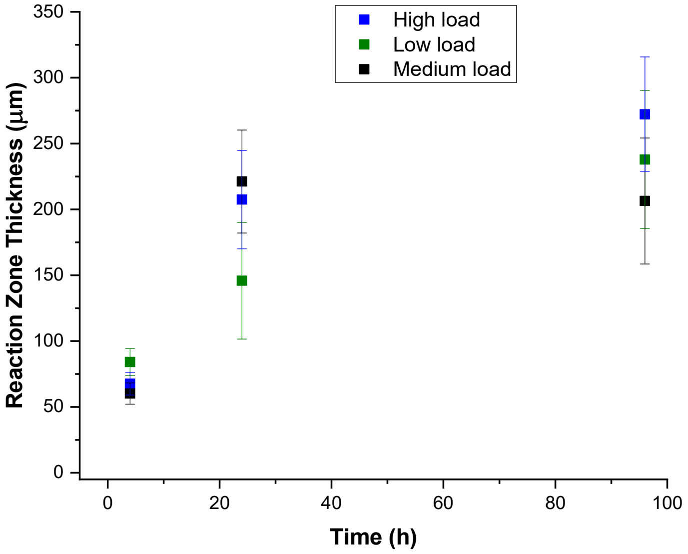

***Figure 2.28**. Reaction zone thickness in YbMT exposed to low, medium, and high CMAS loadings.*

Double loading experiments were performed to evaluate the ability of the crystallized reaction zone to act as a barrier to further CMAS infiltration. The single load reaction zone thickness data is plotted in Figure 2.29. At 96 h, data points for double load reaction zone thicknesses measured after an additional 4, 24, and 96 h at 1300°C (following an initial 96 h at 1300°C) are superimposed.

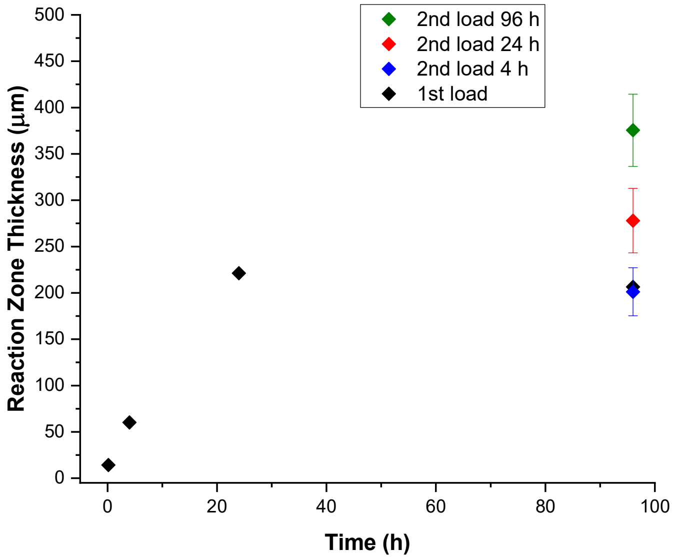

***Figure 2.29**. Reaction zone thickness in YbMT exposed to a single CMAS load (black data points) compared to YbMT exposed to a second CMAS load for 4 (blue data points), 24 (red data points), or 96 h (green data points).*

After an additional 4 h at temperature, the second CMAS load does not increase the reaction zone thickness, compared to the initial 96 h sample. Glass remains at the surface. The Ca/Ti-rich phase is no longer present; instead, $CaSiO_3$ formation was confirmed via XRD. With increasing time, the reaction zone thickens. There is no longer glass at the surface of samples exposed for an additional 24/96 h. The average thickness after an additional 96 h reaches ~375 µm. As seen in the high load samples, glass had also wicked over the sides of the YbMT.

III. Discussion

i. RE_2TiO_5 vs. $RE_2Ti_2O_7$

Reactions between Y titanates and CMAS, of the composition used in this study, were probed using FactSage. At 1300°C, calculated reaction products between CMAS and both $Y_2Ti_2O_7$ and Y_2TiO_5 include $CaTiO_3$ and an assemblage of Y silicates and/or titanates. Experimentally, however, REMT reacted to form REDT, apatite, and, in some cases, garnet, while REDT dissolved in the melt but did not precipitate any new phases. A Ca/Ti-rich phase was evident in dense YbMT exposed to CMAS for times ≥24 h but identification via XRD was not confirmed. Thermodynamic data for the apatite phase are not available, which could explain discrepancies between calculated and experimental observations. In any case, it is clear that REMT is more reactive with CMAS (or CMAS constituents such as SiO_2) than REDT. An attempt to understand why REMT is more reactive with CMAS than REDT will be made with consideration of 1) thermodynamic stability and crystal structure of REMT/REDT, 2) solubility of REMT/REDT in CMAS, and 3) reaction product chemistry.

FactSage and the FToxide database were used, in conjunction with thermodynamic data on Y titanates (provided by Gong et al. [81]), to determine the stability of REMT and REDT with respect to their oxides (Equations 2.5 and 2.6) at RT and 1300°C.

$$Y_2O_3 + TiO_2 \rightarrow Y_2TiO_5 \qquad [2.5]$$

$$Y_2O_3 + 2TiO_2 \rightarrow Y_2Ti_2O_7 \qquad [2.6]$$

Both YMT and YDT were stable with respect to their oxides. YDT was more stable (ΔG = -104 and -151 kJ/mol at RT and 1300°C, respectively) than YMT (ΔG = -62 and -93 kJ/mol at RT and 1300°C, respectively). The enthalpies of formation were also calculated and were -55 and -93 kJ/mol at RT for YMT and YDT, respectively. Enthalpies of formation (from constituent oxides, $\Delta H_{f\text{-}ox}$) have been experimentally determined for pyrochlore $RE_2Ti_2O_7$ (RE = Lu-Sm, Y) and orthorhombic RE_2TiO_5 (RE = La, Nd, Gd) by Helean et al. [89] and Hayun and Navrotsky [90], respectively. Enthalpy is a measure of the total heat content in a system, and can be used to describe bond strength. Enthalpy in the YDT system (Equation 2.6) was determined to be -86 kJ/mol, a value that closely matches that calculated above.

Experimental data for orthorhombic YMT are not available, however GdMT (ionic radius Gd^{3+} = 0.97 Å, Y^{3+} = 0.92 Å) was determined to have a $\Delta H_{f\text{-}ox}$ value of -73 kJ/mol. The enthalpy values reported by Hayun and Navrotsky for orthorhombic RE_2TiO_5 decreased with increasing RE^{3+} ionic radius; since Y^{3+} is slightly smaller than Gd^{3+}, the value calculated via FactSage for YMT appears consistent with experimental observations.

Hayun and Navrotsky determined that the transformation of orthorhombic RE_2TiO_5 to $1/2RE_2Ti_2O_7 + 1/2RE_2O_3$ was endothermic, or unfavorable, but the favorability of REDT over REMT remains uncertain when CMAS is involved. Thermodynamic data for the hexagonal Y_2TiO_5 and cubic fluorite Yb_2TiO_5 studied in this work are not experimentally available. However, Yb_2TiO_5 has a disordered fluorite structure which suggests weaker bonding than in the ordered pyrochlore. The fluorite and pyrochlore structures are compared in Figure 2.30. For both Y_2TiO_5 and Yb_2TiO_5, interaction with CMAS resulted in the formation of $RE_2Ti_2O_7$ (up to 96 h), further evidencing that REDT is more energetically stable than REMT in contact with CMAS.

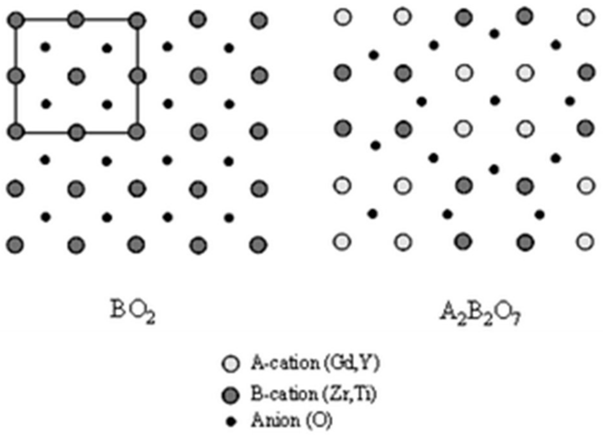

Figure 2.30. *Comparison of fluorite (BO_2) and pyrochlore ($A_2B_2O_7$) structures. In fluorite Y_2TiO_5/Yb_2TiO_5, the B-cations in the structure on the left are instead occupied by both A-cations and B-cations. From [91].*

The second consideration to make in evaluating the behavior of RE titanates with CMAS is relative solubility of REDT and REMT. Based on XRD results for RE titanate powders mixed with CMAS (Figure 2.18), it appears that RE_2TiO_5 is more soluble in CMAS than $RE_2Ti_2O_7$. The remaining REDT content after CMAS exposure stagnates at ~40 wt% (for both RE = Y,Yb) from 10 min to 96 h at 1300°C, while REMT is nearly completely consumed after only 24 h. Similar behavior is observed for REDT at 1500°C; YbMT disappears after only 10 min at this temperature. In looking at the relative amounts of Ti present in REMT/REDT + CMAS reactions (Table 2.7), REDT contributes ~10 mol % more Ti (24-29 mol%) to the reaction than does REMT (15-19 mol%). X-ray and visual results from CMAS + TiO_2 crystallization experiments indicate that CMAS containing ~15 mol% TiO_2 was amorphous upon quenching from 1300°C. While greater amounts of TiO_2 in CMAS were not studied, and RE_2O_3 solubility is not considered, it is possible that the greater Ti content in REDT contributes to its lower solubility in CMAS as compared to REMT. In looking at the SiO_2-TiO_2 phase diagram, it can be seen that the liquidus temperature increases as TiO_2 content is raised from 15 to ~20-25 mol%.

Finally, the third consideration to make in explaining the observed RE titanate + CMAS behavior involves the differing reaction products. The ability of the RE titanate to dissolve in CMAS dictates the chemistry of the evolving melt and ultimately whether new crystalline phases can precipitate from that melt. As mentioned in the above paragraph, REDT compositions contribute more Ti to the titanate/CMAS reaction than does REMT. They also contribute less relative RE. Krause et al. determined that, for $Y_2Zr_2O_7$ immersed in molten CMAS at 1300°C, a high concentration (> 6 at. %) of Y^{3+} was required within a confined volume of melt to precipitate apatite [92]. The greater overall RE content in REMT, along with its higher solubility, suggests that it can better contribute ions that are necessary in the precipitation of new crystalline phases such as apatite.

YbMT reacts more rapidly with CMAS than does YMT during isothermal exposures (Figure 2.18). However, during fast cooling from the melt in the levitation setup, YMT was more efficient than YbMT at transforming into crystallized phases. The difference in observations may be due to YMT having different starting crystal structures in each experiment (please refer to Figure 2.12). Isothermal exposures were performed on hexagonal (β) YMT at 1300°C while cooling experiments, performed from higher temperatures, involved cubic fluorite YMT. Although the orthorhombic phase (α) is expected at 1300°C, the hexagonal (β) phase was observed experimentally. Phase pure β, however, took several weeks to achieve. There was also no β observed in rapidly cooled samples, suggesting that its existence is kinetically hindered. Furthermore, despite differences in RE^{3+} ionic radius, similar reaction phases were observed between both Y_2TiO_5/Yb_2TiO_5 and CMAS. Due to difficulty in preparing YMT, YbMT was used for further experimentation.

ii. YbMT + CMAS: Crystallized reaction layer as a barrier to CMAS attack

Despite the rapid reaction of YbMT with CMAS to form crystalline phases, as observed in powder mixture experiments (2.17a and 2.18a), glass infiltration in YbMT is far too rapid for it to be considered as an actual coating material. Lifetime requirements for EBCs are on the order of tens of thousands of hours. Infiltration in dense YbMT was ~200 µm after only 24 h at 1300°C; typical EBC thicknesses are about 150-200 µm, indicating that a coating composed of YbMT would be completely infiltrated by this time. Although YbMT quickly forms favorable phases such as apatite, it also forms unfavorable phases such as YbDT. YbDT dissolves in CMAS but does not react to form crystalline phases. The reaction interface between a YbMT pellet and CMAS after 10 min at 1300°C is shown in Figure 2.31. It is evident that a significant amount of YbDT is present at this boundary. The presence of YbDT likely contributes to the fast infiltration of YbMT by CMAS, as it can redissolve upon further interaction with the melt. Indeed, “double loading” experiments indicated that the crystalline layer formed was not protective. The thickness of the reaction zone nearly doubled when YbMT exposed to a single load for 96 h was exposed to a second load for an additional 96 h (Figure 2.29).

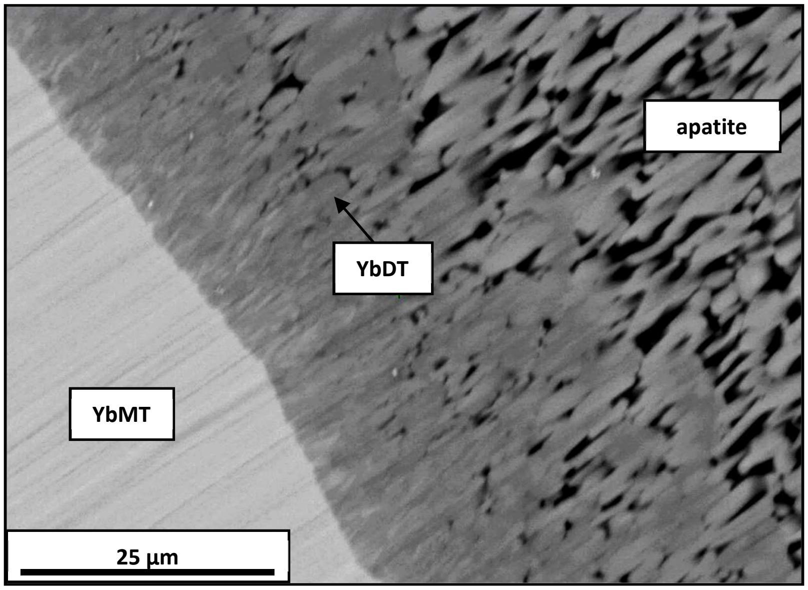

Figure 2.31. *Cross-section BSE image of the YbMT/CMAS reaction interface. Note the presence of YbDT.*

Garnet formation is also not likely favorable compared to apatite, as it is slower growing. This was confirmed by Poerschke et al. in Yb zirconates and hafnates exposed to CMAS [45]. Zirconates/hafnates with larger RE cations (Gd, La) did not form the garnet phase in contact with CMAS, leaving more RE^{3+} available for precipitation of rapidly forming apatite.

Infiltration in YbMT is compared in Figure 2.32 to Yb_2SiO_5 (YbMS) and Y_2SiO_5 (YMS), which have been reported to only form apatite in contact with CMAS. Penetration of YbMT is nearly double that seen for YbMS/YMS at longer times. This confirms that formation of apatite at the coating/glass interface is preferred over other phases such as REDT or garnet in limiting CMAS penetration. The crystallization behavior/CMAS resistance of Yb silicates is discussed in **2.2 (d)**.

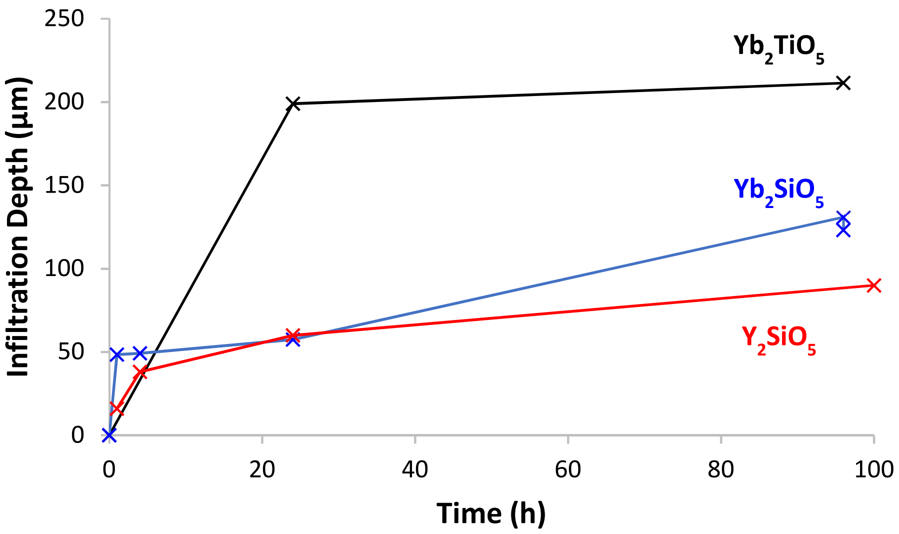

***Figure 2.32**. CMAS infiltration measured in Yb_2TiO_5 for comparison to Yb_2SiO_5 (this work) and Y_2SiO_5 [15].*

iii. CTE of RE titanates

The results presented in Appendix A are the first on thermal expansion in REMT. Appendix A reports experimental values for CTE of YbMT and YMT, as well as YbDT and YDT. The CTE for all RE titanates is too high for them to be considered as topcoat materials for SiC-based composites. The CTE of SiC is ~4.5-5.5 x 10^{-6} $°C^{-1}$ [48], while YbMT and YMT have values between 12-14. The dititanates have lower CTEs, with values around 8-10. This is in reasonable agreement with a previous study on thermal expansion in $RE_2Ti_2O_7$ (to 800°C) [93]. Given the high thermal mismatch between RE titanates and SiC, along with the relatively poor CMAS resistance in RE titanates, these materials should not be considered as EBC candidates.

2.2 (d) RE silicates + CMAS

YbMT is not considered a promising EBC candidate due to fast infiltration rates and a high CTE (Appendix A). Yb silicates ($Yb_2Si_2O_7$—YbDS and Yb_2SiO_5—YbMS) are the current standard for EBCs; however, their interaction with CMAS is not fully understood. Given that past studies report the formation of apatite as the dominant reaction product in YbMS, it is expected that YbMS will perform better in contact with CMAS than YbMT. Additionally, YbDS has been shown to be relatively non-reactive in contact with CMAS [51], meaning that a direct comparison of YbMS and YbDS can help to answer the hypothesis posed regarding competing CMAS mitigation strategies (see Introduction). In the following section, the interaction between CMAS and dense YbMS/YbDS will be evaluated at 1300°C. Infiltration/penetration rates will be compared and related to EBC reactivity.

I. Experimental

i. Sample preparation

Dense YbMS and YbDS were prepared by spark plasma sintering (SPS; Thermal Technology LLC Model SPS 25-10, Santa Rosa, CA). YbMS (Treibacher Industrie AG, Althofen, Austria) and YbDS powders (99% purity, Oerlikon Metco, Pfäffikon, Switzerland) were ball milled with ZrO_2 milling beads for ~24 h. Powders were then prepared as charges (~15 g) in a graphite die 20 mm in diameter. The graphite die was lined with graphite foil (Thermal Technology LLC) prior to transferring sample powders. The SPS chamber was evacuated to at least $2x10^{-2}$ torr and backfilled to 1 atm with Ar gas. SPS conditions and densities are detailed in Table 2.8. In general, the system was heated to 600°C, at which temperature a pressure of 65 MPa was applied. This pressure was maintained at both the peak hold temperature and during initial cooling. Samples were held at the peak temperature for 15-30 min. After cooling to 600°C, the pressure was reduced from 65 MPa to 10 MPa at a rate of 20 MPa/min. Following SPS, samples were annealed in a stagnant air box furnace at 1500°C for 10 h (with a heat up rate of 5°C/min and a cool down rate of 7.5°C/min) to eliminate any oxygen deficiencies formed during the SPS process. Samples were then sectioned into ~10 x 10 x 1 mm specimens. The specimen surfaces were polished to 1200 grit with SiC polishing paper. Sample densities were measured via Archimedes' Method and are reported in Table 2.8.

***Table 2.8**. SPS parameters used to prepare ytterbium silicates and resulting sample densities.*

Material	**Peak Hold Temperature (°C)**	**Hold Time (min)**	**Cooling Rate (°C/min)**	**Approximate % Theoretical Density**
Yb_2SiO_5	1600/1650	30/10	50/75	92-97
$Yb_2Si_2O_7$	1550	15	50	92-96

ii. Isothermal Yb silicate/CMAS exposures

CMAS powders were prepared as pellets, as described in Section **2.2 (c)** I. *ii*. Pellet size was kept between ~35-45 mg for a CMAS loading of ~35-45 mg/cm^2. In some cases, a load of either 12-13 (for YbMS samples) or 18-19 (for YbDS samples) mg/cm^2 was additionally used. CMAS compositions of 33CaO-9MgO-13$AlO_{1.5}$-45SiO_2 (high Ca content, Ca/Si ratio = 0.73, 33Ca-45Si CMAS) and 21CaO-9MgO-13$AlO_{1.5}$-57SiO_2 (low Ca content, Ca/Si ratio = 0.37, 21Ca-57Si CMAS) were investigated. The CMAS pellets were placed on the surface of the YbMS/YbDS samples. Exposures were performed in the stagnant air box furnace for either 1, 4, 24, 96, and/or 200 h at 1300°C with a heating/cooling rate of 10°C/min.

iii. Infiltration and reaction characterization

Following exposure at high temperature, samples were epoxy mounted and sectioned along the sample diagonal. This was done so that the initial sample surface could be imaged along with the reaction zone, enabling accurate measurement of infiltration depth. Half of the sample was used for SEM/EDS and half of the sample was removed from the epoxy mount and analyzed by XRD. EDS analysis was semi-quantitative. XRD samples were analyzed in bulk and powder form. SEM/EDS samples were polished to 1 µm (MetaDi Supreme diamond suspension, Buehler) and coated with a thin layer of gold/palladium prior to characterization. Images were taken in the BSE mode. ImageJ was used to stitch SEM images and measure infiltration depth/reaction zone thickness.

II. Results

Cross-section BSE images for as-prepared Yb_2SiO_5 and $Yb_2Si_2O_7$ samples are given in Figure 2.33. Although density measurements indicated relatively dense samples, it was noted that both YbMS and

YbDS samples contained pores and distinct grain boundaries. YbMS samples also contained a small amount of YbDS, as determined by EDS.

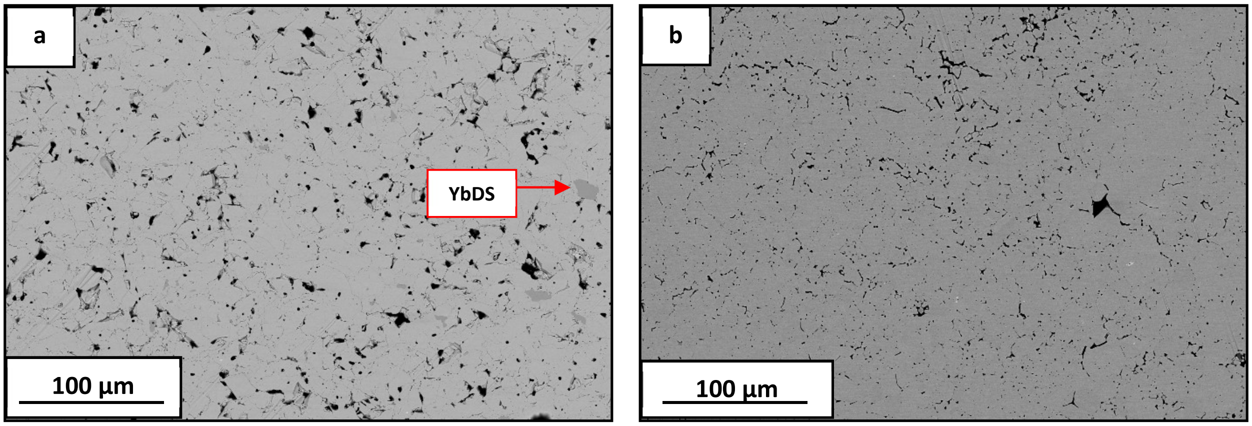

***Figure 2.33**. Cross-section BSE images for as-prepared (a) Yb_2SiO_5 and (b) $Yb_2Si_2O_7$.*

YbMS samples after exposure to 33Ca-9Mg-13Al-45Si and 21Ca-9Mg-13Al-57Si can be seen in Figures 2.34 and 2.35, respectively. In both cases, a crystallized layer formed at the coating/glass interface. At the YbMS/33Ca-45Si CMAS interface, XRD and EDS results were consistent with apatite formation. There appeared to be a small amount of a second phase (pointed out in Figure 2.34 a and e) that was not detectable by XRD. The chemistry of the phase is given in Table 2.9. At the YbMS/21Ca-57Si CMAS interface, YbMS reacts to form a thin layer of YbDS, as suggested by EDS and XRD analysis. After 200 h at temperature, the thickness of the YbDS layer is considerably less than that of the apatite formed between YbMS and 33Ca-45Si CMAS. EDS measurements on YbMS samples exposed to 33Ca-

45Si and 21Ca-57Si CMAS compositions are given in Tables 2.9 and 2.10.

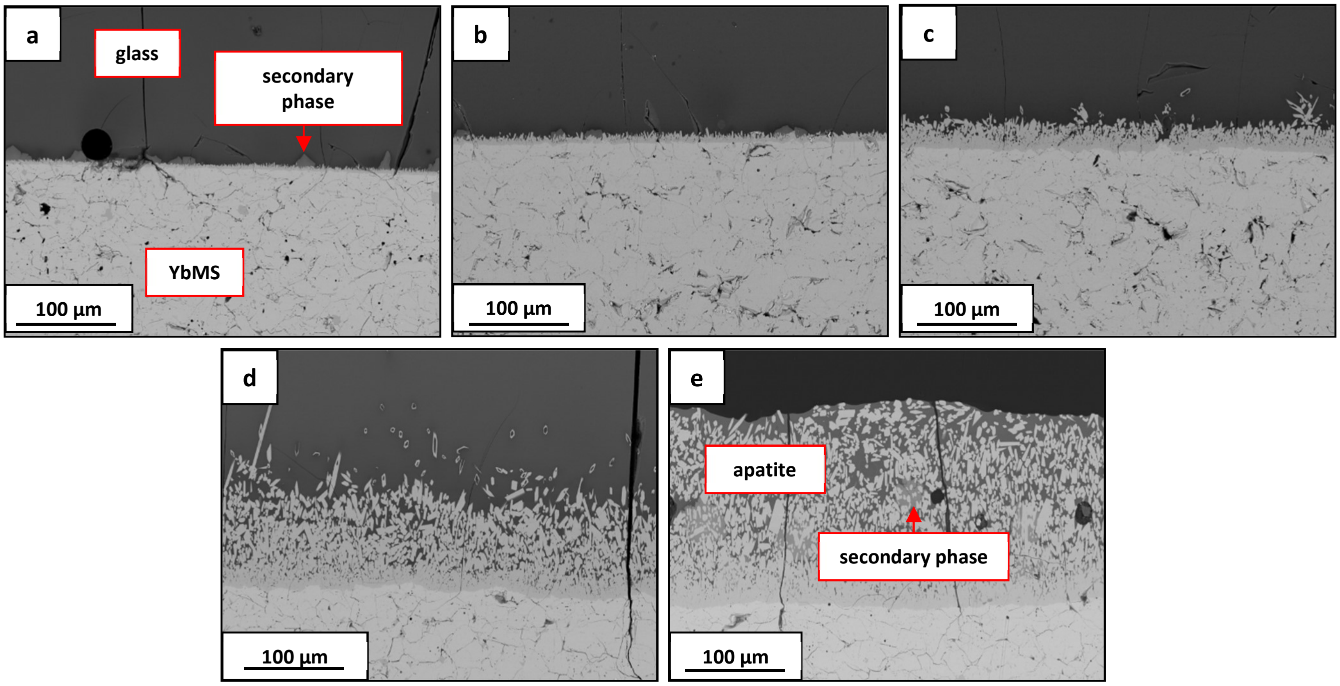

Figure 2.34. *YbMS after exposure to 33Ca-45Si CMAS for (a) 1 h, (b) 4 h, (c) 24 h, (d) 96 h, and (e) 200 h at 1300°C. Reaction products, including apatite, an unidentified secondary phase, and remaining glass, are labeled in (a) and (e).*

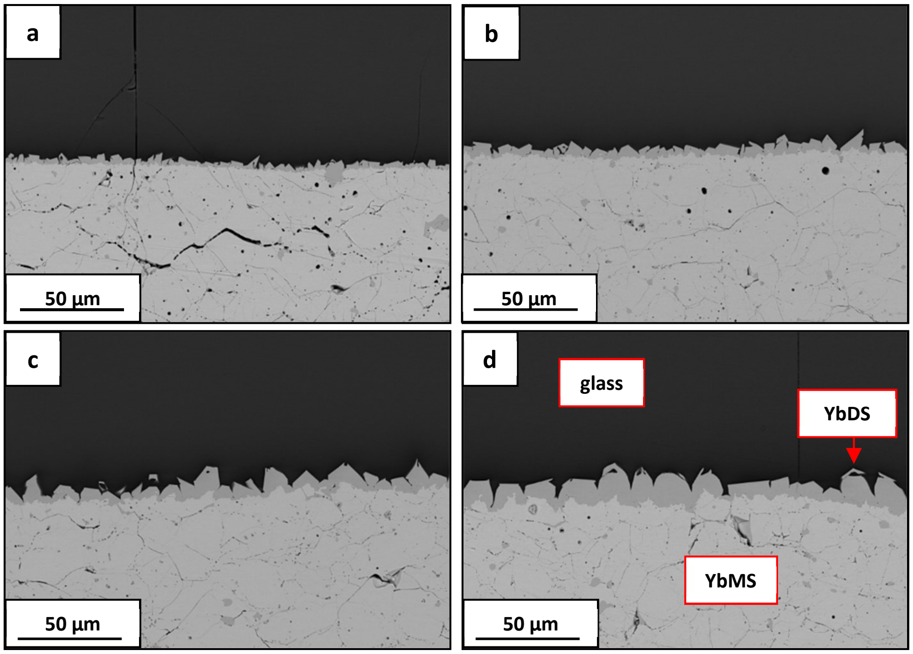

Figure 2.35. *YbMS after exposure to 21Ca-57Si CMAS for (a) 4 h, (b) 24 h, (c) 96 h, and (d) 200 h at 1300°C. Reaction products, including YbDS and remaining glass, are labeled in (d).*

***Table 2.9**. EDS point measurements (at. %) taken on reaction products formed between Yb_2SiO_5 and 33Ca-45Si CMAS at 1300°C (as seen in Figure 2.34).*

	Yb	Ca	Mg	Al	Si	Ca/Si ratio
apatite						
1 h	47.7	13.2			39.1	
4 h	50.2	12.6			37.2	
24 h	52.3	11.0			36.7	
96 h	51.2	11.2			37.6	
200 h	47.1	11.1			41.7	
secondary phase						
1 h	14.1	22.0	12.8	9.9	41.2	
4 h	14.5	22.6	12.7	10.2	39.9	
96 h	14.5	21.6	13.5	10.1	40.3	
remaining glass						
1 h	6.6	29.5	7.6	9.9	46.4	0.64
4 h	8.4	29.1	7.5	9.7	45.3	0.64
24 h	9.2	28.2	7.7	9.9	44.9	0.63
96 h	9.6	26.4	8.1	10.7	45.2	0.58
200 h	4.1	23.5	10.3	15.6	46.5	0.50
Nominal glass		33	9	13	45	0.73

***Table 2.10**. EDS point measurements (at. %) taken on reaction products formed between Yb_2SiO_5 and 21Ca-57Si CMAS at 1300°C (as seen in Figure 2.35).*

	Yb	Ca	Mg	Al	Si	Ca/Si ratio
YbDS						
4 h	52.9				47.1	
24 h	45.7				54.3	
96 h	51.2				48.8	
200 h	47.2				52.8	
remaining glass						
4 h	6.0	22.7	7.6	10.3	53.4	0.43
24 h	6.8	21.8	7.6	10.0	53.8	0.41
96 h	7.4	20.1	7.5	10.1	54.8	0.37
200 h	6.6	19.8	7.4	11.1	55.1	0.36
Nominal glass		21	9	13	57	0.37

YbDS did not react with either CMAS composition to form new crystalline phases. Instead, the disilicate was vigorously attacked, and resulting samples were riddled with pores and "blister cracks" (Figures 2.36 and 2.37). YbDS exposed to the 33Ca-45Si CMAS showed a small amount of apatite formation at short times (1 h). The apatite grains were pushed to the surface of the melt with increasing time. Attack is seemingly less severe in the 21Ca-57Si samples after 4 and 24 h compared to in the 33Ca-45Si samples. However, delamination cracks can be seen in these samples, which is not the case for those exposed to 33Ca-45Si. EDS measurements on remaining glass in these samples is given in Tables 2.11 and 2.12.

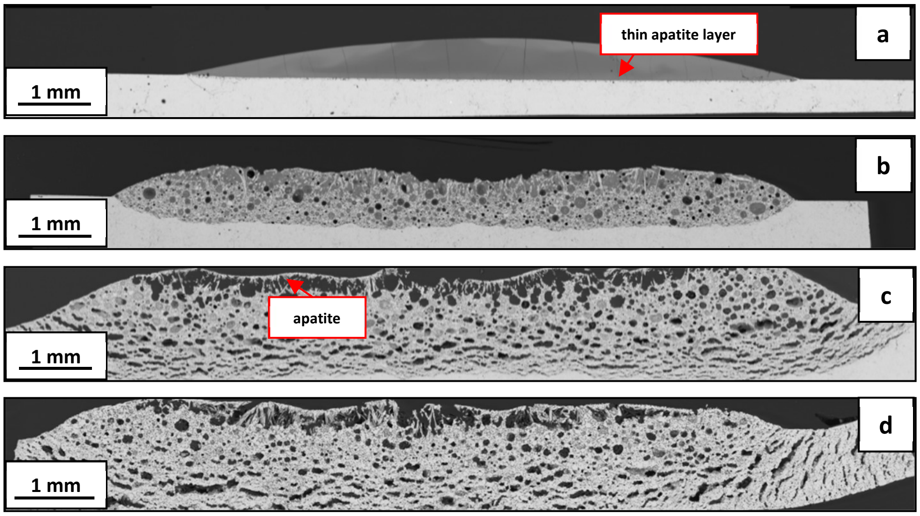

***Figure 2.36**. YbDS after exposure to 33Ca-45Si CMAS for (a) 1 h, (b) 4 h, (c) 24 h, and (d) 96 h at 1300°C. A thin layer of apatite forms at the YbMS/CMAS interface after 1 h (a) but is penetrated with longer exposures (b,c,d).*

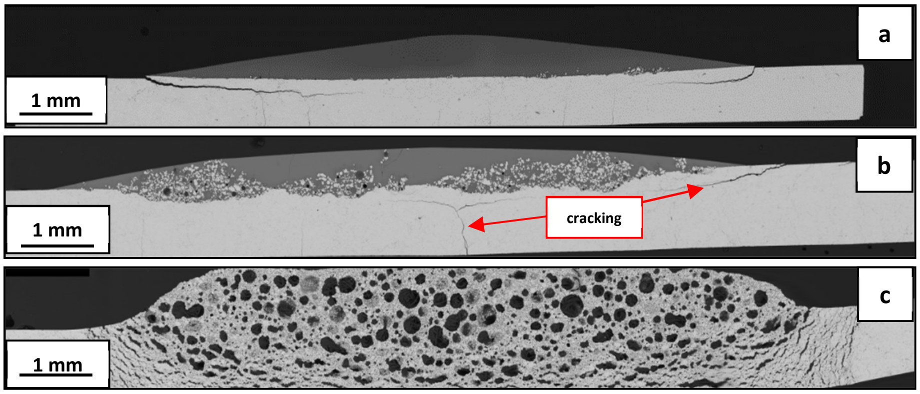

Figure 2.37. *YbDS after exposure to 21Ca-57Si CMAS for (a) 4 h, (b) 24 h, and (c) 96 h at 1300°C. Cracks within the sample are visible in (a) and (b).*

Table 2.11. *EDS point measurements (at. %) taken on apatite and remaining glass in $Yb_2Si_2O_7$ exposed to 33Ca-45Si CMAS at 1300°C.*

	Yb	**Ca**	**Mg**	**Al**	**Si**	**Ca/Si ratio**
apatite						
1 h	51.0	12.2			36.8	
4 h	52.3	11.2			36.4	
24 h	47.6	12.6			39.9	
96 h	47.2	12.5			40.2	
remaining glass						
1 h	6.6	28.6	7.4	10.1	47.2	0.61
4 h	4.8	28.5	7.5	10.8	48.4	0.59
24 h	3.6	28.1	7.6	11.4	49.3	0.57
96 h	4.6	27.3	7.4	11.2	49.5	0.55
Nominal glass		33	9	13	45	0.73

Table 2.12. *EDS point measurements (at. %) taken on remaining glass in $Yb_2Si_2O_7$ exposed to 21Ca-57Si CMAS at 1300°C.*

	Yb	**Ca**	**Mg**	**Al**	**Si**	**Ca/Si ratio**
remaining glass						
4 h	5.1	22.9	7.5	11.2	54.9	0.42
24 h	4.9	22.3	7.6	10.5	54.7	0.41
96 h	3.3	21.0	7.8	11.0	56.8	0.37
Nominal glass		21	9	13	57	0.37

Reaction zone thickness and infiltration depth measurements for YbMS exposed to 33Ca-45Si CMAS can be found in Figure 2.38. Values for reaction zone thickness approach those for infiltration depth with increasing time. Infiltration depth could not be measured for the 200 h sample, as glass had wicked over the sides of the sample, obscuring the original sample surface. Also shown in Figure 2.38 is infiltration depth after exposure to 21Ca-57Si. The data suggest that YbMS quickly dissolved in and reacted with the glass to reach an equilibrium state. Infiltration depth after 96 h is comparable to the 33Ca-45Si sample. Infiltration after exposure to 33Ca-45Si CMAS is compared between YbMS and YbDS in Figure 2.39. Clearly, penetration is significantly faster in YbDS.

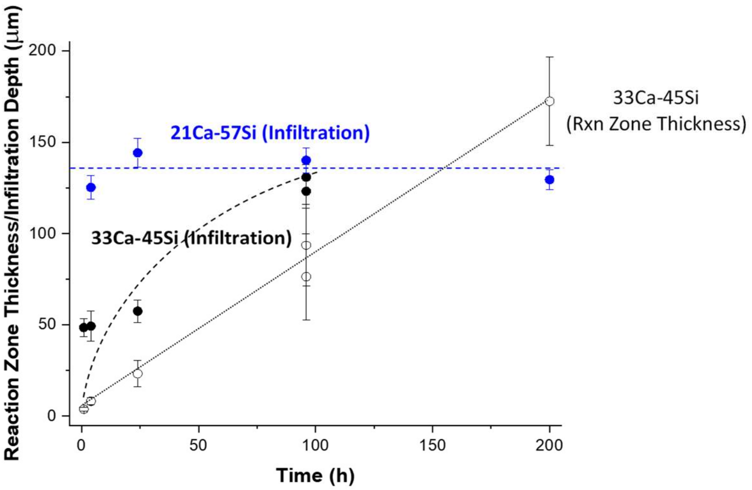

Figure 2.38. *Infiltration measurements in YbMS after exposure to CMAS of composition 33Ca-45Si (black solid data points) and 21Ca-57Si (blue solid data points) at 1300°C. Reaction zone thickness is also plotted for YbMS exposed to 33Ca-45Si CMAS (black open data points).*

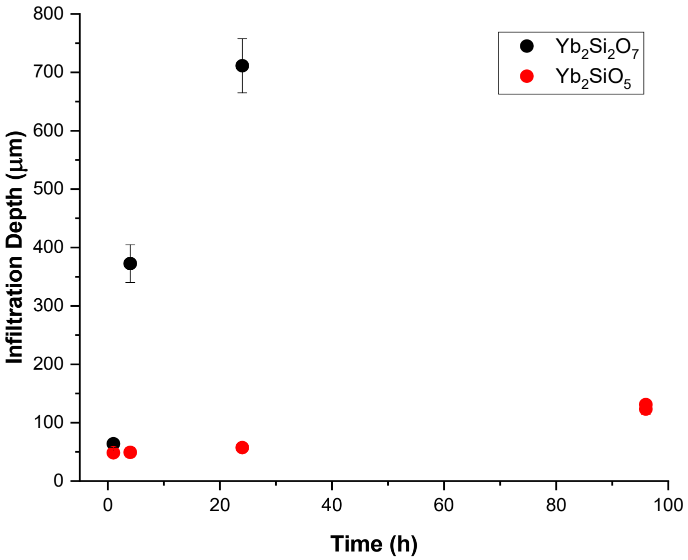

***Figure 2.39**. Comparison of infiltration in Yb_2SiO_5 and $Yb_2Si_2O_7$ after exposure to 33Ca-45Si CMAS at 1300°C.*

The effect of CMAS loading was also investigated in the RE silicates. YbMS and YbDS were exposed to 33Ca-45Si CMAS with loadings of ~12-13 and ~18-19 mg/cm^2, respectively, for direct comparison to the studies by Grant et al. [15] and Poerschke et al. [53] on yttrium silicates. Comparisons of infiltration depth in YbMS/YMS and YbDS/YDS after exposure are given in Figures 2.40 and 2.41, respectively. In the RE_2SiO_5 (REMS) system (Figure 2.40), infiltration depth is essentially identical between YbMS and YMS exposed to similar loadings. YbMS exposed to a higher load (~40 mg/cm^2) shows comparable infiltration at shorter times – when there is a large reservoir of CMAS remaining at the surface – but increased infiltration at longer times. In the $RE_2Si_2O_7$ (REDS) system (Figure 2.41), infiltration in YbDS is considerably higher than in $Y_2Si_2O_7$ (YDS) and does not appear to depend on CMAS loading.

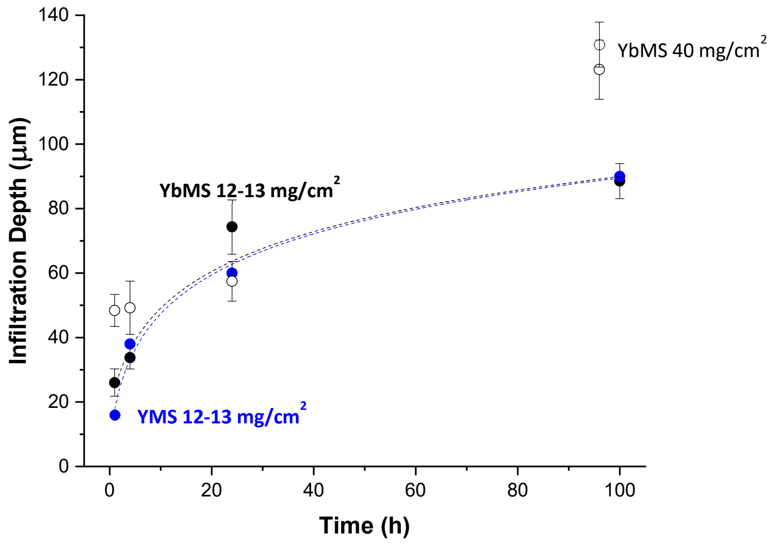

***Figure 2.40**. Infiltration in YbMS (black solid data points) and YMS (blue solid data points) after exposure to 33Ca-45Si CMAS with a loading of ~12-13 mg/cm^2. Lines of best fit were calculated for both materials. Data for YbMS exposed to a loading of ~40 mg/cm^2 is also plotted (black open data points).*

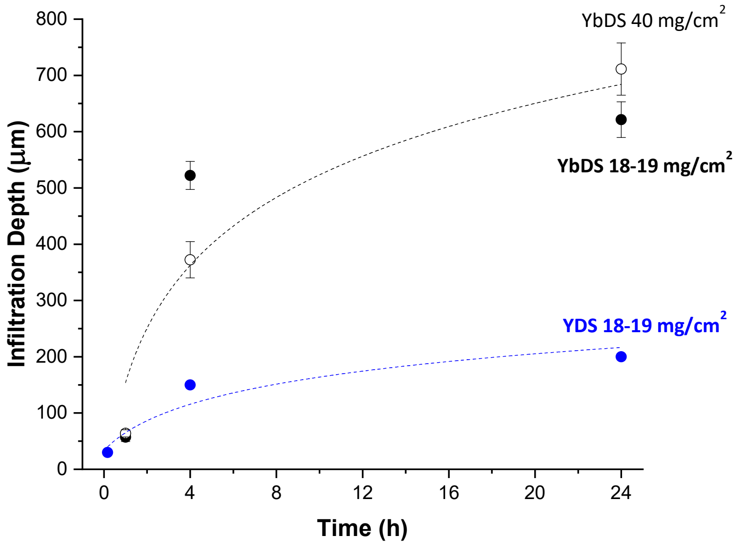

***Figure 2.41**. Infiltration in YbDS (black solid data points) and YDS (blue solid data points) after exposure to 33Ca-45SI CMAS with a loading of ~18-19 mg/cm^2. Lines of best fit were calculated for both materials. Data for YbDS exposed to a loading of ~40 mg/cm^2 is also plotted (black open data points).*

III. Discussion

i. $Yb_2Si_2O_7$

YbDS shows little to no affinity to form crystallized phases, such as apatite, upon interaction with CMAS. This was the case for both CMAS compositions investigated. Instead, YbDS is quickly penetrated along grain boundaries (complete infiltration is observed by 96 h for both CMAS compositions), leading to the formation of horizontal blister cracks within the sample. This mode of attack has been reported previously in YbDS [55]. The authors attributed the formation of the “blisters” to a dilatation gradient in the coating material. As CMAS progresses through the sample, the top region (infiltrated with CMAS) wants to expand with respect to the bottom, or unaffected, region. This results in a build-up of compressive strain in the CMAS-infiltrated (dilated) layer which leads to the formation of blister cracks.

In addition to blister cracks, large pores are also present within exposed samples, especially at longer exposure times. Pores appear to be concentrated in the upper region of infiltrated samples (Figures 2.36 and 2.37). Poerschke et al. reported large pores in CMAS-infiltrated air plasma spray (APS)-deposited YDS samples [53]. The authors did not observe pore formation in model YDS samples prepared by SPS, however, which is in contrast to the observations made here for YbDS. While no concrete basis for their presence could be made, the pores observed in APS YDS were tentatively hypothesized to originate from trapped gas (air, H_2, H_2O) in the coating. This is potentially applicable for the current system, as the SPS-prepared YbDS contained at least 3-8 % porosity. This porosity was also concentrated at the grain boundaries, and grain boundaries were preferentially attacked by CMAS. The presence of glass channels around YbDS grains could have allowed for pores to coalesce. This was observed in dense alumina (containing artificial pores) exposed to molten $CaO-Al_2O_3-SiO_2$ glass [94]. In YbDS samples exposed to 33Ca-45Si CMAS, a thin layer of apatite was found at the coating/glass interface after 1 h at temperature. At later times, apatite grains were only observed above large voids located at the very top of the infiltrated sample (Figure 2.36c and d). Disruption of the apatite layer was likely facilitated by pore migration towards the surface from coalescence and a change in density between glass and air.

The initial CMAS composition had little effect on the overall mechanism of attack in YbDS, however there were some nuances. Firstly, infiltration appeared slower in samples exposed to 21Ca-57Si CMAS as compared to 33Ca-45Si CMAS. This could have resulted from differences in glass viscosity between the two compositions tested. The viscosity of 21Ca-57Si CMAS is about one order of magnitude greater than that of 33Ca-45Si CMAS. Viscosity will be discussed in more detail in Chapter 4, however it is expected that a higher viscosity glass will penetrate coating defects, such as grain boundaries, at a slower rate. Additionally, there was no evidence of any apatite formation in YbDS exposed to 21Ca-57Si CMAS; whereas YbDS exposed to 33Ca-45Si formed some apatite at short times.

Apatite formation has also been studied in YDS as a function of CMAS composition. Summers et al. determined that the ability for YDS to form apatite was reduced with decreasing CMAS CaO content (Figure 2.42) [60]. This behavior was concurrent with decreased recession (infiltration) in YDS as CaO content was lowered (Figure 1.12).

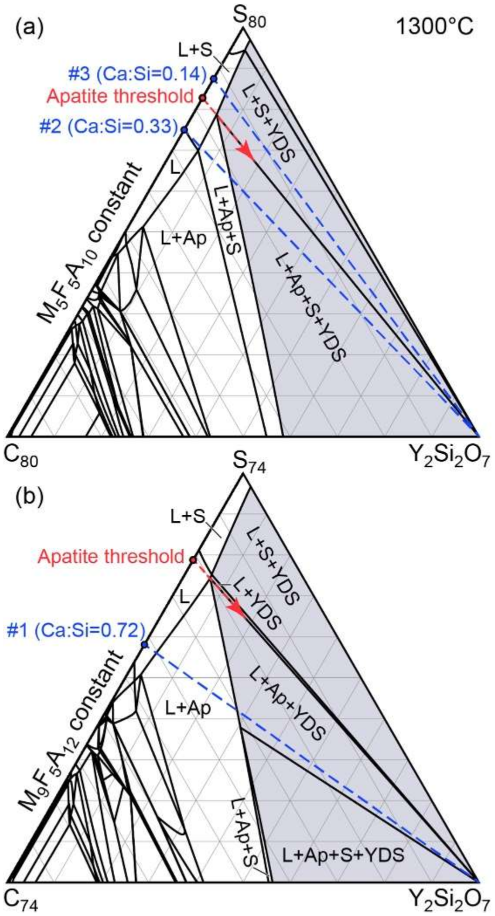

***Figure 2.42**. Phase diagrams for the CaO (C)-SiO$_2$ (S)-Y$_2$Si$_2$O$_7$ system [with constant 5 mol MgO (M), 5 mol FeO$_{1.5}$ (F), and 10 mol AlO$_{1.5}$(A)] showing that (a) interaction of Y$_2$Si$_2$O$_7$ with CMAS having a Ca/Si ratio of 0.14 results in an equilibrium state consisting of liquid (L), crystalline SiO$_2$ (S), and Y$_2$Si$_2$O$_7$ (YDS), while interaction of YDS with CMAS having a Ca/Si ratio of 0.33 results in an equilibrium of L, S, YDS, and apatite (Ap). (b) Interaction of CMAS having a Ca/Si ratio of 0.72 with YDS results in an equilibrium state of L, YDS, and Ap. These diagrams indicate that increasing the CMAS Ca/Si ratio results in greater stability of the apatite phase. From [60].*

Despite the lower initial Ca/Si ratio (and thus higher glass viscosity), and lack of apatite formation, interaction of 21Ca-57Si CMAS with YbDS proved to be nearly as detrimental as was seen for YbDS exposed to 33Ca-45Si CMAS. The difference between the results obtained here and those by Summers et al. may be due to the initial microstructure and porosity of prepared samples. While there was a decrease in the Ca/Si ratio of remaining glass in the 33Ca-45Si system (Table 2.11), no significant changes in glass chemistry were observed in samples subjected to 21Ca-57Si CMAS (Table 2.12). It is odd that such a decrease was observed in YbDS + 33Ca-45Si CMAS, as the formation of new apatite grains was only detected after 1 h. This could have been due to location choices for EDS measurements – local glass chemistry near apatite grains is likely different than in infiltrated YbDS grains. Coarsening of the apatite grains found at the top of the infiltrated sample was also observed, which would contribute to the measured chemistry changes (decrease in Ca and increase in Si, Equation 1.3) in the remaining glass. Finally, it is noted that YbDS + 21Ca-57Si CMAS samples displayed cracks after 4 and 24 h at 1300°C. These cracks seemed to originate at the YbDS/glass/air interface and extend horizontally into the coating. Delamination cracks of this nature have been observed previously in coating materials and are attributed to stresses resulting from CTE differences between the original coating and the reaction layer [14]. The CTE of a synthetic sand glass having a composition of $23.3CaO–6.4MgO–3.1Al_2O_3–62.5SiO_2–4.1Na_2O–0.5K_2O–0.04Fe_2O_3$ (mol%) was measured to be ~9×10^{-6} °C^{-1} [95], which is much greater than the CTE of $Yb_2Si_2O_7$ (~3.5-4.5 [96]). The absence of delamination cracks in YbDS exposed to 33Ca-45Si CMAS is likely a result of either 1) the formation of apatite (at shorter times) or 2) blister cracking (at longer times). The CTE of apatite (for the yttrium system) has been reported as ~5-8.5 [97, 98], a value between that of YbDS and CMAS, which would help to alleviate large differences in CTE between the coating and glass. The CTE of Yb apatite was measured and is given in Appendix B as ~8-10.5. This value is higher than that reported for Y apatite. This suggests that Yb apatite does not alleviate CTE mismatch between YbDS and CMAS.

Halving the CMAS load from 40 to 20 mg/cm^2 had little overall influence on infiltration in YbDS exposed to 33Ca-45Si CMAS (Figure 2.40) for up to 24 h. It is hypothesized that infiltration would be greater under the higher loading at longer times (i.e. 96 h), however these measurements were not achieved due to YbDS samples being completely infiltrated by 96 h. In any case, infiltration in YbDS is considerably faster than in YDS (3-4x at 24 and 96 h). The slower recession kinetics in YDS are likely attributed to increased apatite formation in this system.

ii. *Yb_2SiO_5*

To further illustrate that the reaction of coating material with CMAS to form apatite slows infiltration, Figure 2.39 compares infiltration of 33Ca-45Si CMAS in YbDS (which does not form apatite) to YbMS (which does form apatite). Infiltration of YbMS is considerably slower than infiltration of YbDS. Growth of the apatite layer is linear, while infiltration slows with time (Figure 2.38). Infiltration in YbMS is initially quite rapid, but approaches values measured for apatite thickness by 96/200 h. Rapid initial infiltration is due to dissolution of Yb_2SiO_5 in the glass before apatite grains are able to precipitate. When a continuous apatite layer has formed, and there remains a large reservoir of glass at the sample surface, it has been suggested that the kinetics of infiltration are dominated by diffusion of glass constituents to the coating/apatite interface. This was reported in infiltrated YMS [15]. Infiltration is plotted versus $t^{0.5}$ in Figure 2.43 for YbMS exposed to 33Ca-45Si CMAS of varying load. The apparent relationship between infiltration and $t^{0.5}$ suggests diffusion-controlled kinetics. At longer times, there is a deviation from this $t^{0.5}$ relationship in YbMS exposed to CMAS with a load of 12-13 mg/cm^2 (blue data points). This is likely due to the decreased volume of melt available. A deviation is not seen up to 96 h for YbMS exposed to a greater amount of CMAS (~40 mg/cm^2; black data points).

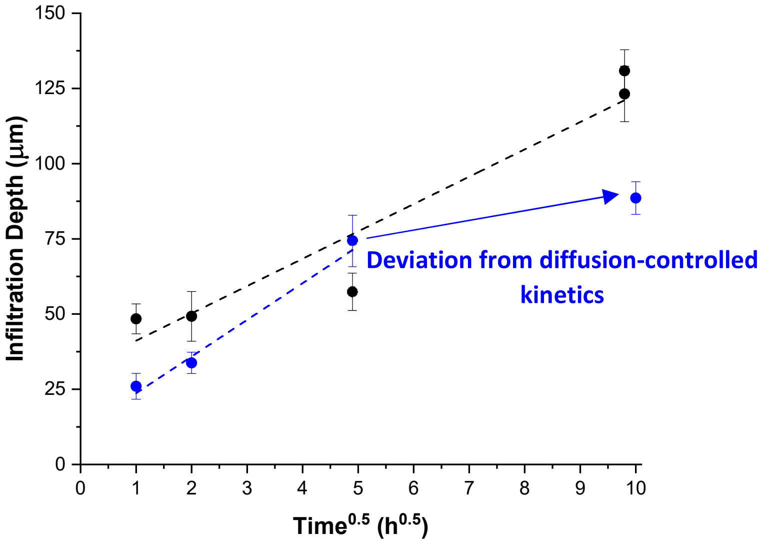

Figure 2.43. *Infiltration vs. $t^{0.5}$ for YbMS exposed to 33Ca-45Si CMAS with a loading of 12-13 mg/cm^2 (blue data points) and ~40 mg/cm^2 (black data points). The relationships between infiltration and $t^{0.5}$ suggest infiltration is controlled by diffusion. There is a deviation from this relationship in YbMS exposed to 12-13 mg/cm^2 CMAS at 100 h.*

While infiltration kinetics are consistent with a diffusion-controlled process, the growth of the apatite layer is linear with time (Figure 2.38). This indicates that the growth of apatite is not related to the ability for CMAS cations to travel to the reaction interface but is instead dominated by the kinetics of the apatite reaction (or conversion of YbMS + CaO + SiO_2 → apatite). This is an important distinction to make when comparing infiltration to reaction thickness. Because reaction thickness is a more intrinsic measure of YbMS/CMAS interaction than infiltration, it is proposed here that interaction of YbMS with CMAS to form apatite is not diffusion-controlled. Differences between infiltration and reaction thickness measurements are likely attributed to the initial dissolution of YbMS in the melt before apatite begins to precipitate.

It is noted, looking at the chemistry of remaining glass in this system as a function of time (Table 2.9), that while the CaO content decreases as expected according to Equation 1.4, the SiO_2 content does not change much (or decrease) as predicted. At shorter times this is also possibly related to the initial dissolution of Yb_2SiO_5, and thus SiO_2, into the melt. However, this behavior at longer times is not currently understood. While there is a secondary phase that forms, the Si-content measured in that phase is comparable to the Si-content in apatite. A constant Si chemistry was also reported by Zhao et al. for APS-deposited Yb_2SiO_5 exposed to CMAS of the same composition [56]. However, they reported that CMAS had reached underlying mullite and Si layers by 250 h exposure, which would have led to an increase in SiO_2 in residual glass.

Infiltration in YbMS exposed to 21Ca-57Si CMAS proceeds in a similar manner to YbMS exposed to 33Ca-45Si CMAS. In these samples, infiltration is independent of time ≥ 1 h (Figure 2.38). Instead of the apatite phase, a thin layer of YbDS forms between YbMS and the glass. Growth of the YbDS layer is linear with time and slower than the growth of apatite (Figure 2.44). The observed infiltration behavior is due to fast initial dissolution of YbMS in the melt followed by the very slow growth (0.0375 µm/h, Figure 2.44) of protective YbDS. It is surprising that YbDS is protective in this state, as it was quite rapidly attacked as a standalone material (Figures 2.36 and 2.37). The difference may be due to differences in YbDS microstructure. In YbDS prepared by SPS, there are pores and grain boundaries (where pores are concentrated) that are susceptible to infiltration. On the other hand, YbDS formed between YbMS and CMAS is denser and contains fewer/cleaner grain boundaries, as observed by SEM (Figure 2.35). This hypothesis remains to be confirmed by TEM analysis of grain boundary regions.

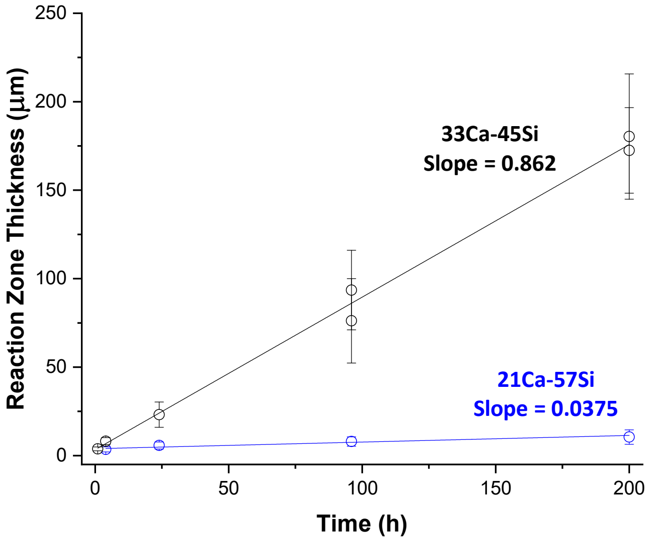

***Figure 2.44**. Reaction zone thickness measurements over time showing linear reaction kinetics in YbMS exposed to 33Ca-45Si (to form apatite) and 21Ca-57Si CMAS (to form YbDS).*

Decreasing the initial glass loading in YbMS exposed to 33Ca-45Si CMAS had little effect at short times (≤24 h) but resulted in decreased infiltration at longer times (~100 h; Figure 2.40). This suggests that the initial CMAS load does not influence penetration when there is a reservoir of glass at the sample surface. As may be expected, higher CMAS loads resulted in greater infiltration at long times due to more glass available for penetration/reaction. Figure 2.40 also shows that there is no difference in infiltration between YbMS and YMS, which is quite different from that observed in the disilicate system. Again, this is a result of both YbMS and YMS reacting with CMAS to form apatite, while only YDS forms apatite in the investigated RE disilicates.

2.2 (e) Apatite + CMAS

I. Experimental

Two types of ytterbium apatite samples were prepared. First, stoichiometric amounts of CaO, Yb_2O_3, and SiO_2 powders were mixed to form nominally defect-free $Ca_2Yb_8(SiO_4)_6O_2$. However, XRD analysis suggested that residual Yb_2O_3 remained in these samples. A powder mixture of 2 mol CaO, 3.5

mol Yb_2O_3, and 6 mol SiO_2 was then prepared for a defective apatite stoichiometry of $Ca_2Yb_7(SiO_4)_6O_{1.5}$ (containing oxygen vacancies). This preparation resulted in phase purity. SPS was used to prepare dense samples of each apatite type. General SPS parameters were as reported in **2.2 (d)** I. *i*. Anneal temperature and time, along with sample densities, are given in Table 2.13. Following SPS, samples were prepared as described in **2.2 (d)** I. *i*. Apatite samples were exposed to CMAS of composition 33CaO-9MgO-13$AlO_{1.5}$-45SiO_2 and 21CaO-9MgO-13$AlO_{1.5}$-57SiO_2 for 1, 4, 24, and/or 96 h at 1300°C in the stagnant air box furnace (ramp rate of 10°C/min). Samples were prepared and characterized as described in Section **2.2 (d)** I. *iii*.

***Table 2.13**. SPS parameters used to prepare ytterbium apatite and resulting sample densities.*

Material	**Peak Hold Temperature (°C)**	**Hold Time (min)**	**Cooling Rate (°C/min)**	**Approximate % Theoretical Density**
Apatite (containing Yb_2O_3)	1550/1600	15	50	n/a
Apatite (phase pure)	1650	30	50	92-94

II. Results

As-prepared Yb apatite samples (both containing residual Yb_2O_3 and phase pure) can be seen in Figure 2.45. Apatite containing some residual Yb_2O_3 is given in Figure 2.45a. Phase pure apatite prepared with a stoichiometry of $Ca_2Yb_7(SiO_4)_6O_{1.5}$ is given in Figure 2.45b and displays large pores at the grain boundaries. Yb apatite containing residual Yb_2O_3 was much denser and was therefore used primarily for CMAS experiments. XRD spectra for these materials are given in Figure 2.46.

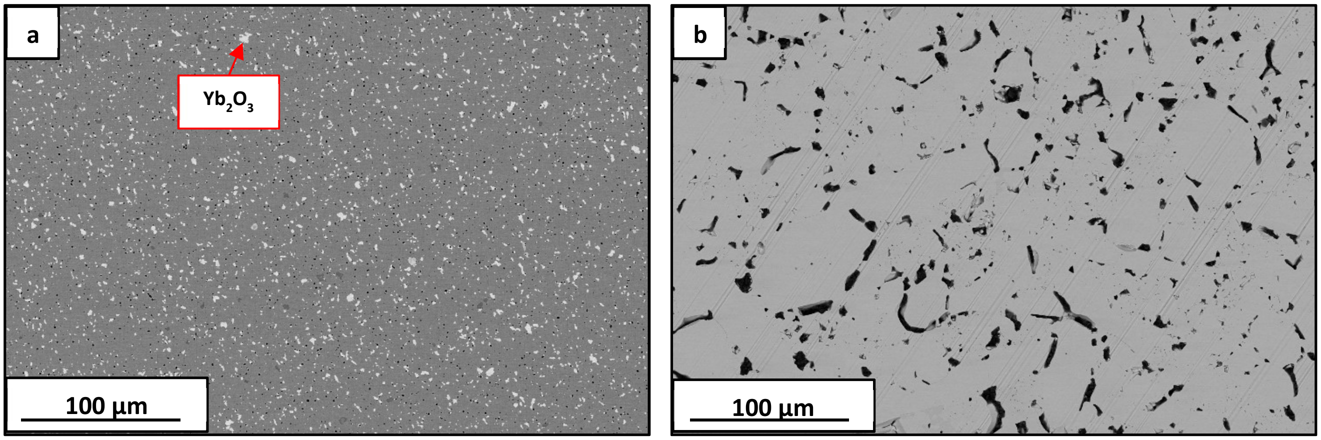

***Figure 2.45**. Cross-section BSE images of as-prepared (a) Yb apatite containing residual Yb_2O_3 and (b) phase pure Yb apatite.*

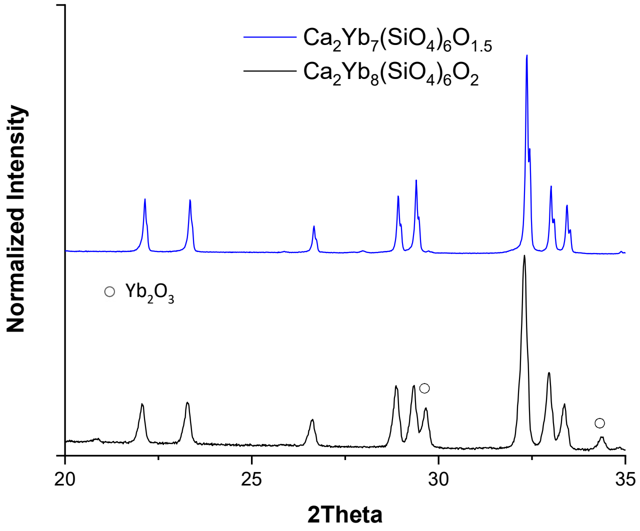

***Figure 2.46**. XRD spectra for phase pure Yb apatite (in blue) and Yb apatite containing residual Yb_2O_3 (in black). Peaks corresponding to Yb_2O_3 are identified.*

Phase pure apatite exposed to 33Ca-45Si CMAS for 4 h at 1300°C was infiltrated via grain boundaries. A "dome" of glass remained at the surface, but glass was also detected at the very bottom of the sample. In some cases, Yb_2SiO_5 and $Yb_2Si_2O_7$ were detected at infiltration sites (Figure 2.47).

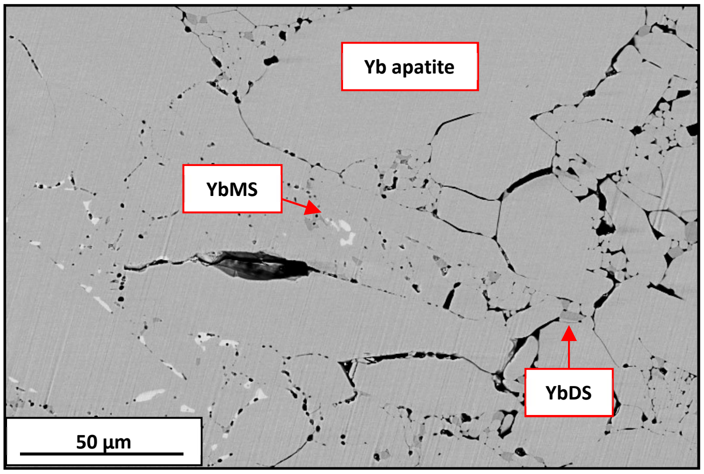

***Figure 2.47**. Cross-section BSE image of phase pure Yb apatite exposed to 33Ca-45Si CMAS for 4 h at 1300°C. YbMS and YbDS were found at grain boundaries penetrated by CMAS.*

In contrast, there is seemingly less penetration in Yb apatite containing residual Yb_2O_3 after exposure to 33Ca-45Si for up to 24 h (Figure 2.48). The glass appears to spread across the surface and edges of the sample, leading to progressive inward attack. By 96 h, the original material is almost completely consumed. Large pores are present in the reaction zone. Yb_2O_3 is no longer detected. XRD analysis did not indicate the formation of any new crystalline products, but SEM/EDS characterization suggested additional phases (Figure 2.49). The chemistry of these phases, determined by EDS, is given in Table 2.14. In addition to phases 1 and 2 (Figure 2.49), a third phase (phase 3) with similar composition to the “secondary phase” described in YbMS exposed to 33Ca-45Si CMAS (Table 2.9) was observed. There was also a fourth oxide phase (phase 4) that was difficult to differentiate from phase 1 in the BSE mode and had a cation chemical composition of ~38Si-33Ca-27Yb-2Mg (at. %).

Yb apatite, containing Yb_2O_3, exposed to 21Ca-57Si was less attacked compared to samples exposed to 33Ca-45Si (Figure 2.50). The mode of penetration was similar, with progressive attack from the surface and edges inwards. A thin layer of YbDS was observed at the coating/glass interface after 4 h but was not seen after 96 h. Similar phases to those seen after exposure to 33Ca-45Si were observed in the affected area. Their chemical compositions are given in Table 2.15. Again, the “secondary phase” described in YbMS exposed to 33Ca-45Si CMAS (Table 2.9) was also observed and is labeled phase 3 in Table 2.15.

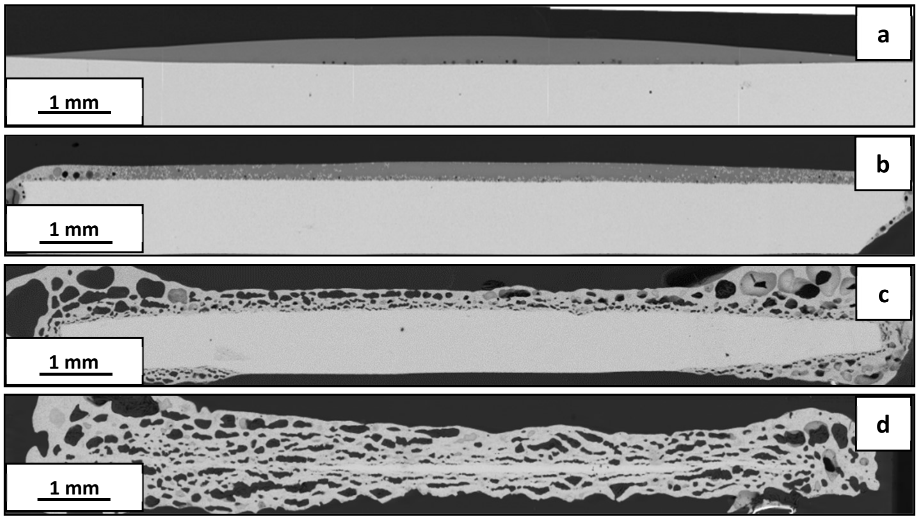

Figure 2.48*. Yb apatite (containing residual Yb_2O_3) after exposure to CMAS of composition 33Ca-45Si for (a) 1 h, (b) 4 h, (c) 24 h, and (d) 96 h at 1300°C.*

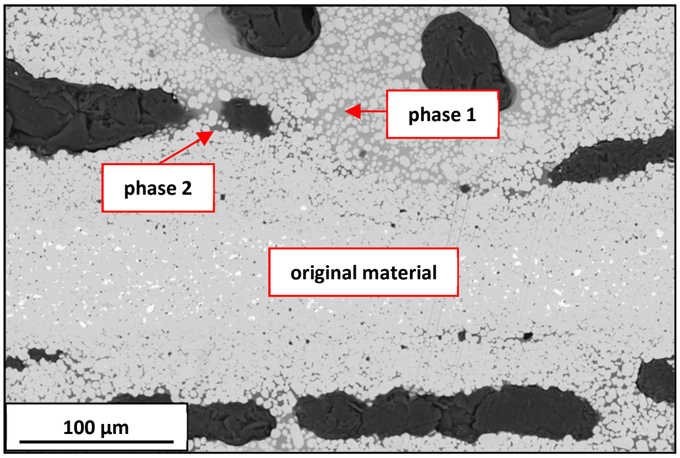

Figure 2.49*. Higher magnification image of the affected region in Figure 2.48d. Two apparently distinct phases are identified in the reaction zone. Notice that residual Yb_2O_3 is no longer present in penetrated material.*

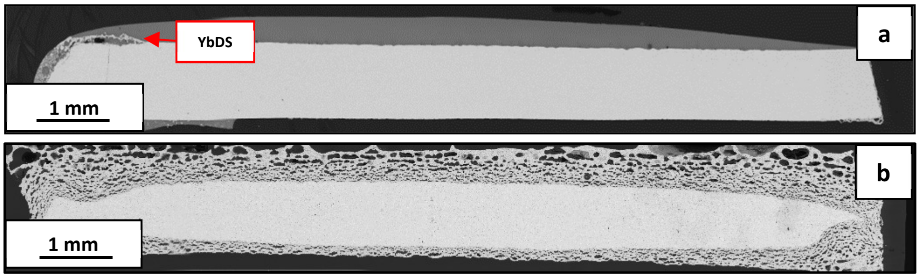

Figure 2.50. *Yb apatite (containing residual Yb_2O_3) after exposure to CMAS of composition 21Ca-57Si for (a) 4 h and (b) 96 h.*

Table 2.14. *EDS point measurements (at. %) taken on phases 1-4 in Yb apatite (containing residual Yb_2O_3) exposed to 33Ca-45Si CMAS at 1300°C.*

	Yb	**Ca**	**Mg**	**Al**	**Si**
phase 1					
96 h	24.6	15.4	11.8	17.1	31.1
phase 2					
96 h	4.6	37.7	5.1	11.2	41.4
phase 3 (“secondary phase”)					
96 h	11.7	26.0	8.5	15.5	38.3
phase 4					
96 h	27.0	33.2	1.8	0.0	38.0

Table 2.15. *EDS point measurements (at. %) taken on phases 1-3 in Yb apatite (containing residual Yb_2O_3) exposed to 21Ca-57Si CMAS at 1300°C.*

	Yb	**Ca**	**Mg**	**Al**	**Si**
phase 1					
96 h	26.2	13.2	13.8	14.8	32.0
phase 2					
96 h	7.5	25.0	8.0	15.0	44.5
phase 3 (“secondary phase”)					
96 h	14.4	22.5	11.8	13.3	38.0

III. Discussion

Standalone apatite is infiltrated much more quickly than YbMS when exposed to CMAS. Even when samples are quite dense (Figure 2.45b vs. Figure 2.45a), there is little remaining original material after 96 h at 1300°C. Yb apatite containing residual Yb_2O_3 is penetrated along grain boundaries when exposed to 33Ca-45Si CMAS, leading to grains being released into the overlaid melt. This is accompanied by the formation of large pores and "cracks" that are similar to the blister cracks observed in infiltrated YbDS. The melt also seems to spread to the edges of the sample with increasing time; the edges of the sample are attacked preferentially as CMAS migrates inward. Affected regions of the sample show that the excess Yb_2O_3 dissolves in the melt. A variety of new phases are observed but have not been identified via XRD. Based on the phase diagram for CaO-SiO_2-$YO_{1.5}$ (Figure 2.51), the observed phases could possibly include cuspidine and $Ca_3Yb_2Si_3O_{12}$. The infiltration of standalone apatite is much faster than the infiltration of YbMS which forms apatite. This may be due to a combination of factors which include differences in layer microstructure. There is a dense layer of apatite at the YbMS/CMAS reaction front that appears to contain less grain boundaries and pores than standalone apatite. Another contributing factor could be evolution of the remaining melt. Residual glass in the YbMS/CMAS system is depleted in Ca, while it is enriched in Ca and depleted in Si in exposed Yb apatite ("phase 2" in Table 2.14). Enrichment of CaO and depletion of SiO_2 in CMAS can decrease glass viscosity, as will be discussed in Chapter 4. This may lead to faster penetration of sample defects.

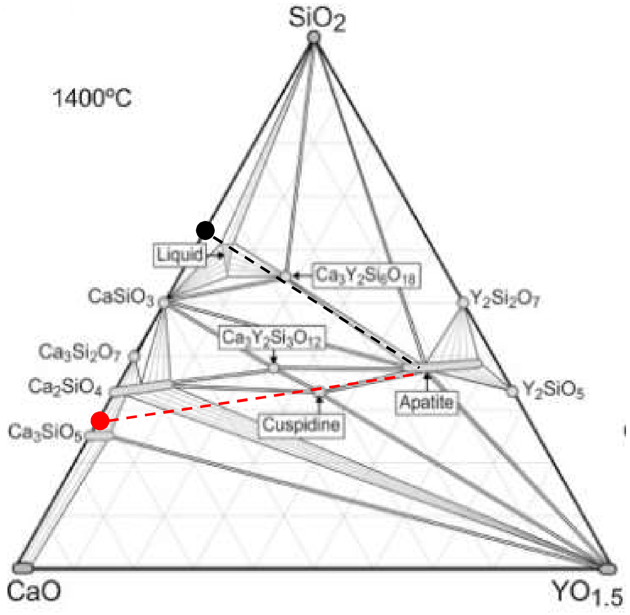

Figure 2.51. *CaO-SiO_2-$YO_{1.5}$ phase diagram. From [47]. The black and red dots indicate CMAS compositions with a Ca/Si ratio of 0.37 and 0.73, respectively. Dashed lines are drawn between the CMAS compositions and apatite to show possible phase relationships during exposure.*

Similar results are seen in Yb apatite exposed to 21Ca-57Si CMAS. After 4 h at temperature, there is a thin layer of YbDS at the apatite/glass interface. By 96 h, however, this layer is no longer observed. Instead, the microstructure of the infiltrated region is dominated by blister cracks and pores. As was seen for apatite exposed to 33Ca-45Si CMAS, the glass appears to spread to the edges of the sample. Penetration of apatite by 21Ca-57Si CMAS is slower than penetration by 33Ca-45Si CMAS; this is, as discussed for YbDS, likely due to differences in glass viscosity. The presence of “phase 4” (observed in 33Ca-45Si CMAS infiltrated apatite, Table 2.14) was not detected after exposure to 21Ca-57Si CMAS.

2.3 Summary

The results of Chapter 2 answer critical questions regarding EBC material selection. The questions originally posed in Table 2.1 are addressed in Table 2.16. Sufficient addition of TiO_2 to CMAS improved the ability for CMAS to crystallize, but TiO_2 did not act as a “nucleating agent” in the process. Interest in TiO_2 was based on the theoretical reaction of RE titanates with CMAS; however, TiO_2 was not experimentally observed as a reaction product as expected. Instead, RE mono-titanates reacted quickly with CMAS to form crystalline phases including apatite, garnet, and REDT. These phases were not protective and were rapidly infiltrated. The formation of REDT contributed to the fast infiltration of dense YbMT by CMAS due to it dissolving in the glass but not reacting to form new crystalline phases. Infiltration was much slower in Yb_2SiO_5, as apatite was the main reaction product formed at the coating/glass interface. YbMS was resistant to CMAS attack even when the initial CMAS chemistry was changed; it reacted with a low-Ca, high-Si glass to form a dense, slow-growing, and protective layer of YbDS. SPS-prepared YbDS performed very poorly in contact with CMAS. Little to no apatite formation was observed, which resulted in penetration of grain boundaries/pores and blister cracking of samples. Standalone apatite was also less resistant to CMAS attack than YbMS and was infiltrated in a manner similar to that observed in YbDS.

***Table 2.16**. Questions posed in Table 2.1 are answered.*

	Research Questions and Answers
(a) CMAS + TiO_2	Do TiO_2 additions nucleate or enhance CMAS crystallization? Nucleate? ✗ Enhance ✓ How much TiO_2 is needed? ~15-20 wt% What phases form? $CaTiO_3$, melilite, paqueite, diopside (depends on temperature and cooling profile)
(b) RE titanates + SiO_2	Do RE titanates react with SiO_2 to form new crystalline phases? REMT ✓ REDT ✗ Does TiO_2 form as expected? No ✗ REMT reacts with SiO_2 to form REDT and REDS. REDT does not react with SiO_2 to form new crystalline phases.
(c) RE titanates + CMAS	How do these materials behave in contact with CMAS (react, don't react)? REMT ✓ REDT ✗ How does that influence coating penetration? REDT dissolves, allows fast penetration What phases form? REMT + CMAS → apatite + REDT + garnet (…+ $CaTiO_3$?) Should this material be considered as an EBC? REMT ✗ REDT ✗
(d) RE silicates + CMAS	How do these materials behave in contact with CMAS (react, don't react)? YbMS ✓ YbDS ✗ How does that influence coating penetration? Penetration of YbDS (via grain boundaries, pores) >>> YbMS What phases form? YbMS + CMAS → apatite Does CMAS composition have an effect on behavior? Yes, especially for YbMS Should this material be considered as an EBC? YbMS ✓ YbDS ✗ (prepared via air plasma spray)
(e) Apatite + CMAS	How do these materials behave in contact with CMAS (react, don't react)? Some reaction, non-continuous How does that influence coating penetration? Penetration via grain boundaries What phases form? Unidentified (via XRD) Does CMAS composition have an effect on behavior? Yes Should this material be considered as an EBC? As a standalone material, no ✗

2.4 Conclusions

The work presented here shows that the most effective route for mitigation of CMAS attack in EBCs requires rapid reaction between coating and glass to form a dense layer of crystalline phase(s) that are stable in contact with CMAS. While an ideal situation between an EBC and CMAS would involve stagnation of the glass at the coating surface, actual coatings deposited by air plasma spray will contain defects, such as grain boundaries and pores, that are vulnerable to infiltration. The results of this work show that inducing crystallization of dense phases at the coating/glass interface reduces the ability for CMAS to penetrate these defects and leads to slower infiltration.

The crystallized phases that form must precipitate quickly and be stable in contact with incoming CMAS. The layer should be dense and devoid of microstructural defects. For RE-based coatings in contact with Ca-rich CMAS deposits, formation of apatite at the coating/glass interface is favorable over other phases, such as garnet. Rare earth-based coatings are less likely to form apatite after exposure to Ca-lean deposits. Ytterbium monosilicate reacted with 21Ca-57Si CMAS to form a dense, protective layer of YbDS. It is hypothesized that the protective nature of the precipitated YbDS is attributed to the minimal number of microstructural defects in its structure; this is unlike observations made between SPS YbDS (containing grain boundaries and pores) and CMAS. This leads to speculation that another promising route for EBC preparation would involve decreasing the number of defects and grain boundaries in the coating, however this is likely a much more expensive solution than reactive crystallization. Another method to reduce infiltration might involve adding a reactive compound (such as TiO_2) that segregates to coating grain boundaries.

Based on the results of this study, YbMS is much better able to resist CMAS infiltration than other coating materials investigated, such as YbDS. However, the CTE of YbMS is greater than that of SiC, which means that as an EBC, it is likely to detach from the underlying CMC with thermal cycling. Thermal expansion in YbDS is similar to that in SiC. Thus, an actual coating system might involve a layered YbDS/YbMS structure to prevent thermal stresses while maintaining good CMAS resistance. Coatings deposited by air plasma spray (APS) are typically composed of both YbDS/YbMS; their structure could be tailored to balance the various needs of an EBC. The behavior of model APS coatings with CMAS is discussed in the following chapter.

2.5 Recommendations for future work

In an actual engine, the combustion environment will contain high-temperature, high-velocity steam. There is a dearth of research on/understanding of how coating materials subjected to CMAS will behave in a water-vapor-containing environment. For example, little is known about apatite reaction and volatility in steam. Yb apatite (containing Yb_2O_3) was subjected to high-velocity steam for 60 h at 1300°C (Appendix C). Preliminary results indicate that apatite transforms into YbMS and then porous Yb_2O_3, suggesting that both Si and Ca volatilize as gaseous hydroxide species. Changes in the chemistry and structure of the coating surface can have significant effects on further CMAS interactions. Additionally, the volatility of CMAS alone in water vapor has not been studied and should be considered in future work.

Another area that requires future work is characterization of reaction products in these systems. There are several crystalline phases that are still not well understood, including the Ca/Ti-rich phase formed between YbMT and CMAS in 2.2 (a), the secondary phase formed between YbMS and 33Ca-45Si CMAS in 2.2 (d), along with precipitated YbDS between YbMS/21Ca-57Si CMAS, and the various phases formed between Yb apatite and CMAS in 2.2 (e). Transmission electron microscopy/diffraction studies are necessary to fully understand why certain reaction products are more effective as barriers. Special efforts should be made to characterize the YbDS formed between YbMS and 21Ca-57Si CMAS, to understand its protective nature.

3. Chapter 3: EBC phase constitution and microstructure effects on CMAS infiltration and reaction

3.1 Introduction

EBCs are typically deposited by air plasma spray (APS), which can lead to a complicated microstructure containing multiple phases and defects such as cracks/pores. An example of a typical APS-deposited EBC can be seen in Figure 3.1, wherein the coating is primarily composed of $Yb_2Si_2O_7$ (YbDS) but also contains some amount of Yb_2SiO_5 (YbMS).

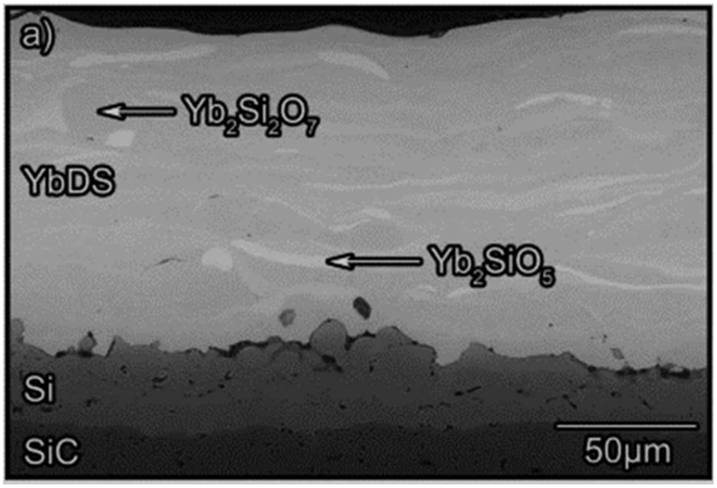

Figure 3.1. *Cross-section BSE image of an APS deposited $Yb_2Si_2O_7$ coating (containing Yb_2SiO_5) atop Si/SiC. From [50].*

It was determined in Chapter 2 that phase pure Yb_2SiO_5 was more resistant to CMAS infiltration than phase pure $Yb_2Si_2O_7$. As such, it is hypothesized that additions of YbMS to YbDS will improve overall EBC infiltration resistance. The objective of this chapter is to explore the effects of phase constitution and distribution on CMAS attack in ytterbium silicate materials, neglecting the effects of any microstrutrural defects. YbDS samples containing controlled amounts of YbMS (10-30 vol%) were prepared as model materials having either a "splat" (as seen in APS coatings, Figure 3.1) or "fine dispersion" microstructure. Model materials were exposed to CMAS having both high and low Ca contents and their behavior was compared to that of the phase pure materials explored in Chapter 2. It was determined that YbMS additions of ≥ 20 vol% significantly decreased glass infiltration in model APS coatings having a "splat" microstructure. Improved CMAS resistance in these materials is related to the reaction between YbMS granules and glass to form the apatite phase. For fine dispersion samples, a novel mode of attack was observed, wherein molten CMAS spread across the surface of the sample to react with sample edges. Implications for coating design related to these behaviors will be discussed. This report is the first to explore the effect of Yb silicate phase concentration and distribution on CMAS infiltration and reaction behavior. It is the first to present evidence that adding YbMS to a YbDS coating improves CMAS resistance. Results will be used to advise optimal microstructures for APS-deposited EBCs.

3.2 Experimental

i. Sample preparation

Spark plasma sintering (SPS) was used to prepare dense $Yb_2Si_2O_7$ samples containing 10, 20, or 30 vol% Yb_2SiO_5 (vol% was converted to wt% using the density of YbMS in order to prepare mixtures). Two types of sample microstructure were synthesized. In the first (referred to as model APS coatings), spherical granules of YbMS (99.9% purity, Praxair Surface Technologies, Indianapolis, IN; Figure 3.2) were added to YbDS (99% purity, Oerlikon Metco, Pfäffikon, Switzerland) that had been ball milled for ~24 h with zirconia media. Pressure applied during the SPS process caused the YbMS granules to flatten in a configuration approximating the splats seen in air plasma spray coatings. In the second (referred to as fine dispersion samples), YbMS and YbDS were ball milled together for ~24 h which resulted in a fine dispersion of YbMS in YbDS after SPS processing. In preparing both microstructure types using SPS, the specimen was first heated to 600°C, at which temperature a pressure of 65 MPa was applied. This pressure was maintained at both the peak hold temperature and during initial cooling. Samples were held at the peak temperature (1550°C) for 15 min. After cooling to 600°C, the pressure was reduced from 65 MPa to 10 MPa at a rate of 20 MPa/min. Samples were then annealed in a box furnace in air at 1500°C for 10 h (with a heat up rate of 5°C/min and a cool down rate of 7.5°C/min) and sectioned into ~10 x 10 x 1 mm coupons. Sample densities were measured in water by Archimedes' Method. Model APS samples were ~92-95% theoretical density and fine dispersion samples were ~88-93% theoretical density.

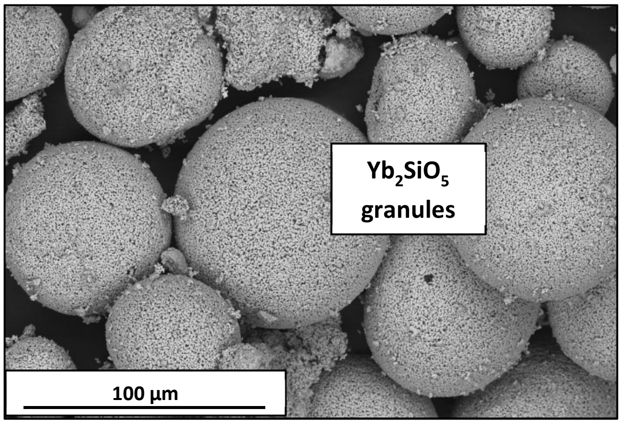

***Figure 3.2**. Spherical Yb_2SiO_5 (YbMS) granules used in the preparation of model APS coatings.*

ii. Isothermal CMAS exposures

CMAS powders were pressed into ¼” diameter pellets that were sintered for 4 h at 1200°C prior to experiments. Two CMAS compositions were investigated – $Ca_{33}Mg_9Al_{13}Si_{45}$ and $Ca_{21}Mg_9Al_{13}Si_{57}$. The loading of CMAS was kept between ~35-45 mg/cm^2. Pellets were placed on the polished surface of the Yb silicate samples. Exposures were performed in the stagnant air box furnace for 4, 24, and/or 96 h at 1300°C with a heating/cooling rate of 10°C/min.

iii. Infiltration and reaction characterization

Following exposure at high temperature, samples were epoxy mounted and sectioned along the sample diagonal. Half of the sample was used for SEM/EDS and half of the sample was removed from the epoxy mount and analyzed by XRD. XRD samples were analyzed in both bulk and powder form. SEM/EDS samples were polished to 1 µm and coated with a thin layer of gold/palladium prior to characterization. Images were taken in the BSE mode. Infiltration was measured across the sample/CMAS interface. Because there was not a continuous reaction zone, a single infiltration measurement was taken as the deepest point at each site where any glass could be discerned. Ten to fifteen infiltration measurements were taken in this manner and averaged (Figure 3.3).

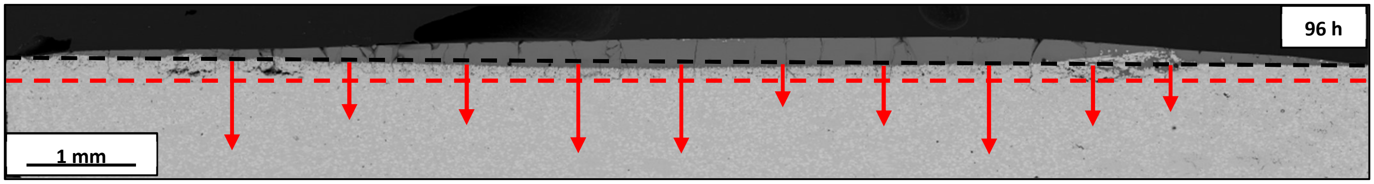

***Figure 3.3**. An example of how infiltration measurements were made in model APS coatings. Each red arrow indicates an infiltration site. The dashed black line represents the original sample surface and the red dashed line represents the depth to which a continuous apatite layer formed beneath the surface. Glass was found below this layer. The deepest point at which any glass could be discerned was measured from the original sample surface and taken as the infiltration depth for that site. Ten to fifteen measurements were taken for each sample.*

3.3 Results

a) Model APS coatings

An example of the initial microstructure for model YbDS materials containing YbMS "splats" is given in Figure 3.4. The starting monosilicate granules (Figure 3.2) were flattened into a configuration such that their horizontal length was ~50 µm. The shape, size, and dispersion of YbMS splats within YbDS are a reasonable approximation of that seen in an actual APS coating (Figure 3.1). ImageJ analysis was used to determine the actual phase percentage of YbMS in YbDS for the range of samples prepared. Taking the average of two measurements on images of as-prepared materials, the area percentage of YbMS within YbDS was calculated to be 12.4, 21.0, and 24.1 for nominal 10, 20, and 30 vol% YbMS mixtures.

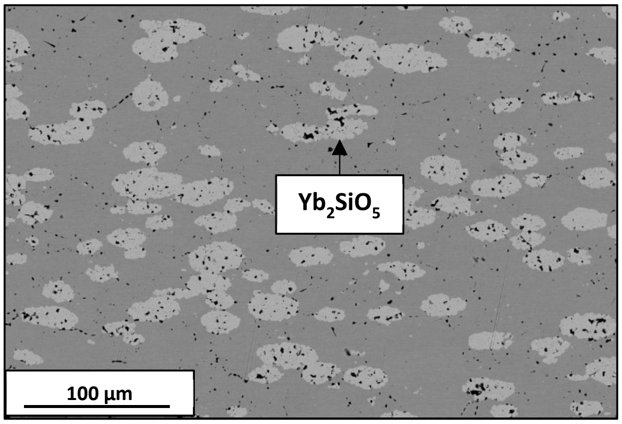

***Figure 3.4**. Cross-section BSE image of as-prepared model APS YbDS containing 20 vol% YbMS.*

Nominal additions of 20 and 30 vol% YbMS to YbDS improve overall CMAS resistance, compared to YbDS alone and YbDS containing 10 vol% YbMS (Figures 3.5 and 3.6). Similar macroscopic behavior is observed for both CMAS compositions studied. By 96 h, samples containing 10 vol% YbMS are completely infiltrated, and appear to have been attacked via mechanisms previously described for phase pure YbDS. Extensive grain boundary penetration was observed with concomitant blister cracking. However, there are far fewer pores than were formed in YbDS, and blister cracks appear less regular/uniform. For samples exposed to 33Ca-45Si CMAS, a layer of apatite was formed at the coating/glass interface after 4 h. This layer was interpenetrated with increasing exposure time. Apatite grains were observed within the bulk of the infiltrated sample (Figure 3.7a and c); their presence was confirmed via XRD.

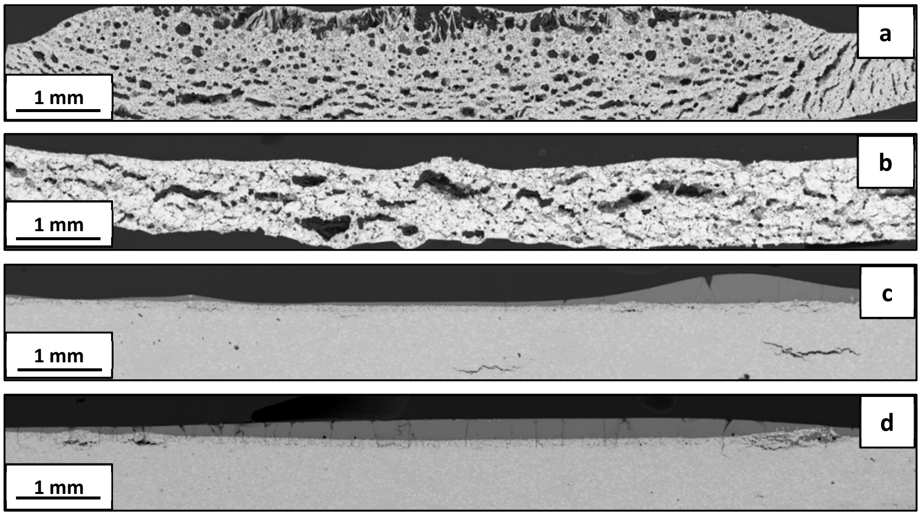

***Figure 3.5**. (a) Phase pure YbDS compared to model APS coatings containing (b) 10, (c) 20, and (d) 30 vol% YbMS after exposure to 33Ca-45Si CMAS for 96 h at 1300°C.*

Despite improvements to coating microstructure, CMAS infiltration was not prevented in model materials exposed to 21Ca-57Si CMAS. There was no formation of a continuous apatite layer after 4 h. Instead, there was evidence that some glass had travelled via grain boundaries to reach the very bottom of the sample. A few apatite grains were observed within the bulk (Figure 3.7b). This was also the case after 96 h (Figure 3.7d). XRD did not indicate the presence of apatite after either exposure time. In addition to the presence of some apatite in YbDS + 10 vol% YbMS samples (exposed to both CMAS compositions), there appeared to be one other distinguishable phase, most notably after 4 h, located near YbMS inclusions. This phase can be seen in Figure 3.7 a and b. Its chemistry is compared to that of apatite and remaining glass in Tables 3.1 and 3.2. Variations in the chemistry of the secondary phase were observed, and were dependent on their location in the sample. Its structure could not be determined by XRD.

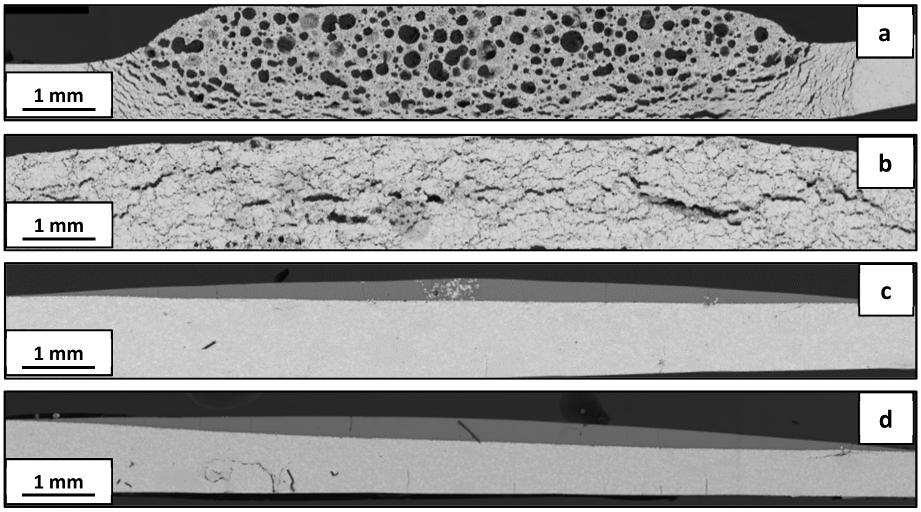

Figure 3.6*. Phase pure YbDS (a) compared to model APS coatings containing (b) 10, (c) 20, and (d) 30 vol% YbMS after exposure to 21Ca-57Si CMAS for 96 h at 1300°C.*

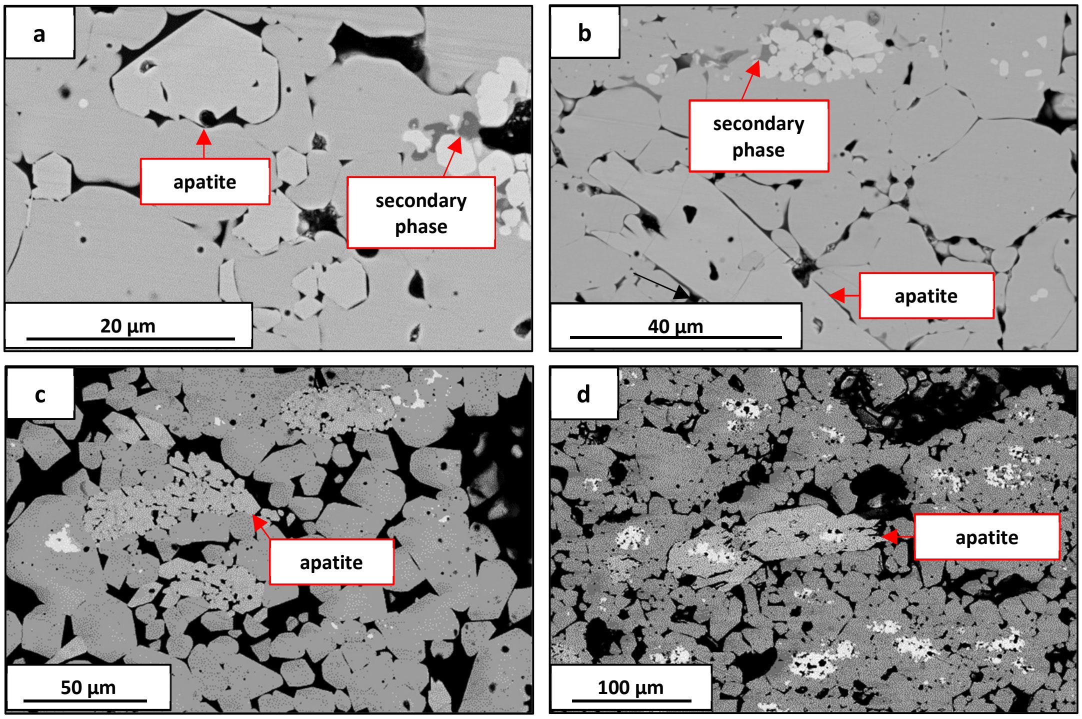

Figure 3.7*. Cross-section BSE images of YbDS + 10 vol% YbMS after exposure to (a,c) 33Ca-45Si CMAS and (b,d) 21Ca-57Si CMAS for (a,b) 4 h and (c,d) 96 h at 1300°C. Reaction phases are labeled.*

***Table 3.1**. EDS point measurements (at. %) taken on reaction products formed between model APS coating samples and 33Ca-45Si CMAS after 96 h at 1300°C. Remaining glass refers to the residual melt found at the surface of the sample.*

	Yb	Ca	Mg	Al	Si	Ca/Si ratio
apatite						
10 vol% YbMS	47.4	11.6			41.0	
20 vol% YbMS	48.4	11.8			39.8	
30 vol% YbMS	48.0	10.8			41.3	
secondary phase						
10 vol% YbMS	24.9	12.9	14.3	13.8	34.0	
20 vol% YbMS	25.6	10.9	8.2	30.2	25.1	
30 vol% YbMS	26.1	11.4	9.9	26.8	25.8	
remaining glass						
10 vol% YbMS	-	-	-	-	-	-
20 vol% YbMS	7.1	22.9	8.2	11.0	50.8	0.45
30 vol% YbMS	8.1	23.3	7.3	10.8	50.6	0.46
Nominal glass		33	9	13	45	0.73

***Table 3.2**. EDS point measurements (at. %) taken on reaction products formed between model APS coating samples and 21Ca-57Si CMAS after 96 h at 1300°C. Remaining glass refers to the residual melt found at the surface of the sample.*

	Yb	Ca	Mg	Al	Si	Ca/Si ratio
apatite						
10 vol% YbMS	47.8	10.8			41.4	
20 vol% YbMS	48.4	10.9			40.7	
30 vol% YbMS	47.7	10.8			41.6	
secondary phase						
10 vol% YbMS	27.3	11.6	9.5	22.1	29.6	
20 vol% YbMS	27.7	12.3	8.8	23.7	27.5	
30 vol% YbMS	32.5	10.9	12.0	10.7	33.9	
remaining glass						
10 vol% YbMS	-	-	-	-	-	-
20 vol% YbMS	6.6	18.8	7.4	10.1	57.0	0.33
30 vol% YbMS	6.5	19.6	7.3	10.4	56.3	0.35
Nominal glass		21	9	13	57	0.37

With increasing YbMS content (20, 30 vol%), the ability for the model coating to form a continuous apatite layer in contact with 33Ca-45Si CMAS was improved. Interaction of YbDS + 20 vol% YbMS with this glass composition is shown in Figure 3.8 as a function of time. As was seen in YbDS + 10 vol% YbMS, a relatively thick layer of apatite formed at the coating/glass interface after 4 h at temperature. Unlike in YbDS + 10 vol% YbMS, this apatite layer remained intact, and grew, with increasing exposure time. However, this layer was not completely protective, as some glass was discerned below it. Infiltration depth measurements for YbDS + 20, 30 vol% YbMS exposed to 33Ca-45Si CMAS are given in Figure 3.9; penetration rates are significantly reduced compared to phase pure YbDS. YbMS grains preferentially reacted with CMAS constituents to form apatite. Grains were consumed from the outside in (Figure 3.10a). A secondary phase, similar to that observed in 10 vol% YbMS samples, was also detected (Figure 3.11a, Table 3.1).

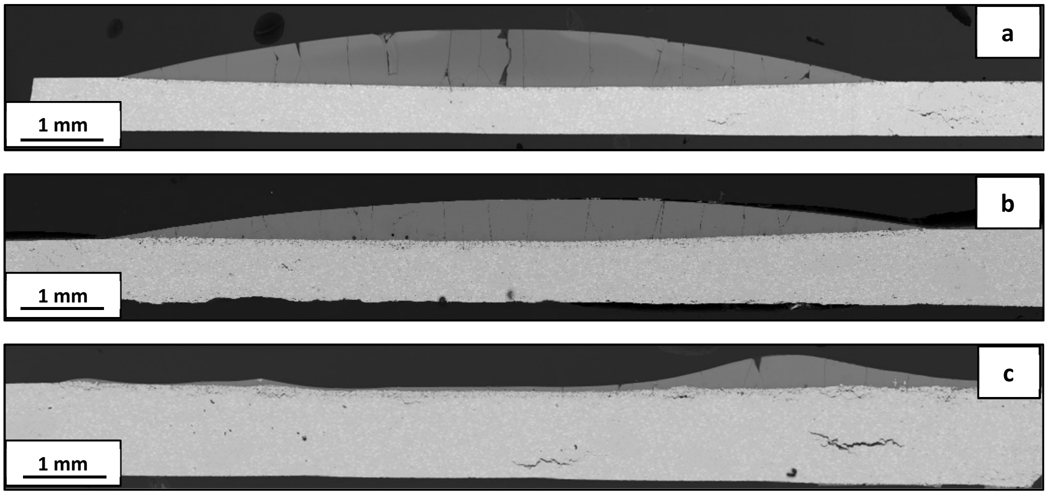

***Figure 3.8**. YbDS + 20 vol% YbMS samples after exposure to 33Ca-45Si CMAS for (a) 4 h, (b) 24 h, and (c) 96 h at 1300°C.*

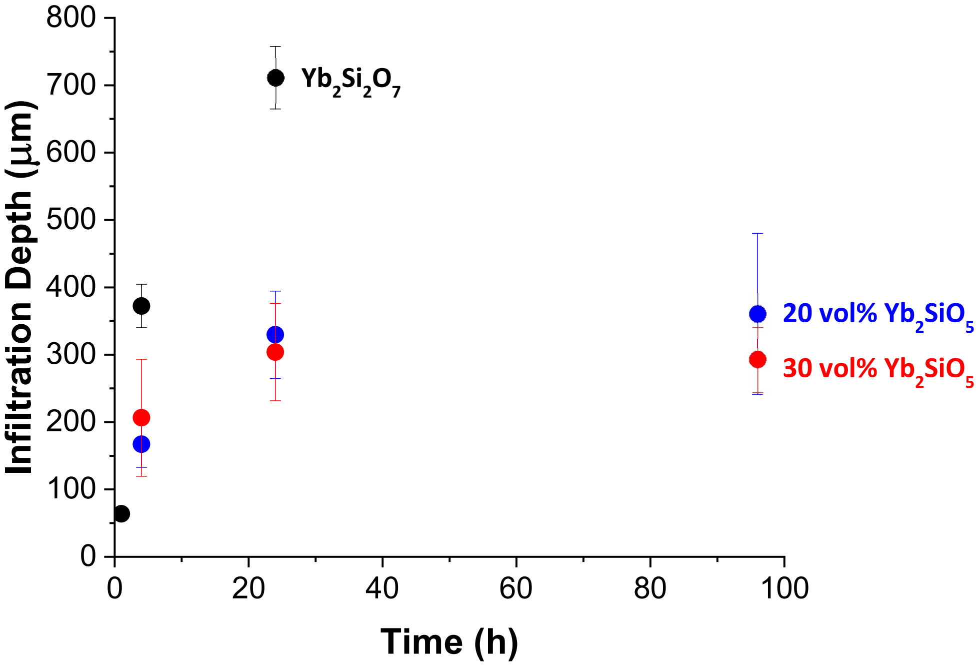

Figure 3.9. *Infiltration depth of 33Ca-45Si CMAS in model APS YbDS containing 20 and 30 vol% YbMS as compared to phase pure YbDS after exposure at 1300°C.*

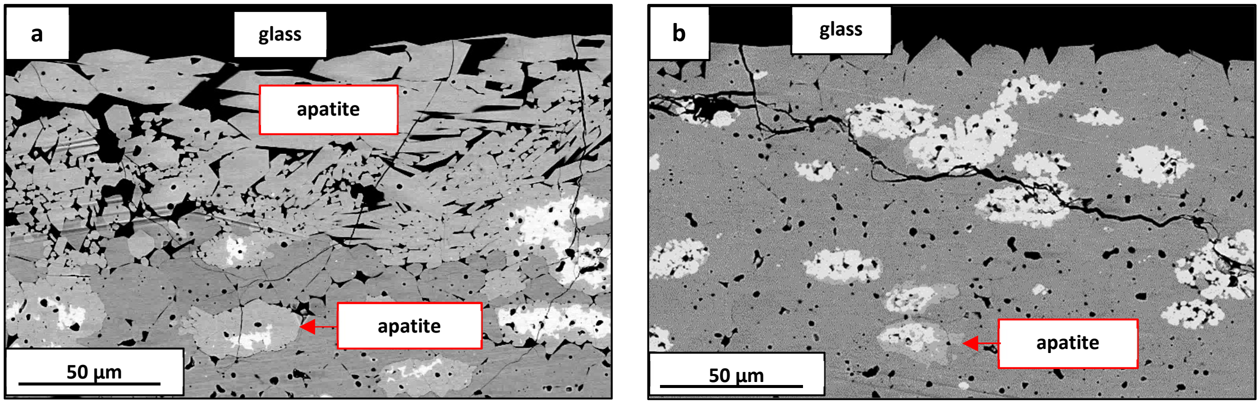

Figure 3.10. *BSE images of the YbDS + 20 vol% YbMS/glass interface after exposure to (a) 33Ca-45Si and (b) 21Ca-57Si CMAS for 96 h at 1300°C.*

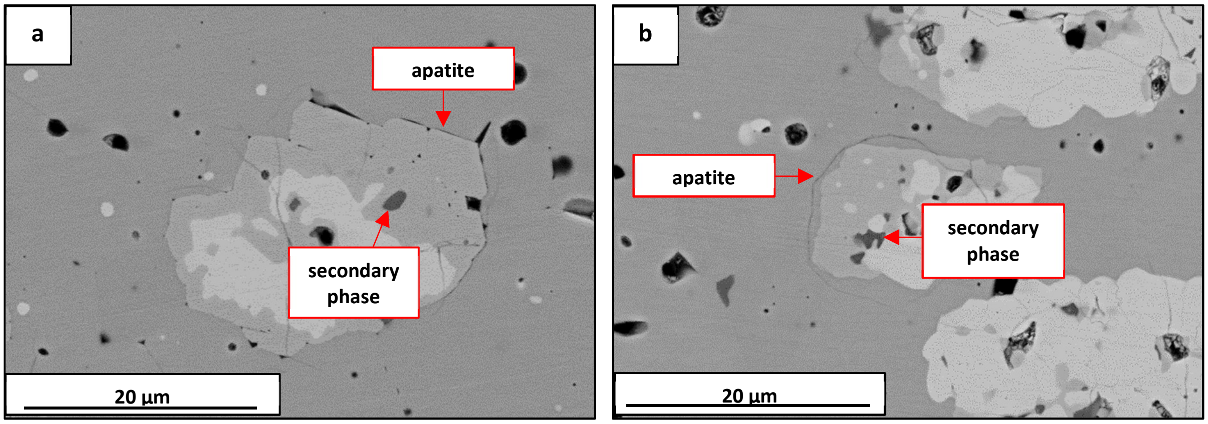

Figure 3.11. *Higher magnification image of a YbMS "splat" within YbDS + 20 vol% YbMS after exposure to (a) 33Ca-45Si and (b) 21Ca-57Si CMAS for 96 h at 1300°C.*

Cross-section images of YbDS + 20 vol% YbMS exposed to 21Ca-57Si CMAS are given as a function of time in Figure 3.12. Unlike after exposure to 33Ca-45Si CMAS, there was no formation of a continuous apatite layer. However, some grains were transformed into apatite in a similar manner to that observed previously (Figure 3.10b, Figure 3.11b). The presence of the secondary phase was also noted (Figure 3.11b). Infiltration was considerably faster in materials exposed to the 21Ca-57Si CMAS (Figure 3.13) compared to the 33Ca-45Si CMAS. This is likely due to the absence of any continuous crystallized zone. However, despite infiltration measurements on the order of that seen in phase pure YbDS, it is clear that microstructural effects due to penetration are not as severe as that seen in phase pure YbDS. Residual glass is present at the surface of samples up to 96 h, and there are no blister cracks within the bulk material. There was no definitive reaction front, which may contribute to the large scatter in measurements taken on YbDS + 20, 30 vol% YbMS (Figure 3.13). Infiltration depth was taken as the deepest point at each "site" (Figure 3.3) at which any glass could be discerned – even if it was a very small amount. Additionally, it is worthy to note that the average infiltration depths for YbDS + 20 vol% YbMS after 24 h and YbDS + 30 vol% YbMS after 24 and 96 h include some data points attributed to through-thickness infiltration, meaning that the values provided in Figure 3.13 could actually be even greater.

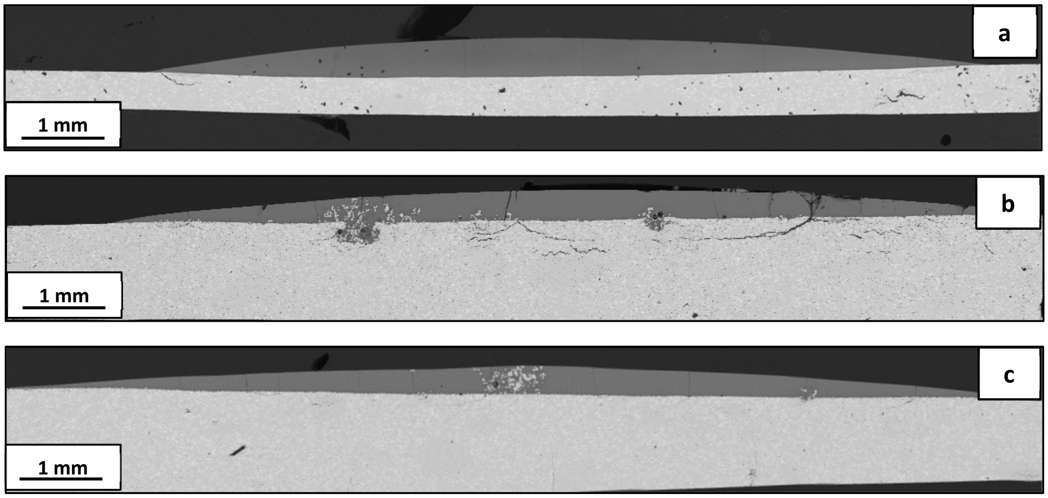

Figure 3.12. *YbDS + 20 vol% YbMS samples after exposure to 21Ca-57Si CMAS for (a) 4 h, (b) 24 h, and (c) 96 h at 1300°C.*

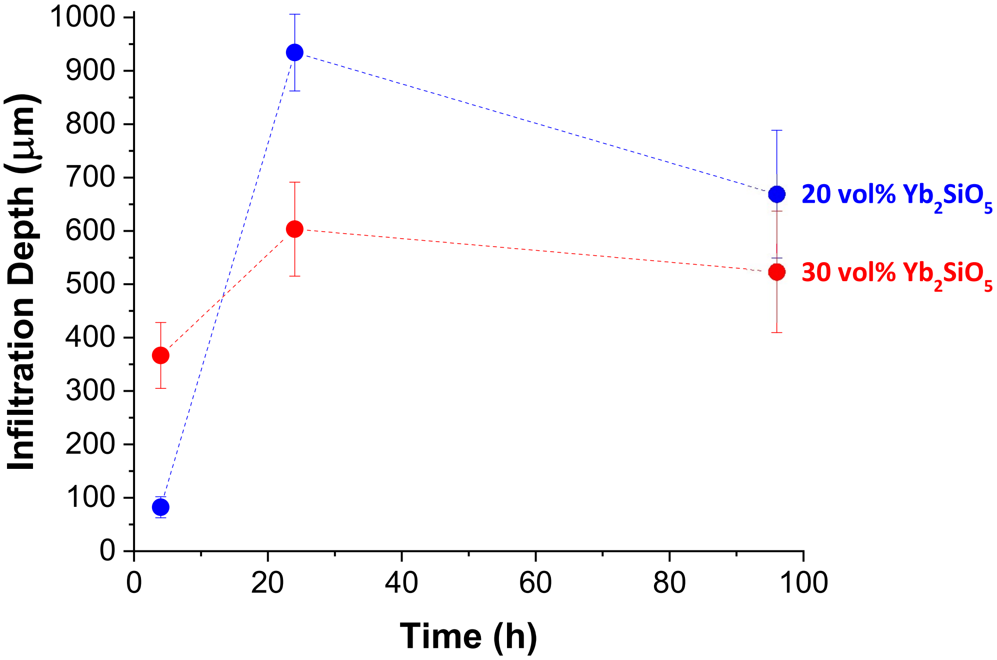

Figure 3.13. *Infiltration of 21Ca-57Si CMAS (at 1300°C) in model APS YbDS containing 20 and 30 vol% YbMS.*

b) Fine dispersion samples

To prepare fine dispersion samples, YbMS granules shown in Figure 3.2 were mixed with YbDS and ball milled to a fine powder. Following SPS, the resulting microstructure was comprised of YbMS particles (up to ~≤5-30 µm across) dispersed within the YbDS matrix (Figure 3.14). As done for the model materials, ImageJ was used to determine the area percentage of YbMS within YbDS in fine dispersion samples. The average of two measurements on images of as-prepared materials gave area percentages of 10.0, 18.7, and 24.8 (compared to nominal volume percents of 10, 20, and 30).

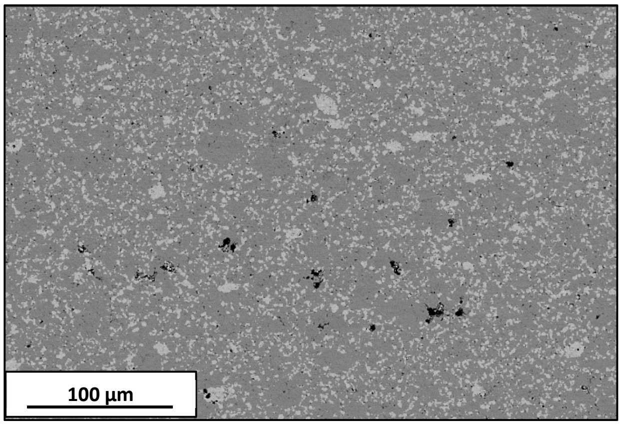

Figure 3.14. *Spherical granules from Figure 3.2 were mixed with YbDS and ball milled to a fine powder. The resulting microstructure was comprised of a fine dispersion of YbMS within YbDS after SPS.*

Cross-section images of fine dispersion samples containing 10-30 vol% YbMS after exposure to 33Ca-45Si and 21Ca-57Si CMAS for 96 h are shown in Figures 3.15 and 3.16, respectively. The mode of CMAS attack in these samples is quite different from that observed for model APS coatings. Regardless of YbMS content or CMAS composition, the glass spread on the sample surface to reach sample edges by 96 h. This led to a large volume of glass present at each edge of the sample, which resulted in vigorous interaction between coating and CMAS (similar to that seen in phase pure YbDS).

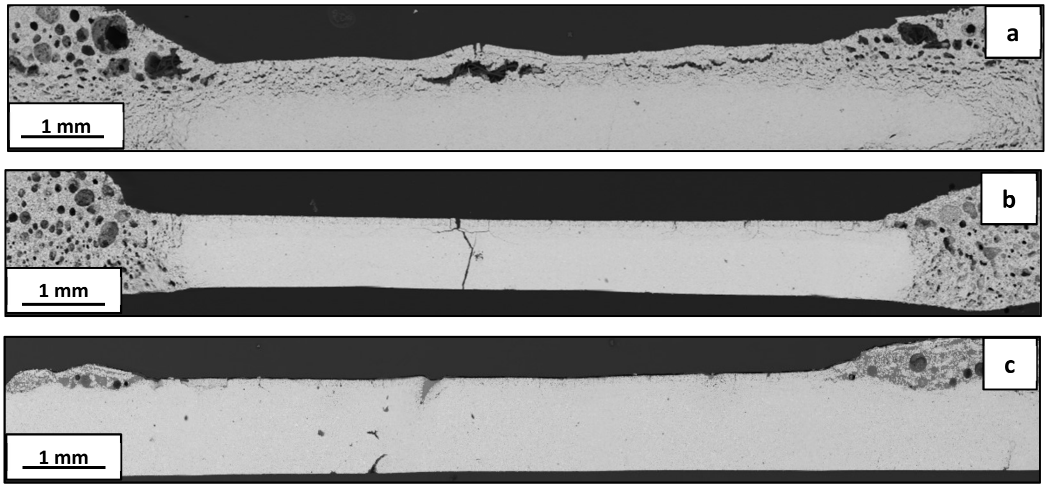

Figure 3.15. *Fine dispersion samples containing (a) 10, (b) 20, and (c) 30 vol% YbMS after exposure to 33Ca-45Si CMAS for 96 h at 1300°C.*

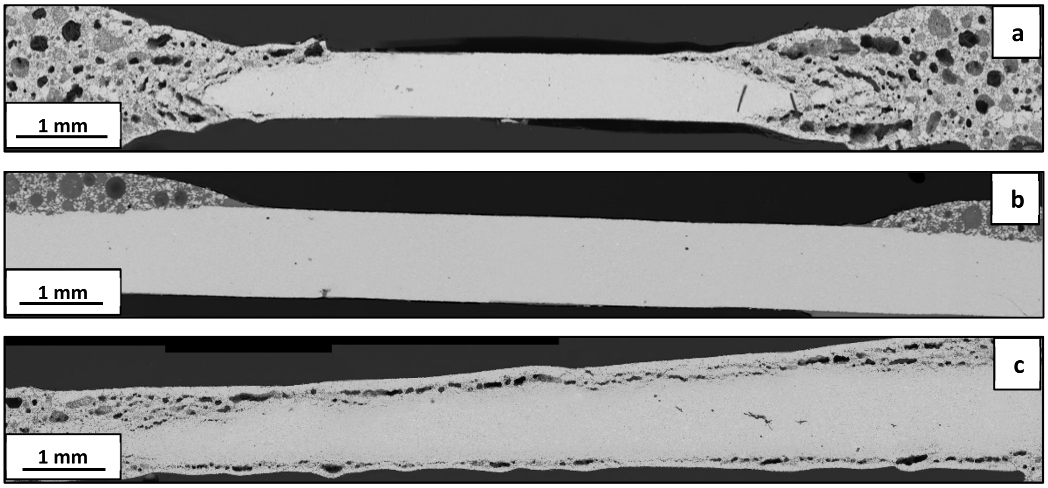

Figure 3.16. *Fine dispersion samples containing (a) 10, (b) 20, and (c) 30 vol% YbMS after exposure to 21Ca-57Si CMAS for 96 h at 1300°C.*

Glass spreading was not apparent after only 4 h exposure, for any sample type (Figure 3.17 and 3.18). Instead, there is the typical CMAS dome present at the surface of samples. This indicates that spreading on the surface begins at some point between 4 and 96 h. Fine dispersion samples subjected to 21Ca-57Si CMAS for 4 h exhibited delamination of the glass dome from the rest of the sample (Figure 3.18a). Because this is not seen after 96 h (Figure 3.18b), delamination occurred upon cooling (at 10°C/min).

Higher magnification images of the surface interaction zone for YbDS + 20 vol% YbMS exposed to CMAS for 96 h are given in Figure 3.19.

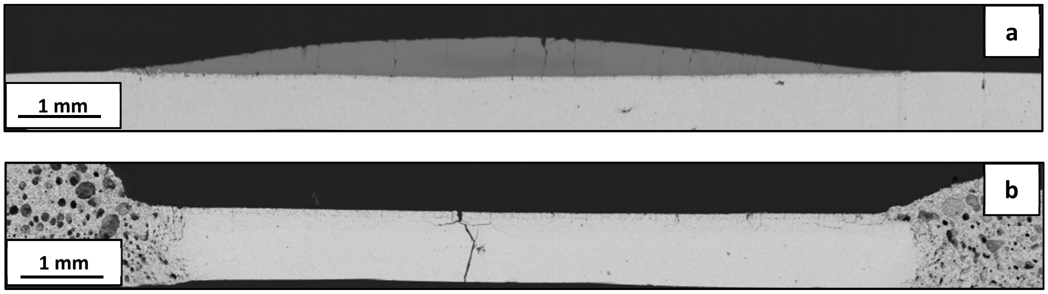

Figure 3.17. *Fine dispersion samples containing 20 vol% YbMS after exposure to 33Ca-45Si CMAS for (a) 4 h and (b) 96 h at 1300°C.*

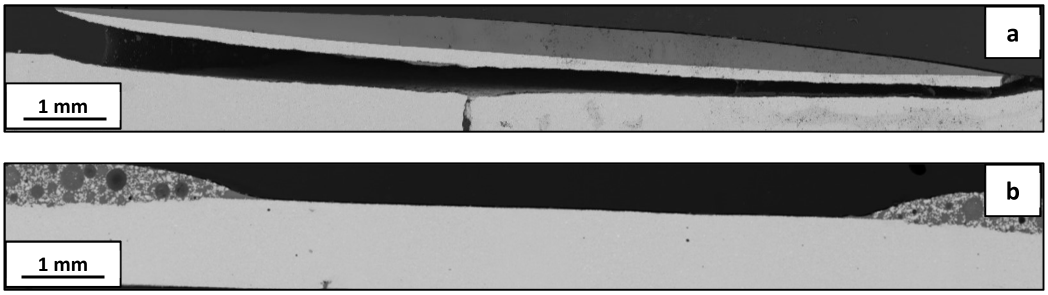

Figure 3.18. *Fine dispersion samples containing 20 vol% YbMS after exposure to 21Ca-57Si CMAS for (a) 4 h and (b) 96 h at 1300°C.*

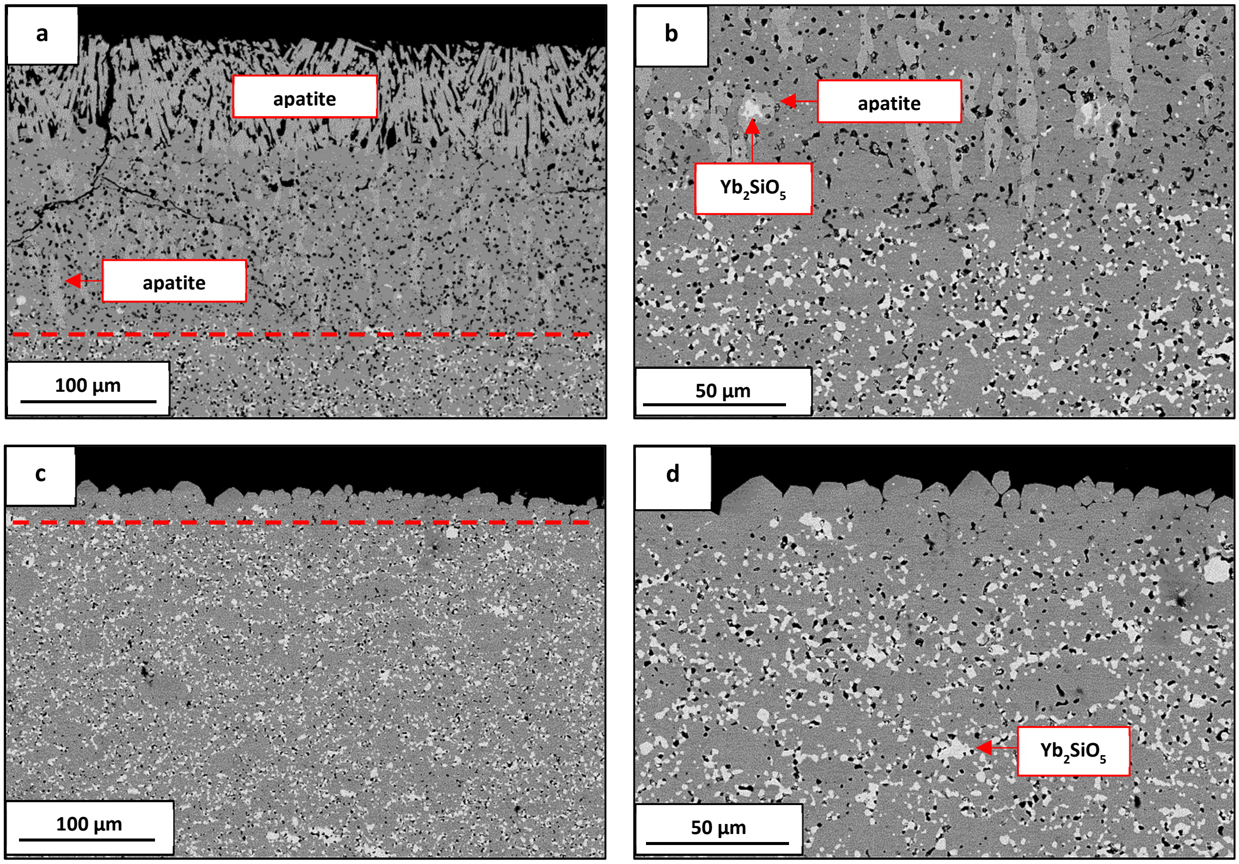

***Figure 3.19**. Cross-section BSE images of the sample surface/glass interaction zone after YbDS + 20 vol% YbMS exposure to (a,b) 33Ca-45Si and (c,d) 21Ca-57Si CMAS for 96 h at 1300°C.*

After exposure to 33Ca-45Si CMAS for 96 h, a layer of apatite (~100 µm in Figure 3.19a) is present at the surface of the sample. This is comparable to that seen in model APS coatings (Figure 3.10a). CMAS penetrates below this layer (by about 150 µm for YbDS + 20 vol% YbMS; Figure 3.19a) and reacts with dispersed YbMS to form apatite. The apatite forms as “needles” normal to the surface (Figure 3.19b). The presence of the “secondary phase” described in model APS coatings is also noted (Figure 3.20a). At the reacted edges, in addition to dispersed YbDS and apatite grains, there appears to be a third crystallized phase (Figure 3.20b). EDS point analyses of apatite and the secondary and third phases are given in Table 3.3 for fine dispersion samples exposed to 33Ca-45Si CMAS. XRD was only able to detect apatite (Figure 3.21a).

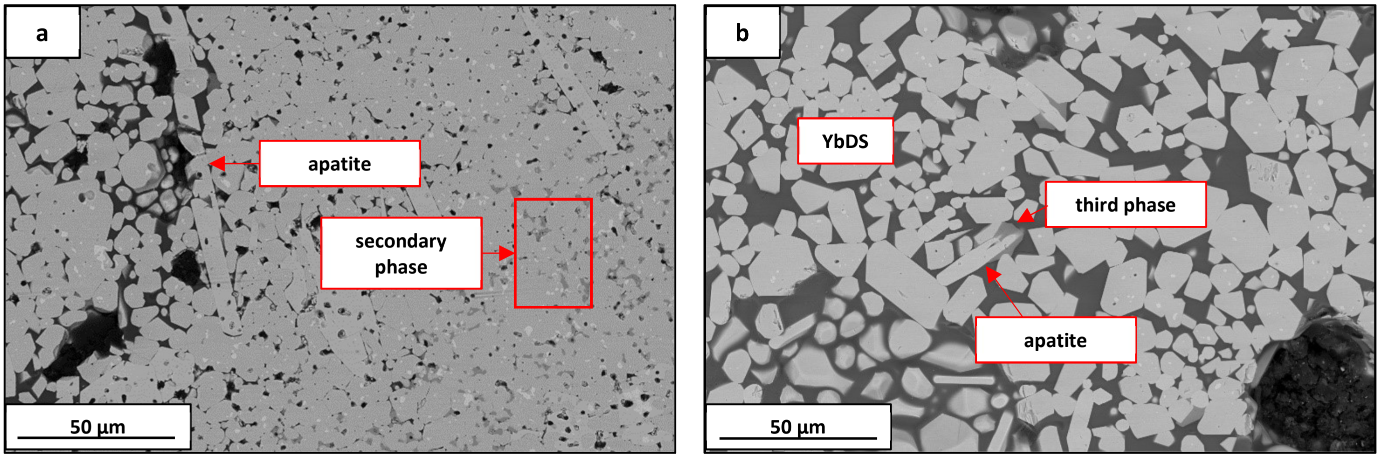

Figure 3.20*. Cross-section BSE images of the sample edge/glass interaction zone after exposure to 33Ca-45Si CMAS for 96 h at 1300°C. In addition to apatite, two other phases are visible – (a) a "secondary phase" and (b) a third phase. The chemistries of these phases, measured by EDS, are given in Table 3.3.*

Table 3.3*. EDS point measurements (at. %) taken on reaction products formed between fine dispersion samples and 33Ca-45Si CMAS after 96 h at 1300°C. Remaining glass refers to glass found at the sample edges.*

	Yb	Ca	Mg	Al	Si	Ca/Si ratio
apatite						
10 vol% YbMS	47.2	11.6			41.2	
20 vol% YbMS	48.5	10.7			40.7	
30 vol% YbMS	47.0	11.4			41.6	
secondary phase						
10 vol% YbMS	27.0	10.3	11.3	22.8	28.7	
20 vol% YbMS	26.5	10.9	11.3	20.6	30.7	
30 vol% YbMS	25.9	10.7	11.4	23.0	29.0	
third phase						
10 vol% YbMS	16.9	17.2	15.7	9.4	40.9	
20 vol% YbMS	16.1	19.5	14.4	8.3	41.8	
30 vol% YbMS	17.7	16.9	16.6	7.0	41.8	
remaining glass						
10 vol% YbMS	3.2	25.3	8.7	14.5	48.2	0.52
20 vol% YbMS	3.6	25.2	8.7	13.3	49.2	0.51
30 vol% YbMS	5.5	23.3	8.7	13.4	49.1	0.47
Nominal glass		33	9	13	45	0.73

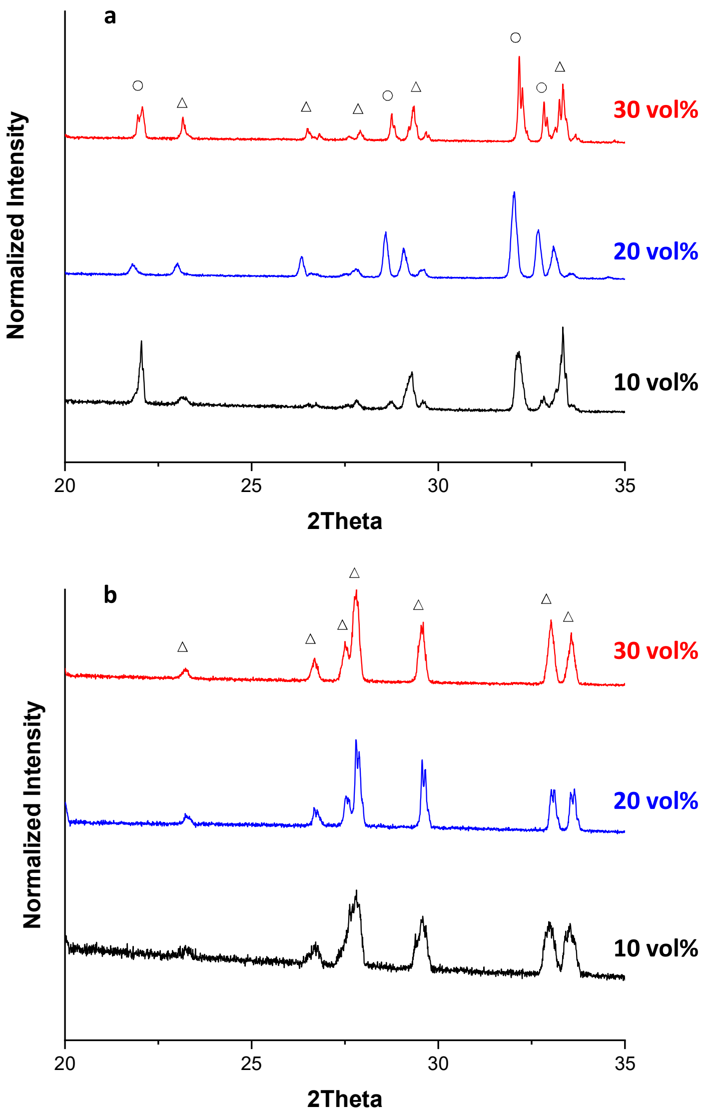

***Figure 3.21**. XRD spectra for fine dispersion samples after exposure to (a) 33Ca-45Si and (b) 21Ca-57Si CMAS for 96 h at 1300°C. Peaks corresponding to apatite are given by circles and peaks corresponding to YbDS are given by triangles. The data shown here were taken from bulk samples.*

For samples exposed to 21Ca-57Si CMAS, no continuous apatite layer was formed. Very little penetration was observed at the sample surface (Figure 3.19c and d) for YbDS + 10, 20 vol% YbMS. YbDS + 30 vol% YbMS, however, did show some penetration and blister cracking at the surface (Figure 3.16c). At the edges of the sample, there was vigorous reaction between coating and glass. Some apatite, as well as the secondary phase and third phase reported in samples exposed to 33Ca-45Si CMAS, was observed in YbDS + 10, 30 vol% YbMS (Table 3.4). However, XRD did not indicate the presence of any of these phases (Figure 3.21b).

Table 3.4*. EDS point measurements (at. %) taken on reaction products formed between fine dispersion samples and 21Ca-57Si CMAS after 96 h at 1300°C. Remaining glass refers to glass found at the sample edges.*

	Yb	**Ca**	**Mg**	**Al**	**Si**	**Ca/Si ratio**
apatite						
10 vol% YbMS	47.7	11.6			40.7	
20 vol% YbMS	-	-			-	
30 vol% YbMS	47.3	11.3			41.3	
secondary phase						
10 vol% YbMS	25.2	12.9	12.8	16.1	33.1	
20 vol% YbMS	-	-	-	-	-	
30 vol% YbMS	25.9	10.3	14.4	16.2	33.2	
third phase						
10 vol% YbMS	14.7	19.1	15.7	9.6	40.9	
20 vol% YbMS	-	-	-	-	-	
30 vol% YbMS	15.5	17.9	15.1	10.2	41.3	
remaining glass						
10 vol% YbMS	3.4	23.5	9.0	13.6	50.5	0.47
20 vol% YbMS	4.8	21.3	8.0	11.0	54.9	0.39
30 vol% YbMS	3.6	22.5	10.1	16.3	47.6	0.47
Nominal glass		21	9	13	57	0.37

3.4 Discussion

a) Model APS coatings

i. Effect of YbMS content and CMAS composition

First, the effect of YbMS content on sample/glass interactions will be summarized. Table 3.5 gives a recap of general observations on model APS materials for comparison to phase pure materials. The threshold for YbMS content leading to improved CMAS resistance in model APS materials appears to be ~20 vol%. YbDS + 10 vol% YbMS samples exposed to CMAS of variable composition show improved or comparable resistance to that of YbDS alone after 4 h, but are infiltrated in a similar manner to phase pure YbDS by 96 h. After 4 h at temperature, samples (containing 10 vol% YbMS) exposed to 33Ca-45Si CMAS show increased infiltration and blistering/pore formation at interfacial areas having decreased localized concentrations of YbMS. Increasing the YbMS content to 20/30 vol% can lead to a significant reduction of the overall glass infiltration depth (Figure 3.9). Even for samples exposed to 21Ca-57Si CMAS, wherein ultimate glass infiltration nears through thickness of the sample (Figure 3.13), macroscopic interaction behavior is much improved. There is little to no blistering within the bulk and no pore coalescence at infiltrated grain boundaries. The maximum infiltration depths measured in these samples correspond to much smaller volumes of glass than observed in phase pure YbDS.

***Table 3.5**. General observations made on model APS YbDS + YbMS samples. Information on phase pure components is also provided. "Through thickness" refers to samples having thicknesses between ~1-2 mm.*

33Ca-45Si CMAS (Ca/Si = 0.73)				
	Average penetration (µm)	**Blistering?**	**Apatite formation?**	**Residual glass Ca/Si ratio**
YbDS	through thickness	Yes	No	0.55
YbMS	127.0	No	Yes	0.58
YbDS + 10 vol% YbMS	through thickness	Yes	Some	-
YbDS + 20 vol% YbMS	360.6	No	Yes	0.45
YbDS + 30 vol% YbMS	292.8	No	Yes	0.46
21Ca-57Si CMAS (Ca/Si=0.37)				
YbDS	through thickness	Yes	No	0.37
YbMS	140.2	No	No (YbDS)	0.37
YbDS + 10 vol% YbMS	through thickness	Yes	Some	-
YbDS + 20 vol% YbMS	669.0	No	Some	0.33
YbDS + 30 vol% YbMS	523.8	No	Some	0.35

For model APS samples exposed to 33Ca-45Si CMAS, the mechanism for decreased infiltration is related to an increased propensity to form apatite. This might be expected based on the results of phase pure components exposed to CMAS, as described in Chapter 2. The presence of YbMS causes the incoming CMAS front to slow as embedded granules are transformed into the apatite phase; the apatite reaction prevents glass from moving along grain boundaries and pores. EDS scans show that Ca ions within the glass preferentially react with YbMS inclusions (Figure 3.22) to form apatite and the "secondary phase."

The Ca/Si ratio of residual glass in mixed materials is lower than that seen in either phase pure YbDS or YbMS (Table 3.5). The reaction of phase pure YbMS with 33Ca-45Si CMAS to form apatite (Equation 1.4) leads to a reduction in Ca content (from 33 to 26.4 at. %) and little change in Si content. Interaction between phase pure YbDS and 33Ca-45Si CMAS results in reduced Ca (27.3 at. %) and increased Si (from 45 to 49.5 at. %; some apatite formation; Equation 1.3). In mixed YbDS/YbMS, there is a combined reduction in Ca content (lower Ca values than observed in residual glass for either phase pure YbMS or YbDS) and the Si content increases (similar to that seen in residual glass for phase pure YbDS). This indicates that the mechanisms of infiltration/reaction described for phase pure YbDS and YbMS (Chapter 2) are working synergistically in model materials. In summary, CMAS forms some apatite in contact with YbDS and travels along sample defects (as observed in phase pure YbDS). Glass penetration is halted upon interaction with embedded YbMS to form apatite. The reaction to form apatite pulls Ca from the melt and reduces the ability for remaining glass to infiltrate.

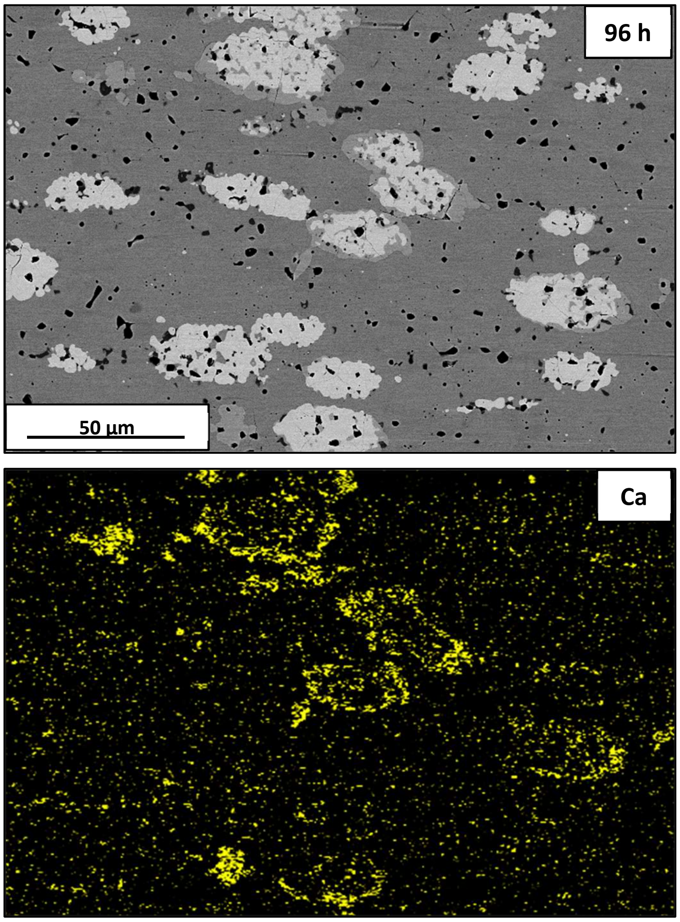

Figure 3.22. *(top) Cross-section BSE image of model APS YbDS + 20 vol% YbMS after exposure to CMAS for 96 h at 1300°C and (bottom) corresponding Ca EDS map.*

As mentioned previously, model mixed phase materials exposed to 21Ca-57Si CMAS did not show reduced infiltration rates. Although some apatite formation was observed, it was minimal in comparison to samples exposed to 33Ca-45Si CMAS. The large scatter in infiltration measurements (Figure 3.13) is likely due to variations in sample microstructure, such as grain boundary porosity. Because crystallization is reduced, glass is more likely to penetrate defect pathways, as seen in phase pure YbDS. The formation of the “secondary phase” does not seem to reduce overall penetration, but does, along with the small amount of apatite formed, pull CaO from the incoming melt. Indeed, the Ca content in residual glass is slightly reduced from its original chemistry (Table 3.2). Phase pure YbMS has been shown to form a protective YbDS layer in contact with 21Ca-57CMAS; the absence of any newly formed YbDS at the YbMS/glass interface is likely a result of 1) YbMS granules already being surrounded by YbDS and 2) the absence of a large reservoir of CMAS directly in contact with YbMS. Despite infiltration in these materials being similar to phase pure YbDS, the severity of attack is reduced. YbMS additions of 20 and 30 vol% prevent blister cracking of infiltrated samples and pore formation. While crystallization is reduced in samples exposed to 21Ca-57Si CMAS, as compared to in samples exposed to 33Ca-45Si CMAS, formation of the “secondary phase” and small amounts of apatite could locally consume glass constituents to slow the penetrating front. Additionally, the presence of relatively dense YbMS granules within the YbDS matrix likely reduces the overall number of open grain boundaries available for glass transport. Further work is needed to understand the observed behavior in this system.

ii. Comparison to actual APS materials

While the interaction behavior between actual APS-deposited EBCs and 21Ca-57Si CMAS is not available, there have been some studies on coatings in contact with 33Ca-45Si CMAS. Zhao et al. investigated CMAS reaction/penetration in APS-deposed YbDS coatings at 1300°C [56]. YbDS coatings contained regions of Si-depleted YbMS. The amount of YbMS in the coating is unknown, but ImageJ analysis of available cross-section images of the microstructure suggest ~25-30%. Similar behavior was observed in their study as reported here for model APS materials containing 20 or 30 vol% YbMS. YbMS inclusions preferentially reacted with incoming CMAS to form the apatite phase (Figure 3.23). Infiltration measurements were not given, but reaction layer thickness was reported to be similar between APS YbDS and APS YbMS. This was assuming, however, that the apatite formed was fully dense.

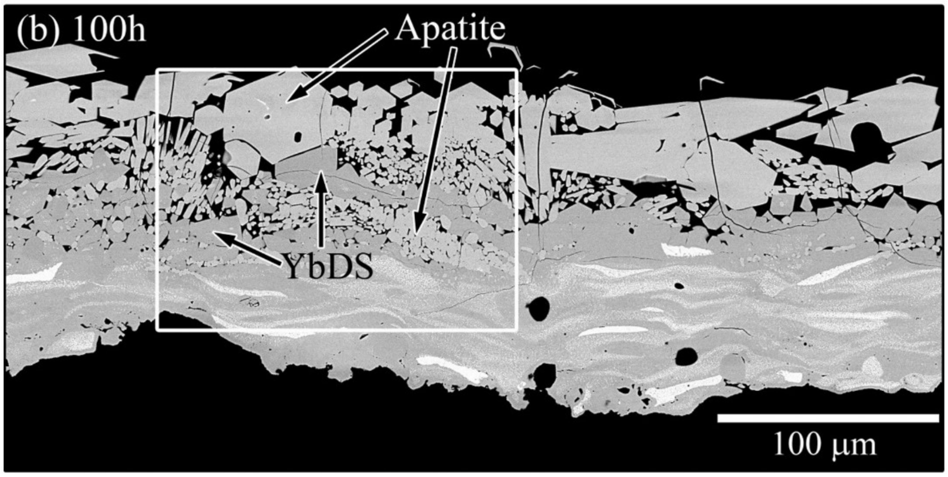

Figure 3.23. *Interaction between 33Ca-45Si CMAS and APS-deposited YbDS at 1300°C. From [56].*

CMAS interactions with APS $Y_2Si_2O_7$ have also been reported at 1300°C [53]. Similar to that seen in the YbDS system, regions of Y_2SiO_5 were present within the coating. ImageJ analysis of available cross-section images suggest a Y_2SiO_5 content of ~25%. Surface recession of coatings was similar to that observed in dense, phase pure $Y_2Si_2O_7$ samples. This is quite different from the results obtained here, assuming that the model YbDS + YbMS materials are a good approximation of an actual EBC. The difference is likely attributed to the increased driving force for $Y_2Si_2O_7$ to form apatite over YbDS. Preferential reaction of CMAS with Y_2SiO_5 was not reported.

b) Fine dispersion samples

i. Glass spreading

The apparent glass spreading mechanism observed in fine dispersion YbDS/YbMS samples has not been reported on previously in EBC materials, to the author's knowledge. It is prudent to recap the sequence of events observed in fine dispersion samples exposed to molten CMAS before considering possible surface energy phenomena. In contact with 33Ca-45Si CMAS, YbDS/YbMS forms a continuous layer of apatite at the sample/glass interface after 4 h at 1300°C. Below this layer, some CMAS penetrates and reacts preferentially with dispersed YbMS to form "needles" of apatite along with some of the “secondary phase.” A dome of glass remains at the surface of the sample. The thickness of the continuous apatite layer grows with increasing time (96 h), but infiltration below this layer is approximately the same. The dome of CMAS at the surface (as seen after 4 h) has “split” and migrated to the edges of the sample by 96 h, where vigorous interaction between coating and glass takes place. In contact with 21Ca-57Si CMAS, YbDS/YbMS does not react to form new phases after 4 h. Surface grains appear rounded, but infiltration is not obvious. A dome of glass is apparent at the surface. After 96 h, this glass has also “split” and moved to the edges of the sample. No apparent infiltration is observed at the initial coating/glass interface.

Wetting of an ideal solid surface (i.e. smooth, rigid, chemically homogeneous, and inert) by a non-reactive liquid (Figure 3.24) can be described by Young’s Equation [99, 100]:

$$\cos\theta_Y = \frac{\gamma_{SV}-\gamma_{SL}}{\gamma_{LV}} \qquad [3.1]$$

where θ_Y is the angle formed at the three-phase boundary (solid/liquid/vapor) between the surfaces of the liquid drop and the solid (referred to as contact angle; Figure 3.24), and γ_{SV}, γ_{SL}, and γ_{LV} refer to the surface tension of the solid, interfacial tension at the solid/liquid interface, and the surface tension of the liquid, respectively. Contact angles <90° indicate wetting while contact angles >90° indicate non-wetting.

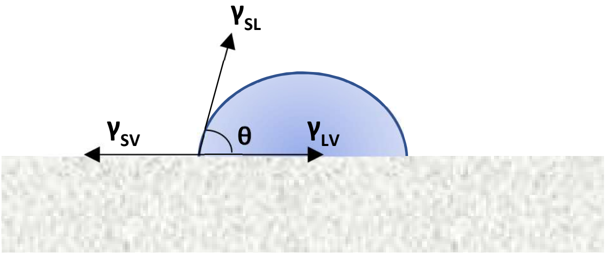

***Figure 3.24**. Schematic showing liquid wetting of a solid surface. Parameters γ_{SV}, γ_{SL}, and γ_{LV} refer to the surface tension of the solid, interfacial tension at the solid/liquid interface, and the surface tension of the liquid, respectively.*

Most solid surfaces are non-ideal, and can be characterized as rough or chemically heterogeneous. Wetting on rough surfaces (Figure 3.25a) can be described by the Wenzel equation [99, 101]:

$$\cos\theta_W = s_r \cos\theta_Y \tag{3.2}$$

where θ_W is the Wenzel-derived contact angle and s_r is the ratio of the actual surface area to the planar surface area (for a rough surface, $s_r > 1$).

In some instances, pockets of air can be trapped beneath roughness grooves (Figure 3.25b). In such a situation, the liquid interacts with a heterogeneous surface consisting of the solid and air. This type of wetting was described by Cassie and Baxter by the following equation [102]:

$$\cos\theta_{CB} = f\cos\theta_Y + f - 1 \tag{3.3}$$

where θ_{CB} is the Cassie-Baxter-derived contact angle and f is the area fraction of the solid in contact with the liquid. It is assumed that the contact angle of the liquid on air is 180°.

The Cassie-Baxter equation can also be used to describe a chemically heterogeneous surface consisting of alternating strips of two phases (α and β; Figure 3.26) [99]:

$$\cos\theta_{CB} = f^{\alpha}\cos\theta^{\alpha} + f^{\beta}\cos\theta^{\beta} \tag{3.4}$$

where θ^{α} and θ^{β} are the contact angles related to phase pure α and β, respectively, and f^{α} and f^{β} are the surface area fractions of α and β, respectively.

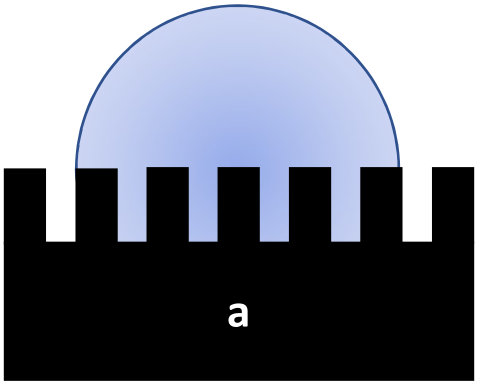

***Figure 3.25**. Wetting of a liquid drop on either (a) a rough solid surface (described by the Wenzel equation) or (b) a rough solid surface containing air pockets in the roughness grooves (described by the Cassie-Baxter equation).*

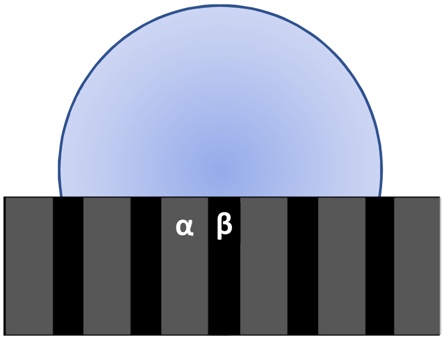

***Figure 3.26**. Wetting on a heterogeneous surface composed of two phases, α and β.*

Additionally, the processes of reactive wetting, involving either dissolution of the solid surface or dissolution followed by crystallization of new phases, must be taken into account. Dissolution of the solid (as seen in YbDS) can lead to changes in the geometry and energetics of the solid/liquid/vapor interface (Equation 3.5, [99]). Dissolution followed by crystallization of new phases (such as that seen in YbMS to form apatite/YbDS) can also lead to changes in the energetics/wettability of the solid/liquid interface. The formation of a dense reaction product between the original solid and the liquid that is more wettable than the original solid will promote overall wettability.

$$\cos\theta(t) = \cos\theta^{\circ} - \frac{\Delta\sigma(t)}{\sigma_{LV}^{\circ}} - \frac{\Delta G(t)}{\sigma_{LV}^{\circ}} \quad [3.5]$$

In Equation 3.5, θ° is the equilibrium contact angle in the absence of any dissolution, Δσ(t) describes the change in σ_{SL} brought about by dissolution, $\sigma°_{LV}$ is the unchanged interfacial energy term for the liquid/vapor boundary, and ΔG(t) is the change in Gibbs free energy per unit area for the dissolution reaction.

Glasses are known to wet oxide materials quite well and it has been shown for both phase pure YbDS and YbMS that wetting by CMAS (of variable composition) does indeed occur (Chapter 2). Based on Equation 3.4 and assuming relatively similar contact angles for YbDS and YbMS, it would not be expected that wetting of mixed YbDS/YbMS would change much relative to phase pure materials. Wetting is still observed in model APS materials and in fine dispersion samples at short times (i.e. 4 h). Destabilization of the glass deposit in fine dispersion samples takes place at some point between 4 and 96 h. Because similar "splitting" behavior is observed in glasses of variable composition – which dictates the presence or absence of the apatite phase – it is unlikely that the wetting characteristics of apatite are strongly influencing overall sample wettability. The mechanism of destabilization in these complicated systems is not currently understood; however, possible explanations for the observed behavior are proposed below.

In addition to contact angle, wetting can also be described by a spreading parameter, S [103]. The spreading parameter describes the difference between the work of adhesion (W_a; attraction between the solid and the liquid), given by the Dupré equation:

$$W_a = \gamma_{SV} + \gamma_{LV} - \gamma_{SL} \qquad [3.6]$$

and the work of cohesion (W_c; repulsion between the solid and the liquid/attraction between solid-solid or liquid-liquid):

$$W_C = 2\gamma_{LV} \qquad [3.7]$$

When the area of a liquid drop on a solid is increased by dA, the change in the surface free energy of the system is approximately $(\gamma_{LV} + \gamma_{SL} - \gamma_{SV})dA$ (Figure 3.27). If $(\gamma_{LV} + \gamma_{SL} - \gamma_{SV})dA$ is negative, spreading occurs spontaneously. Equation 3.8 describes the negative of this relation in terms of the spreading parameter (S):

$$S = W_a - W_C = \gamma_{SV} - (\gamma_{SL} + \gamma_{LV}) \quad [3.8]$$

When S > 0, the liquid completely wets the solid surface ($W_a > W_c$). Favorable conditions in this regime involve a large solid interfacial tension (γ_{SV}) and/or a small liquid interfacial tension (γ_{LV}). When S < 0, the liquid drop does not spread and instead forms the typical liquid "dome" atop the solid surface having wetting characteristics described by contact angle.

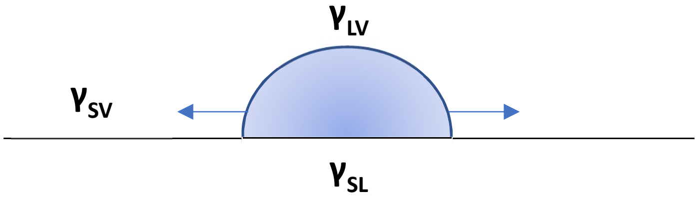

***Figure 3.27**. Spreading of a liquid drop on a solid surface.*

Surface energy is defined as a function of surface area and has units that are identical to those for surface tension (Jm^{-2} or N/m). The surface energy of fine dispersion samples should be much greater than that of model APS materials or phase pure YbDS/YbMS, as there are many more surfaces/interfaces. Assuming that the surface energy of fine dispersion samples is large enough, complete spreading of molten CMAS on the surface could be described by Equation 3.8 and a S value > 1. The observations made on fine dispersion samples are validated by this mechanism, as glass spreads to the very edges of the sample; robust reaction at sample edges is likely an artifact of the glass no longer having a surface to travel on. This explanation is more credible than any describing de-wetting. De-wetting based on Young's Equation (Equation 3.1) would require a low surface energy solid. The formation of apatite and "secondary phase" at the reaction front and/or dissolution of sample surfaces does not seem to influence wetting behavior. According to Equation 3.5 (ignoring interfacial or surface energy terms), a positive ΔG is needed to increase θ(t) and decrease wettability. However, dissolution of fine dispersion samples should be favored (-ΔG) because the surface is composed of small particles and many interfaces. There is more porosity in fine dispersion samples as compared to model APS materials or phase pure YbDS/YbMS, which would increase the contact angle (Equation 3.3); however, differences in porosity between model APS coatings/phase pure materials and fine dispersion samples are less than ~5-10%.

ii. Other crystallized phases

In addition to apatite, several other phases that have not been identified by XRD are present in reacted samples. The chemistries of these phases are given in Tables 3.3 and 3.4 and are referred to as a "secondary phase" and a "third phase." The secondary phase is also observed in model APS materials. While determination of the nature of these small quantity phases requires electron diffraction, the likelihood of them being attributed to one of the phases found in Table 3.6 (seen below) is high based on past work in the CMAS literature. Despite not knowing the structure of these reaction phases, their presence does not appear to strongly influence overall infiltration mechanisms.

Table 3.6. *Reaction phases previously observed between EBC materials and CMAS. From [14].*

Name	Nominal Formula
Garnet	$(Ca,RE)_3(Mg,Al)_2(Si,Al)_3O_{12}$
Cuspidine	$(RE,Ca,Mg)_4(Si,Al)_2O_{9.x}$
Cyclosilicate	$Ca_3RE_2Si_6O_{18}$
Silicocarnotite	$Ca_3RE_2Si_3O_{12}$

c) Application to real systems

As YbMS is added to YbDS in an actual EBC, coating properties other than CMAS resistance need to be considered; these include thermal expansion and water vapor resistance. The CTE of YbMS (~6-9 [104]) is greater than that of YbDS (~3.5-4.5 [96]) and SiC (~4.5-5.5 [48]) and is also highly anisotropic (Cory Parker and Mackenzie Ridley, UVa, unpublished work). The addition of large amounts of YbMS could lead to thermally-induced stresses within the coating that may cause cracking or delamination from the underlying CMC. Cracks within the coating can act as short diffusion paths for incoming oxidative species, such as water vapor. While increasing YbMS content is detrimental in terms of thermal mismatch, YbMS does show improved water vapor resistance over YbDS. Silica activity is lower in the disilicate than in the monosilicate, as determined by Costa et al. [105].

3.5 Summary and conclusions

Adding controlled amounts of YbMS to a YbDS matrix can drastically improve material resistance to CMAS infiltration. It was determined that including ≥ 20 vol% YbMS was beneficial in reducing overall glass penetration, as compared to phase pure YbDS. It is therefore suggested that the APS process for preparation of EBCs be tailored so that this amount of YbMS is available for deposition. The distribution of YbMS inclusions also had a strong effect on CMAS interaction behavior. Model APS coatings exhibited a combination of grain boundary attack (in the YbDS matrix) and crystallization of YbMS granules (most notably to form apatite). Fine dispersion samples were not penetrated as deeply as model APS materials. This was due to glass spreading on the sample surfaces, possibly a result of higher coating surface energies. Glass buildup and extensive attack was seen at the edges of fine dispersion samples; however, in a realistic engine environment, spreading of the glass may allow it to “roll off” engine components and exit with the exhaust. The work presented in this chapter should have a measurable impact on the CMAS community, as it is the first demonstration of an EBC-intrinsic strategy to improve CMAS resistance in these coating materials.

3.6 Recommendations for future work

APS-deposited Yb_2SiO_5 will likely contain some amount of Yb_2O_3 [49]. Similar studies on YbMS/Yb_2O_3 materials can give important insights into the interaction behavior between Yb_2O_3 and CMAS and may provide additional strategies for coating development. Preliminary data (Appendix C) suggest that apatite, exposed to high velocity steam, transforms into, firstly, YbMS and, secondly, Yb_2O_3, meaning that Yb_2O_3 could be important even when it is not included in the initial coating.

The mechanism of glass destabilization on fine dispersion sample surfaces is not well understood. Future work should focus on elucidating the observed spreading behavior. Box furnace exposures at additional time points should be performed. Analysis of wetting using a hot stage microscope would allow for visualization of wetting behavior *in situ*. Contact angle measurements on fine dispersion samples, relative to phase pure materials, should be made in an attempt to determine substrate surface energy [106].

Finally, actual APS coatings containing controlled amounts of YbDS and YbMS should also be studied to confirm that the CMAS mitigation strategy described in this chapter extends to EBCs prepared by commercially viable processing routes.

4. Chapter 4: Viscosity of CMAS melts

4.1 Introduction

As described in the literature review (Chapter 1), the composition of CMAS can vary widely based on deposit source and location geography, leading to variable melting and viscosity behavior that can influence coating/glass interaction. The aims of this chapter were to 1) obtain experimental viscosity data on CMAS melts for comparison to models by FactSage [27], Fluegel [28], and Giordano et al. [26], which are frequently cited by the CMAS community and 2) determine if viscosity has an effect on coating infiltration. The influence of CaO/SiO_2 ratio and MgO and Al_2O_3 contents on CMAS viscosity were determined. A volcanic ash glass obtained from the field was also tested for comparison to model materials.

Of the three models investigated, the FactSage model best described model melts. It consistently gave data that was only 0-3 Pa·s different from that determined experimentally. The only composition with data that was not confirmed by FactSage was the volcanic ash glass. The Fluegel and Giordano et al. models were not good representations of this composition either. Differences between observed and calculated viscosity for the ash glass may be due to the presence of water in the glass structure or to its overall increased chemical complexity. Decreasing the CaO/SiO_2 ratio increased glass viscosity, as did increasing Al_2O_3 content. The addition of MgO decreased glass viscosity.

The effect of glass viscosity on infiltration was considered for YbDS/YbMS materials previously studied (Chapters 2 and 3). Viscosity can likely be used to help understand high temperature infiltration in materials that do not react with CMAS (i.e. YbDS, which is penetrated via grain boundaries/defects) but is not as telling for materials that react with CMAS (i.e. YbMS, which reacts to form apatite or YbDS).

This report is the first to provide experimental viscosity data on specific CMAS compositions under study in the literature. It is the first to provide evidence on the validity of the FactSage, Fluegel, and Giordano et al. models for CMAS-related compositions.

4.2 Experimental

i. Glass preparation and characterization

Glass batches were prepared by mixing stoichiometric amounts of CaO, MgO, Al_2O_3, and/or SiO_2 powders. Compositions under study can be found in Table 4.1. The “Eyja volcanic ash glass” was provided by NASA Glenn Research Center. It was prepared from ash obtained from Iceland’s Eyjafjallajökull volcanic eruption of 2010 and had a composition of $6.2CaO\text{-}4.2MgO\text{-}10.1Al_2O_3\text{-}67.5SiO_2\text{-}4.4Fe_2O_3\text{-}1.4TiO_2\text{-}5.0Na_2O\text{-}1.2K_2O$ (mol %; determined by ICP). Mixtures were dry milled with zirconia media for ~24 h. After mixing, powders were transferred to a Pt-5%Au crucible and were melted at 1500°C for ~1 h before being quenched in water. Glass pieces were dried overnight and their densities measured by Archimedes’ Method (Table 4.1). Powdered samples of each composition were analyzed by DSC, ICP, EDS, and XRD to confirm glass melting, chemistry, and amorphous character (Appendix D). In some cases, Fourier transform infrared spectroscopy (FTIR; Thermo Nicolet Nexus 670, Thermo Fisher Scientific, Waltham, MA) in the transmission mode was used to analyze glass bonding. Specifically, the presence of any hydroxyl groups was of interest.

***Table 4.1**. Glass compositions (with corresponding Ca/Si ratio) for viscosity measurement. Respective densities (experimentally obtained) used to determine glass volume are given.*

Glass composition	**Ca/Si ratio**	**Density (g/cm^3)**	**Comments**
$C_{33}M_9A_{13}S_{45}$	0.73	2.826	baseline high Ca/Si
$C_{21}M_9A_{13}S_{57}$	0.37	2.676	baseline low Ca/Si
$C_{38.1}A_{9.9}S_{52}$	0.73	2.778	effect of Al content
$C_{33.75}A_{20}S_{46.25}$	0.73	2.760	
$C_{29.5}A_{30}S_{40.5}$	0.73	2.750	
$C_{33.75}M_{20}S_{46.25}$	0.73	2.890	effect of Mg content
Eyja volcanic ash glass	0.09	2.520	volcanic ash (from field)

ii. Viscosity measurements using a high temperature rotating viscometer

Viscosity measurements were performed using an Orton RSV-1600 viscometer furnace setup (Westerville, OH) equipped with a Brookfield (Middleboro, MA) HA-DV2T viscosity measuring unit and platinum spindle. The viscometer setup is shown in Figure 4.1. A 50 mL platinum crucible was filled with enough glass (~90 g) so that the resulting molten glass volume was approximately 30 mL. Viscosity measurements were performed between about 1300°C and 1500°C. The viscometer furnace was held at its maximum temperature for at least 20-30 minutes to equilibrate the melt. The spindle was lowered into the melt and allowed to rotate. The rotation speed was automatically adjusted by the software depending on the melt viscosity. Speed was increased as viscosity decreased; the maximum speed allowed was 80 RPM. The furnace was cooled at 25-50°C intervals and held at each temperature for 20-30 minutes. The viscosity of the glass was determined at each temperature after a stable reading was obtained. Experimental viscometer parameters for each glass composition are given in Table 4.2. The viscometer temperature was taken as the average of the temperatures given by control and sample thermocouples. The sample thermocouple resided inside the crucible pedestal (Figure 4.1) with its tip just a few millimeters from the bottom of the crucible. The control thermocouple was located inside of the furnace. The average temperature was taken to accommodate any thermal gradient between the base of the crucible and the surface of the melt. The difference in measured temperatures between the two thermocouples was ~35°C at the highest temperatures tested.

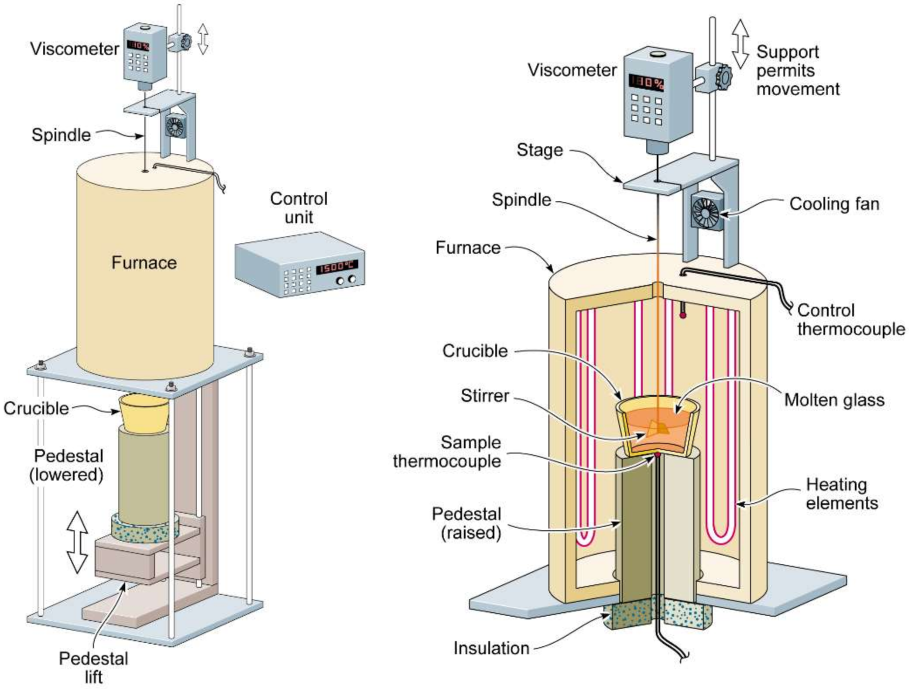

Figure 4.1*. The viscometer furnace setup including Brookfield viscosity measuring unit (viscometer), spindle, crucible, and control unit.*

The viscosity of the glass melt was determined by measuring the percent spindle torque required to maintain the spindle rotation at the desired speed. The viscosity of the melt (η; in centipoise) is related to the spindle torque (τ) and rotational speed (RPM) by the following equation, found in the Orton RSV-1600 instrument manual:

$$\eta = \frac{100}{RPM} \times TK \times SMC \times \tau \qquad [4.1]$$

where TK and SMC are the viscometer torque constant and the spindle multiplier constant, respectively. These values were provided in the Orton viscometer software. The viscosity of a borosilicate glass standard (NIST SRM 717a, Sigma Aldrich; St. Louis, MO) was determined between 1000-1325°C, confirming that the supplied constants gave accurate data (Figure 4.2).

***Table 4.2**. Experimental/viscometer parameters for each CMAS-related glass under study.*

Glass composition	Min./Max. T (°C)	Min./Max. Spindle Speed	Min./Max. Torque (%)	Average Lab. Temp. (°C)/Average Lab. Humidity (% RH)
$C_{33}M_9A_{13}S_{45}$	1225/1410	80	3/17	26/21
$C_{21}M_9A_{13}S_{57}$	1285/1510	n/a	n/a	23/14
$C_{38.1}A_{9.9}S_{52}$	1410/1530	80	2/5	23/14
$C_{33.75}A_{20}S_{46.25}$	1410/1530	80	3/7	22/46
$C_{29.5}A_{30}S_{40.5}$	1410/1530	80	3/11	23/26
$C_{33.75}M_{20}S_{46.25}$	1410/1510	80	0.5/1	23/13
Eyja volcanic ash glass	1310/1500	20/80	25/60	n/a

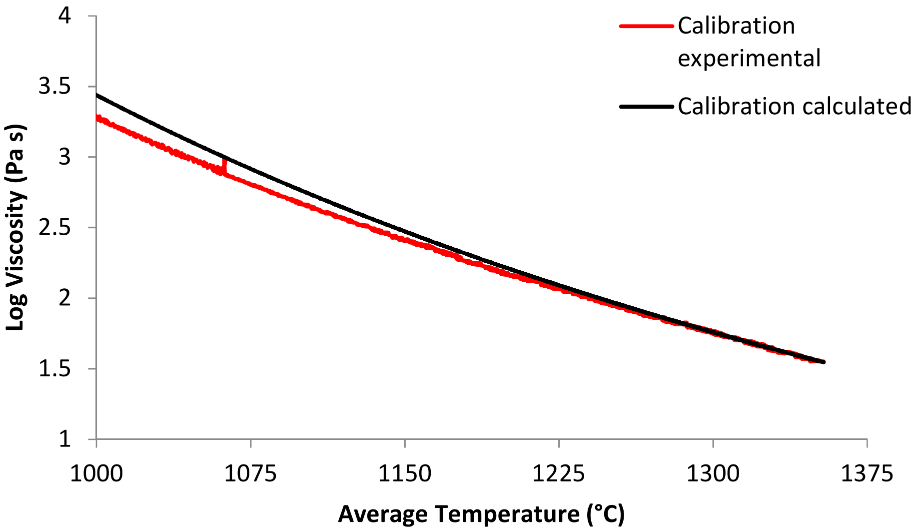

***Figure 4.2**. Experimental viscosity data on a standard borosilicate glass for comparison to the calculated calibration curve.*

iii. Post-viscosity glass analysis

Following viscosity measurements, the viscometer furnace was cooled naturally to room temperature. In some cases, the sample was glassy upon cooling and in some cases, it was crystalline. If the sample was crystalline upon cooling, it was re-heated to 1500°C in a stagnant air box furnace and quenched to the glassy state. As a glass, a small amount of sample was chipped from the crucible for post-analysis by EDS to confirm the glass chemistry. Glass was removed from the crucible by pouring it out in the molten state, and then allowing the crucible to soak in a 1:1:1 (by volume) mixture of $HF:HNO_3:H_2O$.

4.3. Results

Experimental viscosity measurements are plotted vs. calculated model values (FactSage, Fluegel, and Giordano et al.) in Figures 4.3 and 4.4 for CMAS compositions, Figures 4.5-4.7 for CAS compositions, Figure 4.8 for $CM_{20}S$, and Figure 4.9 for the Eyja volcanic ash glass. Across the board, the FactSage model best represents the experimental data obtained. Table 4.3 gives viscosity values calculated via FactSage at specific viscometer temperatures for comparison to experimental data. The difference between measured and calculated viscosity is, at most, ~2-3 Pa·s for model glass compositions. The only glass that is not well described by the FactSage model is the Eyja volcanic ash glass (Figure 4.9). In looking at Table 4.3, it is noticeable that, in most cases (except for $CA_{10}S$ and $CM_{20}S$), the difference between measured and calculated viscosity increases with decreasing temperature. This behavior was also observed in the borosilicate glass standard (Figure 4.2); experimental borosilicate viscosity data was compared to a calibration curve provided in the instrument manual.

There are no outstanding trends discerned for accuracy of viscosity calculated via Fluegel or Giordano et al compared to experimental values. In some cases, the Giordano et al. model matches experimental data fairly well (Figures 4.3, 4.6, and 4.7) but in others, it significantly overestimates (Figures 4.4, 4.5, and 4.8). In general, the Fluegel model seems to underestimate viscosity. Figures 4.4 and 4.8 show instances when this model more reasonably agrees with viscometer results. The FactSage and Fluegel models are also in good agreement with each other for the Eyja glass (Figure 4.9), although they both overestimate viscosity.

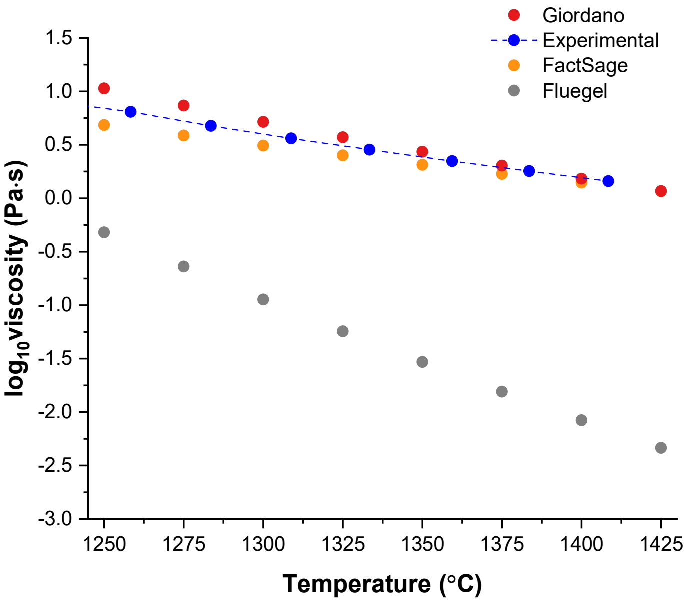

Figure 4.3. *Experimental viscosity (log$_{10}$visosity in Pa·s) plotted versus temperature for $C_{33}M_{9}A_{13}S_{45}$ glass. Viscosity values calculated by the FactSage, Fluegel, and Giordano et al. models are also given.*

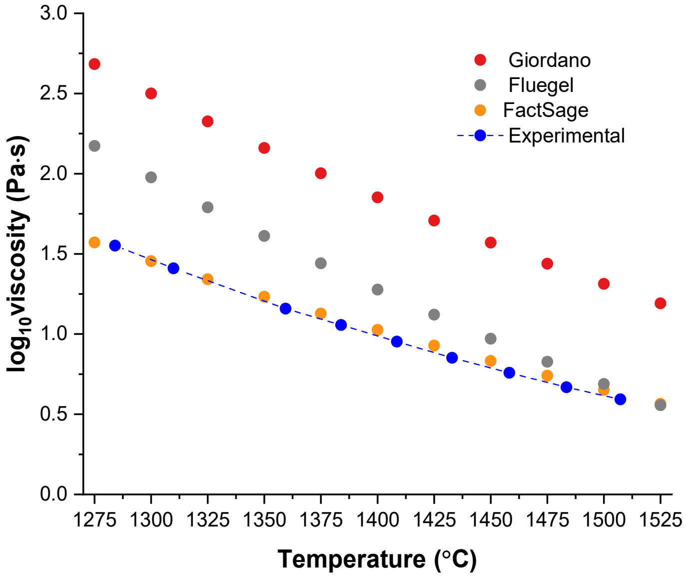

Figure 4.4. *Experimental viscosity (log$_{10}$visosity in Pa·s) plotted versus temperature for $C_{21}M_{9}A_{13}S_{57}$ glass. Viscosity values calculated by the FactSage, Fluegel, and Giordano et al. models are also given.*

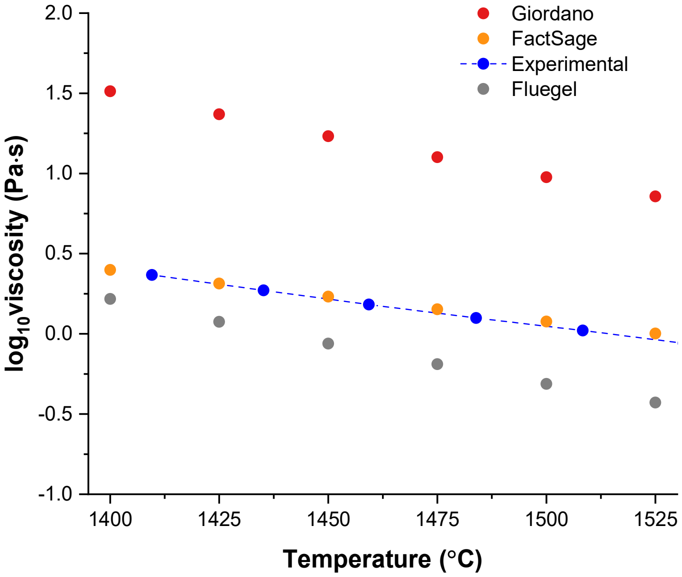

__Figure 4.5__. Experimental viscosity (log$_{10}$visosity in Pa·s) plotted versus temperature for CA$_{10}$S glass. Viscosity values calculated by the FactSage, Fluegel, and Giordano et al. models are also given.

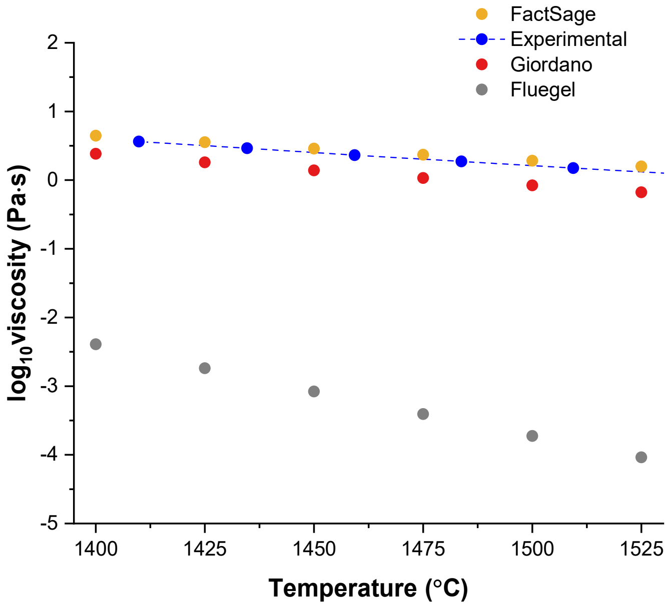

__Figure 4.6__. Experimental viscosity (log$_{10}$visosity in Pa·s) plotted versus temperature for CA$_{20}$S glass. Viscosity values calculated by the FactSage, Fluegel, and Giordano et al. models are also given.

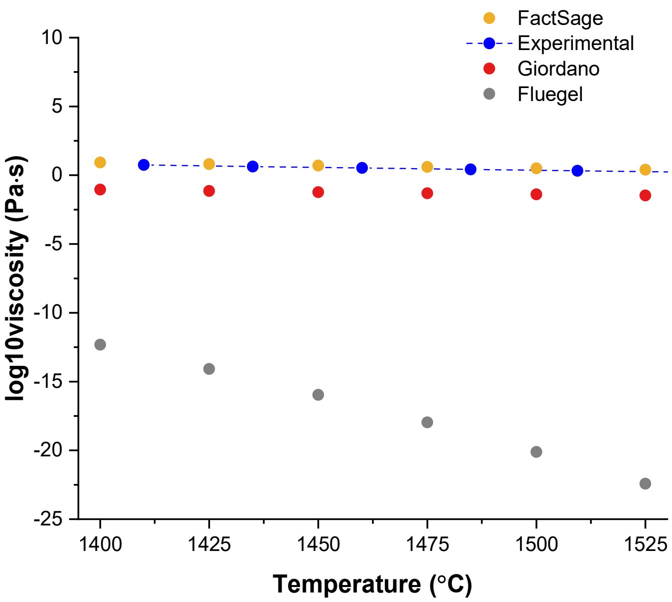

***Figure 4.7**. Experimental viscosity (log$_{10}$visosity in Pa·s) plotted versus temperature for CA$_{30}$S glass. Viscosity values calculated by the FactSage, Fluegel, and Giordano et al. models are also given.*

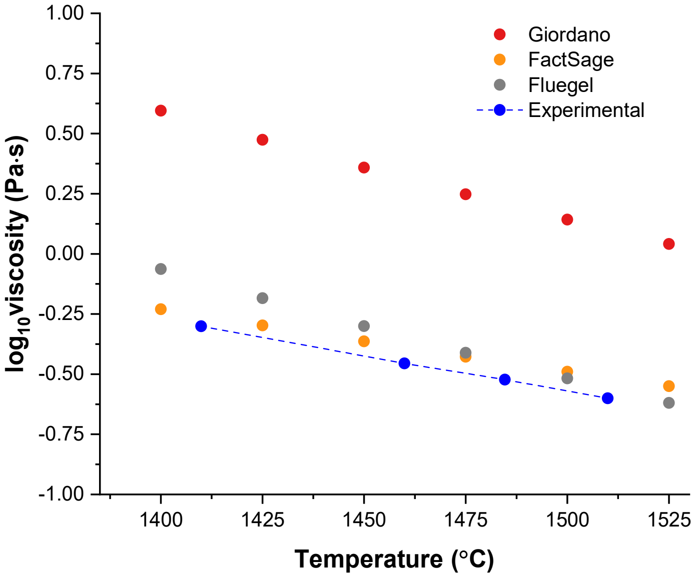

***Figure 4.8**. Experimental viscosity (log$_{10}$visosity in Pa·s) plotted versus temperature for CM$_{20}$S glass. Viscosity values calculated by the FactSage, Fluegel, and Giordano et al. models are also given.*

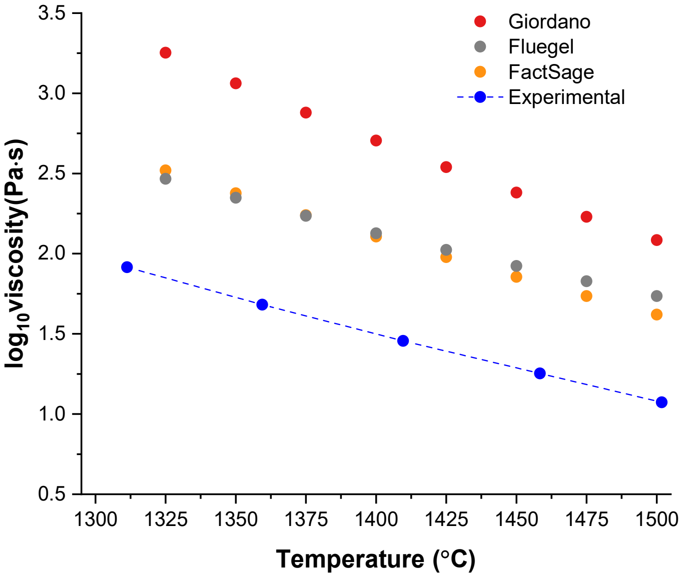

***Figure 4.9**. Experimental viscosity (log$_{10}$visosity in Pa·s) plotted versus temperature for Eyja volcanic ash glass. Viscosity values calculated by the FactSage, Fluegel, and Giordano et al. models are also given.*

***Table 4.3**. Differences in experimental and FactSage-calculated viscosity values (as a function of temperature) for the glass compositions under study.*

Composition	Temperature (°C)	FactSage viscosity (Pa·s)	Experimental viscosity (Pa·s)	$\lvert\Delta\rvert$ (Pa·s)	% Difference (Experimental – calculated)
$C_{33}M_9A_{13}S_{45}$	1408	1.317	1.446	0.129	8.92
	1384	1.577	1.797	0.220	12.24
	1359	1.914	2.224	0.310	13.94
	1333	2.358	2.850	0.492	17.26
	1309	2.878	3.630	0.752	20.72
	1284	3.567	4.749	1.182	24.90
	1258	4.496	6.434	1.938	30.12
	1225	6.109	8.749	2.640	30.17
$C_{21}M_9A_{13}S_{57}$	1507	4.233	3.912	0.321	-8.21
	1483	5.147	4.658	0.489	-10.50
	1458	6.349	5.733	0.616	-10.74
	1433	7.887	7.107	0.780	-10.98
	1409	9.779	8.974	0.805	-8.97
	1384	12.324	11.378	0.946	-8.31
	1359	15.655	14.394	1.261	-8.76
	1310	25.638	25.691	0.053	0.21
	1284	33.776	35.565	1.789	5.03
$C_{38.1}A_{9.9}S_{52}$	1531	0.965	0.874	0.091	-10.41
	1508	1.129	1.048	0.081	-7.73
	1484	1.335	1.254	0.081	-6.46
	1459	1.598	1.523	0.075	-4.92
	1435	1.910	1.866	0.044	-2.36
	1410	2.313	2.328	0.015	0.64
$C_{33.75}A_{20}S_{46.25}$	1533	1.486	1.243	0.243	-19.55
	1509	1.785	1.496	0.289	-19.32
	1484	2.174	1.875	0.299	-15.95
	1459	2.666	2.314	0.352	-15.21
	1435	3.264	2.910	0.354	-12.16
	1410	4.060	3.644	0.416	-11.42
$C_{29.5}A_{30}S_{40.5}$	1532	2.390	1.689	0.701	-41.50
	1509	2.919	2.103	0.816	-38.80
	1485	3.623	2.639	0.984	-37.29
	1460	4.577	3.347	1.230	-36.75
	1435	5.835	4.257	1.578	-37.07
	1410	7.510	5.564	1.946	-34.97
$C_{33.75}M_{20}S_{46.25}$	1510	0.306	0.251	0.055	-21.91
	1485	0.353	0.300	0.053	-17.67
	1460	0.408	0.350	0.058	-16.57
	1410	0.553	0.500	0.053	-10.60
Eyja volcanic ash glass	1502	40.812	11.833	28.979	-244.90
	1458	65.508	17.926	47.582	-265.44
	1410	113.507	28.608	84.899	-296.77
	1359	212.276	48.089	164.187	-341.42
	1311	399.720	82.277	317.443	-385.82

Figure 4.10 compares the experimentally obtained viscosity curves for all glasses under study. Of the compositions tested, $CM_{20}S$ had the lowest observed viscosity and the Eyja volcanic ash glass had the highest. The viscosity of $CA_{10}S$ with a Ca/Si ratio of 0.73 was slightly greater than that of $C_{33}M_9A_{13}S_{45}$

glass (Ca/Si ratio also equal to 0.73). Increasing the Al content resulted in an increase in viscosity. Decreasing the Ca/Si ratio to 0.37 (while maintaining constant Mg and Al contents – $C_{21}M_9A_{13}S_{57}$) resulted in an increase in viscosity (compared to $C_{33}M_9A_{13}S_{45}$) of nearly one order of magnitude. The viscosity of the Eyja glass, which has a Ca/Si ratio of 0.09, was even higher. The Eyja glass also has a lower Mg content (3.5 mol%) and higher Al content (16.7 mol%) than 21Ca-57Si CMAS, which could contribute to its overall higher viscosity.

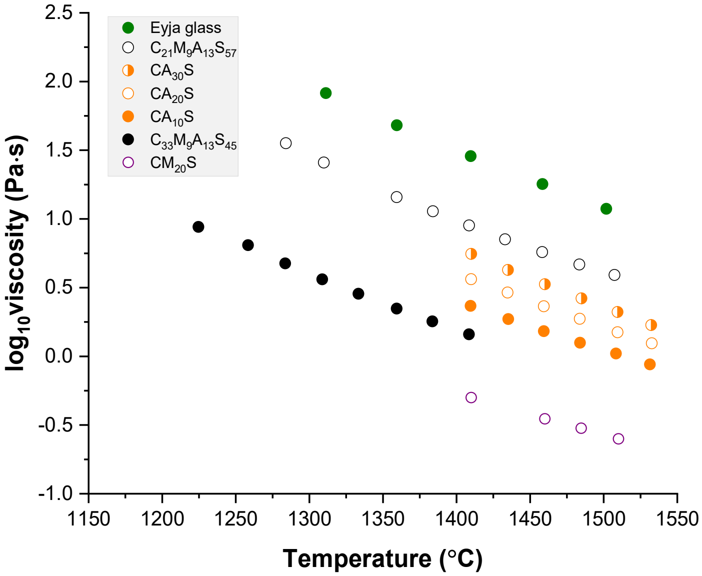

***Figure 4.10**. Experimental viscosity (log_{10}visosity in Pa·s) plotted versus temperature for all glass compositions tested.*

4.4. Discussion

i. Effect of Ca/Si ratio on viscosity and comparison to literature

Increasing the CMAS Ca/Si ratio (leaving Al and Mg contents constant) results in a decrease in glass viscosity (Figure 4.10, 4.13). CMAS with a Ca/Si ratio of 0.73 gave viscosity values nearly one order of magnitude lower than those for CMAS with a Ca/Si ratio of 0.37. The effect of CaO and SiO_2 content on CMAS glass viscosity has been reported previously for different compositions than those studied here. Kim et al. investigated the effect of Ca/Si ratio on CMAS glasses having a Ca/Si ratio of either 1.07 or 1.29, an Al content of ~20 mol%, and a Mg content between ~10-20 mol% [107]. They observed that viscosity was lower in glasses having a Ca/Si ratio of 1.29 compared to those with a Ca/Si ratio of 1.07 (with constant Al and Mg). However, as the amount of MgO in the glass increased, the difference in viscosity between the two ratios was dampened (Figure 4.11). This was attributed to synergistic depolymerization of the glass by CaO and MgO. As the combined CaO and MgO content increased, the individual components' (i.e. CaO's) effect on viscosity became limited. Yan et al. obtained experimental viscosities for CMAS glasses having Ca/Si ratios between 1.15 and 1.60 with constant ~11 mol% Mg, ~13 mol% Al, and ~4 mol% Ti [108]. The authors determined that viscosity decreased as the Ca/Si ratio was increased, but only below a Ca/Si ratio of 1.45 (by mol; 1.35 by mass, Figure 4.12). Above 1.45, very little change in viscosity was observed at constant temperature (Figure 4.12). Initial increases in CaO content resulted in significant depolymerization of the melt; upon reaching the critical Ca/Si ratio, further additions of CaO had a limited effect on glass viscosity, as the glass network had already been highly disrupted.

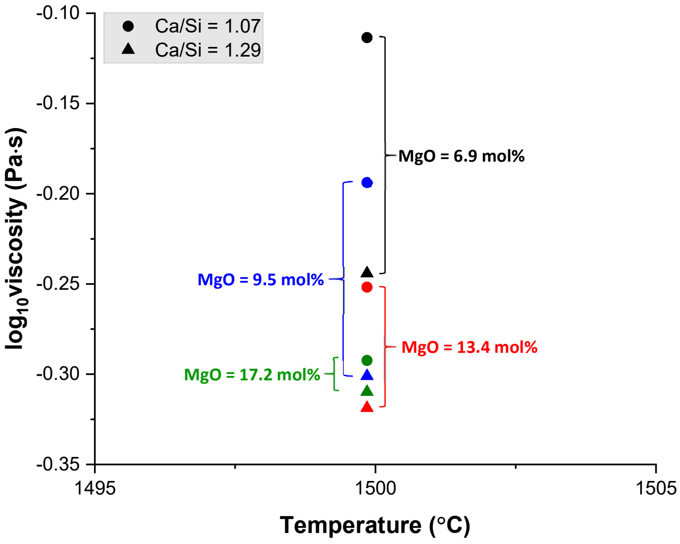

***Figure 4.11**. Viscosity (log$_{10}$visosity in Pa·s) at ~1500°C for CMAS compositions having a Ca/Si ratio of either 1.07 or 1.29, constant Al, and MgO between 6.9-17.2 mol%. The difference in viscosity based on Ca/Si ratio decreases with increasing MgO content. Data obtained from [107].*

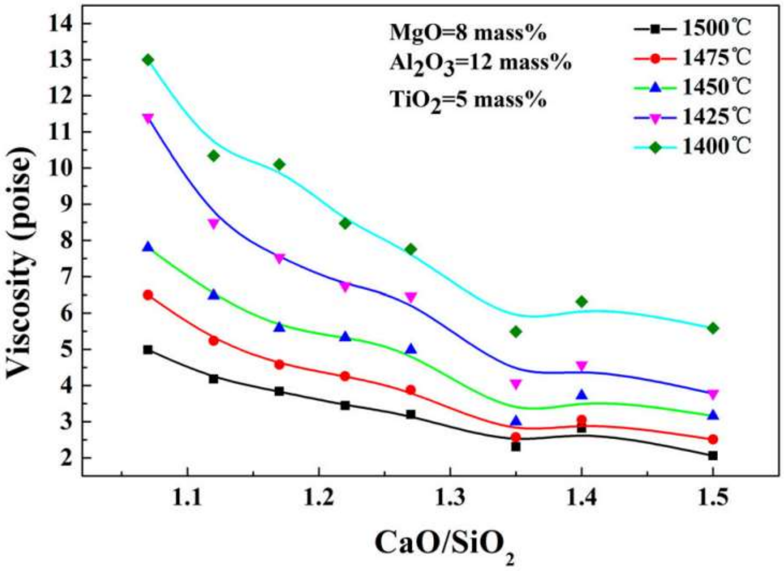

***Figure 4.12**. Viscosity plotted as a function of CaO/SiO$_2$ ratio. No significant changes in viscosity are discerned above a ratio of 1.35 (by mass, 1.45 by mol). From [108].*

The effect of Ca/Si ratio has also been studied in binary CaO-SiO$_2$ glasses. Both Bockris and Lowe [109] and Urbain et al. [110] observed that viscosity decreased with increasing Ca/Si, despite some variations in reported values (i.e. viscosity data from Urbain et al. for a binary glass having a Ca/Si ratio = 0.6 is greater than that for a binary glass with a Ca/Si ratio = 0.44 reported by Bockris and Lowe; Figure 4.13). The viscosities of the CMAS melts studied here are also given in Figure 4.14 for comparison to binary compositions. Viscosity data for binary compositions with Ca/Si ratios of 0.37 and 0.73 were not obtained in this report due to experimental difficulties. The viscometer apparatus was only able to reach a maximum temperature of 1600°C. A binary $CaO-SiO_2$ glass having a Ca/Si ratio of 0.37 requires a temperature of ~1700°C to reach above its liquidus (Figure 4.14). A binary $CaO-SiO_2$ glass having a Ca/Si ratio of 0.73 only requires a temperature of ~1475°C (Figure 4.14), however the glass' inherently low viscosity led to issues with data collection. Attempts at obtaining viscosity in this system resulted in the spindle contacting the bottom of the crucible, which pulled the crucible up and tilted it. This led to spilling of the glass inside the furnace.

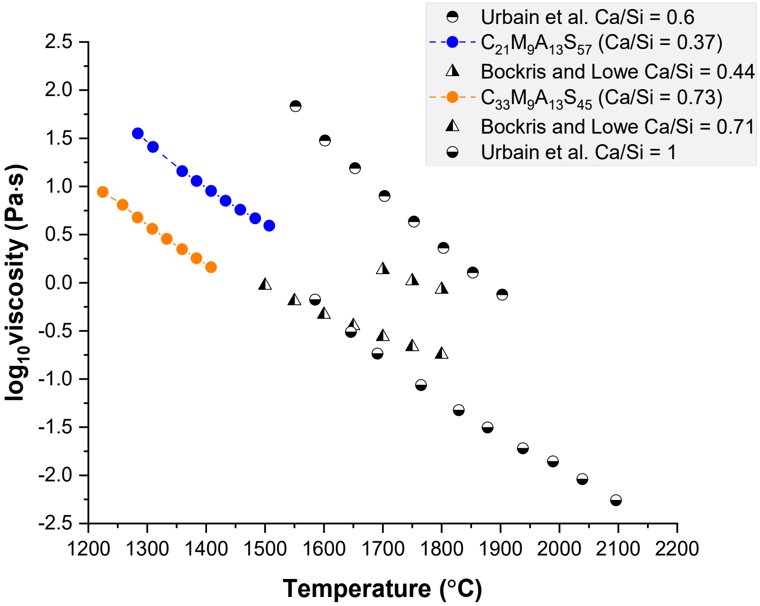

***Figure 4.13**. Viscosity ($\log_{10}$visosity in Pa·s) data for binary $CaO-SiO_2$ compositions studied by [109] and [110]. Viscosity data for the CMAS compositions studied in this report are also provided.*

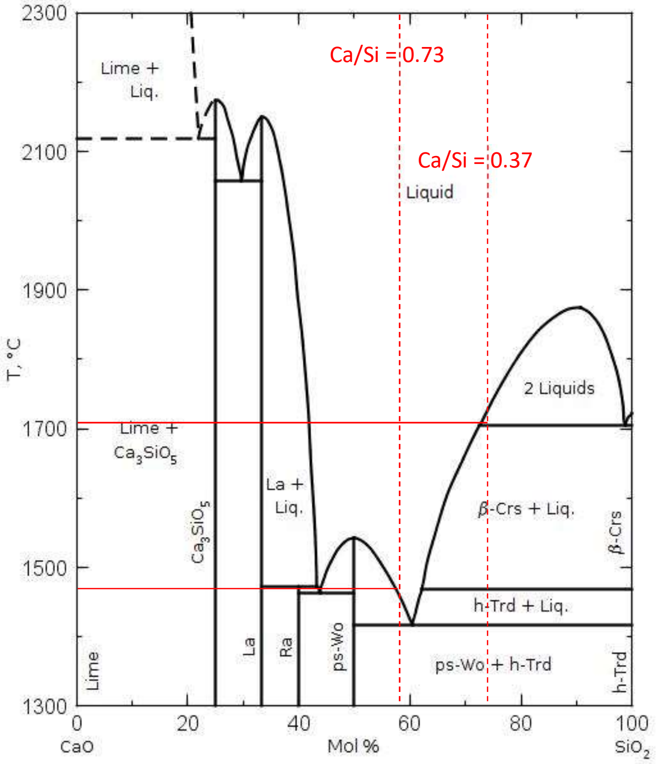

***Figure 4.14**. CaO-SiO_2 binary phase diagram. Lines indicating compositions with Ca/Si ratios of 0.73 and 0.37 are given, along with their expected melting temperatures. From [72].*

The observed viscosity behavior as a function of CaO and SiO_2 content is consistent with the theoretical underpinnings of glass network theory [111]. Glasses have the same atomistic building blocks (cation polyhedral) as their crystalline counterparts, however they lack long range order. Some materials are better able to form glasses than others. Zachariasen noted from empirical observations on oxides that four general rules apply for predicting glass formation: 1) no oxygen atom may be linked to more than two cations, 2) the cation coordination number must be small (3 or 4), 3) oxygen polyhedra must share corners (not edges or faces), and 4) for 3D networks, at least three corners must be shared [112]. If all 4 rules are satisfied, a compound is considered a good glass (or network) former. Silica is known as a good network former, while CaO (and other alkali or alkaline earth oxides) is considered a network modifier. In tetrahedral systems (such as that for a SiO_2-based glass), modifiers disrupt the network former (SiO_2) structure and replace bridging oxygens (BO) by nonbridging oxygen (NBO; Figure 4.15).

Disruption of the glass network lowers glass connectivity/bond strength and leads to a decrease in viscosity.

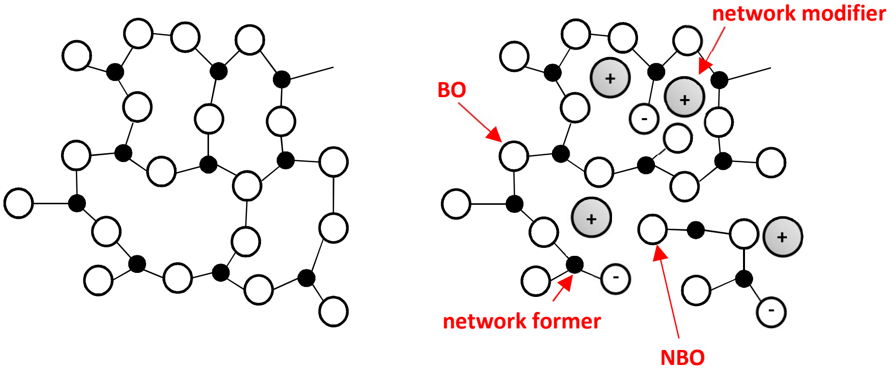

***Figure 4.15**. SiO_2 glass network (left) and network after disruption by modifiers (right).*

ii. Effect of Al content on viscosity and comparison to literature

Al_2O_3 can act as either a network former or a network modifier [113, 114]. A simplified explanation for the amphoteric behavior of Al_2O_3 is described. In silicate melts containing Al_2O_3 and an alkali or alkaline earth network modifier (such as CaO), alumina behaves as a network former when the molar ratio $n\mathrm{Al}/\mathrm{M}^{n+}$ (M being the alkali or alkaline earth cation; *n* being the charge on M and the corresponding multiplier for mol of Al, i.e. $2\mathrm{Al}/\mathrm{Ca}^{2+}$ or $1\mathrm{Al}/\mathrm{Na}^{1+}$) is less than unity. Al-O coordination is tetrahedral (with units of AlO_4), as seen for SiO_2, in these cases. The charge on $[AlO_4]^{5-}$ units is different from that on $[SiO_4]^{4-}$. This means that cations are needed to provide charge balance within the glass. With an $n\mathrm{Al}/\mathrm{M}^{n+}$ ratio ≤ 1, the modifier cations provide charge balance to AlO_4 tetrahedra instead of breaking up the glass network to produce NBO. Above a ratio of 1, Al-O is octahedrally coordinated and modifier cations can alter the glass network as described previously.

In this study, viscosity increased in CAS melts with Al_2O_3 content (Figure 4.10). The $2\mathrm{Al}/\mathrm{Ca}^{2+}$ ratio for all compositions investigated was less than unity, indicating that Al_2O_3 acts as a network former in these glasses. The viscosity of CAS having a Ca/Si ratio of 0.73 and an Al content of 10 mol% was greater than that of $C_{33}M_9Al_{13}S_{45}$. This suggests that the presence of MgO has a depressing effect on glass viscosity, keeping all other components the same. The effect of Al_2O_3 additions on CaO-SiO_2 melt viscosity has been studied previously, keeping Ca/Si ratio constant. Glasses having Ca/Si ratios of either 0.6 or 1 were studied both with and without additions of ~20-25 mol% Al_2O_3 by Urbain et al. For both Ca/Si ratios, the inclusion of Al_2O_3 in the glass network increased melt viscosity (Figure 4.16), as was expected due to *2*Al/Ca^{2+} values being less than unity.

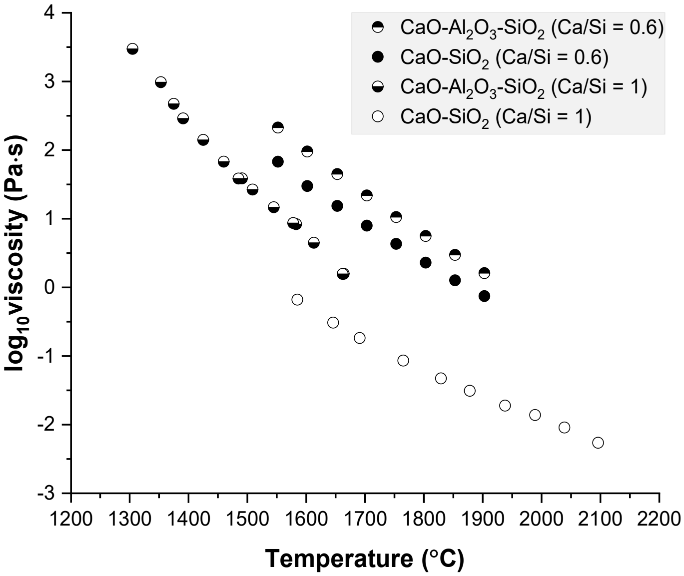

***Figure 4.16**. Viscosity ($\log_{10}$visosity in Pa·s) as a function of Ca/Si ratio and presence/absence of Al_2O_3. Data from [110].*

iii. Effect of Mg content on viscosity and comparison to literature

Magnesia (MgO), like CaO, is a glass modifier. Thus, it is expected that increasing MgO content will decrease glass viscosity. Indeed, this behavior was observed in the current study. CMS viscosity decreased with increasing MgO content, keeping Ca/Si constant (Figure 4.10). Increased viscosity in CMAS compared to CMS demonstrates the ability of Al_2O_3 to increase viscosity, as discussed previously, when all other components are the same.

The influence of MgO on glass viscosity has been studied before in other CMAS-type melts. Both Saito et al. and Kim et al. varied MgO content in CMAS glasses of constant Ca/Si and Al [107, 115]. The Ca/Si was reported as either 1.07 [107, 115] or 1.29 [107]. The Al content was kept constant (~20 mol%) and Mg varied between ~10-20 [107] and ~0-30 [115] mol%. Viscosity data for these studies are provided in Figure 4.17. A marked decrease in glass viscosity was observed with increasing MgO content, despite some variation in reported values.

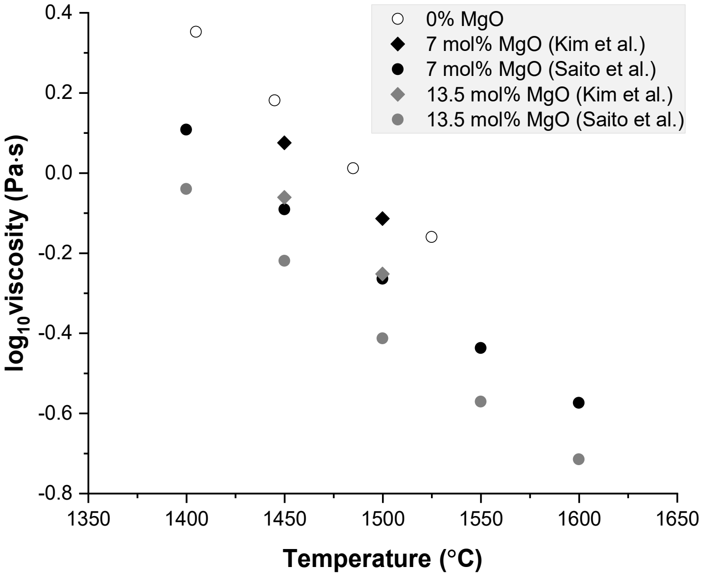

Figure 4.17*. Viscosity ($\log_{10}$visosity in Pa·s) as a function of MgO content and temperature. Data from [107] and [115].*

iv. Model validation

Of the three viscosity models considered (FactSage [27], Fluegel [28], and Giordano et al. [26]), the FactSage model was unequivocally the best at describing experimental viscosity data in model materials (Figures 4.3-4.8). The FactSage viscosity module correlates viscosity to melt structure through thermodynamic properties determined by the Modified Quasichemical Model [27]. In contrast, the

Fluegel and Giordano et al. models are both empirical in nature. They are derived based on the Vogel-Fulcher-Tammann (VFT) equation [116-118]:

$$\log \eta = A + \frac{B}{T-C} \tag{4.2}$$

where A, B, and C are adjustable parameters and T is the temperature (in °C or K for the Fluegel and Giordano et al. models, respectively). The Giordano et al. model connects the VFT constants to an empirical dataset containing temperature and viscosity values for multicomponent (up to 12 oxides) silicate melts encompassing many common volcanic rocks. The Fluegel model predicts VFT constants similarly to the Giordano et al. model, however is based on a global statistical approach combined with experimental viscosity data for commercial silicate glasses containing up to 54 oxides.

The only experimental evidence to validate these models for CMAS, to date, has been reported on by Wiesner et al. [29]. The authors determined that the FactSage and Fluegel models were better able to describe the viscosity of a glass containing 23.3CaO-6.4MgO-3.1Al_2O_3-62.5SiO_2-4.1Na_2O-0.5K_2O-0.04Fe_2O_3 (mol.%) than the Giordano et al. model, which overestimated viscosity by about one order of magnitude (Figure 4.18).

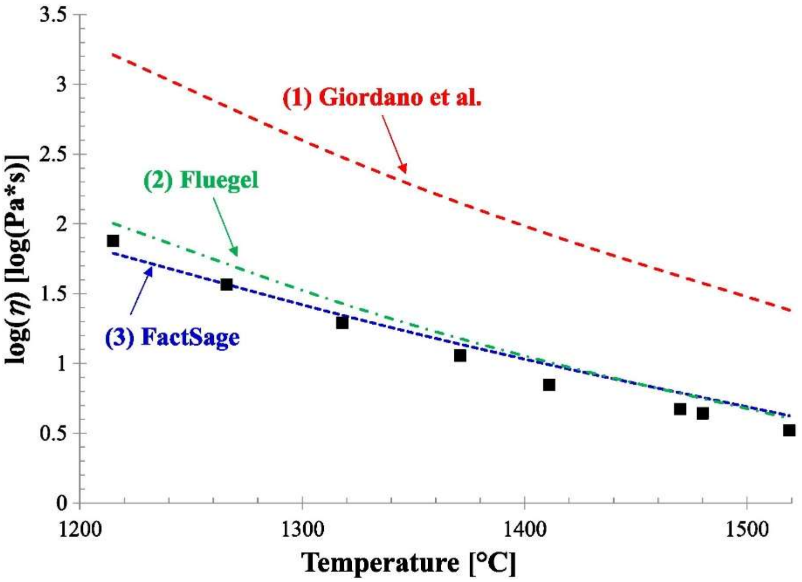

Figure 4.18. *Experimental viscosity (log_{10}visosity in Pa·s) of a synthetic sand CMAS plotted as a function of temperature for comparison to viscosity models by FactSage, Fluegel, and Giordano et al. From [29].*

No consistent trends in the Fluegel or Giordano et al. viscosity models were confirmed in the current study. In general, the Giordano et al. model appeared to overestimate viscosity for most compositions (Figures 4.4, 4.5, 4.8). This model was better able to predict viscosity in $C_{33}M_9A_{13}S_{45}$ and higher Al-containing CAS melts (Figures 4.3, 4.6, and 4.7). In most cases, the Fluegel model underestimated viscosity (Figures 4.3, 4.5, 4.6, and 4.7). It gave a reasonable approximation of viscosity in $C_{21}M_9A_{13}S_{57}$ and $CM_{20}S$ glasses (Figures 4.4 and 4.8). Based on these results and those of Wiesner et al. [29], the Fluegel model may be better suited for low Ca/Si containing melts.

In addition to the FactSage, Fluegel, and Giordano et al. models, there are a host of other viscosity calculators that have been proposed to predict viscosity in CMAS-type glasses. These models are summarized by Han et al. [30] and include both structure-based (such as the FactSage model) and empirical (such as the Fluegel and Giordano et al. models) calculations. Models described by Han et al. include those (in addition to the FactSage and Giordano et al. models) by Bottinga and Weill [119], Gupta et al. [120], Neutral Network [121], Urbain [122], Riboud et al. [123], Iida et al. [124], Mills and

Sridhar [125], Shankar [126], Hu et al. [127], Gan and Lai [128], Tang et al. [129], Suzuki and Jak [130], Shu [131], and Zhang and Chou [132]. Han et al. simplified the empirically-derived Urbain model to accurately predict viscosity in CMAS-related melts. However, the error in their model was between 13.5 and 29.5%, which is greater than or on the order of that reported by FactSage for model glasses (Table 4.3). While the models described above were not used to validate the viscosity data obtained in this report, it is relevant to consider them in addition to those typically reported in the CMAS literature (FactSage, Fluegel, and Giordano et al.).

v. Water incorporation into glass structure and its potential influence on viscosity

As was mentioned in the Results section of this chapter, the Eyja volcanic ash glass was the only CMAS composition not well described by the FactSage viscosity model. While FactSage and Fluegel model predictions more closely match experimental data for the volcanic ash glass than the Giordano et al. model (Figure 4.9), they are still higher by about half an order of magnitude. Preliminary Fourier transform infrared spectroscopy (FTIR) measurements on the volcanic ash glass suggest that H_2O was incorporated into its structure (Figure 4.19). Hydroxide bonding was also evident in model $C_{33}M_9A_{13}S_{45}$ glass, but not to the same degree (Figure 4.19).

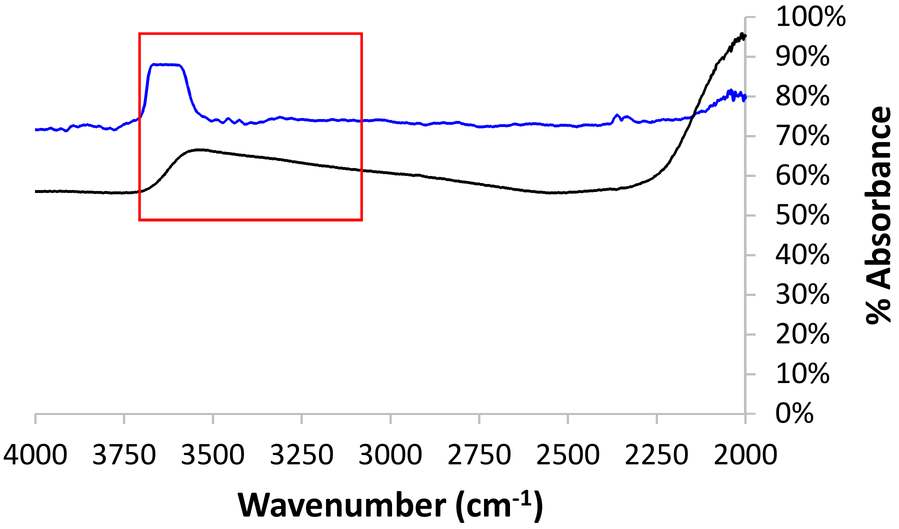

Figure 4.19*. Eyja (blue line) and $C_{33}M_9A_{13}S_{45}$ (black line) glass FTIR absorption spectra upon exposure to white light. The water OH stretch region is outlined in red.*

Water incorporation in model materials is likely a result of glass preparation/quenching in water, while water in the Eyja glass is probably due to the chemical/pressure environment present during volcanic eruption. The bonding of H_2O in these glasses is not fully understood and needs to be explored in future work. The presence of water in glass can significantly lower glass viscosity [133], which is a possible explanation for the lower measured viscosity values in the Eyja glass. Of the viscosity models probed in this study, only the Giordano et al. model allows for H_2O content to be considered. This is a major pitfall for the FactSage model, as it is important to consider the effect of glass bonding with water when modelling CMAS viscosity, especially when considering an actual engine environment wherein high water vapor partial pressures are expected. In theory, the amount of H_2O in the volcanic ash glass could be determined by varying H_2O content in the Giordano et al. model until the calculated viscosity curve matches that of the experimental. However, because the Giordano et al. model did not accurately describe the model materials investigated, this was not attempted for the Eyja glass. It is also possible that none of the models investigated are adequate to describe viscosity for this particular composition. While the Eyja volcanic ash glass is more chemically complex than any of the model materials tested, it seems unlikely that the FactSage model would not be suited to describe its viscosity based on the other compositions investigated and the model's ability to incorporate glass components including Fe_2O_3, Na_2O, and K_2O. Viscosity models that incorporate H_2O in the glass composition should be considered in future studies. Additionally, the exact nature of glass bonding with water needs to be elucidated for CMAS compositions exposed to water vapor-containing environments.

vi. Viscosity and EBC infiltration

The viscosity (η) of CMAS deposits is expected to contribute to infiltration kinetics in T/EBCs. Wiesner et al. [94] used the following relation [35, 134] to estimate the time (t) for CMAS glass to penetrate a 200 µm thick TBC completely:

$$t \sim \left[\frac{k_t}{8D_C}\left(\frac{1-\omega}{\omega}\right)^2 h^2\right]\frac{\eta}{\sigma_{LV}} \qquad [4.3]$$

where k_t (~3, between 1-10) is the tortuosity, D_C (1 µm) is the capillary diameter, ω (~0.1) is the pore fraction open to flow, σ_{LV} (~0.4 J/m^2) is the surface tension of the melt [135], and h is the infiltration depth (200 µm). This relation assumes that there is no reaction between CMAS and the coating and that CMAS does not intrinsically crystallize. The authors reported times based on several η values estimated by models including those described earlier for a single CMAS composition of $23.3CaO$-$6.4MgO$-$3.1Al_2O_3$-$62.5SiO_2$-$4.1Na_2O$-$0.5K_2O$-$0.04Fe_2O_3$ (mol %). At 1300°C, complete infiltration was estimated at 4.3 or 15 min using the FactSage and Giordano models, respectively.

Equation 4.3 was used in conjunction with experimental viscosity data to estimate TBC infiltration times based on model glasses of composition $C_{33}M_9A_{13}S_{45}$/$C_{21}M_9A_{13}S_{57}$ or the Eyja glass. Results are presented in Table 4.4.

***Table 4.4**. Predicted time to infiltration (of a 200 μm thick coating) by $C_{33}M_9A_{13}S_{45}$, $C_{21}M_9A_{13}S_{57}$, and Eyja glasses. Determined using Equation 4.3 and parameter values described by Wiesner et al. [94].*

	Temperature (°C)	η (Pa·s)	t (sec)
$C_{33}M_9A_{13}S_{45}$	1308.8	3.6	10.1
$C_{21}M_9A_{13}S_{57}$	1309.9	25.7	80.3
Eyja glass	1311	82.3	283.8

Assuming the same parameters used by Wiesner et al., a 200 μm thick TBC would be infiltrated in tens to hundreds of seconds. Coating lifetimes are expected on the order of tens of thousands of hours.

The model for TBC infiltration (Equation 4.3) has not been validated experimentally. The derivation of this expression is unknown. It cannot be validated using the results of this study either, as several parameters (k_t, D_C, ω) are likely different in model materials but remain unknown. Bounding values for each parameter were used to estimate their effect on infiltration time, and to determine whether viscosity was a controlling factor in Equation 4.3. These calculations can be found in Table 4.5. The infiltration length (h) was assumed to be 200 μm and σ_{LV} to be 0.4 J/m^2. Infiltration times based on actual σ values calculated from [135] are also compared in Table 4.5.

***Table 4.5**. Calculated infiltration times based on bounding parameters for k_t, D_C, ω, and η.*

	k_t	D_C (μm)	ω	η (Pa·s)	σ_{LV}	time (s)
1	1	1	0.1	3.6	0.4	3.6
2	10	1	0.1	3.6	0.4	36.4
3	10	5	0.1	3.6	0.4	7.3
4	10	5	0.5	3.6	0.4	0.09
5	10	1	0.1	3.6	0.432	33.8
6	1	1	0.1	25.7	0.4	26.0
7	10	1	0.1	25.7	0.4	260.2
8	10	5	0.1	25.7	0.4	52.0
9	10	5	0.5	25.7	0.4	0.64
10	10	1	0.1	25.7	0.389	267.6
11	1	1	0.1	82.3	0.4	83.3
12	10	1	0.1	82.3	0.4	833.3
13	10	5	0.1	82.3	0.4	166.7
14	10	5	0.5	82.3	0.4	2.1
15	10	1	0.1	82.3	0.352	946.9

A change in the tortuosity (k_t) from 1 to 10, keeping all other parameters constant, results in a 10x increase in infiltration time. Changing the capillarity diameter (D_C) from 1 to 5 µm results in a decrease in infiltration time by about 5x, thus showing that k_t and D_C have similar effects on infiltration. When the pore fraction open to flow (ω) is increased from 0.1 to 0.5, there is a ~80x decrease in infiltration time. Finally, a difference in viscosity of ~80 Pa·s ($C_{33}M_9A_{13}S_{45}$ vs. Eyja glass; about one and a half orders of magnitude on the log scale) results in a ~23x change in infiltration time. Calculated σ values were not drastically different from the assumed 0.4 J/m^2. The largest difference was for the Eyja glass (Δ=-0.048 J/m^2). There was a ~1.14x increase in infiltration time associated with this difference. These results indicate that, with respect to coating parameters (k_t, D_C, ω), ω, the fraction of open pores in the coating, is the most important parameter to consider in Equation 4.3. With respect to glass properties (η vs. σ), viscosity is the most important parameter to consider in Equation 4.3.

However, Equation 4.3 assumes no reaction between coating and CMAS. The results of Chapters 2 and 3 on model materials prove otherwise. Specifically, YbMS is known to react with both $C_{33}M_9A_{13}S_{45}$ and $C_{21}M_9A_{13}S_{57}$ to form crystalline phases (apatite and YbDS, respectively). Infiltration of YbMS is only about 100-150 µm after 96 h at 1300°C (Chapter 2), while Table 4.4 predicts that 200 µm of coating will be infiltrated in 0-1 min (assuming the parameters used by Wiesner et al. [94] are applicable). Even when the parameters in Equation 4.3 are changed so that infiltration time is increased (i.e. $k_t = 10$, $D_C = 0.1$, and $\omega = 0.01$), complete infiltration of a 200 µm coating is predicted within 11-12 hours. Clearly, coating/glass reaction and crystallization are important characteristics to consider.

On the other hand, reaction between YbDS and CMAS to form new crystalline phases is minimal. However, infiltration measurements indicate that less than 200 µm of coating is penetrated by 1 h (Chapter 2), further invalidating the model predictions found in Table 4.4. In this case, since there is little to no reaction between coating and glass, the model parameters should be evaluated, as EBC and TBC microstructures are quite different.

Other models that describe infiltration of porous structures (based on diffusion – $h^2 \alpha t$), have been proposed. The early-established Washburn equation (Equation 4.4) relates h to r_{eff} (pore radius), ΔP ($\Delta P = P_0 - P_C$, where P_0 is the atmospheric pressure and P_C is the capillary pressure), η, and t [136, 137]:

$$h^2 = r_{eff}^2 \frac{\Delta P}{4\eta} t \qquad [4.4]$$

For wetting liquids, pressureless infiltration is possible. Taking $P_0=0$ and $P_C=-(2\sigma_{LV}/r_{eff})\cos\theta$, Equation 4.4 becomes:

$$h^2 = r_{eff} \frac{\sigma_{LV} \cos\theta}{2\eta} t \qquad [4.5]$$

and rearranging:

$$t = \frac{h^2}{r_{eff}} \left(\frac{2\eta}{\sigma_{LV} \cos\theta} \right) \qquad [4.6]$$

Input parameters for the Washburn model are similar to those found in Equation 4.3, but include wetting angle (θ). Assuming complete wetting (θ=0°), this value goes to unity. Tortuosity and pore fraction open to flow are not involved. This model, like that described in Equation 4.3, does not take into account the formation of reaction products and is therefore also unlikely to serve as an accurate depiction of reactive infiltration in EBCs.

Reitz et al. [138] looked at the reactive infiltration of porous graphite with Si-based melts to form SiC. The authors determined that infiltration was controlled by the rate of formation of SiC. Infiltration rates were much slower than predicted based on the assumption that viscous drag is rate limiting:

$$\frac{dh}{dt} = \frac{D_C^2}{32\eta h} \left(\frac{4\sigma_{LV} \cos\theta}{D_C} - \rho g h \right) \qquad [4.7]$$

where ρ is the density of the liquid and g is the gravitational constant. The terminal infiltration depths measured in the graphite (having pores on the order of ~1 µm) were controlled by "reaction choking." Reaction choking refers to blocking of pores by reaction products. The authors observed that choking occurred within seconds.

Reactive infiltration has been described by Messner and Chiang [139]. The authors modeled this phenomenon by integrating the following equation [140]:

$$\frac{dh}{dt}\left(\frac{cm}{s}\right) = -\frac{K\Delta P}{\eta h} \qquad [4.8]$$

where K is the permeability which can vary with time and distance. Assuming that K only varies with time, and that the pore geometry is unchanged during reactive infiltration, K(t) is determined by the time rate of change of the controlling pore radius, r(t):

$$\frac{K(t)}{P_i} = \frac{1}{8r_0^2}r(t)^4 = \beta r(t)^4 \qquad [4.9]$$

where P_i is the initial porosity and r_0 is the initial pore radius. Equation 4.8 can thus be written as:

$$\frac{hdh}{P_i} = -\frac{K\Delta P}{P_i\eta}dt = -\frac{\beta\Delta P}{\eta}r(t)^4dt \qquad [4.10]$$

Pores of radius r that shrink with either linear or parabolic time dependence due to reaction product formation can be written as:

$$r(t) = r_0 - kt\ (linear) \qquad [4.11]$$

$$r(t) = r_0 - k't^{\frac{1}{2}}\ (parabolic) \qquad [4.12]$$

where k and k' are the linear and parabolic reaction rate constants, respectively. Integrating Equation 4.10 and considering pore radii described by either Equation 4.11 or 4.12, infiltration can be modeled as:

$$h^2(t) = \frac{2\beta\Delta P}{\eta}\left(r_0^4t - 2r_0^3kt^2 + 2r_0^2k^2t^3 - r_0k^3t^4 + \frac{k^4t^5}{5}\right) \qquad [4.13]$$

or:

$$h^2(t) = \frac{2\beta\Delta P}{\eta}\left(r_0^4t - \left(\frac{8r_0^3k't^{3/2}}{3}\right) + 3r_0^2k'^2t^2 - \left(\frac{8r_0k'^3t^{5/2}}{5}\right) + \frac{k'^4t^3}{3}\right) \qquad [4.14]$$

For the case of YbMS in contact with CMAS, Equation 4.13 would be used due to linear reaction kinetics (Figure 2.44). In order to apply Equation 4.13 to the YbMS/CMAS system, the pore radius, r_0, must be known. Experimental values for the pore volume fraction (V) and surface area (S) may be used to determine an effective pore radius (V/S=r/2 for cylindrical pores). Mercury porosimetry can also be used to determine pore radius. The parameters ΔP (P_0-P_C) and β are needed in addition to r_0. From the Washburn equation, described previously, it can be assumed that P_0=0 and P_C=-($2\sigma_{LV}/r_{eff}$)cosθ. The parameter β, for the simplest case of straight parallel capillaries of identical radii, can be taken as $1/8r_0^2$, as assumed by Messner and Chiang. Assuming complete wetting (θ=0) and an r_0 value of 0.1 µm, Equation 4.15 was used to estimate the ultimate infiltration length (h_f) at which reaction choking occurs in YbMS exposed to 33Ca-45Si CMAS at 1300°C:

$$h_f = \left(\frac{2\beta\Delta P r_0^5}{5\eta k}\right)^{1/2} \tag{4.15}$$

which was found to be ~700 µm (using parameter values given in Table 4.6).

***Table 4.6**. Parameters used to calculate h_f (Equation 4.15).*

β ($1/m^2$)	**σ_{LV} (kg/s^2)**	**ΔP ($2\sigma_{LV}/r_0$)**	**r_0 (m)**	**η (kg/m·s)**	**k (m/s)**
1.25E+13	0.432	8640000	0.0000001	3.6	2.39E-10

This value appears to greatly overestimate, as experimental observations suggest that apatite is forming after 50 µm of the coating has been infiltrated. Taking all of this into consideration, it can be concluded that measurements to determine r_0, β, and θ are required in future studies to successfully apply Equation 4.15 to reactive infiltration in YbMS.

Additional factors such as tortuosity (k_t) and pore fraction open to flow (ω) will also need to be considered in future models (related to pore geometry β). The infiltration model described in Equation 4.3 determined that ω has the strongest influence on infiltration. Pore radius is also important based on Equation 4.15. Viscosity and reaction rate are of secondary importance. The influence of wetting on infiltration is likely minimal.

4.5. Summary and conclusions

Experimental viscosities were obtained for several CMAS compositions. The effect of Ca/Si ratio and Al_2O_3/MgO content on glass viscosity were considered. A volcanic ash glass obtained from the field was also studied to compare to model materials. Viscosity decreased with increasing Ca/Si ratio and

MgO content, since Ca^{2+} and Mg^{2+} are known to behave as glass network modifiers. Al_2O_3, in a similar fashion to SiO_2, acted as a network former, and viscosity was increased with increasing Al content. The validity of three commonly used viscosity models was ascertained. The FactSage model gave more accurate data for CMAS melts than the Fluegel or Giordano et al. models. However, the volcanic ash glass was not well described by any of the models examined. This could be due to the presence of water in the glass structure. Future models should consider the effect of water content on glass bonding since CMAS will be subjected to a water vapor-containing combustion environment in an actual engine. The effect of glass viscosity on infiltration was considered for YbDS/YbMS materials previously studied. It was determined that the current infiltration model for TBCs cannot be used to predict infiltration in model (EBC) materials. The TBC infiltration model gave infiltration times that were much too fast to describe actual penetration rates observed in YbMS. This is likely due to reaction between YbMS and CMAS to form reaction products that block further glass ingress. Other discrepancies in the model arise from unknown input parameters. These parameters were varied to assess their influence on infiltration. In terms of coating parameters, pore fraction open to flow (ω) had the strongest effect. Keeping this (and all other) parameter (s) constant, an increase in viscosity by 1.5 orders of magnitude resulted in a 23x increase in infiltration time. CMAS viscosity is the most important glass-related parameter necessary to describe infiltration and is composition dependent. An existing reactive infiltration model was also unsuccessful in predicting infiltration time in YbMS. It is uncertain whether lack of agreement between experimental results and this model is due to inadequacy of the model or uncertainty in coating parameters.

4.6. Recommendations for future work

The presence of water in glass can have a significant effect on its viscosity. The nature of H_2O bonding in the Eyja glass and model materials needs to be determined. Controlled amounts of H_2O could be added to glass compositions for viscosity and bonding (FTIR/Raman spectroscopy) measurements.

Additionally, the effect of TiO_2 and Fe_2O_3 on glass viscosity should be explored, as these components are typical in actual CMAS compositions. Finally, input parameters for the TBC and reactive melt infiltration models should be assessed for application to EBC infiltration. The influence of coating/glass reactivity and crystallization should be considered. Further development of reactive infiltration models is clearly needed.

Conclusion

The overall objective of this work was to elucidate an optimum strategy for mitigating CMAS degradation in EBCs. Novel coating materials, RE titanates, state-of the art coating materials, RE silicates, and apatite, a common reaction product between RE coating materials and CMAS, were exposed to CMAS at 1300°C to assess their ability to resist glass infiltration. Their behavior was related to previously proposed, and conflicting, mitigation strategies. Model APS materials, composed of YbDS/YbMS were prepared to further investigate the role of coating reactivity on CMAS degradation. Experimental viscosities for several CMAS-related glasses were obtained for comparison to commonly cited viscosity models from the literature. The influence of viscosity on EBC infiltration was assessed.

It was determined that the most effective route for mitigation of CMAS attack in EBCs requires rapid reaction between coating and glass to form a dense layer of crystallized phases that are stable in contact with CMAS. APS-deposited EBCs will contain defects such as grain boundaries and pores that are vulnerable to infiltration. Inducing crystallization at the coating/glass interface reduces the ability for CMAS to penetrate defects and leads to slower infiltration. YbMS was found to be the most promising EBC material, as it quickly reacted with CMAS to form protective phases, such as apatite. Infiltration in YbMS was considerably slower than in other coating materials investigated, such as YbDS.

An actual coating system will likely require the presence of both YbDS and YbMS to manage varying thermochemical and thermomechanical challenges. CMAS infiltration in model APS materials containing both species was investigated. Adding ≥ 20 wt% YbMS to YbDS drastically improves overall material resistance to CMAS infiltration, as compared to phase pure YbDS. The distribution of YbMS within YbDS strongly affected CMAS interaction behavior. Model APS coatings exhibited a combination of grain boundary attack (in the YbDS matrix) and crystallization of YbMS granules (most notably to form apatite). Fine dispersion samples were not penetrated as deeply as model APS materials. Instead, CMAS deposits spread on their surfaces.

Experimental viscosity data established that the FactSage viscosity model, compared to those by Fluegel and Giordano et al., was best able to predict actual glass viscosities. The effect of Ca/Si ratio and Al_2O_3/MgO content on glass viscosity was evaluated and compared to the literature. It was determined that future viscosity models should consider glass H_2O content. Glass viscosity was related to infiltration in EBCs using available TBC and reactive infiltration models. Both model types drastically overestimated infiltration time when compared to experimental data obtained on Yb silicates. Consideration of any crystallization reactions between the coating and glass is necessary. Validation of model input parameters is also required.

In conclusion, the findings from this work address critical questions related to EBC design for CMAS mitigation. EBC material selection should seek to maximize reactivity between the coating and glass to form dense, favorable phases that slow incoming CMAS. The addition of YbMS to YbDS drastically improves the ability for model materials to resist infiltration. As such, the APS process for preparation of EBCs should be tailored so that ≥ 20 vol% YbMS is available for deposition. The FactSage viscosity model should be used in future studies to predict CMAS fluidity. However, future work is needed to evaluate this model’s ability to describe the viscosity of glasses obtained from the field. Additionally, of the glass-related parameters investigated, viscosity is the most important in predicting coating infiltration. Coating-related parameters that describe pore fraction open to flow are also significant based on the current TBC infiltration model. Based on this model, pore fraction open to flow should be minimized in EBCs. Reaction product formation between an EBC and CMAS is also critical and should be considered in the future when predicting CMAS infiltration in coating materials. Further development of reactive infiltration models is needed.

Appendix A: CTE of RE titanates

Powder samples of REMT and REDT were prepared as sample beads for determination of CTE at the Advanced Photon Source. Sample beads were levitated in O_2 and were heated from 1000-2000°C in 100°C intervals. Exposure time was 0.1 s per frame with 300 frames collected per diffraction image. Five diffraction images were collected at each temperature. X-ray data was refined in GSAS and the d-spacing for several different hkl values was used to determine change in lattice parameter with temperature. All REMT and REDT investigated had cubic structures and so Equation A.1 was used to determine lattice parameter *a*. YMT was converted to a solid solution of cubic fluorite/pyrochlore from the initial hexagonal phase after bead preparation; no change in structure was observed with temperature during levitation experiments.

$$d_{hkl} = \frac{a}{\sqrt{h^2+k^2+l^2}} \quad \text{[A.1]}$$

The normalized change in *a* (with respect to its value at 1000°C; *Δa/a*) is given as a function of temperature and hkl value for YbDT, YbMT, YDT, and YMT in Figures A.1, A.2, A.3, and A.4, respectively.

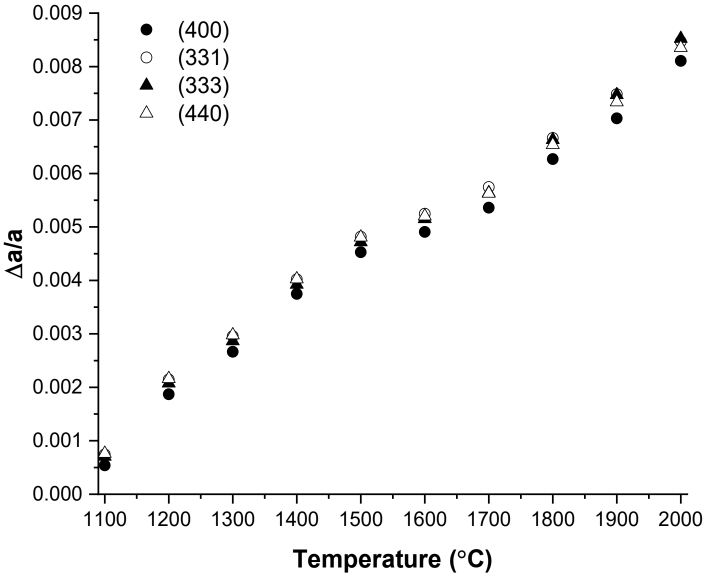

***Figure A.1**. Change in lattice parameter* a *with respect to its value at 1000°C (*Δa/a*) as a function of temperature and hkl value for YbDT. CTEs between 1100-1500°C and 1600-2000°C are reported.*

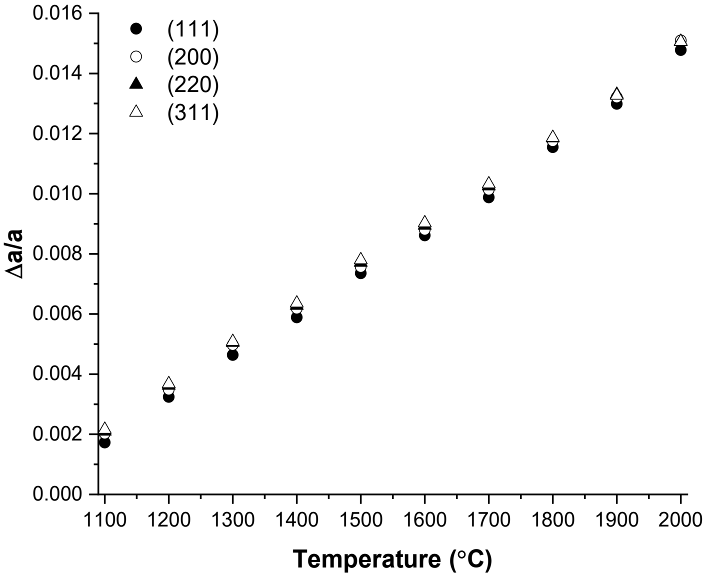

***Figure A.2**. Change in lattice parameter* a *with respect to its value at 1000°C (*Δa/a*) as a function of temperature and hkl value for YbMT.*

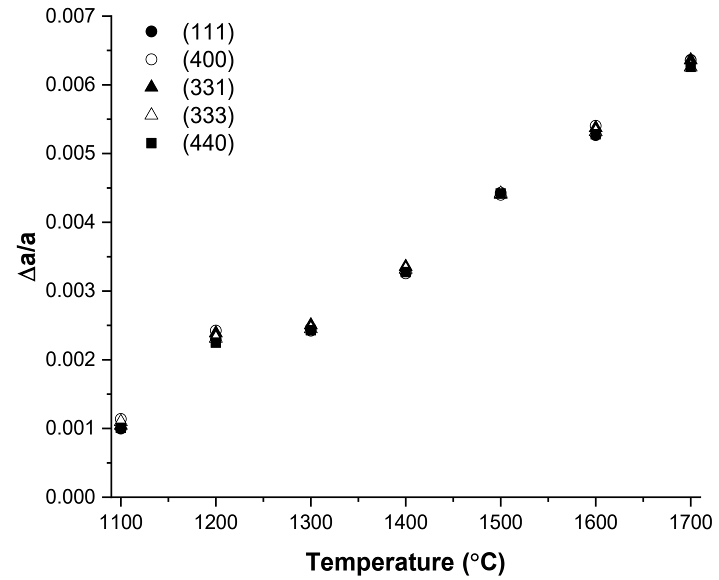

***Figure A.3**. Change in lattice parameter* a *with respect to its value at 1000°C (*Δa/a*) as a function of temperature and hkl value for YDT.*

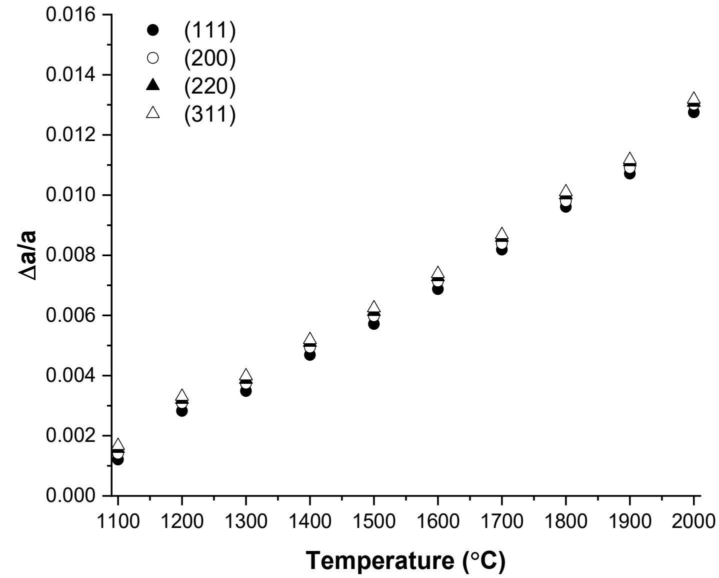

***Figure A.4**. Change in lattice parameter* a *with respect to its value at 1000°C (*Δa/a*) as a function of temperature and hkl value for YMT.*

A line was fit to each set of data points. The average slope (from the set of hkl values monitored) was taken as the linear CTE. CTE values for each material are given in Table A.1. Two slopes were calculated, based on temperature range, for YbDT.

Table A.1. *CTE values based on the slopes of the lines fit to data given in Figures A.1, A.2, A.3, and A.4.*

	YMT	**YbMT**	**YDT**	**YbDT**	
CTE (x 10^{-6} °C^{-1})	12.2 ± 0.01	14.1 ± 0.09	8.9 ± 0.09	9.9 ± 0.08 (1100-1500°C)	8.2 ± 0.26 (1600-2000°C)

The CTEs for RE titanates are too high to consider them as EBC materials. The difference in CTE between RE titanates and SiC will result in thermal stresses that induce coating delamination, as described in Chapter 2 Section **2.2 (c)** III. *iii*.

Appendix B: CTE of Yb apatite

Coefficient of thermal expansion was measured for ytterbium apatite via 1) measurement of lattice parameter shifts with temperature (data obtained at the Advanced Photon Source) and 2) laboratory-based dilatometry. Sample beads of ytterbium apatite containing residual Yb_2O_3 were prepared for determination of CTE at APS. Sample powders were mixed with a solution of ~2 wt% PVA in deionized water and rolled by hand into ~2-3 mm beads. Beads were then annealed in the box furnace for 5 h at 1500°C. Sample beads were levitated in O_2 and were heated from 1000-2000°C in 100°C intervals. Exposure time was 0.1 s per frame with 300 frames collected per diffraction image. Five diffraction images were collected at each temperature. X-ray data was refined and indexed in GSAS to determine lattice parameters as a function of temperature (Table B.1). The structure of the apatite phase is hexagonal, and so Equation B.1 was used to determine lattice parameters *a* and *c*.

$$d_{hkl} = \sqrt{\left(\frac{3}{4}\right)\frac{a^2}{h^2+hk+k^2} + \frac{c^2}{l^2}} \qquad [B.1]$$

***Table B.1**. Lattice parameters* a *and* c *in Yb apatite as a function of temperature. Changes in* a *and* c *with respect to their values at RT* (Δa/a *and* Δc/c*) are also given.*

	a	c	Δa/a	Δc/c
RT	9.362 ± 0.0003	6.714 ± 0.0003		
1000	9.409 ± 0.0065	6.800 ± 0.0103	0.005045	0.01283
1100	9.412 ± 0.0045	6.812 ± 0.0033	0.005403	0.01463
1200	9.414 ± 0.0070	6.817 ± 0.0017	0.005631	0.015349
1300	9.458 ± 0.0441	6.821 ± 0.0029	0.010286	0.015941
1400	9.455 ± 0.0370	6.819 ± 0.0010	0.009911	0.01568
1500	9.500 ± 0.0107	6.827 ± 0.0058	0.014784	0.016908
1600	9.522 ± 0.0700	6.805 ± 0.0173	0.017082	0.013633
1700	9.535 ± 0.0483	6.810 ± 0.0415	0.01846	0.014318
1800	9.542 ± 0.0151	6.786 ± 0.0260	0.019288	0.010726

The normalized change in lattice parameters *a* and *c* (with respect to their values at room temperature; *Δa/a* and *Δc/c*, given in Table B.1) are plotted as a function of temperature in Figures B.1 and B.2, respectively. There is a linear increase in *a* from 1000-2000°C (Figure B.1) and a linear increase in *c* from 1000-1500°C (Figure B.2). Lattice parameter *c* then appears to decrease linearly from 1500-1800°C. The slopes of these lines can be used to determine the linear coefficients of thermal expansion (CTE) for *a* and *c* over the temperature region of interest. Table B.2 provides observed CTE values. The R^2 values given in Figures B.1 and B.2 indicate that there is some scatter in the data. This scatter is likely attributed to sample bead shape/size inconsistencies resulting from the preparation method used.

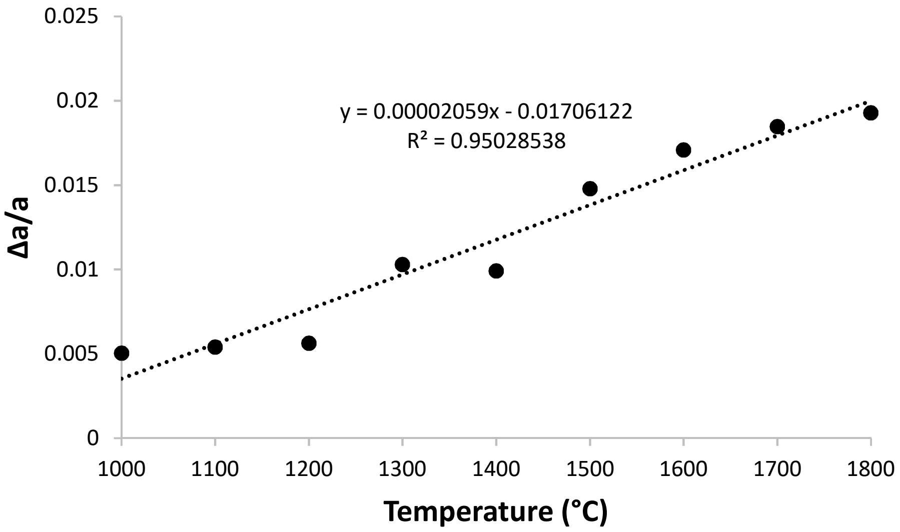

Figure B.1. *Normalized change in lattice parameter* a *as a function of temperature. The slope provided gives the linear CTE for* a *over 1000-1800°C.*

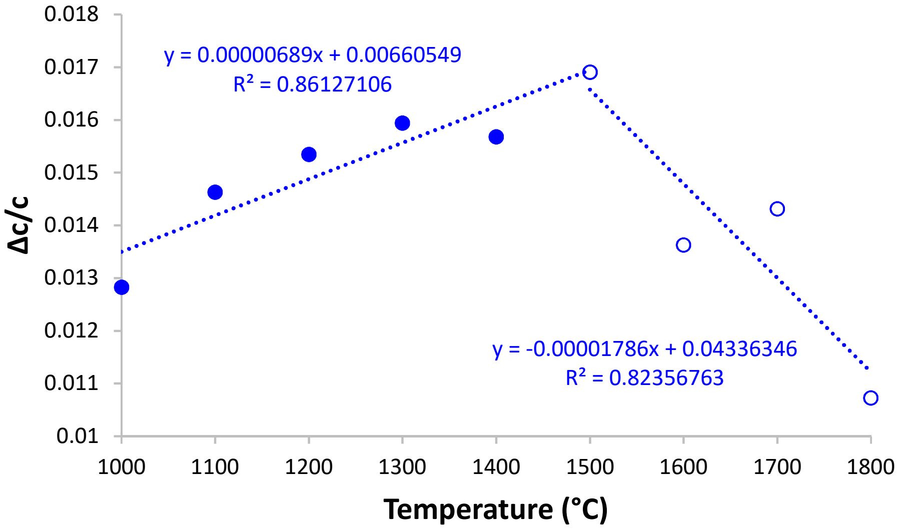

Figure B.2. *Normalized change in lattice parameter* c *as a function of temperature. The slopes provided give the linear CTE for* c *over 1000-1500°C and 1500-1800°C.*

***Table B.2**. Linear CTE values determined from the slopes of lines fit to data in Figures B.1 and B.2.*

	CTE (°C^{-1})	**CTE (x10^6 °C^{-1})**
a (1000-1800°C)	0.00002059	20.59
c (1000-1500°C)	0.00000689	6.89
c (1500-1800°C)	-0.00001786	-17.86

Another method to determine CTE (at a specific temperature) involves the following equations [98]:

$$CTE_a = \frac{1}{T-T_0}\left[\frac{a}{a_0} - 1\right] \tag{B.2}$$

$$CTE_c = \frac{1}{T-T_0}\left[\frac{c}{c_0} - 1\right] \tag{B.3}$$

$$CTE_{bulk} = \frac{(CTE_a \times 2) + CTE_c}{3} \tag{B.4}$$

where *a* and *c* are the lattice parameters at a given temperature (*T*) and a_0 and c_0 are the lattice parameters at room temperature (T_0). The CTEs for *a* and *c* at each temperature are given in Table B.3. Bulk CTE is also provided and plotted in Figure B.3.

***Table B.3**. CTE values for* a, c, *and bulk material at each temperature investigated.*

	a	**c**	**Bulk**
1000	5.164E-06	1.313E-05	7.820E-06
1100	5.017E-06	1.358E-05	7.872E-06
1200	4.784E-06	1.304E-05	7.536E-06
1300	8.055E-06	1.248E-05	9.531E-06
1400	7.197E-06	1.139E-05	8.594E-06
1500	1.001E-05	1.145E-05	1.049E-05
1600	1.083E-05	8.645E-06	1.010E-05
1700	1.101E-05	8.538E-06	1.018E-05
1800	1.085E-05	6.036E-06	9.248E-06

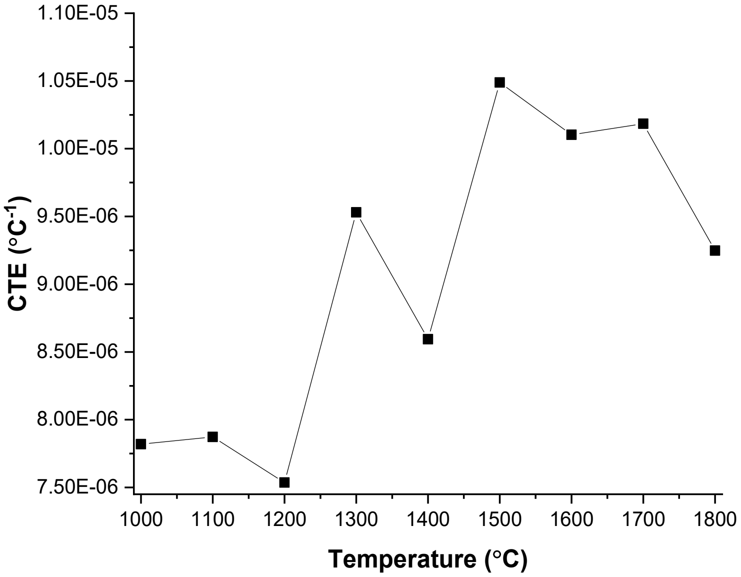

Figure B.3. *Bulk CTE values (given in Table B.3) plotted as a function of temperature.*

Dilatometry was performed using a Netzsch Dil 402 C. Spark plasma sintered Yb apatite samples (both phase pure and containing residual Yb_2O_3) were sectioned into ~15 x 5 x 3 mm samples. The 5 x 3 mm ends were polished to 1200 grit with SiC paper prior to testing. Samples were ramped to 1400°C at a rate of 3°C/min. The force exerted on the samples was 25 cN. Change in sample length was measured as a function of temperature. An alumina standard of similar shape and size was run under the same testing conditions prior to measuring Yb apatite samples. The alumina curve was subtracted from sample curves. The bulk CTE is given in Figure B.4 for Yb apatite samples as a function of temperature.

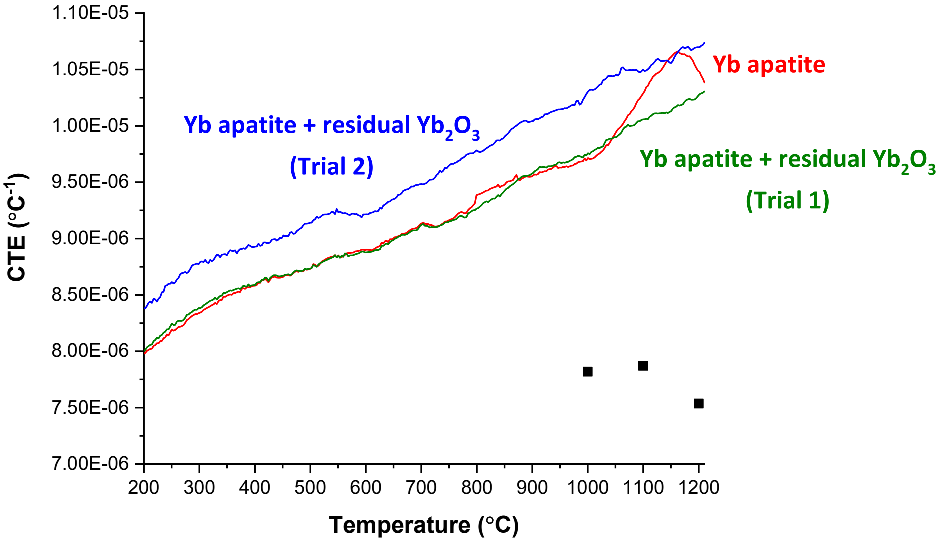

***Figure B.4**. Bulk CTE for Yb apatite samples plotted as a function of temperature. Determined by dilatometry (lines) and from APS data (black data points).*

Bulk CTE determined via dilatometry appears to vary between ~8-10.5 x 10^{-6} °C^{-1} over 200-1200°C. Values are similar between sample runs. Comparing bulk CTE determined by dilatometry to bulk CTE determined from APS data (Figure B.4), dilatometry samples have higher CTEs. Data from APS is more trustworthy, as synchrotron x-rays are able to probe bonding characteristics. Dilatometry only describes overall changes in sample length. It is worthwhile to note that some Yb_2SiO_5 was observed at the edges of Yb apatite + residual Yb_2O_3 dilatometry samples. Its presence was not confirmed via laboratory XRD (Figure 2.39) but levitation experiments suggested that some Yb_2SiO_5 formed with increasing temperature.

The CTE for Yb apatite is greater than SiC/YbDS and YbMS but may be less than that of CMAS (dependent on glass composition): SiC < YbDS < YbMS < Yb apatite < CMAS (Chapter 2, Sections **2.2 (c)** III. *iii*., **2.2 (d)** III. *i*., and 2.4). The CTE for Yb apatite is apparently greater than that for Y apatite (Chapter 2, Section **2.2 (c)** III. *iii*.).

Appendix C: Stability of Yb apatite in high-temperature, high-velocity steam

Yb apatite (containing Yb_2O_3) was exposed to high-temperature, high-velocity steam using a steam-jet apparatus based on a design by Lucato et al. [141] modified by Golden and Opila [142] and Parker (in preparation for J. Am. Cer. Soc.). A schematic of the steam-jet is given in Figure C.1a. The design uses a horizontal tube furnace (CM Furnaces Model 1730-12 HTF, Bloomfield, NJ) with a 1.375" inner diameter alumina tube (99.8% pure; McDanel Advanced Ceramic Technologies, Beaver Falls, PA) and an inlet stainless steel end cap (MDC Vacuum Products LLC, Hayward, CA) that accommodates feedthroughs for thermocouple, gas, and liquid water inlets. A peristaltic pump (Ismatec SA Reglo Analog MS 2/12, Glattburg, Switzerland) fed deionized 18.2 MΩ liquid water into a 1.6 mm OD, 1 mm ID, 650 mm long 90/10 Pt/Rh capillary at a controlled flow rate. The Pt/Rh capillary (Goodfellow, Coraopolis, PA) is inserted through an ultratorr fitting (Swagelok, Solon, OH) on the end cap and extends into the center of the hot zone. Two smaller alumina tubes (23 mm OD) were used inside the furnace tube to support and align the Pt/Rh capillary as shown in Figure C.1 a/b. The weight change of liquid water was measured throughout the experiment to determine the total amount of liquid water that was pumped into the furnace. The average mass flow rate of the liquid water for the experiment was determined by dividing the total weight loss of liquid water by the exposure time. The mass flow rate was ~2 g/min. Liquid water evaporates in the capillary as it enters the hot zone of the furnace resulting in a volume expansion forming a jet of high-temperature, high-velocity steam. The steam-jet velocity was modeled by CFD analysis (ANSYS Inc. ANSYS CFX, Canonsburg, PA). Inputs to the analysis include the mass flow rate of the liquid water, the steam-jet temperature, and the geometry of the Pt/Rh capillary relative to the test specimen. The steam jet velocity at the impingement site was modeled as 234 m/s. A thermocouple (type R) inserted through a second inlet on the end cap extended to the center of the hot zone approximately 4 cm from the specimen and remained stationary during the experiment. Prior to the experiment, the steam-jet temperature was calibrated by placing a second thermocouple (type R) approximately 1 mm from the tip of the capillary (the same position of the specimen during the experiment) and recording the temperature of the steam-jet. This thermocouple was inserted through the open exhaust end of the alumina tube. The steam-jet exposure temperature was 1300°C. The test specimen was mounted in an alumina holder at a 45° angle relative to the steam-jet (Figure C.1b) and held in place by platinum foil and wire. The alumina holder was pushed into the tube furnace and locked into place in front of the capillary. The capillary was adjusted to a position 1 mm away from the surface of the specimen. The experiment was conducted with no outlet endcap so that 1 atm air was present in the tube surrounding the steam-jet. Photographs of the specimen holder were taken before and after the experiment to confirm the specimen did not shift during exposure. The exposure time was 60 h.

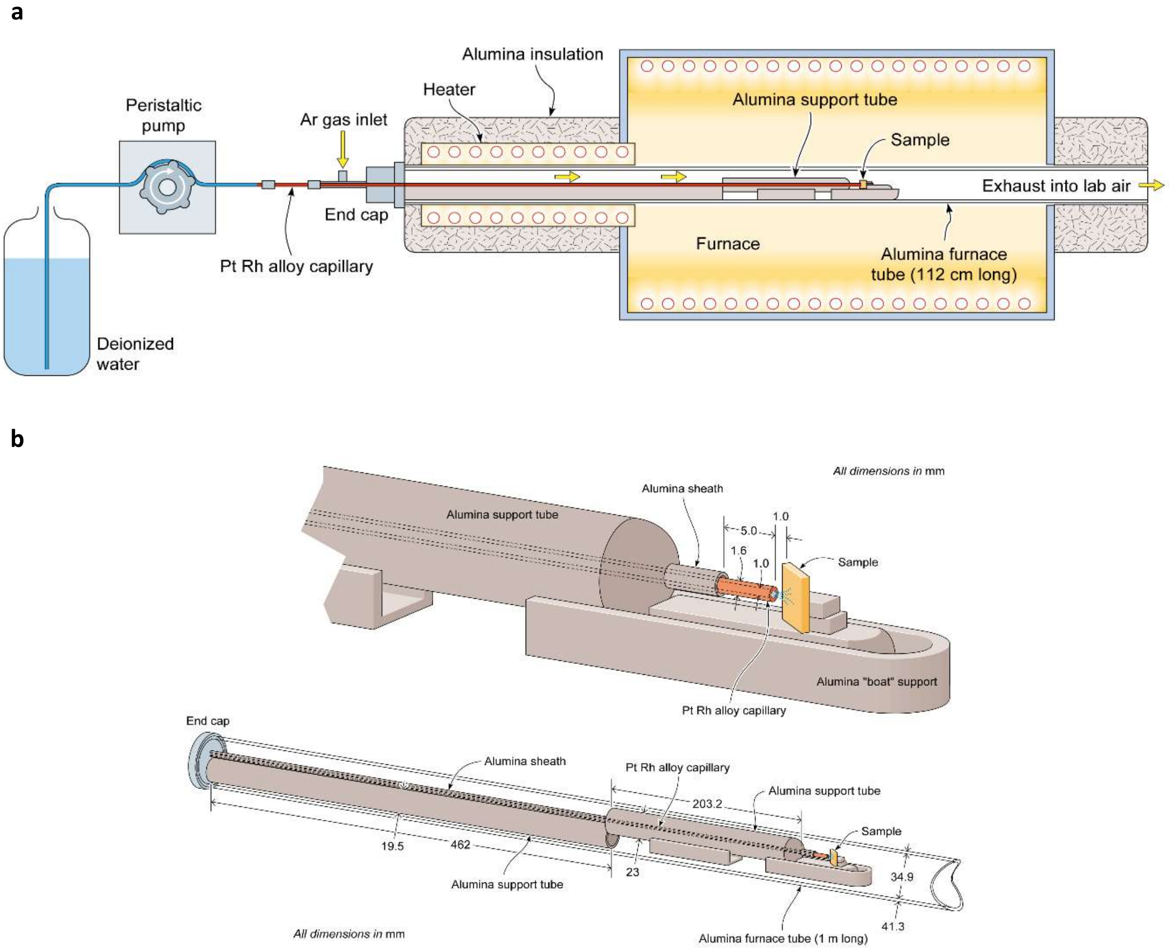

Figure C.1. *Steam jet furnace schematic: (a) shows overall setup and (b) shows details inside the furnace.*

Plan-view and cross-section BSE images of or near the impingement site are given in Figures C.2 and C.3. There is cracking at the impingement site and some grain fallout (Figure C.2a). EDS measurements indicate that the surface is composed of Yb_2O_3. The Yb_2O_3 that forms is porous. The initial Yb_2O_3 within the starting sample appears to remain intact (Figure C.2b).

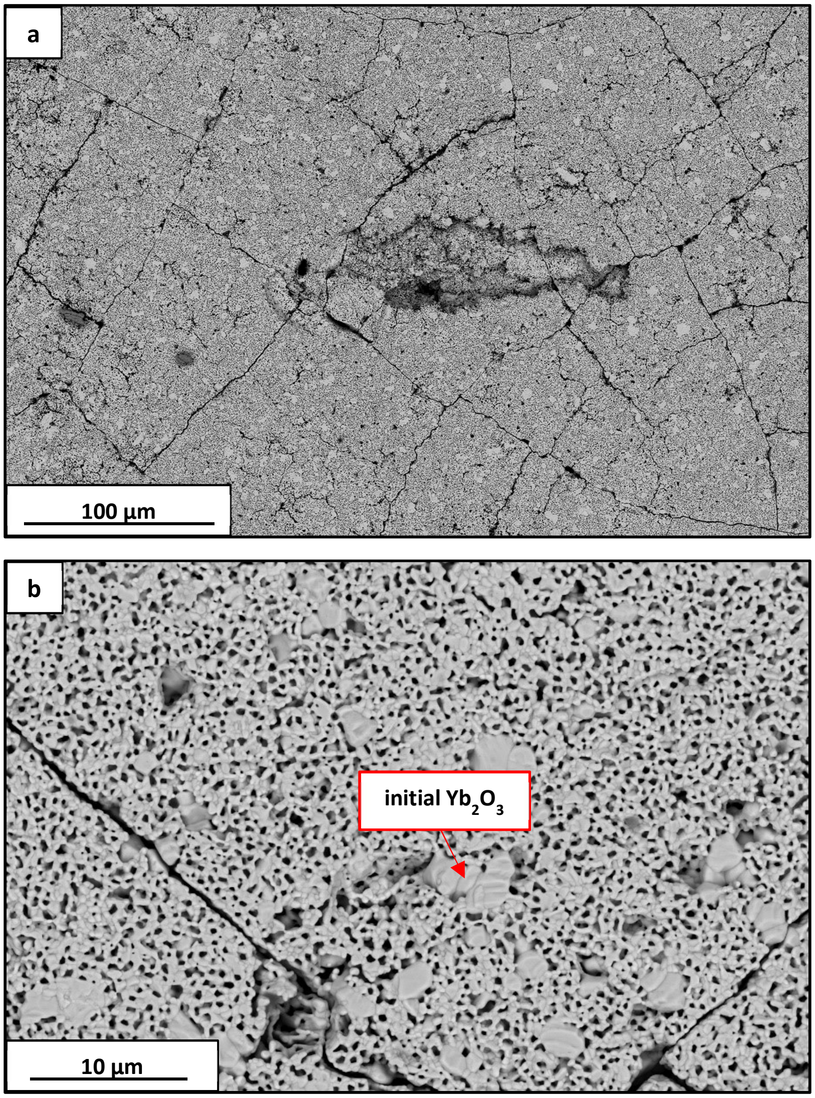

***Figure C.2**. (a) Plan-view BSE image of impingement site and (b) higher magnification of impingement site, showing initial Yb_2O_3 granules and the formation of porous Yb_2O_3. Exposure conditions were 60 h at 1300°C in contact with 234 m/s velocity steam.*

In cross-section, there can be seen a layer of porous Yb_2O_3 across the interaction zone. In looking more closely, it appears that the Yb_2O_3 forms on top of a layer of Yb_2SiO_5 (Figure C.3b). The proposed reaction sequence is as follows:

$$CaYb_4(SiO_4)_3O + 3H_2O(g) \rightarrow 2Yb_2SiO_5 + Ca(OH)_2\,(g) + Si(OH)_4\,(g) \qquad [C.1]$$

$$Yb_2SiO_5 + 2H_2O(g) \rightarrow Yb_2O_3 + Si(OH)_4\,(g) \qquad [C.2]$$

There is a volume change (decrease) of ~15% when converting 1 mol of $CaYb_4(SiO_4)_3O$ (ρ=6.75 g/cm^2) to 2 mol Yb_2SiO_5 (ρ=7.15 g/cm^2). Indeed, pores are present in the Yb_2SiO_5 layer found in Figure C.3b. The conversion of 1 mol Yb_2SiO_5 to 1 mol Yb_2O_3 (ρ=9.17 g/cm^2) is accompanied by a volume percent decrease of ~30%, which accounts for the increased porosity in the Yb_2O_3 layer. Near the impingement site, the sample is disrupted by cracks and large voids beneath the surface. Further work is needed to understand the reactions taking place and to quantify material loss after exposure to high temperature, high velocity steam. Tests at different temperatures and for various times are required.

The results show that apatite formation between an EBC and CMAS is subject to its own stability issues in a combustion environment.

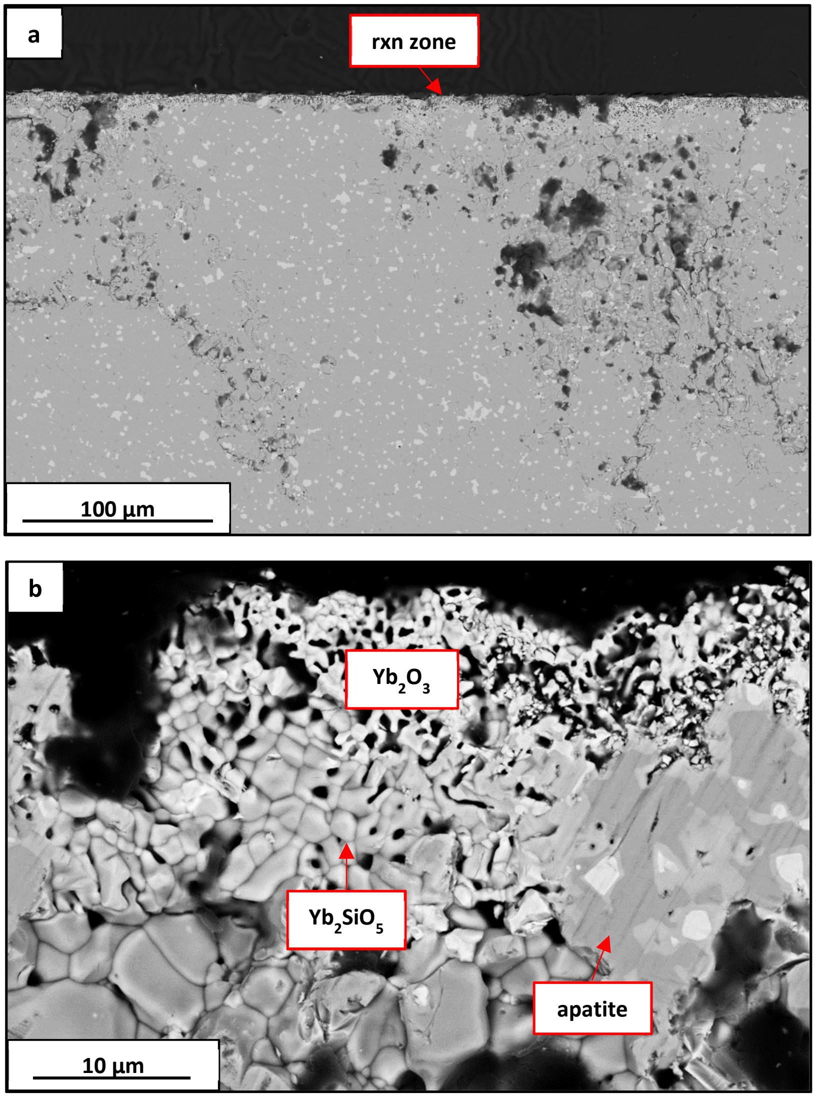

***Figure C.3**. (a) Cross-section BSE image near impingement site showing reaction layer and disruption of apatite beneath the surface of the sample and (b) higher magnification image of reaction layer. There is a layer of Yb_2SiO_5 underneath the porous Yb_2O_3 and surrounding initial Yb_2O_3 granules.*

Appendix D: Glass characterization for viscosity measurements

All pre-viscosity characterizations were performed on either “small batch” or “large batch” glass preparations. Amounts prepared were 75 and 150 g, respectively. Actual viscosity measurements were only carried out on “large batch” compositions as the amount of glass needed to fill the viscometer crucible was around 90 g. The smaller glass batch chemistries are reported here to provide additional data regarding pre-viscosity characterization. Pre- and post-viscosity glass compositions are given in

Table D.1 for both “small batch” and “large batch” glasses. Pre- and post-viscosity composition measurements on the Eyja glass are given in Table D.2. It is important to point out that the chemistries of post-viscosity glasses (determined via EDS) are essentially the same as those for pre-viscosity glasses (determined via EDS or ICP), indicating that composition did not change during experiments.

All glass preparations were amorphous prior to viscosity experiments. Figures D.1, D.2, D.3, and D.4 give XRD spectra for powder CMAS, CAS, CMS, and Eyja samples, respectively. There was one peak discerned in 21Ca-57Si CMAS (Figure D.1). This is likely a result of insufficient quenching from the molten state. DSC scans (Figures D.5, D.6, D.7, D.8, and D.9) provide information on glass melting temperature (Table D.3). The lowest temperature in the viscosity temperature profile was kept above glass melting to ensure that there were no crystallized species in the samples during viscosity experiments. The lowest temperatures reached during viscosity measurements are given in Figures D.5-D.9 by red lines. These temperatures are provided in Table 4.2.

Glass composition, melting temperature, and crystallinity are all important for viscosity measurements. Further discussion is provided in Chapter 4.

Table D.1. *Pre- and post-viscosity glass compositions characterized by EDS and ICP.*

		Nominal composition	Small batch ICP (Pre-viscosity)	Small batch EDS (Pre-viscosity)	Large batch EDS (Pre-viscosity)	Post-viscosity EDS
$C_{33}M_{9}A_{13}S_{45}$	Ca	33	33.0	36.9	33.1	33.7
	Mg	9	9.8	8.2	9.0	9.0
	Al	13	14.0	13.0	13.8	13.7
	Si	45	43.2	41.9	44.1	43.6
$C_{21}M_{9}A_{13}S_{57}$	Ca	21	21.5	27.5	20.1	20.4
	Mg	9	9.3	7.9	9.0	9.2
	Al	13	13.2	12.3	14.0	13.9
	Si	57	56.0	52.3	56.9	56.5
$C_{38.1}A_{9.9}S_{52}$	Ca	38.1	38.6	44.4	38.3	39.7
	Al	9.9	10.0	9.2	10.7	9.9
	Si	52	51.4	46.4	51.0	50.4
$C_{33.75}A_{20}S_{46.25}$	Ca	33.75	34.5	38.3	33.1	32.1
	Al	20	19.8	18.8	21.1	21.3
	Si	46.25	45.7	42.9	45.8	46.6
$C_{29.5}A_{30}S_{40.5}$	Ca	29.5	-	29.2	29.3	29.5
	Al	30	-	31.3	30.9	30.6
	Si	40.5	-	39.5	39.8	39.8
$C_{33.75}M_{20}S_{46.25}$	Ca	33.75	36.5	40.6	33.3	34.1
	Mg	20	21.2	15.5	20.3	19.4
	Si	46.25	42.3	43.9	46.4	46.6

***Table D.2**. Pre- and post-viscosity Eyja glass composition characterized by EDS and ICP.*

		Pre-viscosity ICP	Post-viscosity EDS
Eyja volcanic ash glass	Ca	5.1	5.0
	Mg	3.5	3.2
	Al	16.7	16.3
	Si	55.9	56.2
	Fe	7.3	7.4
	Ti	1.2	1.2
	Na	8.3	8.5
	K	2.0	2.3

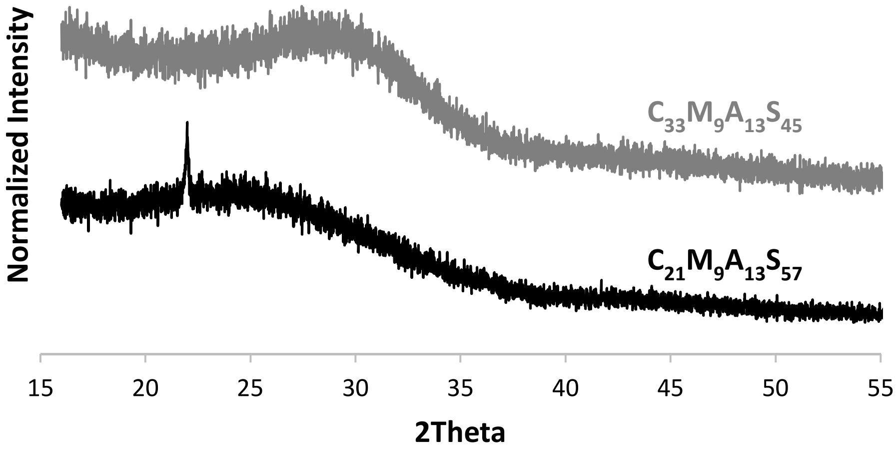

***Figure D.1**. Pre-viscosity XRD spectra for CMAS glass compositions under study. The lone peak discerned in the 21Ca-57Si CMAS is likely due to insufficient cooling upon quenching from the melt.*

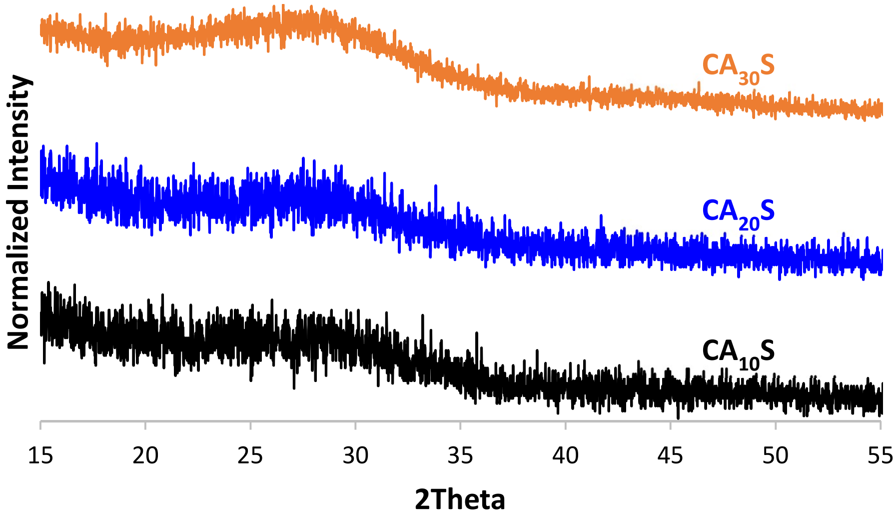

***Figure D.2**. Pre-viscosity XRD spectra for CAS glass compositions under study.*

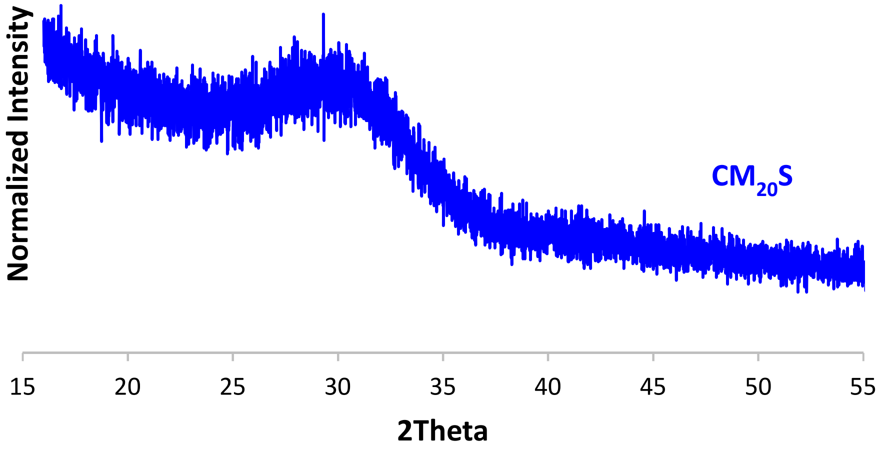

***Figure D.3**. Pre-viscosity XRD spectrum for* $CM_{20}S$.

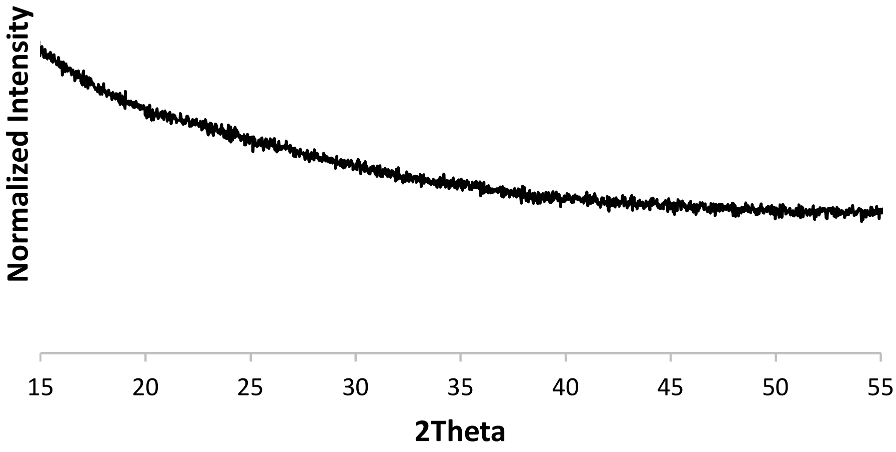

Figure D.4. *Pre-viscosity XRD spectrum for the Eyja volcanic ash glass.*

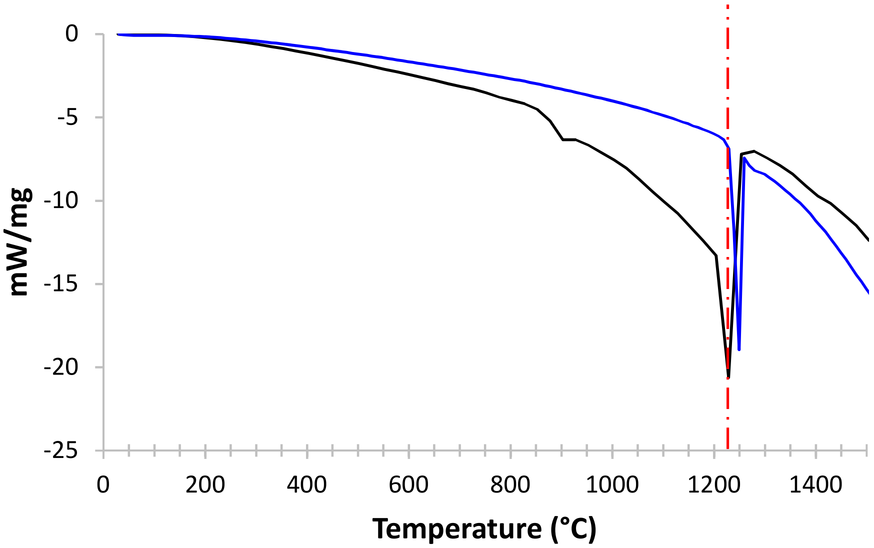

Figure D.5. *DSC scans for 33Ca-45Si CMAS amorphous glass (black line) and glass after sintering for 4 h at 1200°C (blue line). The red dashed line indicates the lowest temperature reached during viscosity experiments.*

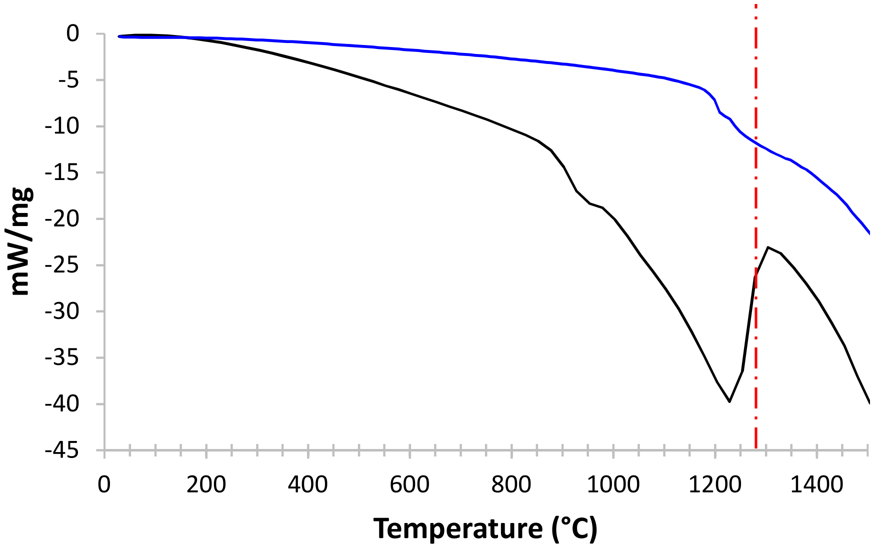

Figure D.6. *DSC scans for 21Ca-57Si CMAS amorphous glass (black line) and glass after sintering for 4 h at 1200°C (blue line). The red dashed line indicates the lowest temperature reached during viscosity experiments.*

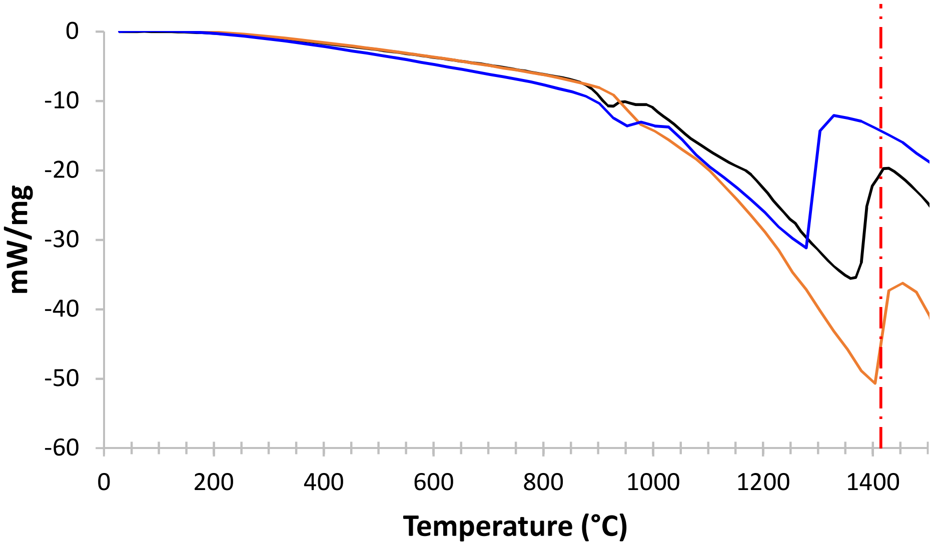

Figure D.7. *DSC scans for CAS glasses under study – 10 mol% Al (black), 20 mol% Al (blue), and 30 mol% Al (orange). The red dashed line indicates the lowest temperature reached during viscosity experiments.*

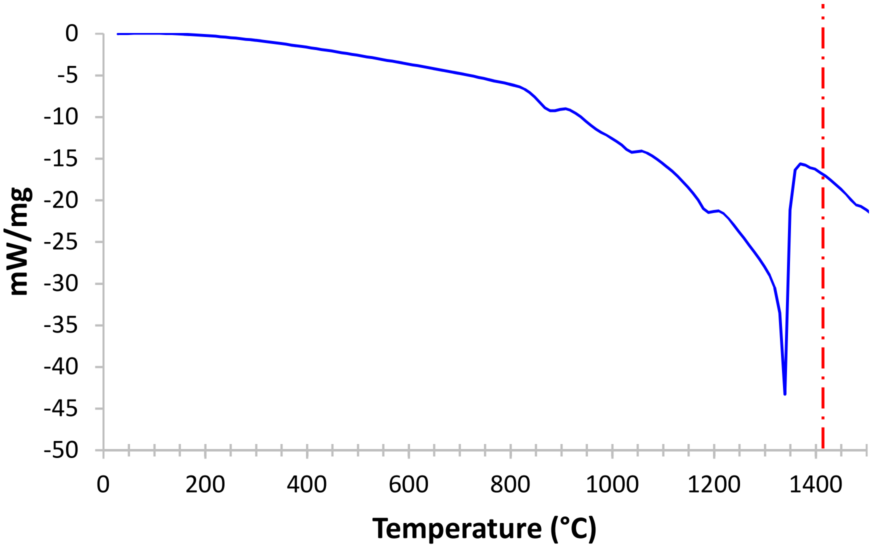

Figure D.8. *DSC scan for $CM_{20}S$ glass. The red dashed line indicates the lowest temperature reached during viscosity experiment.*

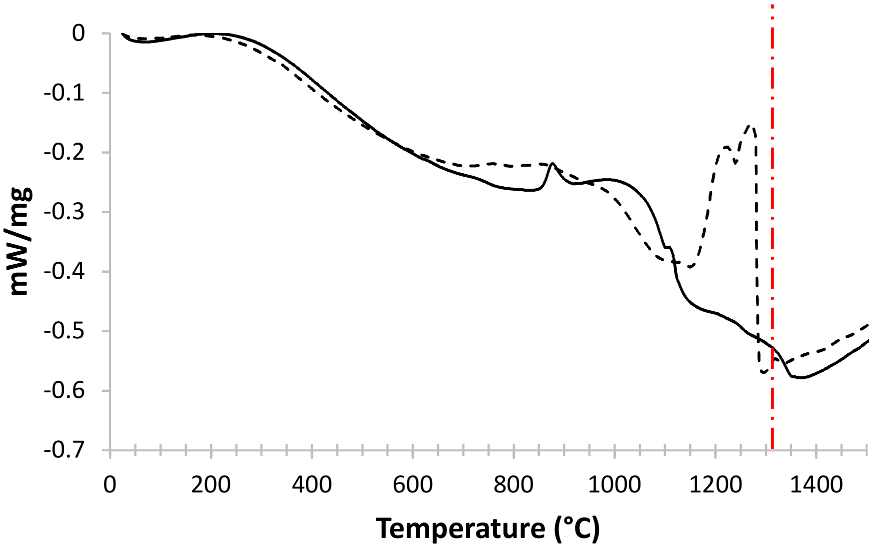

Figure D.9. *DSC scans for the Eyja volcanic ash glass in bulk (solid line) and powder (dashed line) forms. The red dashed line indicates the lowest temperature reached during viscosity experiments.*

***Table D.3**. Approximate melting-related temperatures for glasses under study, as determined by DSC.*

Composition	**Approximate T fully molten (°C)**	**Approximate peak melting (°C)**
$C_{33}M_9A_{13}S_{45}$	1250	1225
$C_{21}M_9A_{13}S_{57}$	1300	1225
$C_{38.1}A_{9.9}S_{52}$	1425	1300
$C_{33.75}A_{20}S_{46.25}$	1425	1350
$C_{29.5}A_{30}S_{40.5}$	1425	1400
$C_{33.75}M_{20}S_{46.25}$	1375	1350
Eyja volcanic ash glass	n/a	1300

References

[1] M.P. Boyce, *Gas Turbine Engineering Handbook*, Fourth Edition. Butterworth-Heinemann, Oxford, 2012.

[2] N.P. Padture, “Advanced structural ceramics in aerospace propulsion,” *Nat. Mater.*, **15** [8] 804–809 (2016).

[3] D.R. Clarke, M. Oechsner, and N.P. Padture, “Thermal-barrier coatings for more efficient gas-turbine engines,” *MRS Bull.*, **37** [10] 891–898 (2012).

[4] J.H. Perepezko, “The Hotter the Engine, the Better,” *Science*, **326** [5956] 1068–1069 (2009).

[5] J.T. DeMasi-Marcin and D.K. Gupta, “Protective coatings in the gas turbine engine,” *Surf. Coat. Technol.*, **68** [1–9] (1994).

[6] J.C. Williams and E.A. Starke, Jr., “Progress in structural materials for aerospace systems,” *Acta Mater.*, **51** [19] 5775–5799 (2003).

[7] F.W. Zok, “Ceramic-matrix composites enable revolutionary gains in turbine engine efficiency,” *Am. Ceram. Soc. Bull.*, **95** [5] 22–28 (2016).

[8] N.R. Council, *Ceramic Fibers and Coatings: Advanced Materials for the Twenty-First Century*. The National Academies Press, Washington, DC, 1998.

[9] I. Spitsberg and J. Steibel, “Thermal and environmental barrier coatings for SiC/SiC CMCs in aircraft engine applications,” *Int. J. Appl. Ceram. Technol*., **1** [4] 291–301 (2004).

[10] L.U. Ogbuji and E.J. Opila, “A Comparison of the Oxidation Kinetics of SiC and Si_3N_4,” *J. Electrochem. Soc*., **142** [3] 925–930 (1995).

[11] N.S. Jacobson, “Corrosion of silicon-based ceramics in combustion environments,” *J. Am. Ceram. Soc*., **76** [1] 3-28 (1993).

[12] E.J. Opila and R.E. Hann, “Paralinear Oxidation of CVD SiC in Water Vapor,” *J. Am. Ceram. Soc*., **80** [1] 197–205 (1997).

[13] K.N. Lee, “Current status of environmental barrier coatings for Si-based ceramics,” *Surf. Coat. Technol*., **133–134** 1–7 (2000).

[14] D.L. Poerschke, R.W. Jackson, and C.G. Levi,” Silicate deposit degradation of engineered coatings in gas turbines: Progress toward models and materials solutions,” *Annu. Rev. Mater. Res*., **47** 297-330 (2017).

[15] K.M. Grant, S. Krämer, G.G.E. Seward, and C.G. Levi, “Calcium-magnesium alumino-silicate interaction withyttrium monosilicate environmental barrier coatings,” *J. Am. Ceram. Soc*., 93 [10] 3504-3511 (2010).

[16] M.P. Borom, C.A. Johnson, and L.A. Peluso, “Role of environment deposits and operating surface temperature in spallation of air plasma sprayed thermal barrier coatings,” *Surf. Coat. Technol*., **86-87 Part 1** 116-126 (1996).

[17] J.L. Smialek, F.A. Archer, and R.G. Garlick, “Turbine airfoil degradation in the persian gulf war,” *JOM*, **46** [12] 39-41 (1994).

[18] F.C. Tom, A.B. Thakker, and S.K. Gupta, J. ASME, 88-GT-279 (1988) (presented at the Gas Turbine and Aeroengine Congress. Amsterdam, The Netherlands, June 6-9, 1988.

[19] F.H. Stott, D.J. de Wet, and R. Taylor, in F.H. Froes et al. (eds.), The Effects of Molten Silicate Deposits on the Stability of Thermal Barrier Coatings for Turbine Applications at Very High Temperatures, Advances in Synthesis and Processes, SAMPE, 3, 1992, M92-MI01.

[20] C.G. Levi, J.W. Hutchinson, M.-H. Vidal-Sétif, and C.A. Johnson, "Environmental degradation of thermal barrier coatings by molten deposits," *MRS Bull*., **37** [10] 932-941 (2012).

[21] J. Kim, M.G. Dunn, A.J. Baran, D.P. Wade and E.L. Tremba, "Deposition of volcanic materials in the hot sections of two gas turbine engines," *J. Eng. Gas Turbines Power*, **115** [3] 641-651 (1993).

[22] J.M. Drexler, A.D. Gledhill, K. Shinoda, A. L. Vasiliev, K. M. Reddy, S. Sampath, and N.P. Padture, "Jet engine coatings for resisting volcanic ash damage," *Adv. Mater*., **23** [21] 2419-2424 (2011).

[23] W.R. Chen and L.R. Zhao, "Review – Volcanic ash and its influence on aircraft engine components," *Procedia Eng*., **99** 795-803 (2015).

[24] W. Song, Y. Lavallée, K.-U. Hess, U. Kueppers, C. Cimarelli, and D. B. Dingwell, "Volcanic ash melting under conditions relevant to ash turbine interactions," *Nat. Commun*., 7 (2016).

[25] D.L. Poerschke, T.L. Barth, and C.G. Levi CG, "Equilibrium relationships between thermal barrier oxides and silicate melts," *Acta Mater*., **120** 302-314 (2016).

[26] D. Giordano, J.K. Russell, and D.B. Dingwell, "Viscosity of magmatic liquids: A model," *Earth Planet. Sci. Lett*., **271** [1-4] 123-134 (2008).

[27] C.W. Bale, E. Bélisle, P. Chartrand, S.A. Decterov, G. Eriksson, K. Hack, I.-H. Jung, Y.-B. Kang, J. Melançon, A.D. Pelton, C. Robelin, and S. Petersen, "FactSage thermochemical software and databases – recent developments," *Calphad*, **33** [2] 295-311 (2009).

[28] A. Fluegel, "Glass viscosity calculation based on a global statistical modelling approach," *Glass Technol. Eur. J. Glass Sci. Technol. Part A*., **48** [1] 13-30 (2007).

[29] V.L. Wiesner, U.K. Vempati, and N.P. Bansal, "High temperature viscosity of calcium-magnesium aluminosilicate glass from synthetic sand," *Scripta Mater*., **124** 189-192 (2016).

[30] C. Han, M. Chen, W. Zhang, Z. Zhao, T. Evans, A.V. Nguyen, and B. Zhao, "Viscosity model for iron blast furnace slags in SiO_2–Al_2O_3–CaO–MgO system," *Steel Res. Int*., **86** [6] 678-685 (2015).

[31] A.R. Krause, B.S. Senturk, H.F. Garces, G. Dwivedi, A.L. Ortiz, S. Sampath, and N.P. Padture, "$2ZrO_2{\cdot}Y_2O_3$ thermal barrier coatings resistant to degradation by molten CMAS: Part I, optical basicity considerations and processing," *J. Am. Ceram. Soc*., **97** [12] 3943-3949 (2014).

[32] M. Craig, N.L. Ndamka, R.G. Wellman, and J.R. Nicholls, "CMAS degradation of EB-PVD TBCs: The effect of basicity," *Surf. Coat. Technol*., **270** 145-153 (2015).

[33] S. Krämer, J. Yang, and C.G. Levi, "Infiltration-inhibiting reaction of gadolinium zirconate thermal barrier coatings with CMAS melts," *J. Am. Ceram. Soc*., **91** [2] 576-583 (2008).

[34] D.R. Clarke and S.R. Phillpot, "Thermal barrier coating materials," *Mater. Today*, **8** [6] 22-29 (2005).

[35] S. Krämer, J. Yang, C.G. Levi, and C.A. Johnson, "Thermochemical interaction of thermal barrier coatings with molten CaO–MgO–$A_{l2}O_3$–SiO_2 (CMAS) deposits," *J. Am. Ceram. Soc*., **89** [10] 3167-3175 (2006).

[36] R. Naraparajua, U. Schulz, P. Mechnich, P. Döbber, and F. Seidel, "Degradation study of 7 wt.% yttria stabilised zirconia (7YSZ) thermal barrier coatings on aero-engine combustion chamber parts due to infiltration by different CaO–MgO–Al_2O_3–SiO_2 variants," *Surf. Coat. Technol*., **260** [15] 73-81 (2014).

[37] A. Aygun, A. L. Vasiliev, N. P. Padture, and X. Ma, "Novel thermal barrier coatings that are resistant to high-temperature attack by glassy deposits," *Acta Mater*., **55** [20] 6734-6745 (2007).

[38] P. Mechnich, W. Braue, and U. Schulz, "High-temperature corrosion of EB-PVD yttria partially stabilized zirconia thermal barrier coatings with an artificial volcanic ash overlay" *J. Am. Ceram. Soc*., **94** [3] 925-931 (2011).

[39] J. Chevalier, L. Gremillard, A.V. Virkar, and D.R. Clarke, "The tetragonal-monoclinic transformation in zirconia: Lessons learned and future trends," *J. Am. Ceram. Soc*., **92** [9] 1901–1920 (2009).

[40] J.M. Drexler, A.L. Ortiz, and N.P. Padture, “Composition effects of thermal barrier coating ceramics on their interaction with molten Ca–Mg–Al–silicate (CMAS) glass,” *Acta Mater*., **60** [15] 5437 5447 (2012).

[41] H. Zhao, C.G. Levi, and H.N.G. Wadley, “Molten silicate interactions with thermal barrier coatings,” *Surf. Coat. Technol*., **251** 74-86 (2014).

[42] N. Chellah, M.-H. Vidal-Setif, C. Petitjean, P.-J. Panteix, C. Rapin, and M. Vilasi, “Calcium magnesium-alumino-silicate (CMAS) degradation of thermal barrier coatings: Solubility of different oxides from ZrO_2-Nd_2O_3 system in a model CMAS,” In Proc. HTCPM8, Les Embiez, Fr. (2012).

[43] L. Gao, H. Guo, S. Gong, and H. Xu, “Plasma-sprayed $La_2Ce_2O_7$ thermal barrier coatings against calcium–magnesium–alumina–silicate penetration,” *J. Eur. Ceram. Soc*., **34** [10] 2553-2561 (2014).

[44] U. Schulz and W. Braue, “Degradation of $La_2Zr_2O_7$ and other novel EB-PVD thermal barrier coatings by CMAS (CaO–MgO–Al_2O_3–SiO_2) and volcanic ash deposits,” Surf. Coat.Technol., **235** 165-173 (2013).

[45] D.L. Poerschke and C.G. Levi, “Effects of cation substitution and temperature on the interaction between thermal barrier oxides and molten CMAS,” *J. Eur. Ceram. Soc*., **35** [2] 681-691 (2015).

[46] M. Wierzbicka-Wieczorek, M. Göckeritz, U. Kolitsch, C. Lenz, and G. Giester, “Crystallographic and spectroscopic investigations on nine metal–rare-earth silicates with the apatite structure type,” *Eur. J. Inorg. Chem*., **2015** [6] 948–963 (2015).

[47] D.L. Poerschke, T.L. Barth, O. Fabrichnaya, and C.G. Levi, “Phase equilibria and crystal chemistry in the calcia–silica–yttria system,” *J. Eur. Ceram. Soc*., **36** [7] 1743-1754 (2016).

[48] K.N. Lee, D.S. Fox, and N.P. Bansal, “Rare earth silicate environmental barrier coatings for SiC/SiC composites and Si_3N_4 ceramics,” *J. Eur. Ceram. Soc*., **25** [10] 1705-1715 (2005).

[49] B.T. Richards, H. Zhao, and H.N.G. Wadley, "Structure, composition, and defect control during plasma spray deposition of ytterbium silicate coatings," *J. Mater. Sci.*, **50** [24] 7939-7957 (2015).

[50] B.T. Richards, K.A. Young, F. de Francqueville, S. Sehr, M.R. Begley, and H.N.G. Wadley, "Response of ytterbium disilicate-silicon environmental barrier coatings to thermal cycling in water vapor," *Acta Mater.*, **106** 1-14 (2016).

[51] F. Stolzenburg, M.T. Johnson, K.N. Lee, N.S. Jacobson, and K. T. Faber, "The interaction of calcium magnesium aluminosilicate with ytterbium silicate environmental barrier materials," *Surf. Coat. Technol.*, **284** 44-50 (2015).

[52] N.L. Ahlborg and D. Zhu, "Calcium-magnesium aluminosilicate (CMAS) reactions and degradation mechanisms of advanced environmental barrier coatings," *Surf. Coat. Technol.*, **237** 79-87 (2013).

[53] D.L. Poerschke, J. H. Shaw, N. Verma, F.W. Zok, and C.G. Levi, "Interaction of yttrium disilicate environmental barrier coatings with calcium-magnesium-iron alumino-silicate melts," *Acta Mater.*, **145** 451-461 (2018).

[54] L. R. Turcer, A. R. Krause, H. F. Garces, L. Zhang, and N. P. Padture, "Environmental-barrier coating ceramics for resistance against attack by molten calcia-magnesia-aluminosilicate (CMAS) glass: Part I, $YAlO_3$ and γ-$Y_2Si_2O_7$," *J. Eur. Ceram. Soc.*, **38** [11] 3905-3913 (2018).

[55] L. R. Turcer, A. R. Krause, H. F. Garces, L. Zhang, and N. P. Padture, "Environmental-barrier coating ceramics for resistance against attack by molten calcia-magnesia-aluminosilicate (CMAS) glass: Part II, β-$Yb_2Si_2O_7$ and β-$Sc_2Si_2O_7$," *J. Eur. Ceram. Soc.*, **38** [11] 3914-3924 (2018).

[56] H. Zhao, B.T. Richards, C.G. Levi, and H.N.G. Wadley, "Molten silicate reactions with plasma sprayed ytterbium silicate coatings," *Surf. Coat. Technol.*, **288** 151-162 (2016).

[57] L.H. Ahrens, "The use of ionization potentials Part 1. Ionic radii of the elements," *Geochim. Cosmochim. Acta*, **2** [3] 155-169 (1952).

[58] F. Jiang, L. Cheng, and Y. Wang, “Hot corrosion of RE_2SiO_5 with different cation substitution under calcium–magnesium–aluminosilicate attack,” *Ceram. Int*., **43** [12] 9019-9023 (2017).

[59] J. Liu, L. Zhang, Q. Liu, L. Cheng, and Y. Wang, “Calcium–magnesium–aluminosilicate corrosion behaviors of rare-earth disilicates at 1400°C,” *J. Eur. Ceram. Soc*., **33** [15-16] 3419-3428 (2013).

[60] W.D. Summers, D.L. Poerschke, D. Park, J.H. Shaw, F.W. Zok, and C.G. Levi, “Roles of composition and temperature in silicate deposit-induced recession of yttrium disilicate,” *Acta Mater*., **160** 34-46 (2018).

[61] B.-K. Jang, F.-J. Feng, K. Suzuta, H. Tanaka, Y. Matsushita, K.-S. Lee, and S. Ueno, “Corrosion behavior of volcanic ash and calcium magnesium aluminosilicate on Yb_2SiO_5 environmental barrier coatings,” *J. Ceram. Soc. Jpn*., **125** [4] 326-332 (2017).

[62] W. Vogel, *Glass Chemistry*. Springer, Berlin, Germany, 1994.

[63] E.J. Opila, “Rare earth silicate environmental barrier coatings having improved CMAS resistance,” U.S. Provisional Patent 15/218,867. 2017.

[64] R.I. Webster and E.J. Opila, “The effect of TiO_2 additions on $CaO–MgO–Al_2O_3–SiO_2$ (CMAS) crystallization behavior from the melt,” *J. Am. Ceram. Soc*., https://doi.org/10.1111/jace.16180.

[65] L. Guo, M. Li, C. Yang, C. Zhang, L. Xu, F. Ye, C. Dan, and V. Ji, “Calcium-magnesium-alumina-silicate (CMAS) resistance property of $BaLn_2Ti_3O_{10}$ (Ln=La, Nd) for thermal barrier coating applications,” *Ceram. Int*., **43** [13] 10521-10527 (2017).

[66] E.M. Zaleski, C. Ensslen, and C.G. Levi, “Melting and crystallization of silicate systems relevant to thermal barrier coating damage,” *J. Am. Ceram. Soc*., **98** [5] 1642-1649 (2015).

[67] V.L. Wiesner and N.P. Bansal, “Crystallization kinetics of calcium-magnesium aluminosilicate (CMAS) glass,” *Surf. Coat. Technol*., **259 Part C** 608-615 (2014).

[68] H. Xiao, Y. Cheng, and H. Liu, “A study on the preparation of CMAS glass-ceramics by in situ crystallization,” *Mater. Sci. Eng. C*, **431** [1-2] 191-195 (2006).

[69] A.T. Prince, “Liquidus relationships on 10% MgO plane of the system lime-magnesia-alumina-silica,” *J. Am. Ceram. Soc.*, **37** [9] 402-408 (1954).

[70] L.J. Shelestak, R.A. Chavez, J.D. Mackenzie, and B. Dunn, “Glasses and glass-ceramics from naturally occurring CaO-MgO-Al_2O_3-SiO_2 materials. II. Crystallization behavior,” *J. Non-Cryst. Solids*, **27** [1] 83-97 (1978).

[71] M. Rezvani, V.K. Marghussian, and B.E. Yekta, “Crystal nucleation and growth rates, time temperature transformation diagram, and mechanical properties of a SiO_2-Al_2O_3-CaO-MgO (R_2O) glass in the presence of Cr_2O_3, Fe_2O_3, and TiO_2 nucleants,” *Int. J. App. Ceram. Technol.*, **8** [1] 152-162 (2011).

[72] C. DeCapitani and M. Kirschen, “A generalized multicomponent excess function with application to immiscible liquids in the system CaO-SiO_2-TiO_2,” *Geochim. Cosmochim. Acta.*, **62** [23-24] 3753-3763 (1998).

[73] M. Kirschen and C. DeCapitani, “Immiscible silicate liquids in the CaO-SiO_2-TiO_2-Al_2O_3 system,” *Schweiz. Mineral. Petrogr. Mitt.*, **78** [1] 175-178 (1998).

[74] Z.P. Lu and C.T. Liu, “Glass formation criterion for various glass-forming systems,” *Phys. Rev. Lett.*, **91** 115505 (2003).

[75] R. Golovchak, M.J. Davis, P. Vullo, C. Saiyasombat, and H. Jain, “Nature of Pd and Ti metals in the structure of CMAS glass and ceramics,” *J. Am. Ceram. Soc.*, **97** [6] 1971-1978 (2014).

[76] W.D. Kingery, H. K. Bowen, and D.R. Uhlmann, *Introduction to Ceramics*. Wiley, New York, United States, 1975.

[77] S.D. Stookey and R.D. Maurer, “Catalyzed crystallization of glass – theory and practice,” In: J.E. Burke, ed. Chapter 2 in Progress in Ceramic Science, Volume 2. Pergamon Press, Oxford, England, 1961.

[78] W. Zdaniewski, "Crystallization and structure of a MgO-Al_2O_3-SiO_2-TiO_2 glass-ceramic," *J. Mater. Sci.*, **8** [2] 192-202 (1973).

[79] G.V. Shamrai, A.V. Zagorodnyuk, R.L. Magunov, and A.P. Zhirnova, "Yb_2O_3-TiO_2 system," *Inorg. Mater.*, **28** 1633-1635 (1992).

[80] N. Mizutani, Y. Tajima, and M. Kato, "Phase relations in the system Y_2O_3-TiO_2," *J. Am. Ceram. Soc.*, **59** [3-4] 168 (1976).

[81] W. Gong, D. Li, Z. Chen, F. Zheng, Y. Liu, Y. Du, and B. Huang, "Phase equilibria of the TiO_2-Y_2O_3 system," *Calphad*, **33** [3] 624-627 (2009).

[82] O. Fabrichnaya, H.J. Seifert, R. Weiland, T. Ludwig, F. Aldinger, and A. Navrotsky, "Phase equilibria and thermodynamics in the Y_2O_3-Al_2O_3-SiO_2 system," *Z. Metallkd.*, **92** [9] 1083-1097 (2001).

[83] C.R. Hubbard, "RIR - measurement and use in quantitative XRD," *Powder Diffr.*, **3** [2] 74-77 (1988).

[84] J.K.R. Weber, C.J. Benmore, G. Jennings, M.C. Wilding, and J.B. Parise, "Instrumentation for fast in situ X-ray structure measurements on non-equilibrium liquids," *Nucl. Instrum. Methods Phys. Res. Sect. A*, **624** [3] 728-730 (2010).

[85] J.K.R. Weber, A. Tamalonis, C.J. Benmore, O.L.G. Alderman, S. Sendelbach, A. Hebden, and M.A. Williamson, "Aerodynamic levitator for in situ x-ray structure measurements on high temperature and molten nuclear materials," *Rev. Sci. Instrum.*, **87** [7] 073902 (2016).

[86] A.P. Hammersley, "FIT2D: An introduction and overview," ESRF Internal Report (1997).

[87] B.H. Toby and R.B. Von Dreele, "GSAS-II: The genesis of a modern open-source all purpose crystallography software package," *J. Appl. Crystallogr.*, **46** [2] 544-549 (2013).

[88] C.A. Schneider, W.S. Rasband, and K.W. Eliceiri, "NIH Image to ImageJ: 25 years of image analysis," *Nat. Methods*, **9** 671-675 (2012).

[89] K.B. Helean, S.V. Ushakov, C.E. Brown, A. Navrotsky, J. Lian, R.C. Ewing, J.M. Farmer, and L.A. Boatner, "Formation enthalpies of rare earth titanate pyrochlores," *J. Solid State Chem*., **177** [6] 1858-1866 (2004).

[90] S. Hayun and A. Navrotsky, "Formation enthalpies and heat capacities of rear earth titanates: RE_2TiO_5 (RE=La, Nd and Gd)," *J. Solid State Chem*., **187** 70-74 (2012).

[91] A. Navrotsky, "Thermodynamics of solid electrolytes and related oxide ceramics based on the fluorite structure," *J. Mater. Chem*., **20** [47] 10577-10587 (2010).

[92] A.R. Krause, X. Li, and N.P. Padture, "Interaction between ceramic powder and molten calcia magnesia-alumino-silicate (CMAS) glass, and its implication on CMAS-resistant thermal barrier coatings," *Scr. Mater*., **111** 118-122 (2016).

[93] L.G. Shcherbakova, L.G. Mamsurova, and G.E. Sukhanova, "Rare earth titanates," *Uspekhi Khimii*., **48** 423-447 (1979).

[94] W. Dong, H. Jain, and M.P. Harmer, "Liquid phase sintering of alumina, II. Penetration of liquid phase into model microstructures," *J. Am. Ceram. Soc*., **88** [7] 1708-1713 (2005).

[95] V.L. Wiesner and N.P. Bansal, "Mechanical and thermal properties of calcium–magnesium aluminosilicate (CMAS) glass," *J. Eur. Ceram. Soc*., **35** [10] 2907-2914 (2015).

[96] A.J. Fernández-Carrión, M. Allix, and A.I. Becerro, "Thermal expansion of rare-earth pyrosilicates," *J. Am. Ceram. Soc*., **96** [7] 2298-2305 (2013).

[97] R.H. Hopkins, J. de Klerk, P. Piotrowski, M.S. Walker, and M.P. Mathur, "Thermal and elastic properties of silicate oxyapatite crystals," *J. Appl. Phys*., **44** 2456-2458 (1973).

[98] T.S. Key, K.F. Presley, R.S. Hay, and E.E. Boakye, "Total Thermal Expansion Coefficients of the Yttrium Silicate Apatite Phase $Y_{4.69}(SiO_4)_3O$," *J. Am. Ceram. Soc*., **97** [1] 28-31 (2014).

[99] N. Eustathopoulos, M.G. Nicholas, B. Drevet, and B. Drevet, *Wettability at High Temperatures*. Pergamon-Elsevier Science Ltd., Oxford, United Kingdom, 1999.

[100] T. Young, "An essay on the cohesion of fluids," *Phil. Trans. Roy. Soc.*, **95** 65-87 (1805).

[101] R.N. Wenzel, "Resistance of solid surfaces to wetting by water," *Ind. Eng. Chem.*, **28** 988-994 (1936).

[102] A.B.D. Cassie and S. Baxter, "Wettability of porous surfaces," *Trans. Faraday Soc.*, **40** 546-551 (1944).

[103] D.J. Shaw, *Introduction to Colloid and Surface Chemistry*. Butterworth Heinemann, Oxford, United Kingdom, 1966.

[104] B.T. Richards and H.N.G. Wadley, "Plasma spray deposition of tri-layer environmental barrier coatings," *J. Eur. Ceram. Soc.*, **34** [12] 3069-3083 (2014).

[105] G.C.C. Costa and N.S. Jacobson, "Mass spectrometric measurements of the silica activity in the Yb_2O_3–SiO_2 system and implications to assess the degradation of silicate-based coatings in combustion environments," *J. Eur. Ceram. Soc.*, **35** [15] 4259-4267 (2015).

[106] S.K. Rhee, "A method for determining surface energy of solids," *Mater. Sci. Eng.*, **11** [6] 311-318 (1973).

[107] H. Kim, W.H. Kim, I. Sohn, and D.J. Min, "The effect of MgO on the viscosity of the CaO-SiO_2-20 wt% Al_2O_3-MgO slag system," *Steel Res. Int.*, **81** [4] 261-264 (2010).

[108] Z. Yan, X. Lv, J. Zhang, Y. Quin, and C. Bai, "Influence of MgO, Al_2O_3 and CaO/SiO_2 on the viscosity of blast furnace type slag with high Al_2O_3 and 5 wt-% TiO_2," *Can. Metall. Quart.*, **55** [2] 186-194 (2016).

[109] J.O'M. Bockris and D.C. Lowe, "Viscosity and the structure of molten silicates," *Proc. Royal Soc. A*, **226** [1167] 423-435 (1954).

[110] G. Urbain, Y. Bottinga, and P. Richet, "Viscosity of liquid silica, silicates and alumino-silicates," *Geochim. Cosmochim. Acta*, **46** [6] 1061-1072 (1982).

[111] J.E. Shelby, *Introduction to Glass Science and Technology*. Royal Society of Chemistry, London, United Kingdom, 2005.

[112] W.H. Zachariasen, “The atomic arrangement in glass,” *J. Am. Chem. Soc.*, **54** [10] 3841-3851 (1932).

[113] M.J. Toplis and D.B. Dingwell, “Shear viscosities of CaO-Al_2O_3-SiO_2 and MgO-Al_2O_3-SiO_2 liquids: Implications for the structural role of aluminium and the degree of polymerisation of synthetic and natural aluminosilicate melts,” *Geochim. Cosmochim. Acta*, **68** [24] 5169-5188 (2004).

[114] B.O. Mysen, *Structure and properties of silicate melts*. Elsevier Science & Technology Books, Amsterdam, Netherlands, 1988.

[115] N. Saito, N. Hori, K. Nakashima, and K. Mori, “Viscosity of blast furnace type slags,” *Metall. Mater. Trans. B*, **34** [5] 509-516 (2003).

[116] D.H. Vogel, “Temperaturabhängigkeitsgesetz der Viskosität von Flüssigkeiten,” *Phys. Z.*, **22** 645-646 (1921).

[117] G.S. Fulcher, “Analysis of recent measurements of the viscosity of glasses,” *J. Am. Ceram. Soc*. **8** [6] 339-355 (1925).

[118] G. Tammann and W. Hesse, “Die abhängigkeit der viskosität von der temperatur bei unterkühlten Flüssigkeiten,” *Zeitschrift für Anorganische und Allgemeine Chemie*, **156** 245-357 (1926).

[119] Y. Bottinga and D.F. Weill, “The viscosity of magmatic silicate liquids; a model calculation,” *Am. J. Sci.*, **272** [5] 438-475 (1972).

[120] V.K. Gupta, S.P. Sinha, and B. Raj, “A model for describing viscosity-composition relationship for continuous casting mould fluxes,” *Steel India*, **21** 22-29 (1998).

[121] M. Hanao, M. Kawamoto, T. Tanaka, and M. Nakamoto, “Evaluation of viscosity of mold flux by using neural network computation,” *ISIJ Int.*, **46** [3] 346-351 (2006).

[122] G. Urbain, “Viscosity estimation of slags,” *Steel Res. Int.*, **58** [3] 111-116 (1987).

[123] P. Riboud, Y. Roux, L. Lucas, and H. Gaye, *Fachber. Hutetenprax. Metallweiterverarb.*, **19** 859- (1981).

[124] T. Iida, H. Sakai, Y. Kita, and K. Shigeno, "An equation for accurate prediction of the viscosities of blast furnace type slags from chemical composition," *ISIJ Int.*, **40** S110-S114 (2000).

[125] K.C. Mills and S. Sridhar, "Viscosities of ironmaking and steelmaking slags," *Ironmak. Steelmak.*, **26** [4] 262-268 (1999).

[126] A. Shankar, *Studies on High Alumina Blast Furnace Slags*. Royal Institute of Technology, Sweden, 2007.

[127] X.-J. Hu, Z.-S. Ren, G.-H. Zhang, L.-J. Wang, and K.-C. Chou, "A model for estimating the viscosity of blast furnace slags with optical basicity," *Int. J. Min. Met. Mater.*, **19** [12] 1088-1092 (2012).

[128] L. Gan and C. Lai, "A general viscosity model for molten blast furnace slag," *Metall. Mater. Trans. B*, **45** [3] 875-888 {2014).

[129] X.L. Tang, M. Guo, X.D. Wang, Z.T. Zhang, and M. Zhang, *Beijing Keji Daxue Xuebao*, **32** 1542- (2010).

[130] M. Suzuki and E. Jak, "Quasi-chemical viscosity model for fully liquid slag in the Al_2O_3-CaO-MgO SiO_2 system. Part II: Evaluation of slag viscosities," *Metall. Mater. Trans. B*, **44** [6] 1451-1465 (2013).

[131] Q. Shu, "A viscosity estimation model for molten slags in Al_2O_3-CaO-MgO-SiO_2 system," *Steel Res. Int.*, **80** [2] 107-113 (2009).

[132] G.-H. Zhang and K.-C. Chou, "Modeling the viscosity of alumino-silicate melt," *Steel Res. Int.*, **84** [7] 631-637 (2013).

[133] E. Stolper, "Water in silicate glasses: An infrared spectroscopic study," *Contrib. Mineral. Petrol.*, **81** [1] 1-17 (1982).

[134] D.R. Poirier and G.H. Geiger, *Transport Phenomena in Materials Processing*. Springer International Publishers, Switzerland, 2016.

[135] A. Kucuk, A.G. Clare, and L. Jones, "An estimation of the surface tension of silicate glass melts at 1400°C using statistical analysis," *Glass Technol*. **40** [5] 149-153 (1999).

[136] E.W. Washburn, "The dynamics of capillary flow," *Phys. Rev*., **17** [3] 273-283 (1921).

[137] N. Eustathopoulos, "Wetting by liquid metals—application in materials processing: The contribution of the Grenoble group," *Metals*, **5** [1] 350-370 (2015).

[138] R. Reitz, F.W. Zok, and C.G. Levi, "Reactive alloy melt infiltration for SiC composite matrices: Mechanistic insights," *J. Am. Ceram. Soc*., **100** [12] 5471-5481 (2017).

[139] R.P. Messner and Y.-M. Chiang, "Liquid-phase reaction-bonding of silicon carbide using alloyed silicon-molybdenum melts," *J. Am. Ceram. Soc*., **73** [5] 1193-1200 (1990).

[140] A.E. Scheidegger, *The Physics of Flow through Porous Media*. University of Toronto Press, Toronto, Canada, 1974.

[141] S.L. dos Santos e Lucato, O.H. Sudre, and D.B. Marshall, "A method for assessing reactions of water vapor with materials in high-speed high-temperature flow," *J. Am. Ceram. Soc*., **94** s186- s195 (2011).

[142] R.A. Golden and E.J. Opila, "A method for assessing the volatility of oxides in high-temperature high-velocity water vapor," *J. Eur. Ceram. Soc*., **36** [5] 1135-1147 (2016).